

DISSERTATION

Primary ^{222}Rn emanation standards for low-level applications

Von der Fakultät für Mathematik und Physik der
Gottfried Wilhelm Leibniz Universität Hannover

zur Erlangung des akademischen Grades
Doktor der Naturwissenschaften
Dr. rer. nat.

genehmigte Dissertation von

Florian Mertes, M. Sc.

in Kooperation mit



Physikalisch-Technische Bundesanstalt
National Metrology Institute

2023

Referent	Prof. Dr. Clemens Walther Institut für Radioökologie und Strahlenschutz Gottfried Wilhelm Leibniz Universität Hannover
Korreferent	Prof. Dr. em. Rolf Michel Institut für Radioökologie und Strahlenschutz Gottfried Wilhelm Leibniz Universität Hannover
Korreferent	Prof. Dr. Klaus Wendt Institut für Physik Johannes Gutenberg-Universität Mainz
Tag der Promotion	25.09.2023

Zusammenfassung

Keywords: Radon, Emanation, primärer Standard, Inversion, Aktivitätskonzentration, Referenzatmosphären, Kalibrierung

In dieser Dissertation wird die Darstellung von Referenzatmosphären des radioaktiven Edelgases ^{222}Rn im Bereich niedriger Aktivitätskonzentrationen, unter 300 Bq m^{-3} , beschrieben. Diese sind beispielsweise zur, auf das internationale Einheitensystem SI rückgeführten, Kalibrierung von Radonmessgeräten notwendig. Dies ist Voraussetzung für die internationale Vergleichbarkeit und Harmonisierung von Radonmessungen.

Dieser Konzentrationsbereich macht es notwendig, dass die Herstellung solcher Referenzatmosphären nicht mittels abklingender, gasförmiger ^{222}Rn Standards, sondern mit sogenannten Emanationsquellen erfolgt. Dies sind ^{226}Ra Quellen die derart beschaffen sind, dass ein Teil des entstehenden Tochternuklids ^{222}Rn kontinuierlich freigesetzt wird. Dadurch kann beispielsweise in einem geschlossenen Referenzvolumen im Laufe einiger Halbwertszeiten ein Gleichgewichtszustand mit einer zeitlich stabilen Aktivitätskonzentration hergestellt werden.

Der Grad dieser Freisetzung ist abhängig vom Herstellungsverfahren der Quelle und den Umgebungsparametern, wie beispielsweise Temperatur und relative Luftfeuchte, was im Laufe dieser Arbeit empirisch belegt wird. Verschiedene Ansätze zur Herstellung solcher Quellen auf dem Prinzip einer Dünnschichtgeometrie des ^{226}Ra wurden untersucht, nämlich die Elektrodeposition, die Ionenimplantation und die physikalische Gasphasenabscheidung. Die Rückführung der so deponierten ^{226}Ra Aktivität auf das SI erfolgte, für ^{222}Rn Emanationsquellen erstmals, über die Absolutmethode der Alphaspektrometrie unter definiertem Raumwinkel.

Die Bestimmung der Emanation erfolgte zunächst im Gleichgewichtszustand der Quellen basierend auf der Gammaspektrometrie der kurzlebigen ^{222}Rn Folgeprodukte. Im Laufe der Arbeit konnte gezeigt werden, wie sich solche Messungen durch Methoden der statistischen Inversion auf dynamische Verhältnisse übertragen lassen. Dadurch können erstmals dynamische Änderungen der Emanation, beispielsweise in Folge von Änderungen in den Umgebungsparametern, messtechnisch, zunächst basierend auf der Gammaspektrometrie, erfasst werden.

Auf Basis dieser Erkenntnis wurde ein System, der integrated Radon Source/Detector (IRSD), konzeptioniert und implementiert, welches die ^{222}Rn Quelle mit einem alphaspektrometrischen Detektor vereint. Dieses System erlaubt es kontinuierlich durch hocheffiziente Alphaspektrometrie die verbleibende ^{222}Rn Aktivität in der Quelle zu bestimmen und mittels der statistischen Inversion annähernd in Echtzeit die Emanation von ^{222}Rn zu bestimmen, selbst wenn diese nur wenige ^{222}Rn Atome pro Sekunde beträgt. Somit ist es erstmals möglich Referenzatmosphären auch im typischen Konzentrationsbereich der Außenluft rückgeführt und unter wechselnden klimatischen Bedingungen darzustellen. Abschließend beinhaltet diese Dissertation praktische, zum Teil neue, Anwendungsmethoden für die Kalibrierung von Radonmessgeräten mit Hilfe der entwickelten Emanationsquellen.

Abstract

Keywords: Radon, Emanation, Primary standard, Inversion, Activity concentration, reference atmospheres, calibration

In this dissertation, the preparation of reference atmospheres of the radioactive noble gas ^{222}Rn in the range of low activity concentrations, under 300 Bq m^{-3} , is described. These are necessary, for example, for the calibration of radon measuring instruments traceable to the international system of units, the SI. This is integral for international comparability and harmonization of radon measurements. This concentration range requires that the production of such reference atmospheres is not done by means of decaying, gaseous ^{222}Rn standards, but with so-called emanation sources. These are ^{226}Ra sources which are of such nature, that a part of the daughter nuclide ^{222}Rn is continuously released. Thus, for example, in a closed reference volume, an equilibrium is established at a time-stable activity concentration over the course of a few half-lives.

The degree of this release depends on the source manufacturing process and details and environmental parameters such as the temperature and relative humidity, which is empirically demonstrated throughout this work. Different approaches to fabricate such sources on the principle of a thin-film geometry of ^{226}Ra have been investigated, namely electrodeposition, ion implantation and physical vapor deposition. The traceability of the ^{226}Ra activity deposited in this way to the SI was performed, for the first time for such emanation sources, via the absolute method of defined solid angle alpha-particle spectrometry.

The emanation was initially determined only in its equilibrium state based on gamma-ray spectrometry of the short-lived ^{222}Rn progeny. In the course of this work, it could be shown how such measurements can be adapted to dynamic conditions by means of statistical inversion, whereby for the first time dynamic changes of the emanation, for example as a consequence of changes in the environmental parameters, can be quantified, initially based on gamma-ray spectrometry.

Based on this insight, a system, the so-called integrated Radon Source/Detector (IRSD), was conceptualized and implemented, which combines the ^{222}Rn source with an alpha-spectrometric detector. This system allows for continuous, highly efficient alpha-particle spectrometry to determine the remaining ^{222}Rn activity in the source and, using statistical inversion, to quantify in near real time the emanation of ^{222}Rn , even if it only amounts to some ^{222}Rn atoms per second. This makes it possible for the first time to realize reference atmospheres even in the typical concentration range of outdoor air and under changing climatic conditions. Finally, this dissertation contains practical and partly new application methods for the calibration of radon measurement instruments using the developed emanation sources.

Contents

1	Introduction	1
1.1	Radon and Radium	1
1.2	Aim and motivation of this work	2
1.3	Traceability chains and ^{226}Ra and ^{222}Rn standards	4
2	Theory and background of applied methods	6
2.1	Radioactive decay kinetics	6
2.2	Emanation of ^{222}Rn as a time-dependent quantity	7
2.2.1	Emanation into a closed volume	10
2.2.2	Emanation into open volumes	11
2.2.3	Statistical inversion	12
	Recursive Bayesian estimation	14
	Recursive Bayesian estimation in linear, time-invariant dynamical models	16
	Considerations for an application to radioactivity measurements	18
2.3	Measurement techniques	23
2.3.1	Spectrometric methods	23
	Spectrometry of γ -radiation	23
	Spectrometry of α -particles	24
2.3.2	Defined solid-angle alpha-particle spectrometry	25
	Determination of the effective counting efficiency	25
2.3.3	Autoradiography	29
2.3.4	Data analysis	30
2.4	Source preparation techniques	35
2.4.1	Purification of radium	35
2.4.2	Electrodeposition of radium	36
2.4.3	Ion implantation	38
	Resonant laser ionization	40
	Mass spectrometry using surface ionization	41
2.4.4	Physical vapor deposition	41
	Selection of a suitable ^{226}Ra -compound	43
	Choice of evaporator geometry	44
2.4.5	Comparison of α -particle spectra of the differently produced sources	46
3	Publication I: A new primary Rn-222 emanation standard	48
4	Publication II: Ion implantation of ^{226}Ra for a primary ^{222}Rn emanation standard	54
5	Publication III: Approximate sequential Bayesian inference to estimate ^{222}Rn emanation from ^{226}Ra sources from spectral time-series	65
6	Publication IV: Development of ^{222}Rn emanation sources with integrated quasi 2π active monitoring	81

7	Suitability of solid-state scintillators to monitor ^{222}Rn emanation	104
8	Case Studies	108
8.1	ANSTO 200 L static calibration at the ambient level	108
8.2	ANSTO 200 L pulse calibration method	110
8.3	AlphaGuard Calibration using IRSD and State-Space Modeling	119
8.3.1	Model specification	119
8.3.2	Experimental results in a 50 L reference volume	120
8.3.3	Experimental results in a 600 L reference volume	122
8.3.4	Comparison to a source from the Czech Metrology Institute	122
9	Discussion and Outlook	125
A	Derivation of integrated Gaussian process joint density	128
B	Monte-Carlo method for solid-angle calculations	132
	Bibliography	135
	Declaration of Authorship	144
	Curriculum Vitae	145
	Publications	146
	Acknowledgments	148

Chapter 1

Introduction

1.1 Radon and Radium

Radium, specifically its isotope ^{226}Ra , is generated within the decay chain of primordial ^{238}U . While it is one of the rarest elements on earth with an average concentration of only some 10^{-12} % in the earth's crust, it is ubiquitous in nature. During its discovery by Pierre and Marie Curie, it was found to have similar chemical properties as its lighter earth-alkaline homologue barium, and so it was discovered among insoluble BaSO_4 during the processing of Pitchblende, an uranium ore. Radium is a very reactive metal with a standard reduction potential of -2.8 V (Bratsch, 1989). Therefore, its known chemical occurrences are in the form of Ra^{2+} within ionic compounds. Even with chelating agents, radium forms only comparably weak complexes and consequently the chemistry of radium is relatively shallow (Kirby and Salutsky, 1964). Just like its barium homologues, the sulfate, chromate and carbonate salts of radium are hardly soluble in water, whereas the halides and the nitrate are the most important soluble forms. Barium is commonly used as an inactive carrier of radium, since no stable isotopes of radium exist.

^{226}Ra undergoes α -decay with a half-life of approximately 1600 a, mainly by the emission of a 4.6 MeV α -particle to a 186 keV isomeric state of ^{222}Rn (5.95 %) and a 4.78 MeV α -particle to the ground state of ^{222}Rn (94.038 %) (Bé et al., 2008). The 186 keV level of ^{222}Rn has a high internal conversion coefficient, which results in an emission probability of only 3.5 % for a 186 keV γ -ray (Marouli et al., 2017).

Consequently, ^{222}Rn (henceforth also referred to as radon) is generated, where ^{226}Ra is present, which is practically everywhere on earth. Radon is a noble gas and is therefore colorless, odorless and chemically inert. Due to this, it has a very high mobility in the environment. From its sources, for example in soil, it can diffuse through the pore space and be released into the ambient air, where it takes part in transport processes like diffusion and advection and accumulates within buildings, especially when the exchange with fresh ambient air is impaired by well insulated side walls and windows.

Radon itself decays by α -decay with a half-life of 3.8 days into the radioactive ^{218}Po . The decay is not accompanied by significant emission of γ -rays. Along the decay chain of ^{218}Po , the isotopes ^{214}Pb and ^{214}Bi emit strong γ -rays, mostly in the energy range between 240 keV and up to 2.5 MeV, however, most of the excess energy emitted along the decay chain to somewhat more stable ^{210}Pb is carried by the emitted α -particles of short-lived ^{218}Po , ^{214}Po and ^{210}Po . The inhalation of aerosols covered with ^{218}Po and ^{214}Po from the decay of airborne ^{222}Rn is known to cause significant radiation dose to the lungs and therefore, exposure to elevated levels of radon is supposed to be a serious health concern. Exposure to radon causes the most significant contribution to the annual effective dose from natural sources experienced by the general public, and was estimated to be one of the most important causes for

lung cancer, second, to this day, only to smoking. The relative excess risk for lung cancer is assumed to follow a *linear no threshold model* (LNT) with the ^{222}Rn activity concentration, e.g. (Darby et al., 2005) among others. For this reason, many states implemented regulation concerning occupational as well as residential ^{222}Rn activity concentration levels. For example, residential ^{222}Rn activity concentration in buildings among EU member states is addressed in the Council directive 2013/59/EURATOM (European Union, 2013), where the *Basic Safety Standards* (BSS) laid down therein stipulate a reference level of $300 \text{ Bq} \cdot \text{m}^{-3}$, after which ^{222}Rn mitigation actions should be taken. The World Health Organization (WHO) suggested that mitigating actions should generally be taken if indoor concentrations exceed even $100 \text{ Bq} \cdot \text{m}^{-3}$ (World Health Organisation, 2021; World Health Organisation, 2009).

^{222}Rn has a very well known decay behavior, and besides the harmful effects caused by its radiation does not chemically or biologically interact with the environment apart from transportation processes. Since it is radioactive with a comparably high specific activity, radon concentration can be measured much more easily and with orders of magnitude lower detection limits than inactive noble gases. For example, the stipulated $300 \text{ Bq} \cdot \text{m}^{-3}$ in the BSS corresponds to the remarkably low concentration of only approximately one ^{222}Rn atom per 10^{17} air molecules, and this concentration is even much higher than the outdoor levels. With special instruments designed for ambient level measurements, detection limits several orders of magnitude smaller can be achieved. Consequently, ^{222}Rn activity concentration measurements have numerous interesting applications in the environmental sciences as a tracer or proxy. Examples include its use as a tracer of terrestrial influence on air masses (Chambers et al., 2016; Chambers et al., 2018), as a tool for estimating integrated local- to regional-scale emission of trace gases with similarly distributed sources, such as methane or carbon-dioxide (Biraud et al., 2002; Laan et al., 2010; Levin, 1987; Levin et al., 2021) or for classification of the atmospheric mixing state (Perrino et al., 2001; Williams et al., 2013; Williams et al., 2016; Chambers et al., 2019b; Chambers et al., 2019a), among others.

For both these scientific communities, the radiation protection as well as for the application of radon-based methods in the environmental sciences, traceable ^{222}Rn measurements even at low activity concentrations are needed. This requires a profound definition and dissemination of the SI units of activity and activity concentration concerning ^{222}Rn in air, *becquerel* and *becquerel per cubic meter* respectively, with the smallest possible uncertainty in the respective range. In this range, but especially at the ambient levels below $100 \text{ Bq} \cdot \text{m}^{-3}$, the metrological infrastructure is lacking, for example, no reliable traceability chains and associated methods for dissemination for the ^{222}Rn activity concentration below $300 \text{ Bq} \cdot \text{m}^{-3}$ exist to this day, as indicated in the database for *Calibration and Measurement Capabilities* (CMC) of the Bureau International des Poids et Mesures (BIPM) (BIPM, 2022). This is addressed in the EMPIR (*European Metrology Programme for Innovation and Research*) projects *MetroRADON* and *traceRadon*, which aim to provide a solid metrological basis for the activity concentration of ^{222}Rn in air in the regime below $300 \text{ Bq} \cdot \text{m}^{-3}$ and the ambient concentration levels far below $100 \text{ Bq} \cdot \text{m}^{-3}$ respectively. The present work was carried out in the scope of these two projects.

1.2 Aim and motivation of this work

This cumulative dissertation deals with new methods to realize primary ^{222}Rn emanation standards, independent of the Hönigschmid standards (section 1.3) in the regime between $10 \text{ Bq} \cdot \text{m}^{-3}$ corresponding to the ambient levels and up to several $100 \text{ Bq} \cdot \text{m}^{-3}$, more typical of indoor ^{222}Rn activity concentrations, where currently, no traceability to the SI exists (

BIPM, 2022). Emanation standards, in this work, refer to sources consisting of ^{226}Ra , that release a certain, known amount of ^{222}Rn per unit time.

It contains of the following publications

Mertes, F., S. Röttger, and A. Röttger (Oct. 2019). "A new primary emanation standard for Radon-222". In: *Applied Radiation and Isotopes* 156, p. 108928. DOI: 10.1016/j.apradiso.2019.108928.

Mertes, F., N. Kneip, R. Heinke, T. Kieck, D. Studer, F. Weber, S. Röttger, A. Röttger, K. Wendt, and C. Walther (Dec. 2021). "Ion implantation of ^{226}Ra for a primary ^{222}Rn emanation standard". In: *Applied Radiation and Isotopes* 181, p. 110093. DOI: 10.1016/j.apradiso.2021.110093.

Mertes, F., S. Röttger, and A. Röttger (Apr. 2023). "Approximate sequential Bayesian filtering to estimate ^{222}Rn emanation from ^{226}Ra sources using spectral time series". In: *Journal of Sensors and Sensor Systems* 12, pp. 147–161. DOI: 10.5194/jsss-12-147-2023.

Mertes, F., S. Röttger, and A. Röttger (Jan. 2022). "Development of ^{222}Rn Emanation Sources with Integrated Quasi 2π Active Monitoring". In: *International Journal of Environmental Research and Public Health* 19, p. 840. DOI: 10.3390/ijerph19020840.

To achieve the required standardization of the ^{226}Ra activity, in this work, defined solid angle α -particle spectrometry is applied, section 2.3.2, while the emanation of ^{222}Rn is measured by the assessment of residual ^{222}Rn in the respective emanation source using different methods involving γ -ray and, for the first time, direct α -particle spectrometry under ambient conditions. Three source production methods for ^{226}Ra -sources were examined with respect to their performance in α -particle spectrometry as well as concerning the magnitude and stability of ^{222}Rn emanation including electrodeposition, Publication I, ion implantation, Publication II, and thermal physical vapor deposition, Publication IV. While ion implantation of ^{226}Ra has not been reported before, physical vapor deposition methods for ^{226}Ra have been previously published, albeit scarcely and mainly for accelerator target production. On the other hand, electrodeposition, as used in Publication I, is a well established technique in the analysis of ^{226}Ra mostly from environmental samples.

Ideally, the emanation from the produced emanation sources is stable with respect to all environmental parameters and time, however, in practice this was not experienced to be a readily achievable characteristic and thus, a method to derive the emanation from on-line measurements was developed in Publication III. In Publication IV, this method is used to directly integrate the ^{226}Ra source with an α -spectrometric detector, which thus allows continuous surveillance of low-level ^{222}Rn emanation at the smallest achievable uncertainty to this day, further denoted as the *Integrated ^{222}Rn Source/Detector* (IRSD). The IRSD provides a unique method to correct for ambient environmental influences, such as relative humidity, of the emanation, and therefore, is especially well suited for future use in in-situ calibration procedures.

In conjunction with these publications, a discussion of solid-state scintillator based γ -ray spectrometers for the same purpose is given based on experimental measurements and theoretical considerations in chapter 7. A thorough theoretical discussion, extending the current knowledge, of how the produced source and the developed surveillance system can be used to realize reference atmospheres in different scenarios is given in chapter 2. Finally, chapter 8 illustrates specific application scenarios of the developed methods, including the first SI-traceable calibrations of a ^{222}Rn monitor at the ambient concentration levels with the sources presented in Publication II, providing insight of how the produced sources may be applied in practice. Therein, a previously scarcely used method for pulsed calibration, with

the potential of future *in-situ* applications was investigated for the calibration of ^{222}Rn monitors with very high active volumes, as usually employed in the environmental sciences.

1.3 Traceability chains and ^{226}Ra and ^{222}Rn standards

For comparative measurements and to determine the atomic weight of radium, Prof. Dr. Otto Hönigschmid prepared practically pure $^{226}\text{RaCl}_2$ in 1912 (Hönigschmid, 1912) and 1934 after invitation by the International Radium Standards Commission. ^{226}Ra was the first radioactive isotope to be standardized, and through its mass defined the unit of activity used at the time, the *curie*, by gravimetry. While the unit of activity since then changed to its current SI unit, the *becquerel*, even to this day many of the ^{226}Ra standards, e.g., solutions, provided by the National Metrology Institutes (NMIs) like the Physikalisch-Technische Bundesanstalt (PTB, Germany), the National Institute of Science and Technology (NIST, USA), the National Physical Laboratory (NPL, UK) and the Czech Metrological Institute (CMI) are in some form related to the original national primary standards prepared by Hönigschmid and handed out to several countries in 1937. The activity of those primary standards was defined through the mass of $^{226}\text{RaCl}_2$ contained in a flame-sealed ampoule. For example, standard solutions related to the primary Hönigschmid standard can be prepared by gravimetric dilutions and by comparative measurement instruments for example with ionization chambers, which are used to establish a traceability chain, keeping track of all intermediate secondary standards. Since the release of ^{222}Rn from any form of ^{226}Ra is rarely a quantitative process, establishing a traceability chain of the activity of ^{222}Rn obtained in this way to the Hönigschmid ^{226}Ra standard is difficult and prone to errors and requires subsequent secondary radiometric techniques like γ -ray spectrometry.

The seminal work of (Picolo, 1996) provided an absolute method to directly measure ^{222}Rn gas for the first time, which can be used to realize gaseous ^{222}Rn activity standards independent of the Hönigschmid standards in terms of the meter and the second. In this method, which nowadays is applied, among others, at the PTB and the Laboratoire National Henri Becquerel (LNHB, France), ^{222}Rn generated by ^{226}Ra is condensed on a cold point using a cryostat. The α -particles emitted from the condensed ^{222}Rn are measured spectrometrically under a defined and well known solid angle. The determined amount of ^{222}Rn is subsequently transferred quantitatively into reference containers intended for the dissemination of the defined activity, e.g., to produce reference atmospheres of known concentration for the calibration of airborne radon measurement devices. A significant drawback pointed out and addressed in the work of (Linzmaier and Röttger, 2013) at PTB, also discussed in (Hofmann et al., 2015), results from the decaying nature of reference atmospheres generated by this procedure. During the exponential decay of the initial activity concentration, only a limited number of decays are observed and if radon measuring devices of low counting efficiency are intended to be calibrated at the low activity concentration range, the Poisson statistics of the counting process results in high statistical uncertainty of the calibration factors obtained in this way (Röttger and Honig, 2011).

The immediate solution to this shortcoming is to replace the decaying airborne ^{222}Rn by fresh ^{222}Rn nuclei, such that in a closed and known volume, an equilibrium activity concentration is established. This is achieved by so called ^{222}Rn emanation sources, which are sources containing ^{226}Ra that release a known quantity of the generated daughter nuclide.

One of the earliest ^{222}Rn emanation standards was constructed at the National Institute of Science and Technology (NIST) and consists of a ^{226}Ra solution surrounded by a polymer capsule through which the generated ^{222}Rn is released by diffusion, however, the authors mention several concerns with this technique, including the loss of liquid by evaporation

through the sealing polymer (Colle et al., 1990). Relatively decent stability with respect to environmental parameters was reported, supposedly since the humidity content of the polymer capsule is always in equilibrium with the liquid inside in contrast to the outside airborne humidity.

At PTB, traceable low-level ^{222}Rn emanation sources were first constructed throughout the work of (Linzmaier and Röttger, 2013). The ^{222}Rn activity released from these sources is known by gravimetric drop-casting of a ^{226}Ra solution and thus, related back to the Hönigschmid standard and comparative γ -ray measurements of the residual ^{222}Rn progeny in the source. Reportedly, the ^{222}Rn release of the Linzmaier sources is in the range of $(16 \pm 3) \text{ s}^{-1}$ to $(957 \pm 17) \text{ s}^{-1}$, however, relative humidity was observed to impact the emanation of these strongly and the emanation was observed to drop rapidly when low amounts of ^{226}Ra activity are employed. In their work, these sources are used under static conditions, i.e., placed inside of ^{222}Rn tight volumes to realize the reference atmospheres. To correct all potential environmental influences, (Linzmaier and Röttger, 2013; Röttger et al., 2014) monitored the sources during their operation using costly and bulky high-purity germanium detectors, which makes it infeasible to disseminate the unit to other institutes in this way.

Nowadays, the CMI provides ^{222}Rn sources, with traceable ^{226}Ra activity to the Hönigschmid standards and with supposedly almost complete ^{222}Rn emanation by dispersing fatty acid ^{226}Ra salts into a silicon rubber support. Currently, the range of these sources spans some 10^4 to $10^6 \text{ Bq } ^{226}\text{Ra}$ and no experimental evidence concerning the stability with respect to environmental parameters has been made available to the scientific community thus far. An effort to extend the range to the lower levels is currently being undertaken, reported among others in (Fialova et al., 2020). The CMI sources are generally designed to be used in a flow-through mode, i.e., the mean activity concentration within a reference volume is controlled by an intended leakage using a mass-flow controller (MFC) and a theoretical model, assuming the instantaneous mixing within the reference volume and the negligibility of diffusive transport across the leak.

The target of the developments of this work is to extend the currently achievable range of ^{222}Rn emanation at improved uncertainties, such that reference atmospheres in the ambient range can be generated, to reveal, quantify or correct potential environmental influences of the constructed sources, and, ideally, to provide traceability to the SI that is independent of the legacy of the Hönigschmid standards.

Chapter 2

Theory and background of applied methods

2.1 Radioactive decay kinetics

While the radioactive decay of a single nucleus is a purely stochastic process, the decay of a large enough population of nuclei can be described by a first order decay equation working on the expected values of the decay, with a certain, nuclide specific decay constant λ . A system of coupled differential equations with constant coefficients is obtained when the decay of a radioactive nucleus results in another radioactive nucleus, for example, as during the decay chain of ^{226}Ra . This results in distinct equilibria of the activity of each isotope in the chain, depending on the ratio of the decay constants involved along the chain, referred to as secular and transient equilibria respectively. In the secular equilibrium, which describes the case when the parent nucleus has a far greater half-life than the daughter(s), the activity of the daughter equilibrates to amount to the same as the mother isotope, with a characteristic ingrowth curve described by their own decay constants. This is the type of equilibrium encountered in both, the relationship between the ^{226}Ra and ^{222}Rn activity of a sample (provided that no ^{222}Rn is released) and between ^{222}Rn and its short-lived progeny ^{218}Po and following. The exact solution to the resultant set of differential equations is historically expressed in terms of the Bateman equations (Bateman, 1910). More recently, and in this work, however, it was experienced to be more convenient to express the kinetics in terms of vector-valued differential equations (Pressyanov, 2002; Amaku et al., 2010; Levy, 2019). For unbranched and undistorted radioactive decay starting from a nuclide indexed by n of N_n atoms, the first order decay equations may be written as

$$d\mathbf{N} = d \begin{bmatrix} N_0 \\ N_1 \\ \vdots \\ N_n \end{bmatrix} = \begin{bmatrix} -\lambda_0 & \lambda_1 & 0 & \dots \\ 0 & -\lambda_1 & \lambda_2 & \dots \\ \dots & \dots & \dots & \dots \\ 0 & 0 & 0 & -\lambda_n \end{bmatrix} \begin{bmatrix} N_0 \\ N_1 \\ \vdots \\ N_n \end{bmatrix} dt \quad (2.1)$$

where \mathbf{N} denotes a vector of the stacked, nuclide specific number of atoms and λ_i denotes the decay constant of the i -th nuclide.

Given the relationship

$$A_i = \lambda_i N_i \quad (2.2)$$

equation (2.1) can be equivalently expressed in terms of the nuclide specific activities A_i , stacked in a vector \mathbf{A}

$$d\mathbf{A} = d \begin{bmatrix} A_0 \\ A_1 \\ \vdots \\ A_n \end{bmatrix} = \begin{bmatrix} -\lambda_0 & \lambda_0 & 0 & \dots \\ 0 & -\lambda_1 & \lambda_1 & \dots \\ \dots & \dots & \dots & \dots \\ 0 & 0 & 0 & -\lambda_n \end{bmatrix} \begin{bmatrix} A_0 \\ A_1 \\ \vdots \\ A_n \end{bmatrix} dt = \mathbf{F} \mathbf{A} dt \quad (2.3)$$

Note, that the fundamental matrix \mathbf{F} in (2.3) may always be constructed in a way such that it consists only of the respective decay constants on its diagonal and first super-diagonal, if and only if the decay chain does not involve branching. The solution to Equation (2.3) is given in terms of the Matrix exponential function, which can be evaluated numerically and symbolically in some cases, for example, by diagonalization of \mathbf{F} , e.g. through its Eigendecomposition. It is easy to then see that $\mathbf{A}(t)$ is related to $\mathbf{A}(t_0)$ by the following linear map, the solution to the initial value problem in Equation (2.3),

$$\mathbf{A}(t) = \exp(\mathbf{F}(t - t_0)) \mathbf{A}(t_0) \quad (2.4)$$

which allows for straight forward uncertainty propagation, when $\mathbf{A}(t_0)$ has a multivariate Gaussian distribution. If $\mathbf{A}(t_0)$ follows a multivariate Gaussian distribution of covariance matrix Σ_0 , the covariance matrix of $\mathbf{A}(t)$, Σ_A is given by

$$\Sigma_A = \exp(\mathbf{F}(t - t_0)) \Sigma_0 \exp(\mathbf{F}(t - t_0))^T \quad (2.5)$$

if the uncertainty contributions of \mathbf{F} are negligible.

(Moler and Loan, 2003) give an overview over possible methods to compute the Matrix exponential numerically, however, for the fundamental matrices \mathbf{F} encountered throughout this work, it was found to be easily computed by symbolic computation of the Eigenvalues and corresponding Eigenvectors of \mathbf{F} , which ultimately reflect the factors contained in the original Bateman equations. Despite this, routines for numerical evaluation of the Matrix exponential are readily available in most mathematical computing packages such as MatLab, Mathematica, SciPy (Virtanen et al., 2020) and alike.

2.2 Emanation of ^{222}Rn as a time-dependent quantity

Under certain circumstances, the generated ^{222}Rn is released from materials containing ^{226}Ra , throughout this work referred to as ^{222}Rn emanation. In the environment, as mentioned before, this leads to the release of ^{222}Rn into the pore-space of a soil, where it subsequently takes part in diffusion processes that ultimately lead to its release (exhalation) into the ambient air. The recoil energy of 86 keV carried by the emerging ^{222}Rn nuclei following the α -decay of ^{226}Ra is thought to have a central role in this process, leading to the ejection of ^{222}Rn nuclei from grains of the soil into the air-filled pore-space. According to calculations with the computer program *the Stopping and Range of Ions in Matter*, SRIM, (Ziegler et al., 2010), 86 keV ^{222}Rn nuclei possess a projected range of several μm in ambient pressure air, but only several 10 nm in typical solid materials like SiO_2 . It was previously observed that the amount of released ^{222}Rn from the soil correlates strongly with its moisture content. It is thought, that this is due to both, the strong effect of absorbed water on the projected range of the emerging ^{222}Rn nuclei, as well as the impact of moisture on the diffusion properties

and the amount of air filled pore space, (Miklyaev and Petrova, 2012; Zhou et al., 2020; Porstendörfer, 1994; Strong and Levins, 1982; Strandén et al., 1984; Megumi and Muro, 1974) among others. The water content of soil thus impacts both the emanation, i.e. the release of ^{222}Rn into the pore-space of the soil as well as the exhalation, i.e. the ability of the pore-space ^{222}Rn to be released into the ambient air. In a similar vein, ^{222}Rn is ejected from the crystals of a poly-crystalline material containing ^{226}Ra , and subsequently diffuses away from the material. For thin-layers of ^{226}Ra , it may be estimated that the process of ^{222}Rn exhalation is even more strongly dominated by the recoiling of ^{222}Rn atoms, rather than the diffusion of ^{222}Rn through the very small bulk volume of the layer, i.e. that the diffusion length of ^{222}Rn is many orders of magnitude higher than the layer-thickness. For this reason, and because of the associated measurement techniques covered in section 2.3.2 and following, thin-layers of ^{226}Ra have been chosen as a starting point for the construction of ^{222}Rn emanation sources throughout this work.

The most fundamental relationship between the released ^{222}Rn from a ^{226}Ra source, conservation of amount of substance, can be expressed by the following first-order continuity equation,

$$\frac{\partial N_{^{222}\text{Rn}}^s}{\partial t} = -\lambda_{^{222}\text{Rn}} N_{^{222}\text{Rn}}^s + \lambda_{^{226}\text{Ra}} N_{^{226}\text{Ra}}^s - \eta(t) \quad (2.6)$$

where N_i^s describes the number of atoms in the emanation source concerning the nuclide i , λ_i the respective decay constants and $\eta(t)$ denotes the amount of released ^{222}Rn nuclei per unit time as a function of time.

Using relationship (2.2), equation (2.6) may also be expressed in terms of activities as

$$\frac{\partial A_{^{222}\text{Rn}}^s}{\partial t} = -\lambda_{^{222}\text{Rn}} A_{^{222}\text{Rn}}^s + \lambda_{^{226}\text{Ra}} A_{^{226}\text{Ra}}^s - \lambda_{^{222}\text{Rn}} \eta(t) \quad (2.7)$$

where $A_{^{222}\text{Rn}}^s$ and $A_{^{226}\text{Ra}}^s$ describe the activity of the source concerning ^{222}Rn and ^{226}Ra respectively, λ_i describes the respective decay constants and $\eta(t)$ denotes the amount of released ^{222}Rn nuclei per unit time as a function of time.

(Linzmaier and Röttger, 2013) introduced an emanation coefficient χ without rigorous derivation, understood as the ratio of generated and released ^{222}Rn nuclei of an emanation source. They define

$$\chi = 1 - \frac{A_{^{222}\text{Rn}}^s}{A_{^{226}\text{Ra}}^s} \quad (2.8)$$

where $A_{^{222}\text{Rn}}^s$ and $A_{^{226}\text{Ra}}^s$ describe the activity of the source concerning ^{222}Rn and ^{226}Ra respectively and χ describes the emanation coefficient.

The measurement of the emanation was therein realized by measuring the activity of the retained short-lived γ -ray emitting ^{222}Rn progeny, ^{214}Pb and ^{214}Bi , in equilibrium with ^{222}Rn , in comparison with a reference source of similar geometry for which $\chi = 0$ is assumed, i.e., by sealing against the emanation of ^{222}Rn . (Linzmaier and Röttger, 2013) claimed that this allows to perform on-line emanation measurements (cf. Fig 3.9 in (Linzmaier, 2013)) using high purity germanium detectors (HPGe), however, as will be pointed out below, this procedure is only valid in the steady-state. It should, however, be noted, that this observation does not change the general applicability of the former calibration methods described,

among others in (Röttger et al., 2014), because the method was only applied once steady-states had been reached, i.e. after 5-10 half-lives of ^{222}Rn .

While their procedure was directly adopted for the emanation measurements in Publication I and Publication II of this work, it does not allow for direct near real-time measurements of the emanation. This follows from theoretical considerations and was commonly observed in the experimental spectrometric time-series collected throughout this work, for example, in response to changes of the relative humidity. Based on the first principle of conservation of amount of substance encoded in (2.7), it can be readily shown that (2.8) only applies in a steady state by observing that, by an equivalent definition, $\chi(t) = \frac{\eta(t)}{A_{226\text{Ra}}^s}$, which yields

$$\chi(t) = 1 - \frac{A_{222\text{Rn}}^s}{A_{226\text{Ra}}^s} - \frac{1}{\lambda_{222\text{Rn}} A_{226\text{Ra}}^s} \frac{\partial A_{222\text{Rn}}^s}{\partial t} \quad (2.9)$$

Conversely, considering the rigorous solution to (2.7) expressed using the formalism introduced in section 2.1, trivially found, e.g., by the *Integrating Factor* method,

$$\begin{bmatrix} A_{222\text{Rn}}^s \\ A_{226\text{Ra}}^s \end{bmatrix}_{(t)} = \exp[\mathbf{F}(t - t_0)] \begin{bmatrix} A_{222\text{Rn}}^s \\ A_{226\text{Ra}}^s \end{bmatrix}_{(t_0)} - \int_{t_0}^t \exp[\mathbf{F}(t - \tau)] \begin{bmatrix} \lambda_{222\text{Rn}} \\ 0 \end{bmatrix} \eta(\tau) d\tau \quad (2.10)$$

where $\mathbf{F} = \begin{bmatrix} -\lambda_{222\text{Rn}} & \lambda_{222\text{Rn}} \\ 0 & -\lambda_{226\text{Ra}} \end{bmatrix}$

reveals the inverse nature of this type of measurement, which was not pointed out previously. As can be observed by the right-hand side of (2.10), the measurement of the residing activity of ^{222}Rn in the source only allows to observe a convolution integral of the time-dependent emanation, $\eta(t)$. Through correlation of the diffusion properties of the source material with, e.g., the relative humidity, a time dependence of $\eta(t)$ is suggested. In contrast to the statements made by (Linzmaier and Röttger, 2013), and the line of thought that is conveyed in (2.8), $\eta(t)$ and equivalently $\chi(t)$ can only be recovered from the observed measurements of $A_{222\text{Rn}}$ by a mathematical deconvolution procedure in non-steady state regimes. It is well known, that such inversion methods need to address the resultant amplification of high frequency components in the signal, i.e., the statistical noise and that commonly only non-unique solutions exist to these ill-posed problems. Specifically, the convolution kernel in the convolution contained in (2.10) has an infinitely long response characteristic, characterized by the half-life of ^{222}Rn . Therefore, the direct approach of (2.8) is unsuitable for a quantitative characterization of the complex interdependencies of the emanation of each source with each of the environmental parameters, since for each environmental condition, the source needs to first re-equilibrate in about 20 to 30 days before (2.8) can be applied. As such, application of the previously available procedures is limited to situations, in which the source behaviour is stable, or can be stabilized through controlled conditions, over a prolonged period of time.

In Publication III, a new method is established with near optimal use of the gained information by estimating the retained ^{222}Rn activity through a recursive statistical inference algorithm, allowing for the estimation of the statistical moments of $\eta(t)$ in near real time. The theoretical basis of this approach is given in section 2.2.3. In Publication IV, a close to optimal method is presented for the implementation of this method, specifically by a significant increase in the signal to noise ratio of the measurement of the remaining ^{222}Rn activity in the source, through a highly efficient measurement setup.

As an illustration and to provide intuition on the effects of this, Figure 2.1 shows the evolution of the theoretical volumetric activity concentration accumulated in a closed volume in which a ^{222}Rn emanation source is placed at the time $t = 0$, the activity ratio of ^{222}Rn and ^{226}Ra of the source, and the differential release of ^{222}Rn atoms from the source for different characteristics of time-changing emanation.

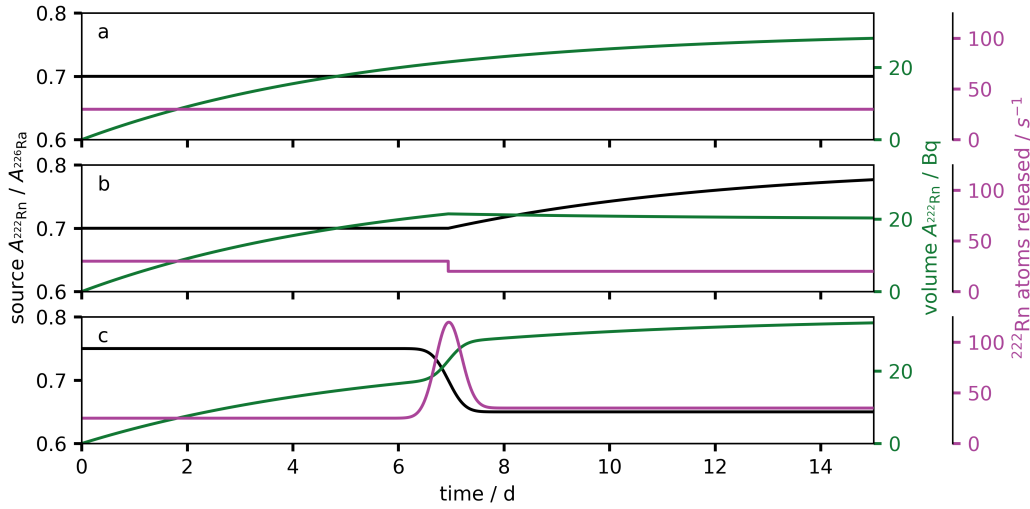


FIGURE 2.1: Different typical examples of ingrowth of the volumetric Radon activity (green) in response to specific emanation source behaviour. Differential release of Radon atoms from the source is shown in violet, whereas the activity ratio between remaining Radon and Radium of the source is shown in black. Panel a shows the behaviour of a completely stable source, panel b shows the response to a step-like drop of the emanation and panel c shows the behaviour of a step-increase superimposed by a Gaussian peak.

2.2.1 Emanation into a closed volume

Despite the theoretical observations from the previous section, in case of perfectly hermetically closed accumulation volumes, the volumetric activity concentration of ^{222}Rn may be calculated as a function of time from observations of the residual ^{222}Rn in the source, without explicitly solving for the deconvolved $\eta(t)$. In this scenario, the ^{222}Rn activity inside the free volume evolves by

$$\frac{\partial A_{222\text{Rn}}^v}{\partial t} = -\lambda_{222\text{Rn}} A_{222\text{Rn}}^v + \lambda_{222\text{Rn}} \eta(t) \quad (2.11)$$

where $A_{222\text{Rn}}^v$ denotes the volumetric ^{222}Rn activity, which results in a convolution integral analogous to (2.10).

$$A_{222\text{Rn}}^v(t) = \exp(-\lambda_{222\text{Rn}}(t - t_0)) A_{222\text{Rn}}^v(t_0) + \int_{t_0}^t \exp(-\lambda_{222\text{Rn}}(t - \tau)) \lambda_{222\text{Rn}} \eta(\tau) d\tau \quad (2.12)$$

In this specific case, the volumetric activity concentration can thus be computed from time-resolved measurements of the residual ^{222}Rn activity in the source, assuming constant ^{226}Ra activity within the measurement time, without explicit estimation of $\eta(t)$ by solving (2.10)

for the convolution integral and substituting into (2.12), as shown in the following. Assuming constant ^{226}Ra activity, i.e. $\frac{dA_{226\text{Ra}}^s}{dt} = 0$, justified by its long half-life, means that \mathbf{F} from equation (2.10) can be rewritten as

$$\mathbf{F} = \begin{bmatrix} -\lambda_{222\text{Rn}} & \lambda_{222\text{Rn}} \\ 0 & 0 \end{bmatrix}$$

and therefore, that

$$\exp(\mathbf{F}(a-b)) = \begin{bmatrix} \exp(-\lambda_{222\text{Rn}}(a-b)) & 1 - \exp(-\lambda_{222\text{Rn}}(a-b)) \\ 0 & 1 \end{bmatrix}.$$

This can be used to obtain from (2.10)

$$A_{222\text{Rn}}^s(t) = \exp(-\lambda(t-t_0)) (A_{222\text{Rn}}^s(t_0) - A_{226\text{Ra}}^s) + A_{226\text{Ra}}^s - \int_{t_0}^t \exp(-\lambda(t-\tau)) \lambda \eta(\tau) d\tau \quad (2.13)$$

where $A_{222\text{Rn}}^s(t) = A_{226\text{Ra}}^s$ is assumed and the subscript ^{222}Rn on λ has been dropped for notational brevity.

Equation (2.13) and (2.12) can be combined to finally yield

$$A_{222\text{Rn}}^v(t) = \exp(-\lambda\Delta t) (A_{222\text{Rn}}^v(t_0) + A_{222\text{Rn}}^s(t_0) - A_{226\text{Ra}}^s) - A_{222\text{Rn}}^s(t) + A_{226\text{Ra}}^s \quad (2.14)$$

with $\Delta t = t - t_0$. This extends the formalism provided by (Linzmaier and Röttger, 2013), consisting of the evaluation of the volumetric activity concentration by

$$c(t) = c_0 (1 - \exp(-\lambda t)) \quad (2.15)$$

with $c_0 = \frac{\chi A_{226\text{Ra}}^s}{V}$,

to the time-span before equilibrium has been reached in the source and to scenarios in which the emanation characteristic is unstable with time or environmental parameters.

2.2.2 Emanation into open volumes

In recent years, the use of emanation sources in flow-through mode has gained more and more attention for the calibration of ^{222}Rn measurement devices. Therein, a calibrated mass flow controller (MFC) is used to generate an intended leakage of a reference volume, which allows to alter the ingrowth characteristics of the volumetric ^{222}Rn concentration. Using this technique, the steady-state activity concentration values can be reached much quicker, depending on the relative magnitude of the air exchange ratio across the intended leak in comparison with the decay constant of ^{222}Rn . Moreover, the need for perfectly closed volumes is not as stringent in these methods, since the transport across the intended leak can be chosen to be much greater than the diffusion across any unintended leaks. Among others, (Fialova et al., 2020) presented such a method, using a 5 kBq ^{226}Ra emanation source

manufactured by the CMI together with a MFC and a 300 L reference volume to obtain activity concentrations in the theoretical range of $100 \text{ Bq} \cdot \text{m}^{-3}$ to $300 \text{ Bq} \cdot \text{m}^{-3}$. A simplified schematic example of such a configuration is shown in Figure 2.2.

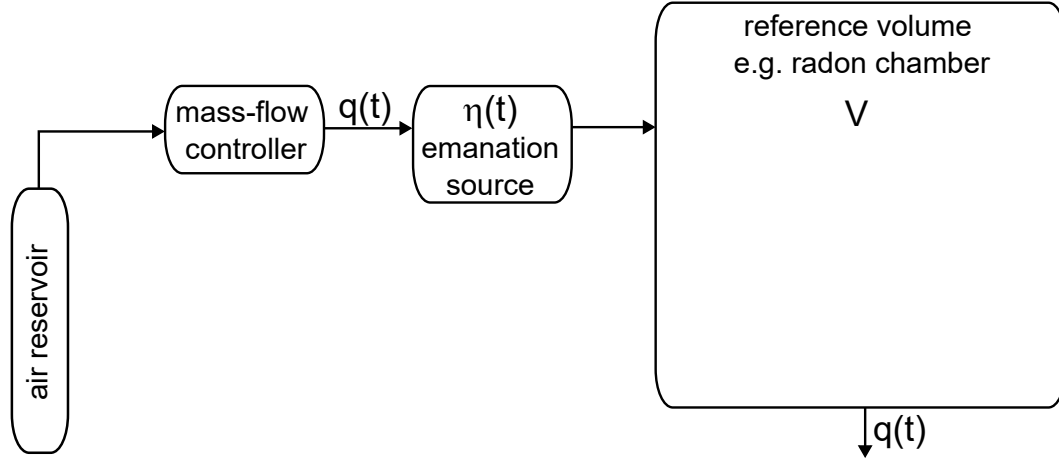


FIGURE 2.2: Schematic drawing of the operation of a radon emanation source with emanation $\eta(t)$ together with a mass-flow controller that provides a stream of air of strength $q(t)$, in terms of unit volume per unit time, into an open reference volume V .

In this case, however, monitoring the residual ^{222}Rn in the emanation source does not allow to directly calculate the ^{222}Rn activity concentration. Following the derivations of the previous section, an additional sink-term must be added to Eq. (2.12), accounting for ^{222}Rn losses across the leak as,

$$\frac{\partial A_{222\text{Rn}}^v}{\partial t} = -\lambda_{222\text{Rn}} A_{222\text{Rn}}^v + \lambda_{222\text{Rn}} \eta(t) - \frac{q(t)}{V} A_{222\text{Rn}}^v \quad (2.16)$$

where q is the rate of outflow across the leak in units of volume per unit time and V is the total volume.

The solution to this adapted form of the dynamics involves a different kernel function in the convolution term, and thus Equation (2.14) does not apply in this case. Therefore, if environmental influences need to be corrected in this method based on observation of the residual ^{222}Rn in the emanation source, a deconvolution technique must be applied to infer the temporal evolution of $\eta(t)$, or preferentially, the inference of the evolution of the volumetric activity and η may be carried out jointly, as illustrated in chapter 8.

2.2.3 Statistical inversion

On the basis of equation (2.7), the emanation may be computed from supporting measurements of the residual ^{222}Rn activity in the emanation source. Evidently, and following Eq. (2.7), the direct application of this equation requires the computation of the (temporal) gradient of the ^{222}Rn activity.

Radioactivity measurements inherently underly statistical fluctuations due to the Poisson statistics of the radioactive decay and the associated counting process, which is especially relevant in the low counting rate scenario resulting from either low activity or low counting efficiency. Therefore, the most straight-forward method to compute the gradient, *finite*

differences, can not be readily applied to compute the emanation because it leads to the amplification of this statistical noise. Such an argument can also be made in terms of the well-known *Convolution theorem* and the Fourier transform of Eq. (2.7), e.g. (Särkkä and Solin, 2019). Consequently, filtering techniques are necessary which attempt to filter the statistical fluctuations and suppress the unavoidable amplification of them as best as possible. Due to this amplification, high signal to noise ratios are especially desirable for applications of deconvolution procedures.

One reasonable candidate is given by the *Savitzky Golay Filter* (Savitzky and Golay, 1964), which is a more performant method to estimate the gradient on the basis of smoothing the time-series of the count-rates using piecewise polynomial regression, thereby effectively filtering some of the amplified noise, albeit associated uncertainties are difficult to estimate in this case.

In any case, computation of $\eta(t)$, evaluated at some finite set of time-instants, from a time-series of activity measurements is an inverse problem: The activity retained within the emanation source can be measured. However, the emanation, which represents a latent continuous variable, cannot be directly determined experimentally. Usually, inference of such latent variables requires some form of regularization to prevent said amplification of high frequency components as best as possible. Additionally, the inference is required to capture, at least, the stochastic uncertainty associated with the inferred η .

To achieve both of these requirements, it is beneficial to cast the system into the state space form and to propose a stochastic process associated with the temporal evolution of η . It should be noted, that in this specific case, the randomness does not imply that the process is truly supposed to be stochastic in nature, it is merely used as a mathematical tool to capture the uncertainty associated with imperfect knowledge of the true dynamics and all relevant parameters and dependencies, leading to imperfect predictions of future state. Specifically, this is due to the fact that the true evolution of η , e.g. through its dependency on humidity or any other factor, is not known in practice, and hence, the true η may change at any point in time.

In the general multivariate case, such a process may be expressed as the following stochastic differential equation (SDE) in the Itô sense, acting on some state vector x , which in the present case contains at least $A_{222\text{Rn}}^s, A_{226\text{Ra}}^s$, denoting the activities of ^{222}Rn and ^{226}Ra in the source respectively, and η corresponding to some time t .

$$dx = f(x, t, \theta) dt + g(x, t, \theta) d\beta_t \quad (2.17)$$

where $x \in \mathbb{R}^k$ denotes the state vector, $f : \mathbb{R}^k \rightarrow \mathbb{R}^k$ denotes the drift function which captures the deterministic dynamics of the system and $g : \mathbb{R}^k \rightarrow \mathbb{R}^{k \cdot m}$ denotes the diffusion function, which determines how the increments $d\beta_t$ of an m -dimensional Wiener process enter the system. f and g may be parameterized by a parameter vector θ . Note, that f and g may represent arbitrary operations on their respective input parameters explaining their potentially different output dimensionality.

In this general case, the temporal evolution of the probability density function p of x is given as the solution to the Fokker-Planck partial differential equation (e.g. Särkkä and Solin, 2019)

$$\frac{\partial}{\partial t} p(\mathbf{x}, t) = - \sum_{i=1}^N \frac{\partial}{\partial x_i} (f_i(\mathbf{x}, t, \boldsymbol{\theta}) p(\mathbf{x}, t)) + \sum_{i=1}^N \sum_{j=1}^N \frac{\partial^2}{\partial x_i \partial x_j} \left(\frac{1}{2} [g(\mathbf{x}, t, \boldsymbol{\theta}) g^T(\mathbf{x}, t, \boldsymbol{\theta})]_{i,j} p(\mathbf{x}, t) \right) \quad (2.18)$$

Stochastic processes subject to an Itô SDE obey the *Markov Property* (e.g. (Øksendal, 2003)), that is, that future states are independent of the past given the present state, as

$$p(\mathbf{x}_{n+1} | \mathbf{x}_{1:n}) = p(\mathbf{x}_{n+1} | \mathbf{x}_n)$$

where \mathbf{x}_{n+1} denotes the state vector at some time $t_{n+1} \geq t_n$ and $\mathbf{x}_{1:n}$ denotes the collection of state vectors corresponding to the set of times $[t_1, \dots, t_n]$.

In light of this property, such a stochastic process may be entirely described by a transition density $p(\mathbf{x}_{n+1} | \mathbf{x}_n)$, which can formally be extracted by solving the Fokker-Planck equation for a degenerate Dirac distribution centered on \mathbf{x}_n . Using this transition density, the probability density function of \mathbf{x} may be propagated in time by the Chapman-Kolmogorov equation (Särkkä and Solin, 2019) as

$$p(\mathbf{x}_{n+1}) = \int p(\mathbf{x}_{n+1} | \mathbf{x}_n) p(\mathbf{x}_n) d\mathbf{x}_n \quad (2.19)$$

Despite some select few special cases, the solution to the Fokker-Planck equation may, however, not be found analytically.

Recursive Bayesian estimation

Recursive Bayesian estimation refers to a class of algorithms that allows to perform statistical inference in systems generally described by Equation (2.17). The derivations given in this section are adapted from (Särkkä, 2013; Särkkä and Solin, 2019). In such algorithms, it is assumed that some quantity $\mathbf{y} \in \mathbb{R}^l$ is observed, that is related to the state $\mathbf{x} \in \mathbb{R}^k$ through some function $h : \mathbb{R}^k \rightarrow \mathbb{R}^l$. The measurement may be noisy, which may be modeled by a transformed white-noise sequence.

$$\mathbf{y}_t = h(\mathbf{x}, t, \boldsymbol{\theta}) + k(\mathbf{x}, \mathbf{y}_t, t, \boldsymbol{\theta}, \mathbf{W}_t) \quad (2.20)$$

where $\mathbf{W}_t \in \mathbb{R}^l$ is a random variable from a white noise sequence and k and h are arbitrary functions of appropriate output dimensionality.

For the present specific case of a continuous time process as in Equation (2.17) coupled with discrete observations as in Equation (2.20), the interest lies in estimating the joint density $p(\mathbf{x}(\tau) | \mathbf{y}_T) \forall \tau \in \mathcal{T}$ for a certain time interval \mathcal{T} and for a finite set of measurements \mathbf{y}_T obtained at a finite set of measurements times $T \in \mathcal{T}$, which is generally intractable to compute, due to the continuity of τ . Even for arbitrary, finite discretization, the computation of the full joint density at the discretized times is computationally infeasible, as computation time scales at least cubically with the number of time-steps (Särkkä, 2013). Furthermore, it is then difficult to include new measurements \mathbf{y} into the inference procedure, once available.

Therefore, in practice, only the marginal distributions $p(\mathbf{x}_n | \mathbf{y}_{1:n})$ and $p(\mathbf{x}_n | \mathbf{y}_T)$ are of interest, where marginalization has taken place over the states of all other time instants and $n \in T$. These distributions are referred to as the filtering and the smoothing distributions

respectively, where for the filtering density, only information that was available up to time t_n is included. The smoothing density, on the other hand, contains all information contained in a specified time interval T .

Note, that the measurement function h may ignore some of the components of x , and in conjunction with the process model in Equation (2.17), such estimation thus generally also allows to estimate the unobserved, latent components of x . Hence, such a technique may be classified as a form of statistical inversion, and may be used to achieve the goal of estimating η in light of supporting measurements of the residual ^{222}Rn in the emanation source.

Typically, and additionally to the *Markov Property* of x , it is assumed that the measurements are conditionally independent from one another given the state at the corresponding time and therefore, that the following two identities are fulfilled.

$$p(\mathbf{x}_n | \mathbf{x}_{0:n-1}, \mathbf{y}_{0:n-1}) = p(\mathbf{x}_n | \mathbf{x}_{n-1}) \quad (2.21)$$

i.e. given \mathbf{x}_{n-1} , neither $\mathbf{y}_{0:n-1}$ nor $\mathbf{x}_{0:n-2}$ include any additional information on \mathbf{x}_n and

$$p(\mathbf{y}_n | \mathbf{x}_n, \mathbf{y}_{0:n-1}) = p(\mathbf{y}_n | \mathbf{x}_n) \quad (2.22)$$

i.e. given \mathbf{x}_n , $\mathbf{y}_{0:n-1}$ does not include any additional information about the outcome of \mathbf{y}_n .

Due to these two properties, the computation of the filtering densities, $p(\mathbf{x}_n | \mathbf{y}_{1:n})$ may be decomposed into a recursive formulation consisting of the prediction and the update step (Särkkä, 2013). The recursion starts at some initial prior distribution $p(\mathbf{x}_0)$. Assuming, that the filtering density of the previous time-step $p(\mathbf{x}_{n-1} | \mathbf{y}_{1:n-1})$ is known, one may propagate to t_n by Equation (2.19) as

$$p(\mathbf{x}_n | \mathbf{y}_{1:n-1}) = \int p(\mathbf{x}_n | \mathbf{x}_{n-1}) p(\mathbf{x}_{n-1} | \mathbf{y}_{1:n-1}) d\mathbf{x}_{n-1} \quad (2.23)$$

The information contained in the measurement of \mathbf{y}_n may then be incorporated by Bayes theorem to form an updated, posterior filtering distribution at the respective time-step, as

$$p(\mathbf{x}_n | \mathbf{y}_{1:n}) = \frac{p(\mathbf{y}_n | \mathbf{y}_{1:n-1}, \mathbf{x}_n) p(\mathbf{x}_n | \mathbf{y}_{1:n-1})}{\int p(\mathbf{y}_n | \mathbf{x}_n, \mathbf{y}_{1:n-1}) p(\mathbf{x}_n | \mathbf{y}_{1:n-1}) d\mathbf{x}_n} \stackrel{(2.21),(2.22)}{=} \frac{p(\mathbf{y}_n | \mathbf{x}_n) p(\mathbf{x}_n | \mathbf{y}_{1:n-1})}{\int p(\mathbf{y}_n | \mathbf{x}_n) p(\mathbf{x}_n | \mathbf{y}_{1:n-1}) d\mathbf{x}_n} \quad (2.24)$$

and the iteration for the next time-step t_{n+1} may be carried out from the result of Equation (2.24). Clearly, such a formulation easily allows to incorporate new measurements, e.g. obtained in a streaming fashion.

From the filtering densities $p(\mathbf{x}_n | \mathbf{y}_{1:n})$, one may compute the smoothed densities by the following identities. Correcting the filtering result into the smoothing result takes the form of a backward recursion: At the last time step in the set T , the smoothing and the filtering density are equal. Assuming, that the smoothing density at time t_{n+1} is known, one may observe by expansion of the smoothing density that

$$\begin{aligned}
p(\mathbf{x}_n | \mathbf{y}_T) &= \int p(\mathbf{x}_n, \mathbf{x}_{n+1} | \mathbf{y}_T) d\mathbf{x}_{n+1} \stackrel{(2.21)}{=} \int p(\mathbf{x}_n | \mathbf{x}_{n+1}, \mathbf{y}_{1:n}) p(\mathbf{x}_{n+1} | \mathbf{y}_T) d\mathbf{x}_{n+1} = \\
&= \int \frac{p(\mathbf{x}_n, \mathbf{x}_{n+1} | \mathbf{y}_{1:n})}{p(\mathbf{x}_{n+1} | \mathbf{y}_{1:n})} p(\mathbf{x}_{n+1} | \mathbf{y}_T) d\mathbf{x}_{n+1} \stackrel{(2.19)}{=} \\
&= p(\mathbf{x}_n | \mathbf{y}_{1:n}) \int \frac{p(\mathbf{x}_{n+1} | \mathbf{x}_n)}{p(\mathbf{x}_{n+1} | \mathbf{y}_{1:n})} p(\mathbf{x}_{n+1} | \mathbf{y}_T) d\mathbf{x}_{n+1}
\end{aligned} \tag{2.25}$$

which only requires the results of the filtering procedure and the forward transition density of the model.

In this general formulation of such models, the filtering and smoothing recursions can not be solved analytically, for the exception of the linear, time-invariant Gaussian case outlined in the next section, which is the focus of application of filtering and smoothing techniques in the present work. Such models are also closely related and in some cases can be equivalently expressed as *Hidden Markov Models*, where a recent review is given in (Mor et al., 2021). For non-linear and non-Gaussian models on the other hand, numerous approximation schemes have been developed in the past, among others, the Extended Kalman-Filter, the Unscented Kalman-Filter, Particle-Filters, Numerical integration based filters and Gaussian sum filtering. A relatively thorough overview over these methods is given in the book of (Särkkä and Solin, 2019).

Recursive Bayesian estimation in linear, time-invariant dynamical models

In the case of linear, time-invariant models with independent Gaussian noises, Equations (2.17) and (2.20) reduce to

$$d\mathbf{x} = \mathbf{F}xdt + \mathbf{L}d\beta_t \tag{2.26}$$

where $\mathbf{x} \in \mathbb{R}^k$, $\mathbf{F} \in \mathbb{R}^{k \times k}$, $\mathbf{L} \in \mathbb{R}^{k \times m}$ and $d\beta_t$ signifies the increments of a m -dimensional standard Wiener process and

$$\mathbf{y}_t = \mathbf{H}x_t + \mathbf{W}_t \tag{2.27}$$

where $\mathbf{y}_t \in \mathbb{R}^l$, $\mathbf{H} \in \mathbb{R}^{l \times k}$ and \mathbf{W}_t is a white noise sequence of covariance matrix $\mathbf{R} \in \mathbb{R}^{l \times l}$, independent of $d\beta_t$.

In this specific case, the solution to the SDE in Equation (2.26) is given analogously to the non-stochastic case in terms of Itô's definition of the stochastic integral as (Särkkä and Solin, 2019)

$$\mathbf{x}_t = \exp(\mathbf{F}(t - t_0)) \mathbf{x}_0 + \int_{t_0}^t \exp(\mathbf{F}(t - \tau)) \mathbf{L}d\beta_\tau \tag{2.28}$$

and the transition density $p(\mathbf{x}_t | \mathbf{x}_{t-1})$ is well known to be Gaussian (signified by the Symbol $\mathcal{N}(\boldsymbol{\mu}, \boldsymbol{\Sigma})$ and parameterized by a mean vector $\boldsymbol{\mu}$ and covariance matrix $\boldsymbol{\Sigma}$) as (Särkkä and Solin, 2019)

$$p(\mathbf{x}_t | \mathbf{x}_0) = \mathcal{N}(\boldsymbol{\Psi}_{t|t_0} \mathbf{x}_0, \mathbf{U}_{t|t_0}) \tag{2.29}$$

which may be proven by solving the Fokker-Planck equation. Therein, the matrices $\Psi_{a|b}$ and $\mathbf{U}_{a|b}$ are given as (Särkkä and Solin, 2019)

$$\Psi_{a|b} = \exp(\mathbf{F}(a - b))$$

$$\mathbf{U}_{a|b} = \int_a^b \exp(\mathbf{F}(a - \tau)) \mathbf{L} \mathbf{L}^T \exp(\mathbf{F}(a - \tau))^T d\tau$$

The covariance $\mathbf{U}_{a|b}$ may also be derived from Itô isometry and the definition of the variance. Since the measurement equation (2.27) only involves a linear transformation of the state, and linear transformation of Gaussian random variables yield another Gaussian distribution, it is clear that $p(\mathbf{y}_t | \mathbf{x}_t)$ is Gaussian, and the forward transition density is also Gaussian. For this specific scenario, the Bayesian filtering and smoothing equations are analytically tractable, as outlined below.

Marginalization and conditioning of multivariate Gaussians is particularly easy and accessible in closed form, as in Lemma 1, from which the standard Kalman-Filtering and Rauch-Tung-Striebel smoothing equations may be derived as the solutions to the recursive Bayesian estimation equations (2.23), (2.24) and (2.25) and are given in Equations (2.30) and (2.31) respectively, as pointed out e.g. in (Särkkä and Solin, 2019; Särkkä, 2013) among others, albeit the original derivation of the Kalman-Filter (Kalman, 1960) was not carried out using this formalism. For a given model, the Kalman-Filter and Rauch-Tung-Striebel smoother provide the optimal estimator for the states in terms of minimum variance in the linear Gaussian case. Even in a naive implementation, the Kalman-Filter and Rauch-Tung-Striebel smoother have linear time-complexity, $\mathcal{O}(N)$, where N represents the number of measurement \mathbf{y}_k , but can be improved on using parallel processing and prefix-summation of an associative operator formulation of the filtering and smoothing equations, as in (Hassan et al., 2021).

Lemma 1 (Searle, 2006) *If the distribution of the random vector $[\mathbf{a} \ \mathbf{b}]^T$ is given as*

$$p(\mathbf{a}, \mathbf{b}) \propto \mathcal{N} \left(\begin{bmatrix} \boldsymbol{\mu}_a \\ \boldsymbol{\mu}_b \end{bmatrix}, \begin{bmatrix} \boldsymbol{\Sigma}_{aa} & \boldsymbol{\Sigma}_{ab} \\ \boldsymbol{\Sigma}_{ab}^T & \boldsymbol{\Sigma}_{bb} \end{bmatrix} \right)$$

the conditional distributions $p(\mathbf{a} | \mathbf{b})$ and $p(\mathbf{b} | \mathbf{a})$ are given in terms of the Schur complements of the (block) covariance matrix as

$$p(\mathbf{a} | \mathbf{b}) \propto \mathcal{N} \left(\boldsymbol{\mu}_a - \boldsymbol{\Sigma}_{ab} \boldsymbol{\Sigma}_{bb}^{-1} (\mathbf{b} - \boldsymbol{\mu}_b), \boldsymbol{\Sigma}_{aa} - \boldsymbol{\Sigma}_{ab} \boldsymbol{\Sigma}_{bb}^{-1} \boldsymbol{\Sigma}_{ab}^T \right)$$

$$p(\mathbf{b} | \mathbf{a}) \propto \mathcal{N} \left(\boldsymbol{\mu}_b - \boldsymbol{\Sigma}_{ab}^T \boldsymbol{\Sigma}_{aa}^{-1} (\mathbf{a} - \boldsymbol{\mu}_a), \boldsymbol{\Sigma}_{bb} - \boldsymbol{\Sigma}_{ab}^T \boldsymbol{\Sigma}_{aa}^{-1} \boldsymbol{\Sigma}_{ab} \right)$$

and the marginal distributions $p(\mathbf{a})$ and $p(\mathbf{b})$ are given as

$$p(\mathbf{a}) = \int p(\mathbf{a}, \mathbf{b}) d\mathbf{b} \propto \mathcal{N}(\boldsymbol{\mu}_a, \boldsymbol{\Sigma}_{aa})$$

$$p(\mathbf{b}) = \int p(\mathbf{a}, \mathbf{b}) d\mathbf{a} \propto \mathcal{N}(\boldsymbol{\mu}_b, \boldsymbol{\Sigma}_{bb})$$

Kalman Filter recursion (Särkkä and Solin, 2019)

$$\begin{aligned}
\boldsymbol{\mu}_{n|n-1} &= \boldsymbol{\Psi}_{t_n|t_{n-1}} \boldsymbol{\mu}_{n-1|n-1} \\
\boldsymbol{\Sigma}_{n|n-1} &= \boldsymbol{\Psi}_{t_n|t_{n-1}} \boldsymbol{\Sigma}_{n-1|n-1} \boldsymbol{\Psi}_{t_n|t_{n-1}}^T + \mathbf{U}_{t_n|t_{n-1}} \\
\mathbf{S} &= \mathbf{H} \boldsymbol{\Sigma}_{n|n-1} \mathbf{H}^T + \mathbf{R} \\
\mathbf{G} &= \boldsymbol{\Sigma}_{n|n-1} \mathbf{H}^T \mathbf{S}^{-1} \\
\boldsymbol{\mu}_n &= \boldsymbol{\mu}_{n|n-1} + \mathbf{G} \left(\mathbf{y}_n - \mathbf{H} \boldsymbol{\mu}_{n|n-1} \right) \\
\boldsymbol{\Sigma}_n &= \boldsymbol{\Sigma}_{n|n-1} - \mathbf{G} \mathbf{S} \mathbf{G}^T
\end{aligned} \tag{2.30}$$

where $\boldsymbol{\mu}_{n-1|n-1}$ and $\boldsymbol{\Sigma}_{n-1|n-1}$ denote the filtering mean and covariance of the previous time-step t_{n-1} .

In addition, the Kalman-Filter can be used to compute the joint marginal likelihood of the measurement sequence $p(\mathbf{y}_1, \dots, \mathbf{y}_n) = p(\mathbf{y}_1) \prod_{i=2}^n p(\mathbf{y}_i | \mathbf{y}_{1:i-1})$ from the normalization constant of Equation (2.24), which can and was used to tune any parameters of the models by maximum likelihood estimation (Särkkä, 2013).

Rauch Tung Striebel smoother backwards recursion (Särkkä and Solin, 2019)

$$\begin{aligned}
\boldsymbol{\mu}_{n+1|n} &= \boldsymbol{\Psi}_{t_{n+1}|t_n} \boldsymbol{\mu}_n \\
\boldsymbol{\Sigma}_{n+1|n} &= \boldsymbol{\Psi}_{t_{n+1}|t_n} \boldsymbol{\Sigma}_n \boldsymbol{\Psi}_{t_{n+1}|t_n}^T + \mathbf{U}_{t_{n+1}|t_n} \\
\mathbf{G} &= \boldsymbol{\Sigma}_n \boldsymbol{\Psi}_{t_{n+1}|t_n}^T \boldsymbol{\Sigma}_{n+1|n}^{-1} \\
\boldsymbol{\mu}_n^s &= \boldsymbol{\mu}_n + \mathbf{G} \left(\boldsymbol{\mu}_{n+1}^s - \boldsymbol{\mu}_{n+1|n} \right) \\
\boldsymbol{\Sigma}_n^s &= \boldsymbol{\Sigma}_n + \mathbf{G} \left(\boldsymbol{\Sigma}_{n+1}^s - \boldsymbol{\Sigma}_{n+1|n} \right) \mathbf{G}^T
\end{aligned} \tag{2.31}$$

where $\boldsymbol{\mu}_n^s$ and $\boldsymbol{\Sigma}_n^s$ signify the mean and covariance of the smoothing distribution at time step t_n and $\boldsymbol{\mu}_n$ and $\boldsymbol{\Sigma}_n$ the respective filtering mean and covariance.

Considerations for an application to radioactivity measurements

For Bayesian recursive estimation techniques to be applicable to radioactivity measurements, the act of measuring, in this work mainly by spectrometric methods such as γ -ray and α -particle spectrometry, needs to be modeled.

It is clear, that recording a spectrum between time instants t_n and t_{n+1} is generally related to the decays that occurred within this time span. Therefore, some measurement \mathbf{y}_n , which may for example be the measured spectrum itself or any derived quantity, is related not directly to the activity, but to the time-integrated activity that is further subject to some (potentially matrix valued) mapping function \mathbf{h} . It is generally assumed in radioactivity measurements, that \mathbf{h} is a linear operator acting on the time-integrated activity (or activity vector in case of multiple isotopes),

$$\mathbf{y}_k = \mathbf{h} \int_{t_n}^{t_{n+1}} A(\tau) d\tau \tag{2.32}$$

Such a formulation is, for example, used to derive the usual approaches of correcting for decay or ingrowth during the integration time of the measurement device. In the most common applications of radioactivity measurements, the decay and ingrowth equations are well known, and therefore, the above integral may be solved in closed form and the change of A during the integration time of the measurement device may hence be simply corrected for.

In the present case, however, this is not true, since any change of the emanation η across the time-span t_n to t_{n+1} impacts the temporal evolution of A , and thus the time integrated quantity in Equation (2.32).

Additionally, it should be noted, that the very nature of the radioactive decay is described by a Poisson process of rate A . For this reason, in radioactivity measurements, it is generally assumed that

$$\mathbf{y}_n | A_{t_n} \sim \text{Poisson}(\mathbf{h} \int_{t_n}^{t_{n+1}} A(\tau) d\tau)$$

signifying, that \mathbf{y}_n is a Poisson random-variable, and, where it is assumed that the temporal evolution of A is deterministic. Strictly, one may thus state, that after measuring some realization of \mathbf{y}_n , the posterior distribution of A_{t_n} has a Gamma-Distribution if the dynamics of the respective decay at hand are perfectly known, since the Gamma-distribution is the conjugate prior of the rate parameter of the Poisson distribution, as mentioned in (Klump et al., 2018) among others. If, however, the evolution of A itself is a stochastic process, as in the case of uncertain temporal evolution, one ends up with a Poisson process that has itself a stochastic process as its rate parameter, a certain doubly stochastic process referred to as the *Cox-Process* (Cox, 1955). In this case, the recursions of the Bayesian estimators in the previous sections are not analytically tractable, which is why a Gaussian approximation to the process is derived in the following that allows for Bayesian inference analogous to the closed forms provided by the standard Kalman-Filter and the Rauch-Tung-Striebel smoother instead.

The models described in an SDE equivalent to Equation (2.26) in the previous section takes the form of a Gaussian process: Any finite collection of $x_{\mathcal{K}}$ where \mathcal{K} is a finite subset of time is jointly distributed according to a multivariate Gaussian.

Integration, for example by the definition of Riemann, is a linear operator, and in the above formulation, \mathbf{h} is also assumed to be a linear operator, and therefore, it is clear that the integral must be distributed as a Gaussian distribution as long as x takes continuous sample paths and is assumed to be integrable. Time in this case is discretized in non-overlapping partitions, each of which signifies a measurement period with the radioactivity detector. The definition of the measurement time is such that for the measurement formally corresponding to t_n the integration took place from $t_{n-1} + \delta$ to $t_n = t_{n-1} + \delta + r$, in other words, that t_n matches the endpoint of each of the measurements. Note, that this choice is arbitrary. For now, it is assumed that the measurement is deterministic with respect to this integral and one may thus write

$$\mathbf{y}_n = \mathbf{H} \int_{t_{n-1}+\delta}^{t_{n-1}+\delta+r} \mathbf{x}(\tau) d\tau \quad (2.33)$$

where H is assumed to be a time-invariant matrix (or other linear operator) that maps the state integral to the measurement space, which may be of differing dimension. In this definition, y_n has a Gaussian distribution, since it is determined by linear operators acting on a Gaussian process. Figure 2.3 demonstrates this system for the arbitrary case of a scalar Gaussian process x .

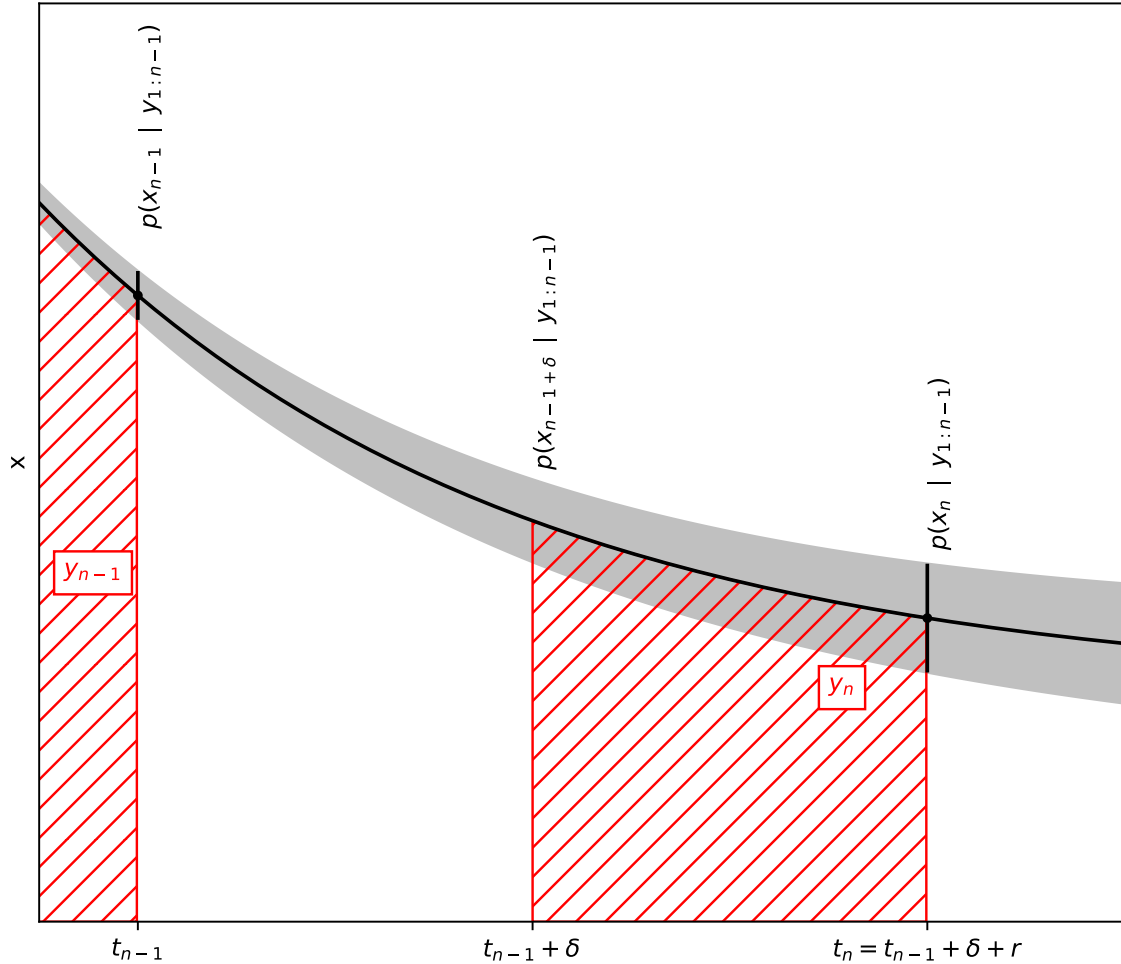


FIGURE 2.3: Outline of a continuous Gaussian process and its integrated discrete process. The black line refers to the mean of x , whereas the shaded area corresponds to the interval covering 1σ of the density of x . The shaded areas in red correspond to the transformed integrated quantity y over non-overlapping partitions of time.

Approximate filtering recursion derivation

In the following, a potentially mathematically sub-optimal Bayesian filtering recursion algorithm for the outlined setting is derived, which is, e.g., required for an application such as the one presented in Publications III, IV and chapter 8 of this work.

It is assumed that an approximation of $p(x_{n-1} | y_{1:n-1}) \propto \mathcal{N}(\mu_{n-1}, \Sigma_{n-1})$ is known from filtering of the previous step. From this distribution and Equations (2.33) and (2.28), one may derive the full joint density of $p(x_{n-1}, x_{n-1+\delta}, x_n, y_n | y_{1:n-1})$ assuming a linear Gaussian time-invariant model and conditionally independent measurements with the deterministic measurement equation (2.33) analytically as follows.

One may note that the combination of these equations yields,

$$\mathbf{y}_n = \mathbf{H} \int_{t_{n-1}+\delta}^{t_{n-1}+\delta+r} \left[\exp(\mathbf{F}(s - t_{n-1})) \mathbf{x}_{n-1} + \int_{t_{n-1}}^s \exp(\mathbf{F}(s - \tau)) \mathbf{L} d\beta_\tau \right] ds$$

which may be equivalently written as follows, by swapping the order of integration, adjusting the respective integration limits and using the definition $\Psi_{a|b} = \exp(\mathbf{F}(a - b))$.

$$\mathbf{y}_k = \mathbf{H}\mathbf{K}_r \mathbf{x}_\delta + \int_0^r \int_\tau^r \exp(\mathbf{F}(s - \tau)) \mathbf{L} d\beta_\tau ds$$

Marginalizing the joint density $p(\mathbf{x}_{n-1}, \mathbf{x}_{n-1+\delta}, \mathbf{x}_n, \mathbf{y}_n | \mathbf{y}_{1:n-1})$ over $\mathbf{x}_{n-1+\delta}$ and \mathbf{x}_{n-1} yields

$$p(\mathbf{x}_n, \mathbf{y}_n | \mathbf{y}_{1:n-1}) = \mathcal{N} \left(\begin{bmatrix} \Psi_r \Psi_\delta \boldsymbol{\mu}_{\mathbf{x}_{n-1}} \\ \mathbf{H}\mathbf{K}_r \Psi_\delta \boldsymbol{\mu}_{\mathbf{x}_{n-1}} \end{bmatrix}, \begin{bmatrix} \Psi_r \Sigma_\delta \Psi_r^\mathbf{T} + \mathbf{U}_r & \Psi_r \Sigma_\delta \mathbf{K}_r^\mathbf{T} \mathbf{H}^\mathbf{T} + \mathbf{C}\mathbf{H}^\mathbf{T} \\ \mathbf{H}\mathbf{K}_r \Sigma_\delta \Psi_r^\mathbf{T} + \mathbf{H}\mathbf{C}^\mathbf{T} & \mathbf{H}\mathbf{K}_r \Sigma_\delta \mathbf{K}_r^\mathbf{T} \mathbf{H}^\mathbf{T} + \mathbf{H}\mathbf{B}\mathbf{H}^\mathbf{T} \end{bmatrix} \right) \quad (2.34)$$

proof of which is given in Appendix A and where the matrices are defined as follows:

$$\Psi_r = \exp(\mathbf{F}r)$$

$$\mathbf{U}_r = \int_0^r \exp(\mathbf{F}(r - \tau)) \mathbf{L}\mathbf{L}^\mathbf{T} \exp(\mathbf{F}^\mathbf{T}(r - \tau)) d\tau$$

$$\mathbf{K}_r = \int_0^r \exp(\mathbf{F}s) ds$$

$$\mathbf{C}_r = \int_0^r \int_\tau^r \exp(\mathbf{F}(r - \tau)) \mathbf{L}\mathbf{L}^\mathbf{T} \exp(\mathbf{F}^\mathbf{T}(s - \tau)) ds d\tau$$

$$\mathbf{B}_r = \int_0^r \int_\tau^r \int_\tau^r \exp(\mathbf{F}(a - \tau)) \mathbf{L}\mathbf{L}^\mathbf{T} \exp(\mathbf{F}^\mathbf{T}(b - \tau)) da db d\tau$$

Conditioning of this Gaussian distribution according to Lemma 1 onto the measurement \mathbf{y}_n yields the update step of the derived filtering equations, i.e., $p(\mathbf{x}_n | \mathbf{y}_{1:n})$. The backwards smoothing (RTS-smoother) algorithm does not change, however, since the measurement sequence \mathbf{y}_n is no longer needed at the point of smoothing the time-series. For the measurements at hand in this work, one may observe that $\mathbf{y}_{i,n} \gg 30$ for all cases and all elements of \mathbf{y}_n indexed by i , at which the Gaussian distribution is a good approximation to the Poisson distribution. The variance of this Gaussian may be estimated from the prediction step of the Kalman-Filter, which allows to derive the expected value of counts for the measurement \mathbf{y}_n based on the knowledge of the state at t_{n-1} , similarly reported in (Ebeigbe et al., 2020). Filtering of the time-step t_{n-1} yields the best estimate of the state, and therefore, the choice to evaluate the variance of the next measurement is intuitive and was also suggested by (Ebeigbe et al., 2020) in a different context, which shows that such a scheme remains unbiased and the optimal linear filter for the setting at hand.

With the approximation that the covariance terms for \mathbf{y}_n in equation (2.34) are independent from the counting noise, one may hence simply adopt an additive variance term given formally by

$$\mathbf{R} = \text{diag} \left(\mathbf{H} \mathbf{K}_r \mathbf{\Psi}_\delta \boldsymbol{\mu}_{x_{n-1}} \right)$$

where the diagonal elements of \mathbf{R} additionally need to be numerically bounded to some non-zero, small value in order to avoid numerical underflow and degeneracy of the Gaussian distributions.

Thus the following linear filtering equations in close resemblance of equations (2.30) were obtained, which forms the basis of recursive Bayesian modeling to estimate the emanation based on time-series of measurements of the residual ²²²Rn activity in the source, such as the methods presented in Publication III and IV. This hence considers Gaussian process models for η , such as the Gaussian random walk

$$d\eta = d\beta_t \quad (2.35)$$

It however, applies to all Gaussian processes that can be specified in terms of vector valued stochastic differential equations, such as the Gaussian processes with *Matérn* type covariance (Stein, 1999), a popular covariance function for spatial statistics, which was also pointed out for other application contexts in (Hartikainen and Särkkä, 2012).

Kalman-Filter for state-integrating, discretized Gaussian processes

$$\begin{aligned} \boldsymbol{\mu}_{\delta|n-1} &= \mathbf{\Psi}_\delta \boldsymbol{\mu}_{n-1|n-1} \\ \boldsymbol{\Sigma}_{\delta|n-1} &= \mathbf{\Psi}_\delta \boldsymbol{\Sigma}_{n-1|n-1} \mathbf{\Psi}_\delta^T + \mathbf{U}_\delta \\ \boldsymbol{\mu}_{n|n-1} &= \mathbf{\Psi}_r \boldsymbol{\mu}_{\delta|n-1} \\ \boldsymbol{\Sigma}_{n|n-1} &= \mathbf{\Psi}_r \boldsymbol{\Sigma}_{\delta|n-1} \mathbf{\Psi}_r^T + \mathbf{U}_r \\ \mathbf{S} &= \mathbf{H} \mathbf{K}_r \boldsymbol{\Sigma}_{\delta|n-1} \mathbf{K}_r^T \mathbf{H}^T + \mathbf{H} \mathbf{B}_r \mathbf{H}^T + \mathbf{R} \\ \mathbf{G} &= (\mathbf{\Psi}_r \boldsymbol{\Sigma}_{\delta|n-1} \mathbf{K}_r^T \mathbf{H}^T + \mathbf{C}_r \mathbf{H}^T) \mathbf{S}^{-1} \\ \boldsymbol{\mu}_{n|n} &= \boldsymbol{\mu}_{n|n-1} + \mathbf{G} \left(\mathbf{y}_n - \mathbf{H} \mathbf{K}_r \boldsymbol{\mu}_{\delta|n-1} \right) \\ \boldsymbol{\Sigma}_{n|n} &= \boldsymbol{\Sigma}_{n|n-1} - \mathbf{G} \mathbf{S} \mathbf{G}^T \end{aligned} \quad (2.36)$$

As a result of the derivations, this method inherently accounts for both the discretization errors stemming from the possible change of η and thus activity throughout the integration intervals as well as approximating the statistical properties of the Poisson distributed measurements. Intuitively, this is reflected by an additional variance term $\mathbf{H} \mathbf{B}_r \mathbf{H}^T$ in the measurements, that accounts for the partially unknown changes during the integration, which is proportional to the diffusion matrix of the Wiener process in the original model formulation in equation (2.26). Additional uncertainty terms that are related to the statistical uncertainty of the measurement (such as additional parametric peak area uncertainty) may be formally absorbed into \mathbf{R} .

On the other hand, the choice of the underlying Gaussian process model may incorporate its own uncertainty, most notably due to its effect during smoothing the time-series. Thereby,

fidelity in steep gradients in the emanation may be lost by a choice of a Gaussian process that only allows for smooth functional realizations, such as the exponentiated quadratic kernel. This effect is discussed in Publication III, and a strategy to alleviate these implications is given therein, mainly, by modeling the system as a switching dynamical system, e.g. (Barber, 2006) among others and also referred to as a *jump Markov-model*, with several models for several different regimes within the time-series.

2.3 Measurement techniques

2.3.1 Spectrometric methods

Spectrometry refers to techniques which rely on the assessment of the spectral properties of emitted radiation. In the context of ionizing radiation, this generally entails the employment of a detection material, sensitive to the incoming ionizing radiation that allows to quantify, in most cases electronically, the energy deposited by the physical interaction of radiation quanta with the respective material. Due to physical interaction effects of the ionizing radiation with the detection material, spectra obtained in this way are generally distorted versions of the true emission spectrum of the source.

Spectrometry of γ -radiation

The spectrometry of γ -radiation is nowadays typically either based on solid-state scintillating materials whose scintillation is analyzed by a light-sensitive device, such as a photomultiplier tube or silicon diodes, or based on semiconductor radiation detectors. The processes by which γ -radiation interacts with the detection- and surrounding materials, such as the Photoelectric effect, Compton scattering and pair production, define distinct features in γ -ray spectra, most notably, but not limited to, the full-energy peak, the Compton edge and continuum and escape peaks. These features can be used to quantify the activity of certain isotopes in the sample, due to a generally linear relationship between the count-rate of such features and the source strength over a relatively wide dynamic range.

In general, semiconductor detectors offer a higher energy resolution, nowadays typically by the use of high-purity germanium (HPGe), while being more costly and more difficult to maintain than scintillator based spectrometers. HPGe detectors require cooling, typically by employing liquid nitrogen or electrical coolers. The spectrometry of ionizing radiation with semiconductor detectors can be achieved by analyzing the current pulses across a reversely biased p/n-junction that result from incoming radiation. Energy deposited by this incident radiation leads to the population of the conduction band and thus to a current pulse from charge carrier migration along the externally applied electrical field. The applied semiconductor depends strongly on the type of radiation and the correspondingly different properties required for a suitable detector. Spectrometry of γ -radiation requires high density, large single crystals for high detection efficiencies and small band-gaps and low leakage currents for good energy resolution.

Scintillator based γ -spectrometers on the other hand offer a reduced energy resolution but at significantly smaller initial and maintenance costs and less required infrastructure in comparison with HPGe at the same relative efficiency. While the traditional use of thallium doped sodium iodide (NaI:Tl) offered low energy resolution, the ongoing search for newer scintillation materials nowadays enables the use of much better performing scintillators such as cerium doped lanthanum bromide or intrinsic cerium bromide, both of which show much better energy resolution (e.g. Schotanus et al., 2013; Khateeb-ur-Rehman et al., 2016). While an assessment of emanation sources by the method of (Linzmaier and Röttger, 2013) was

initially not possible with NaI:Tl detectors due to strong overlaps in the spectrum, it may be with newer scintillators. This applicability is investigated in chapter 7 of this work.

In general, γ -ray spectrometry may only be applied as a secondary measurement technique. Specifically, the interaction probability of γ -rays with a given detector must be calibrated using another radiation source of the same geometry and ideally the same isotope in order for quantitative analysis. Commonly, a parametrization such as the one given in (Jäckel et al., 1987), of the energy dependence of the detector efficiency is carried out for the quantification of differing isotopes between the source and the calibration standard, requiring also the knowledge of the γ -emission probabilities of both the isotope in question and the calibration isotope(s). Both of these factors contribute to the uncertainty that may be achieved by a γ -ray spectrometric measurement. Typically, the overall full-energy counting efficiency in γ -ray spectrometry is on the order of permille to few percent leading also to a relatively high statistical counting uncertainty of such methods, exacerbated by a ubiquitous γ -radiation background and a general background in the spectrum mainly formed by interaction of higher-energy γ -rays through Compton scattering. γ -ray spectrometry at relatively low activity levels also requires shielding, typically by using several centimeters of lead, against the impact of the natural background. This background can not be entirely avoided and is formed by γ -rays originating from primordial and cosmogenic nuclides, remaining dispersed anthropogenic nuclides and ultimately also by contributions of cosmic radiation.

Spectrometry of α -particles

Most α -particle spectrometric measurements are performed by using semiconductor detectors. The requirements for the employed semiconductor are more relaxed than these for the previously mentioned γ -ray spectrometry. The deposited energy by α -particles is often orders of magnitude higher than for γ -rays, and as such, the band-gap and leakage current requirements are not as stringent. For these reasons, α -particle semiconductor detectors are usually manufactured from silicon.

Further, α -particles have a very high linear energy transfer and therefore, only relatively thin depletion layers are needed to achieve practically unity detection probabilities. Conversely, any intermitten matter between the depletion zone formed by reverse biasing of the p/n-junction and the point of emission of the α -particles can cause significant energy loss. Hence, the entrance window of such detectors should be as thin as possible and sources for measurements are ideally massless. Both of these factors have a tremendous impact on the energy resolution that can be achieved. This also means that α -particle spectrometry is typically performed in a reduced pressure environment. Background contributions in α -particle spectrometry are typically very small, especially in comparison with γ -ray spectrometry and mostly stem from previous contamination of the setup with α -emitters. As such, the signal to noise ratio is usually several orders of magnitude higher in case of α -particle spectrometry compared with γ -ray spectrometry, especially in low-level measurements.

Historically, such detectors were constructed on the principle of a Shottky-Diode by evaporated metallic contacts on the front- and back-side of a planar silicon wafer, so called surface barrier detectors (Choppin et al., 2002). Nowadays, ion-implanted silicon detectors, such as the *PIPS* by *Mirion technologies* or equivalent products from other manufacturers, can be seen as the standard for α -particle spectrometry. These offer superior energy resolution provided by very thin entrance windows, general ruggedness and reduced leakage currents. *PIPS* detectors are typically operated at room temperature.

2.3.2 Defined solid-angle alpha-particle spectrometry

As mentioned in the previous section, α -particles have a very high linear energy transfer and are therefore detected with practically unity probability if they enter the depletion zone of a semiconductor detector. Due to this almost non-stochastic absorption of the incident α -particles, the counting efficiency of a spectrometry setup is practically entirely defined by its geometry. In the case of perfect knowledge of the counting geometry, one may thus compute the detection efficiency analytically or by numerical methods, which entails the computation of the solid-angle of the radiation source subtended by the detector. Therefore, α -particle spectrometry may be applied as a primary measurement method, and it nowadays is one of the most precise and accurate methods for the primary standardization of α -emitters, typically traceable to the second and the meter. This technique is referred to as defined solid-angle (DSA) α -particle spectrometry, since it entails the definition of the solid-angle by a well specified geometry, usually consisting of several apertures of well determined geometry. This technique is applied for example at the LNHB, the Joint Research Center of the European Commission in Geel (JRC Geel) and the PTB. Recent reviews of this technique, also considering potential sources for systematic uncertainty are given in (Pommé and Sibbens, 2008) and (Pommé, 2015).

Figure 2.4 shows a cutaway-model of the PTB primary DSA α -particle spectrometry setup that was used for the primary standardization of ^{226}Ra throughout the works in Publication I, Publication II and Publication IV as well as the determination of the emanation coefficients in Publication II. The effective solid-angle of the source subtended by the detector is defined by an aperture of well quantified geometry with an opening diameter of (20.002 ± 0.002) mm at a fixed distance of (50.034 ± 0.030) mm to the surface of the radiation source. The source itself is spring loaded against a bottom aperture, fixing it in place and ensuring the respective distance. In this system, α -particles emitted to within the opening of the aperture are detected by a passivated implanted planar silicon (PIPS) detector of a nominal specified resolution of 20 keV at 5.5 MeV, which is assumed to detect all impinging α -particles. It is ensured, that the detector covers the entire opening of the aperture. The counting efficiency of the system is on the order of 1 % and the solid-angle is known to about 0.2 % standard uncertainty. The dead-time of the system is corrected by the pulser method, i.e., by feeding synthetically generated pulses into the pre-amplifier of the system using a calibrated high-precision pulse generator of 50.0000 Hz with negligible uncertainty and assessing the number of recorded pulses in the respective integration time. The entire system shows almost perfect rotational symmetry along the perpendicular axis that passes through the midpoint of the detector aperture. The setup is placed within a vacuum chamber, typically operated on the order of 0.1 Pa.

Determination of the effective counting efficiency

For simple source geometries, such as centered or eccentric points or homogeneous disk sources, the solid-angle subtended by the detector may be computed analytically, where specific formulas for different situations are given in (Ruffle, 1967; Ruby and Rechen, 1968; Gotoh and Yagi, 1971; Shelyuto, 1989; Ruby, 1994; Tryka, 1997; Pommé et al., 2003; Pommé, 2004; Conway, 2006; Pommé and Paepen, 2007) among others.

For the simplest case of a point-source located in the intersection point of the rotational-axis of the DSA setup with the plane of the source, the counting efficiency is given by the fraction between the solid-angle subtended by the detector and 4π sr as

$$\epsilon = \frac{\Omega}{4\pi} = \frac{1}{2} \left[1 - \cos \left(\tan^{-1} \left(\frac{r}{d} \right) \right) \right] \quad (2.37)$$

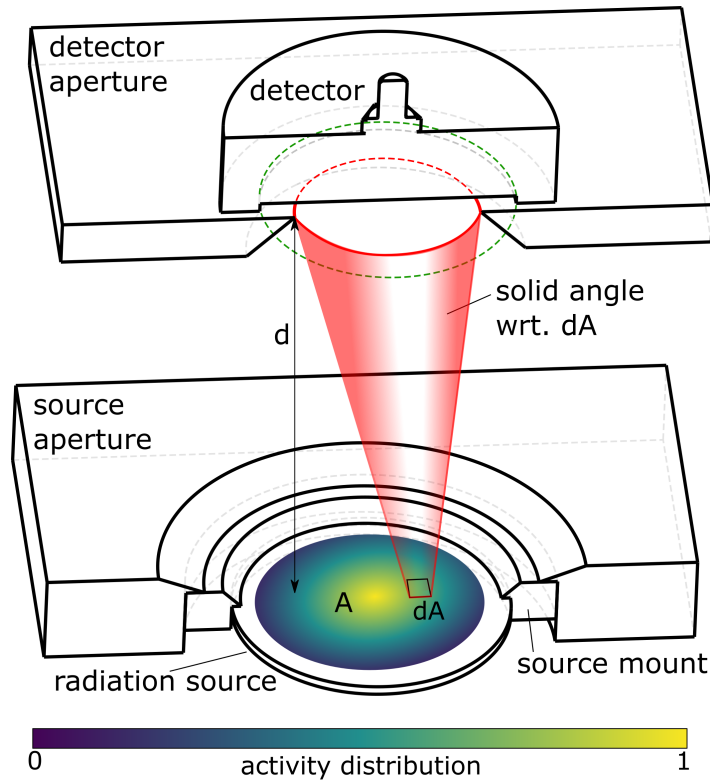


FIGURE 2.4: Cutaway model of the PTB primary DSA α -particle spectrometer.

where Ω signifies the solid-angle, r signifies the radius of the detector aperture and d signifies the distance of the detector aperture to the point-source, see Figure 2.4 for reference.

In practice, sources are never infinitesimally small and never perfectly homogeneous across their domain A . In this case, the counting efficiency may be computed by averaging the fractional solid-angle of each area element dA in the source domain A weighted by the relative activity content w_{dA} in dA , which leads to the following relationship for the effective counting efficiency ϵ of the DSA setup.

$$\epsilon = \frac{1}{4\pi} \frac{\int_A \Omega_{dA} w_{dA} dA}{\int_A w_{dA} dA} \quad (2.38)$$

where ϵ refers to the effective counting efficiency, dA refers to an area element in the source area A , Ω refers to the solid angle, w refers to the fractional activity and the subscript dA signifies the dependency of the quantity on the respective area element.

Applying equation (2.38) one may thus account for any inhomogeneity of activity in the source, given that w_{dA} can be inferred from experimental data or modelling. In general, equation (2.38) is not tractable analytically, especially when irregular or complex activity distributions, rotational asymmetry and eccentricity are considered.

While numerical approaches for solid-angle calculations have numerous been reported before, reports of incorporation of the source's activity distribution are relatively scarce. For example, (Sibbens et al., 2003) published a method relying on first computing Ω as a function of distance to the midpoint of the source and then using a discrete convolution of the computed data with experimental radial distance activity distributions to incorporate the influence of the activity distribution. However, this method can not account for rotational

asymmetry and furthermore it is challenging to propagate the uncertainty of the geometrical parameters.

In this work, a novel, yet simple method was implemented and applied, relying on Monte-Carlo ray-tracing to compute the integrals in equation (2.38). Therein, random rays are generated within the source domain A and their passage through the known and defined geometry is analyzed using simple vector arithmetic. For more information on the formalism, the reader is directed to Appendix B. Potential asymmetry and aperture tilting is accounted for by this method. It should be noted, that physical processes of the α -particles, such as energy loss from the penetration of matter and scattering are not considered in this calculation, since merely the solid-angle is required for equation (2.38).

The initial generation of rays, i.e. their origins, are sampled from user defined activity distributions, including simple parametric forms such as the 2D-Gaussian case as well as arbitrary discrete distributions, e.g. obtained from experimental methods such as digital autoradiography. Equation 2.38 is solved by computing the fraction of rays that passed the detector aperture and the total number of generated rays. The implementation is carried out such that for each parameter defining the geometry, experimental uncertainty as well as an underlying probability density function (Uniform, Gaussian, etc.) may be specified. These parametrized distributions are used to resample the geometrical parameters after a set number of generated rays, typically chosen to be on the order of 10^7 . Thereby, each iteration of this resampling yields a draw from the distribution of ϵ , characterized by all included uncertainty contributions. Thus, the combined uncertainty resulting from all uncertain geometrical parameters as well as their influence on ϵ may be analyzed concerning a specific activity distribution.

Nowadays, graphical processing units (GPUs) are well equipped for such a task, because their architecture is tailored to both vector arithmetic, trigonometric functions and the required high parallel throughput. Using current mid-range GPUs, computation times for reasonable statistically powerful (10^5 geometrical realizations, 10^7 rays per geometry) results may be obtained within a few hours, and hence, the counting efficiency as well as the complete interdependency of the geometrical uncertainties was computed individually for each manufactured source. Computation throughput of this implementation is nowadays typically on the order of up to 10^9 rays/s. A similar approach was recently published in (Arinc et al., 2016), albeit without employing GPUs for this task. Using such a method yields a very good estimation of the resulting uncertainty in ϵ , especially when carried out for each specific activity distribution.

This method of computing the efficiency was compared to results of an analogous GEANT4 (Allison et al., 2006) simulation in order to analyze the contribution of (back)-scattering. It should be noted, that it is not computationally feasible to resample the geometry also in the GEANT4 simulations, as such a simulation takes up to several days. Therefore, both the influence of the experimentally determined activity distribution of the source and the effect of the uncertainty in the geometrical parameters on the resulting counting efficiency cannot be feasibly determined using GEANT4, since it would require far too many GEANT4 runs.

Deviations of up to 0.3 % were observed between the GEANT4 simulated efficiency and the efficiency computed by the implemented formalism, which are thought to be due to scattering. A scattering correction factor was thus introduced into all DSA analyses in Publications I, II and IV to account for the uncertainty due to this effect. Specifically, the simulation was carried out using a point-source and an emission of $5 \cdot 10^8$ α -particles with an initial energy of 5 MeV that are emitted isotropically. The DSA setup was modeled following the depiction in Figure 2.4, using the known geometrical dimensions. To include forward scattering

contributions, a hypothetical source layer of 500 nm of Barium-Hydroxide was added to the source backing. Energy deposited within time-frames of $0.5 \mu\text{s}$ is bunched up, in order to simulate the detection mechanism of a real detector. Nuclear recoil was modeled in this simulation by GEANT4's implementation of the scheme given in (Mendenhall and Weller, 1991), namely in the C++ class *G4ScreenedNuclearRecoil* of the GEANT4 libraries.

Figure 2.5 shows a two-dimensional histogram of energy deposited in the modeled detector per initial emission angle θ against the rotational symmetry axis of the simulated DSA setup. It can be seen, that scattering is only a minor contributor to the counts in close proximity to the full-energy events in the resultant α -spectrum, while it contributes exceedingly to the lower energy region. The contributions to the low-energy region in the spectrum appear to be maximal for $\theta \approx \frac{1}{2}\pi$. At this emission angle, the path length through the hypothetical source material and correspondingly the amount of generated low-energy secondary particles (mainly electrons and photons from the relaxation of ionized materials) reaches its maximum, leading also to maximal contributions in a corresponding energy range to the spectrum at such values for θ . At emission angles $\theta > \frac{1}{2}\pi$, the emitted α -particles hit the source backing and create secondary particles therein, which are mostly self-absorbed within the source backing or the hypothetical source material. On the other hand, at angles $\theta < \frac{1}{2}\pi$, the path length through the hypothetical source material is relatively small and therefore, contributions to the spectrum from these angles are relatively low. Furthermore, at some critical value for θ , the α -particles hit the edge of the detector aperture, which leads to contributions to the spectrum directly from α particles that lost significant energy or even from secondary electrons and photons due to ionization processes in the aperture itself. Furthermore, the path length through the detector dead-layer increases with increasing θ , also contributing to α -particle energy loss at greater angles of incidence. It should also be noted that the generation of emission directions in these simulations is isotropic, which means that $\frac{1}{2}\pi$ is also the most likely value for θ .

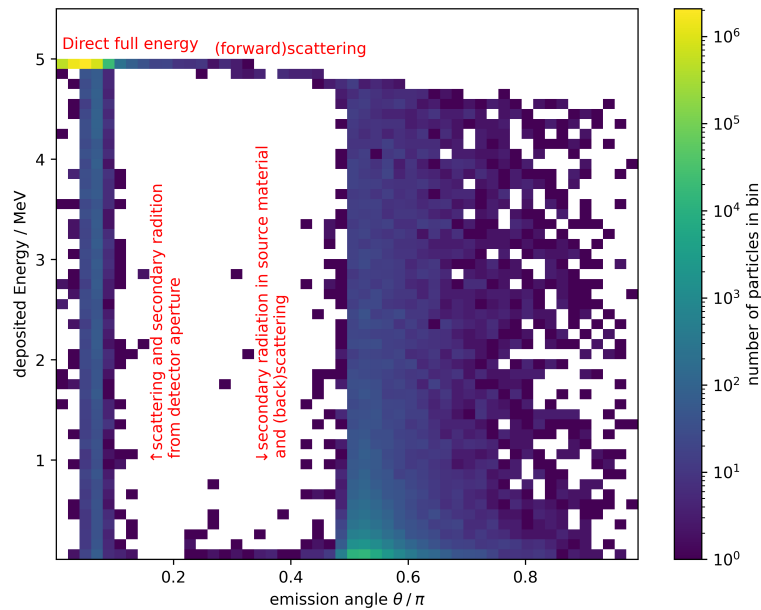


FIGURE 2.5: GEANT4 simulated distribution of polar angle and deposited energy of 5 MeV emitted α -particles in the PTB DSA α -particle spectrometry. Distribution over $5 \cdot 10^8$ isotropically emitted particles.

2.3.3 Autoradiography

As described in the previous section, the actual distribution of radioactive isotopes in the source has to be taken into account in the computation of the solid-angle for the DSA α -particle spectrometry.

A common technique that was also applied throughout this work for this purpose is given by digital autoradiography (e.g. Sibbens et al., 2003), in which an imaging plate (Amemiya and Miyahara, 1988) sensitive to impinging ionizing radiation is placed in close proximity to the source. Energy deposited by interaction of ionizing radiation with the phosphorescent material on the imaging plate leads to its excitation. Readout is carried out by scanning with a laser that leads to the stimulated emission of optical photons which is converted into digital information. For this purpose, commercially available standard imaging plates were used in conjunction with a FUJIFILM FLA-9000 readout device, which yields digitized intensity values on a resolution of 0.04 mm² square pixels. The imaging plates are brought into a distance of approximately 1 mm to the source surface. It was not attempted to discriminate the contributions of the different radiation types emerging from ²²⁶Ra and its daughters in the source to the signal of the radiography. It is assumed, that each type of radiation contributes, at least through the generation of secondary radiation, to the radiography signal. Both (Pommé, 2015) and (Sibbens et al., 2003) also assume that the emitted α -particles directly contribute to the radiography signal obtained from comparable imaging plates and thus, supposedly, that they are the main contributor to the signal.

In order to retain information about the global geometry, a machined source holder is used, into which the source in question is inserted together with four ²³⁸Pu reference point sources. These allow to position a readout grid, centered with respect to the source support. Generally, the geometrical uncertainty stemming from the source holder dimensions as well as the position of the readout grid is considered negligible throughout this work.

It is important to mention, however, that this digital autoradiography does not yield the true activity distribution, due to three reasons given in (Pommé, 2015).

For one, the autoradiography image is subject to the Poisson statistics commonly observed with radioactivity measurements. In this type of measurement, however, the raw count values are not available, so care was taken in order to obtain images that utilize the entire dynamic range of the readout device. Since only the relative intensity values are of interest here, this stochastic component is considered negligible.

Secondly, the true activity distribution is three dimensional in nature, whereas the autoradiography only yields a two dimensional, i.e. projected, image. Since sources used in this work are very thin, on the order of few 100 nm at most, the depth component was disregarded in the computation of the solid-angle.

Finally and most importantly, however, the radiation is emitted isotropically from each volume element within the source domain. This leads to interaction of the radiation with pixels adjacent to the projected position of the decaying nuclides, and therefore, the radiography image only represents a convolved version of the true activity distribution. This can be considered with respect to a point spread function (PSF), with which the true activity distribution is convolved in the measuring process. This point spread function depends on the penetrating properties and interaction probabilities within the imaging plate of the different types of radiation. While principally such considerations are commonly encountered in image processing, deconvolution generally requires knowledge of the underlying PSF and considerably complicates the issue with respect to uncertainty estimation procedures. In practice, it is also hardly possible to measure this PSF, since for one, the emission of β - or

α -particles is almost always accompanied by the emission of photons, and vice-versa, and since point-sources do not exist in reality.

However, the ion-implanted sources from Publication II can be considered as an ideal approximation here, since the ion-beam profile with which they have been created was well characterized in previous work (Kieck et al., 2019). Indeed, the autoradiography images obtained from the implanted sources showed a broader activity distribution than suggested by the beam-profile, which may also not entirely be explained by the lateral straggling of implanted ions in the target material. By comparison of the solid-angle of the DSA spectrometer computed using the beam-profile of the implantation device with the one obtained using the autoradiography image, a standard uncertainty of 0.1 % in the solid-angle due to the described effect was estimated in Publication II.

This can be seen as the upper limit of the uncertainty due to the described effects, since the impact on the computed solid-angle is maximized when the true distribution is a delta distribution centered on the point where the rotational axis of the spectrometer crosses the source. Hence, the contribution of the described components was disregarded for the analyses of more extended sources in Publications I and IV, since the uncertainty of the solid-angle therein is dominated by the geometrical uncertainty of the aperture system.

2.3.4 Data analysis

As pointed out before, the strength of the features of a spectrum are considered to be given by a linear transformation of the integrated activity of the source. The analysis of spectrometric data in order to quantify the activity of a source entails quantification of the features of a spectrum. Typically, the analyzed features are the areas under peaks in the γ -ray and α -particle spectra respectively.

In both HPGe- and scintillator-based γ -ray spectrometry, the shape of the full-energy peaks is well described by a Gaussian profile, and therefore, regression of a Gaussian density function allows to determine the area under the peak. Generally, events that are non-specific to the full-energy peak also contribute to its area, which mostly form a linear background under the peak that has to be included in the peak-shape model, for example due to Compton scattering of higher energy photons in the detector. Peak areas in γ -ray spectra can also be derived from a simple algorithm, which computes the sum of all channels in a specific region of interest and subtracts a background value derived from linear interpolation of adjacent regions. Both of these approaches have been used throughout this work for the analysis of γ -ray spectra, depending on the specific situation and spectra at hand. Furthermore, in γ -ray spectra, the number of counts in each channel are well above 30 in most cases, and therefore, the usual approaches of non-linear least-squares regression, which assume the data to be distributed as a multivariate Gaussian, were considered to yield the unbiased estimators as well as reliable uncertainty estimates.

In the case of α -particle spectra, however, the peak-shapes are more complicated. Peaks in α -particle spectra typically feature more or less pronounced left-handed tailing. This is explained by the variance of the energy-loss of impinging α -particles, which is in part due to the variance of the path length through intermingled materials such as the detector dead-layer and the source material itself. For this reason, the left-handed tailing is generally more pronounced for sources with higher areal density and at low source to detector distances. Despite that the full width at half maximum (FWHM) is often reported in α -particle spectrometry as a general indicator of quality of the spectrum, it fails to describe the strength of the tailing. In practically all cases, the tailing leads to the overlaps between the tail of a higher energy peak with a lower energy peak. Conversely, the DSA α -particle spectrometry

method can only provide absolute activity values when all contributions of a specific isotope to the entire spectrum are accounted for in the analysis including any events contained in the left-handed tails of each peak. Consequently, the method performs best at low tailing and thus ideally for massless sources at infinite source to detector distance. Therefore, it requires a thorough analysis of obtained spectra in order to accurately determine the area under each of the observed peaks, more so in comparison with methods that are subject to a calibration with a standard source.

One of the most successful techniques in α -particle spectrometry is given by the regression of a specific peak-shape model made up of the sum of exponentially modified Gaussians. The exponentially modified Gaussian (ExGaussian) is given by the convolution of an exponential density with a Gaussian density as derived in (Bortels and Collaers, 1987) and given by equation (2.39).

$$f(x, \mu, \sigma, \tau) = \frac{A}{2} \tau \exp \left[(x - \mu) \tau + \frac{1}{2} \sigma^2 \tau^2 \right] \operatorname{erfc} \left[\frac{1}{\sqrt{2}} \left(\frac{x - \mu}{\sigma} + \sigma \tau \right) \right] \quad (2.39)$$

where x refers to the channel or energy values in the spectrum, μ refers to the position of the mode in terms of channel number or energy respectively, σ signifies the standard deviation of the convoluting Gaussian and τ refers to the decay parameter of the exponential density with unit of reciprocal channels or energy respectively and A describes the area under the component.

Often, a single such ExGaussian density fails to accurately describe the tailing, and therefore, each peak is typically described by a linear combination of ExGaussian densities. While initial developments of these models included up to 3 components per peak (Bortels and Collaers, 1987), newer extensions include up to 10 (Pommé and Caro Marroyo, 2015) to more accurately describe the peak shape. The authors are not precise, whether the corresponding shape parameters are shared among all peaks, shared among only the peaks caused by each isotope or not shared among any of the peaks. In some cases, peaks can also show a less pronounced right-handed tailing that is supposedly due to coincidence effects and which also has to be taken into account.

However, the straight forward approach reported by (Pommé and Caro Marroyo, 2015) was often experienced to fail throughout this work due to a number of reasons, which are discussed below. Specifically, this lead to significant modifications and extensions of their original algorithm, which improve both the numerical behaviour and the success of such models of finding a physically meaningful result.

The parametrization of the ExGaussian as given in (2.39) leads to numerical overflow due to overflow of the exponential factor. This may be overcome by a well-known alternative parametrization in terms of the scaled complementary error function $\operatorname{erfcx}(x)$, $\operatorname{erfcx}(x) = \exp(x^2) \operatorname{erfc}(x)$, as given by the piecewise definition in equation (2.40) that is stable over the entire $x \in \mathbb{R}$ (Delley, 1985). This requires a method to evaluate the scaled complementary error function, such as the one given in (Shepherd and Laframboise, 1981).

$$f(x, \mu, \sigma, \tau) = \begin{cases} \frac{A}{2} \tau \exp(a) \operatorname{erfc}(b) & \forall a \leq 0 \\ \frac{A}{2} \tau \exp(c) \operatorname{erfcx}(b) & \forall a > 0 \end{cases} \quad (2.40)$$

where $a = (x - \mu) \tau + \frac{1}{2} \sigma^2 \tau^2$, $b = \frac{1}{\sqrt{2}} \left(\frac{x - \mu}{\sigma} + \sigma \tau \right)$ and $c = -\frac{(x - \mu)^2}{2\sigma^2}$.

Each peak in the spectrum may thus, following (Pommé and Caro Marroyo, 2015) and (Bortels and Collaers, 1987), be described as the weighted sum over different realizations of equation (2.40) and hence, the profile of a single peak in the spectrum is given by equation (2.41), which may be seen as the scaled probability density function of a mixture of ExGaussians.

$$P_n(x, \boldsymbol{w}_n, \boldsymbol{\mu}_n, \boldsymbol{\sigma}_n, \boldsymbol{\tau}_n) = \sum_{i=0}^k w_{n,i} f(x, \mu_{n,i}, \sigma_{n,i}, \tau_{n,i}) \quad (2.41)$$

where n describes the peak-index, i describes the tail-index and k signifies the total number of tails in the n -th peak.

In order to directly obtain the respective peak areas from regression, the weights $w_{n,i}$ have to be constrained for each n : The components may only be between zero and one, and they have to sum to one, and hence, within the weights the degrees of freedom are actually only $k - 1$. As such, the vector \boldsymbol{w}_n , containing the stacked weights of peak n , lies on the $k - 1$ dimensional (probability) simplex. When applying regression using first- or second-order methods, it is often desirable to obtain unconstrained parameters, which may be achieved by parameter transformations. To obtain a vector $\hat{\boldsymbol{w}}_n$ with support on \mathbb{R}^{k-1} such that \boldsymbol{w}_n lies on the $k - 1$ dimensional (probability) simplex, the *isometric logratio transformation* (Egozcue et al., 2003) was used and the regression was carried out with respect to the transformed $\hat{\boldsymbol{w}}_n$. Similarly, the elements of the vectors $\boldsymbol{\mu}_n$, $\boldsymbol{\sigma}_n$ and $\boldsymbol{\tau}_n$ are restricted to positive values, which is achieved by the commonly applied *softplus* transformation (i.e. $\hat{\sigma} = \ln(1 + e^\sigma)$ to transform $\sigma \in \mathbb{R}$ to a positive parameter $\hat{\sigma}$).

Often the peak areas are the parameter for which the gradient of common objective functions, such as the sum of squared residuals, is smallest. Therefore, initial steps of gradient descent or second-order methods lead to strong changes of the tailing parameters, often such that the shape of peaks diverges from each other strongly. Of course, such results can not be motivated physically, because the tailing of different peaks should generally be similar, unless it must be assumed that the physical position of the different nuclides is significantly different.

By extracting the peak areas A_n from the peak-shape parametrizations, stacking them into a vector \boldsymbol{A} and stacking the peak-shapes of each peak in the spectrum into a matrix \boldsymbol{R} , the peak areas can be identified as a linear parameter and the modeled spectrum $\hat{\boldsymbol{S}}$ can be written as

$$\hat{\boldsymbol{S}} = \boldsymbol{R}\boldsymbol{A} \quad (2.42)$$

which signifies, that the modeled spectrum is given by a linear combination of the contributions of each peak to the spectrum.

Consequently, for a given realization of \boldsymbol{R} , the sum of squared residuals with respect to a measured spectrum \boldsymbol{S} is minimized by the solution to the normal equation of weighted linear regression as

$$(\boldsymbol{R}^T \boldsymbol{W} \boldsymbol{R}) \boldsymbol{A} = \boldsymbol{R}^T \boldsymbol{W} \boldsymbol{S} \quad (2.43)$$

where \boldsymbol{W} signifies a matrix of weights, which should generally be chosen to reflect the reciprocal variance in \boldsymbol{S} , and due to the Gaussian approximation to the Poisson statistics as $\text{diag}(\boldsymbol{S}^{-1})$. Such linear problems can be efficiently solved using decomposition methods,

such as the Cholesky decomposition or Singular Value decompositions for example. As such, the optimization of peak area parameters can be split from the optimization of the non-linear shape parameters in order to improve convergence. This circumvents the issue with the small gradients of the objective function with respect to \mathbf{A} , as for each realization of \mathbf{R} obtained throughout the non-linear optimization procedure, the best-fitting peak areas are implicitly found.

Obtaining the best fitting peak-shape parameters, which describe \mathbf{R} , on the other hand involves non-linear regression, minimizing an objective function such as the one given in (2.44). In parts of this work, mainly Publication IV, a regularization function $g(\boldsymbol{\theta})$ described below was introduced into the negative log-likelihood under Gaussian distributed observations in order to achieve better convergence properties. For spectra, in which the Gaussian assumption of the observed spectrum is not sufficient, for example IRSD spectra obtained in a time period so short that the number of counts in some channels is < 30 , a modified log-likelihood function assuming Poisson distributed observations was used instead, as described in Appendix A of Publication IV.

$$\begin{aligned} \mathcal{L}(\boldsymbol{\theta}) &= \frac{1}{2l} (\mathbf{s} - \hat{\mathbf{s}})^T \mathbf{W} (\mathbf{s} - \hat{\mathbf{s}}) + g(\boldsymbol{\theta}) \stackrel{(2.43)}{=} \\ &= \frac{1}{2l} \left(\mathbf{s} - \mathbf{R} (\mathbf{R}^T \mathbf{W} \mathbf{R})^{-1} \mathbf{R}^T \mathbf{W} \mathbf{s} \right)^T \mathbf{W} \left(\mathbf{s} - \mathbf{R} (\mathbf{R}^T \mathbf{W} \mathbf{R})^{-1} \mathbf{R}^T \mathbf{W} \mathbf{s} \right) + g(\boldsymbol{\theta}) \end{aligned} \quad (2.44)$$

where $\boldsymbol{\theta}$ describes a vector containing all parameters and l signifies the number of channels the regression is carried out over.

However, convergence into an unphysical minimum where the shape of the tails diverges from one another is still possible, which will lead to unreliable area determinations. Since for a single source, the isotopes making up the α -particle spectrum can generally be considered to be at very similar physical locations, one expects their tails to be similar. Nonetheless, small differences in intermitten absorbing material, the initial α -particle energies and the different decay properties leading to the potential occurrence of true α -photon and α -electron coincidence can lead to differences in the peak shapes.

The regularization function $g(\boldsymbol{\theta})$ was introduced, specifically for Publication IV, which penalizes solutions in which the tailing parameters are strongly dissimilar by a penalty function evaluating the sum of scaled quadratic deviations of the transformed weight vector $\hat{\mathbf{w}}$ and untransformed $\boldsymbol{\tau}$ vectors from a common one, such as the one for the 0-th peak as in (2.45). The reason why this is specifically relevant for Publication IV lies in the strongly tailed α -particle spectra obtainable by the IRSD system.

$$g(\boldsymbol{\theta}) = \frac{1}{2} \sum_{n=1}^j \left[(\hat{\mathbf{w}}_0 - \hat{\mathbf{w}}_n)^T (\kappa \hat{\mathbf{w}}_0^2) (\hat{\mathbf{w}}_0 - \hat{\mathbf{w}}_n) + (\boldsymbol{\tau}_0 - \boldsymbol{\tau}_n)^T (\gamma \boldsymbol{\tau}_0^2) (\boldsymbol{\tau}_0 - \boldsymbol{\tau}_n) \right] \quad (2.45)$$

where κ and γ are parameters that signify how strong the regularization is in comparison with the log-likelihood term given in (2.44).

As a side note, an equation very reminiscent of equation (2.44) can be derived for a Bayesian model, in which one assumes the likelihood of the measurement is a Gaussian and the tailing parameters are distributed according to a common Gaussian distribution.

Due to the non-linear *softplus* transformation of $\boldsymbol{\tau}$ which produces the actual input values to the peak-shape, this penalizes the deviations across the strongly tailed contributions much

more than those across the weakly tailed ones. This is a desirable property, since the deviations in the different tailings are often stronger close to the mode.

The outlined extensions of the regression algorithms lead to much better convergence properties and where the sensitivity towards starting parameters is significantly reduced in comparison to the original formulations in (Pommé and Caro Marroyo, 2015). Consequently, less user interactions and domain knowledge is required, and it allows to drop the commonly made simplifying assumption that peaks share common tailing parameters. Since the number of required parameters to accurately describe the obtained ^{226}Ra spectra using the outlined models is often on the order of 100, this regularization was found to be a requirement. In general, the strength of the regularization was hand-tuned by comparing reduced χ^2 values obtained for different values for κ and γ .

The outlined scheme above was implemented using the Python libraries *Jax* (Bradbury et al., 2018) and *Scipy* (Virtanen et al., 2020). *Jax* enables to compute gradients and potentially even higher order derivatives, such as the Hessian matrix, the Hessian vector product and the Jacobian vector product of (2.44) with respect to the parameters by automatic reverse and forward mode differentiation, which are subsequently used as the input to the quasi-Newton minimization routines provided by *Scipy*, such as the *Broyden-Fletcher-Goldfarb-Shanno* (BFGS) algorithm, e.g. (Broyden, 1970).

The standard approach of estimating the parameter uncertainty in non-linear regression models lies in assessment of the curvature of the objective function around the optimal point, which has also been employed to similar models before (Pommé and Caro Marroyo, 2015; Caro Marroyo et al., 2013). As such, the covariance matrix of the parameters of such non-linear models may in principle be obtained by linearization as the scaled inverse of the Hessian matrix of the objective function at the optimal point, proof of which is given e.g. in section 3 of (Nelles, 2020). This can in some sense be seen as the Laplace Approximation (i.e. the Gaussian approximation) to the posterior distribution of the model parameters (Amaral Turkman et al., 2019). Despite the previous reports applying this method for α -particle spectra models, it was unfortunately experienced to be unreliable in for the determination of the covariance matrix of the model parameters in this work, where (Pommé and Caro Marroyo, 2015) have also already hinted at the shortcomings of this estimator. It should be noted, that the Hessian inverse approximation is indeed often considered to be unreliable regardless, discussion of which can be found, among others, in (Dosne et al., 2016; Doví et al., 1991; Peddada and Haseman, 2005; Gill and King, 2004), both because of numerical properties of the Hessian and because it inherently assumes that the parameters are jointly distributed as a Gaussian. It is unknown, whether in this specific case it is caused by numerical precision considering the commonly observed bad conditioning of the Hessian or by specification of the model, however, often, the Hessian matrix computed for the objective function in (2.44) is not positive definite at the optimal parameter values even without considering the regularization term. As a result, the Laplace approximation fails since it requires a positive definite Hessian. In principle, a Monte-Carlo assessment of the uncertainty may be possible, however, this is complicated by the sheer number of parameters and the high computational cost of evaluating \mathbf{R} , and is hence not feasible using the currently available computational resources. Moreover, the model outlined above may also be viewed as a mixture model, for which the application of Markov-Chain Monte-Carlo methods is well-known to be problematic. This is mainly due to the fact, that the element indices of the \mathbf{w} , σ and τ vectors may be jointly shuffled without changing the value of the likelihood function, which is also known as the *label switching problem* in the literature, e.g. (Stephens, 2000).

As such, the estimation of the peak uncertainty was generally instead carried out by evaluating the square roots of the determined peak areas to account for the stochastic uncertainty

and by a heuristic approach of analyzing the regions adjacent to the peak. In general, this approach yields systematic uncertainty estimates on the order of 0.3 % in case of the IRSD spectra, that are due to unresolved or incorrectly modeled tailing.

2.4 Source preparation techniques

2.4.1 Purification of radium

Practically all subsequent techniques applied throughout this work are sensitive towards chemically and physically interfering impurities. Therefore, it was deemed necessary to prepare a ^{226}Ra solution with suitable purity. At PTB, ^{226}Ra solutions are available as its chloride in solution, carried by the addition of 0.5 % m/m BaCl_2 in 0.1 M HCl and with known activity, traceable to the primary national Hönigschmid ^{226}Ra activity standard. However, the knowledge of the precise activity of the used ^{226}Ra solution in this work is not required, since the deposited activity will be determined using an absolute measurement technique and therefore, the best purification method could be freely chosen among the current knowledge. Depending on the activity of the employed standard solution, barium ions are present in amounts several thousand times the amount of Ra^{2+} , which was expected to interfere with the following experiments. Therefore, especially the barium content of the solution needed to be reduced.

While the classical method for the separation of radium from barium is the fractionated crystallization of the halides (Hönigschmid, 1912) or fractionated precipitation (Kirby and Salutsky, 1964; Salutsky and Stites, 1955), those are not the methods of choice in this work, since it was presumed that they only reasonably apply to macroscopic amounts of radium. For the separation of barium and radium, several chromatographic techniques have been studied and established in earlier work, for example in the field of environmental radioactivity measurements, commonly based on strong, sulfonic- or phenyl-sulfonic acid anionic exchange resins like Dowex AG50W, (Tompkins, 1948; Flores-Mendoza et al., 1992; Lagacé et al., 2017) among others.

These processes are generally superior to the crystallization-based methods considering enrichment of radium for the amount of manual labor, provided that radium is already present in a relatively high quantity. An adaptation of the established ion-exchange processes to the present work was expected to have two important drawbacks. On these resins, due to the lack of strong selectivity, barium is eluted before radium, which results in the tailing of barium into the radium fraction, especially when a high excess of barium is present and flow rates are not precisely controlled. Moreover, the elution is usually carried out with highly concentrated nitric acid, which reportedly leads to the breakdown of the polymer backbone of the resin and thus introduces impurities containing sulfate, which is presumed, and in some cases was already reported to, strongly interfere with later experimental procedures (Whitehead et al., 1992).

Alternatively, the strontium selective crown-ether 4,4'(5'')-di-tertbutyl-di-cyclohexano-18-crown-6, commonly referred to and commercially available in dispersed form on a SiO_2 powder as Sr-Resin, has shown modest, but different, affinities for radium and barium respectively (Horwitz et al., 1992; Chabaux et al., 1994). Importantly, the affinity towards radium is smaller than that towards barium. Therefore, radium is eluted first from such a chromatographic column, which prevents the considerations with the tailing of barium. It has been applied in the past to both the purification of radium from barium at environmental levels (Chabaux et al., 1994; Larivière et al., 2005) as well as the purification of radium

with the intent of ^{226}Ra target production for cyclotron irradiations on the mg scale (Marx, 2014).

In this work, extraction chromatography using Sr-Resin was applied to reduce the barium content in the available RaCl_2 solutions, where the protocol was loosely based on the optimization work carried out by (Marx, 2014). Specifically this regards the acid concentration of 0.6 M HNO_3 at which the loading and elution was carried out. While it appears from the data published in (Horwitz et al., 1992) that the affinity towards barium is highest at an acid concentration of 2 M and that the greatest difference between the affinities towards barium and radium is also at this concentration, (Marx, 2014) observed the greatest difference at 0.6 M HNO_3 .

Three Sr-Resin cartridges (2 mL each, 50 - 100 μm particle sizes, Eichrom Technologies Inc.) were connected in series and pre-conditioned by passing 30 mL of 0.6 M HNO_3 through the column at a flow rate of $0.5 \text{ mL} \cdot \text{min}^{-1}$. A mixture of 71 kBq $^{226}\text{RaCl}_2$ in 2 mL 0.5 % m/m BaCl_2 in 0.1 M HCl and 13 kBq $^{133}\text{BaCl}_2$ in few μL of the same carrier solution was prepared and evaporated to dryness in a glass jar using a sand-bath at $100 \text{ }^\circ\text{C}$. ^{133}Ba was added as a radio tracer for inactive barium allowing for the employment of HPGe γ -ray spectrometry to monitor the chromatography process. To the resultant residue, 1 mL of concentrated HNO_3 was added and evaporated to dryness for conversion into the nitrates, which were quantitatively transferred onto the pre-conditioned Sr-Resin column using a total of 1 mL of 0.6 M HNO_3 . Elution was carried out by passing 0.6 M HNO_3 at a flow rate of $0.5 \text{ mL} \cdot \text{min}^{-1}$ through the column and collecting fractions of 5 mL. Fractions in which no, or a sufficiently small amount of ^{133}Ba could be detected in the γ -ray spectrum on a high-purity germanium (HPGe) detector were pooled and aliquoted for later use. Thereby, solutions containing roughly the same masses of inactive barium and radium were obtained, as later evidenced in section 2.4.3. Theoretically, ^{226}Ra could be recovered almost quantitatively from the Sr-Resin column, but a variable amount of ^{226}Ra was disposed of due to non-satisfying amounts of detectable ^{133}Ba in the respective elution fraction. By pooling the first 15 mL of elution, typically > 80 % of ^{226}Ra could be recovered while suppressing barium by a factor of above 1400. A typical elution profile of this procedure is given in Figure 2.6.

2.4.2 Electrodeposition of radium

Electrodeposition, especially of the actinides uranium, plutonium and americium, is a well-established method for the production of α -particle emitting sources, which generally provides sources of relatively good energy resolution, often applied to the assaying of environmental samples. The actinides can undergo a number of electrochemical reactions in the electrochemical window of water, enabled by the stability and co-existence of multiple oxidation states in the range of 0 to +VI. Previously, it was suggested that this process leads to the electrodeposition of the respective actinide dioxide by electrochemical reactions.

An analogous process for ^{226}Ra does not occur, since the possible oxidation states of ^{226}Ra are +II and 0. The standard reduction potential of -2.8 V for the pair Ra(II)/Ra(0) (Bratsch, 1989) prohibits its reduction in aqueous solution by excessive hydrogen formation.

Despite this, (Parker and Grunditz, 1963) published a technique referred to as molecular plating, allowing for the manufacture of thin layers of a wide variety of isotopes, seemingly, regardless of the chemical species. As such, it was applied to the deposition of ^{137}Cs and ^{90}Sr layers (Parker et al., 1964; Getoff et al., 1967). Both elements are similarly difficult to reductively deposit due to their reactivity. Molecular plating generally applies relatively high voltages and uses a mixture of simple organic solvents such as ethanol and iso-propanol and water to achieve the electrodeposition. Despite recent efforts to understand the mechanisms

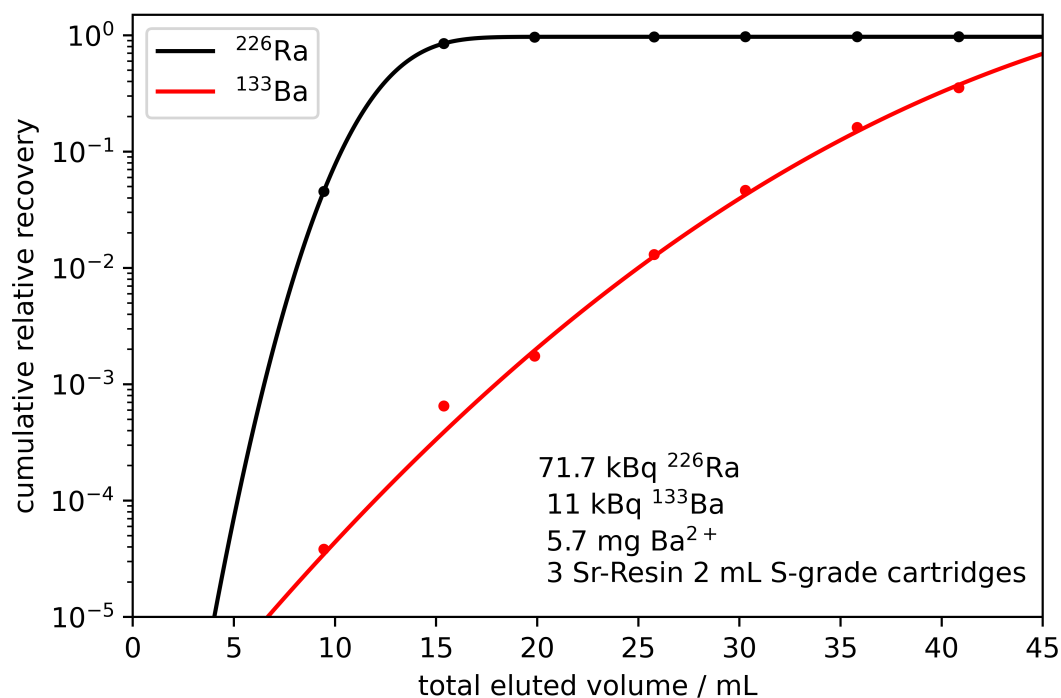


FIGURE 2.6: Typical elution profile of radium and barium from the Sr-resin based extraction chromatography employed in this work. In this example, (97.1 ± 1.1) % of the loaded ^{226}Ra could be recovered in the first 30 mL. Data points represent cumulative recovery values determined by γ -ray spectrometry and lines represent the results of non-linear regression of scaled Gaussian cumulative densities on these data. Uncertainty in recovery determinations is < 3 % and uncertainty indicators are invisible due to logarithmic y-scale.

behind this procedure in (Vascon et al., 2013; Vascon et al., 2014), among others, the mechanisms are not yet fully understood. Supposedly, the plate out is a result of migration of species under the applied external electrical field, electrochemical reactions, low solubility in the respective solvents and possible local concentration gradients as a result of electrode polarization.

Seemingly unconnected with these results, (Whitehead et al., 1992) and (Hancock and Martin, 1991) published comparable protocols for the electrodeposition of ^{226}Ra from slightly aqueous alcoholic solutions, specifically for the assaying of environmental samples. These procedures, however, are thought to be related to the original technique of molecular plating, specifically, regarding the solvents used. On the other hand, (Marx, 2014) attributes the deposition of ^{226}Ra using these or comparable protocols to the electrochemical formation of its peroxide, RaO_2 , however, no detailed mechanistic explanation or experimental evidence was given therein. Due to extrapolation of the chemical properties of the analogous BaO_2 , this is considered an unlikely mechanism due to its instability in acidic aqueous solutions.

Despite these mechanistic uncertainties, modified protocols based on the works of (Whitehead et al., 1992) and (Hancock and Martin, 1991) have been used in Publication I to achieve the manufacture of thin-layer sources of ^{226}Ra from the solutions obtained in the previous section 2.4.1. Therein, the high deposition yields reported by those authors could not be reproduced, even though different solvents (ethanol, iso-propanol), different applied potentials ranging from 20 to 200 V and different control mechanisms (potentiostatic and

galvanostatic control) have been applied. While a high yield is a desirable characteristic, it was not considered to be a crucial factor in this work and so this was not optimized further, also in light of the experimental properties of the electrodeposited sources evidenced later, e.g. their humidity dependency in Publication III and their comparatively low α -spectrum resolution.

Irrespective of the detailed deposition mechanism, it is very likely for any residual barium carrier to be plated alongside ^{226}Ra and therefore, the presence of barium has a significant impact on both the α -particle energy resolution of a source produced in this way and on the fraction of ^{222}Rn emanating from it. Experimental investigation of this dependence was previously carried out in (Vargas and Soto, 1995) underpinning this theoretical consideration, stressing the need for a purification procedure such as the one described in section 2.4.1 for an application towards emanation sources.

Additionally, due to the applicability of molecular plating to virtually any isotope (Parker and Grunditz, 1963; Parker et al., 1964; Getoff et al., 1967; Vascon et al., 2013; Vascon et al., 2014; Eberhardt et al., 2014; Drebert et al., 2013), it is suggested that this line of thought applies not only to barium, but to virtually all other metal impurities in the electrolyte mixture. Even for analytical grade solvents and considering that roughly 10 mL of electrolyte were used in the studies in Publication I, the quantity of other metal ions present is not negligible in comparison with the specifically low ^{226}Ra and barium content of the solutions obtained from section 2.4.1. It is thought that these circumstances lead to a difficulty of experimental control of the properties of resultant sources regarding its resolution in α -particle spectrometry and the magnitude and stability of their emanation coefficients.

2.4.3 Ion implantation

Ion implantation describes a process where ions are injected into a target after being accelerated, typically within a strong electric field. After impinging on the target, the incident particle loses energy quickly due to inelastic and elastic scattering processes. Since accelerated ions are needed for the implantation, it can readily be combined with a mass to charge ratio selection mechanism prior to implantation into the target, e.g., by traversal of a magnetic sector field, a quadrupole filter, a Wien filter or alike to obtain ion beams that practically only contain ions of a specified m/z mass to charge ratio.

Thereby, the local chemical and/or isotopic composition of a target close to its surface can be altered with a high degree of controllability and accuracy, concerning both the spatial distribution of injected atoms as well as the chemical purity. Therefore, the properties of a source manufactured in this way can be considered ideal, especially in light of the considerations given in the previous section 2.4.2.

The implantation depth depends on the implantation energy, the implanted ion type and the target material. The rate of change of the energy of the incident particle per unit length of penetrated material, $\frac{dE}{dx}$, is referred to as the stopping power, $S(E)$, which depends on both the incident particle energy and the properties of the penetrated material. The cross-section for inelastic scattering with target electrons decreases with decreasing energy, whereas the cross-section for nuclear-nuclear elastic scattering increases strongly. Due to this, $\frac{dE}{dx}$ increases along with decreasing energy which results in the characteristic Bragg curve of the penetration depth with a characteristic mode at the Bragg Peak, the most likely penetration depth. The mean traversed distance of the implanted ions can be calculated from the integral of the reciprocal stopping power, as

$$\langle \Delta x \rangle = \int_0^{E_{\text{incident}}} S^{-1}(E) dE \quad (2.46)$$

As a result of the deposited energy and the corresponding displacement of atoms within the structure of the solid target, ion implantation of even relatively few ions causes considerable damage to the microstructure of the target. Prolonged implantation therefore leads to amorphization of the target structure. The damage caused by implanted ions can be in part cured by a subsequent treatment of the target, e.g., using high temperature annealing to re-align the crystalline structure, which is a commonly applied step after ion implantation in semiconductor manufacturing. Since this process enhances the diffusion of implanted ions along the target, it is supposed to change the emanation characteristics of ^{222}Rn and was therefore not applied within this work.

^{222}Rn nuclei emerging from the decay of ^{226}Ra carry a recoil energy of 86 keV. Therefore, if ^{226}Ra is implanted into a solid substrate at energies much lower than 86 keV, a certain fraction of the emerging ^{222}Rn nuclei are ejected from the substrate body due to this recoil energy and are thus released from the source into the ambient air. However, the direction of the momentum of the emerging ^{222}Rn is isotropic with respect to the position of the ^{226}Ra nucleus and therefore, only a fraction of the generated ^{222}Rn undergoes ejection from the solid target. Neglecting secondary effects, the solid angle under which ejection happens from the target can be estimated by relating the mean range of 86 keV ^{222}Rn with the mean range of ^{226}Ra with a given incident energy in the respective target material as

$$\frac{\Omega}{4\pi} \approx \frac{1}{2} \cdot \left(1 - \frac{\int_0^{E_{\text{incident}}} S_{226\text{Ra}}^{-1}(E) dE}{\int_0^{E_{\text{recoil}}} S_{222\text{Rn}}^{-1}(E) dE} \right) \quad (2.47)$$

Since the stopping applies to both the implantation and the recoiling process alike, the approximation given by Eq. (2.47) depends only slightly on the target material. However, due to the transfer of momentum onto the target nuclei during the implantation, the resultant collision cascades lead to their ejection from the target bulk, a process referred to as sputtering. As the dose of incident ions per unit area increases, so does the amount of sputtered target material which results in a decrease of the effective implantation depth and can also lead to the loss of already implanted ions. Both the sputtering cross-section as well as the effect of each sputtered target nucleus on the resultant depth distribution of implanted ^{226}Ra depends strongly on the target material. Moreover, the diffusion properties of generated ^{222}Rn within the target may vary depending on the target material, hence the effective emanation coefficient is expected to depend strongly on the properties of the target.

Since in this case, the emanation process is largely dominated by the recoil process and if metals or even single crystals are used as targets, the substrate is not porous and does not adsorb large quantities of water from the surrounding air, it is expected that the emanation from implanted ^{226}Ra does not strongly depend on the relative humidity of the environment. However, the temperature of the substrate increases the diffusion of ^{222}Rn within the target material, such that it can be presumed that elevated temperatures lead to a higher fraction of ^{222}Rn that diffuses out of the material after being recoil implanted. To investigate the relative magnitude of these discussed effects and its general suitability for ^{222}Rn emanation source production, ion implantation of $^{226}\text{Ra}^+$ ions at 30 keV was carried out in Publication II. Two very different target materials have been used, aluminum and tungsten, which differ strongly in both Z and density. Ionization of ^{226}Ra was achieved by the technique of resonant laser ionization. The work was carried out at the RISIKO device of the University of Mainz,

which combines a resonant laser ion source with mass separation in a magnetic sector field and thus allows the generation and implantation of ultra-pure, practically mono-isotopic ion beams.

Resonant laser ionization

A crucial step in the implantation process is the generation of the ions to be implanted. The simplest method for this entails the thermal ionization of the species. This usually creates singly positively charged ions. For an atomic species in contact with a hot surface of work-function ϕ , the relative occupation of ground-state (neutral) and ionized state can be calculated from the Saha-Langmuir equation (Dresser, 1968),

$$\frac{N_+}{N_0} = \frac{g_+}{g_0} \exp\left(\frac{\phi - E_I}{kT}\right) \quad (2.48)$$

where E_I denotes the ionization energy, kT the thermal energy and g_+ and g_0 the degeneracies of the ionized- and ground-state respectively.

The electron configurations of Ra(0) and Ra(I) are 1S_0 and $^2S_{1/2}$ respectively, and hence, the ratio of degeneracies equates to 2 (including electron spin). Thereby, the ionization efficiency of elemental radium in contact with a hot tantalum surface ($\phi \approx 4.5$ eV, $E_I \approx 5.3$ eV) at 2300 K is estimated to 4 % at thermal equilibrium. (Goodacre et al., 2018) arrive at a comparable surface ionization rate estimate for radium from a hot tantalum surface. Therefore, the implantation of ions generated solely by surface ionization is a relatively inefficient process, which would require a large initial sample of radium to achieve the desired implanted activities.

Another widely used approach is to ionize an atomic gas by collisions with high energy electrons, referred to as electron impact ionization. This process generally creates multiply charged ions. As a result, the transmission efficiency across a mass separator of any kind is relatively low at a selected m/z charge ratio, such that ion implantation by electron impact ionization is a very inefficient process.

Resonant laser ionization on the other hand is a well established tool to produce ions of a single charge state at high efficiency. It is commonly applied, among others, at on-line radioactive ion beam facilities such as CERN-ISOLDE (Fedosseev et al., 2017) and TRIUMF-ISAAC and a recent review of this technique is given in (Marsh, 2013). Resonant laser ionization uses step-wise excitation of a desired atom in the gas-phase using a cascade of optical transitions excited with lasers matching the energy of the respective transitions. Therein, ionization generally takes place by three distinct mechanisms, which are the population of unstable Rydberg levels, the population of autoionizing states or the direct, non-resonant ionization starting from an intermediate excited state (Marsh, 2013). As the optical transitions of each atom are highly specific regarding the chemical element, and, through the fine- and hyperfine-splitting also partly the isotope, this process allows to selectively ionize only desired elements or even isotopes. Thereby, initial contaminations in the sample on the same mass (isobaric contaminations) and potentially isotopic contaminations of a resultant ion-beam are strongly suppressed, allowing for the injection of practically only the desired isotope into the target.

Considering the ionization of ^{226}Ra , multiple ionization schemes have been published previously (Goodacre et al., 2018; Raeder et al., 2014). Similar to (Raeder et al., 2014), the strong optical transition at 482.7 nm obtained through second harmonic generation of a Ti:Sa laser was used to populate the $7s^1 7p^1 \ ^1P_1^o$ level starting from the $7s^2 \ ^1S_0$ ground state of radium.

From this populated intermediate state, different second step laser frequencies were tested in Publication II by a long-range frequency scan of a second laser with matched pulse characteristics. Thereby, non-resonant excitation into the ionization continuum was found most practicable with the laser system at hand and overall implantation efficiencies between 40 % and 60 % were observed, which allowed to efficiently produce several emanation sources in the range of 500 Bq to 1 kBq.

Mass spectrometry using surface ionization

At the RISIKO mass separator, a mass spectrum of the ions produced purely by surface ionization was recorded by sweeping the magnetic sector field strength.

Thereby, a non-quantitative overview of the impurities in the solution obtained from the methods in section 2.4.1 was gained. It should be noted that the surface ionization rate (cf. Equation (2.48)) varies significantly among the chemical elements and the hot cavity ion source introduces its own impurities. Figure 2.7 shows the mass spectrum obtained in this way, at a sample reservoir temperature of about 1700 K and an atomizer temperature of about 2300 K (Atomizer set up and temperature estimates according to (Kieck et al., 2019)). The identification of ion peaks was carried out concerning the respective (natural) isotope ratios and the m/z ratios computed from the sector field separator magnetic field strength. Naturally, the alkaline and earth alkaline elements appear in this mass spectrum due to their high ionization rates as well as the chemical similarity between radium and the earth alkalis. Evidently, chloride and fluoride remained in part in the solution after turnover with concentrated nitric acid, and lead to the formation of the respective earth alkali subhalide ions, most notably $[\text{BaF}]^+$, $[\text{BaCl}]^+$, $[\text{RaF}]^+$ and $[\text{RaCl}]^+$.

The formation of such monohalides upon strong heating of mixtures of barium and the respective halide was reported elsewhere before and is well known, (Styris, 1984; Human and Zeegers, 1975; Derkatch et al., 2000; Cubicciotti et al., 1947) among others. Recently, even first laser-spectroscopic studies of RaF have been published (Ruiz et al., 2020). Assuming equal surface ionization rate for barium and radium, the atomic fraction of barium/radium in the sample is estimated from these data to be 0.85, taking into account all indicated monohalide ion peaks. Since the ionization rates for the alkali metals is significantly higher, a direct comparison of these respective ion peaks with the radium peaks does not allow to estimate their content in the initial sample. Despite the age of the initial radium solution, which is on the order of tens of years, and the specifically high volatility of lead and bismuth, the spectrum only shows a rather unstructured shape in the range of 200-210 m/z . Sr-Resin is known to have a high affinity towards lead and polonium (Horwitz et al., 1992). However, it is uncertain if significant quantities of both ^{210}Pb and ^{206}Pb have been removed during the extraction chromatography described in section (2.4.1) or if the specifically low ionization rate of lead and bismuth caused the absence of the corresponding signals. Nonetheless, by selection of the desired m/z charge ratio, practically, only ^{226}Ra ions have been implanted into the respective targets, also indicated by an overall good match between the determined implanted activities of ^{226}Ra and the recorded ion-current on the target in Publication II.

2.4.4 Physical vapor deposition

Physical vapor deposition refers to thin layer deposition techniques that rely on the condensation of a vapor onto a substrate, usually under vacuum conditions. Since the deposition mechanism does not rely on chemical reactions at the solid/gas interface the technique is

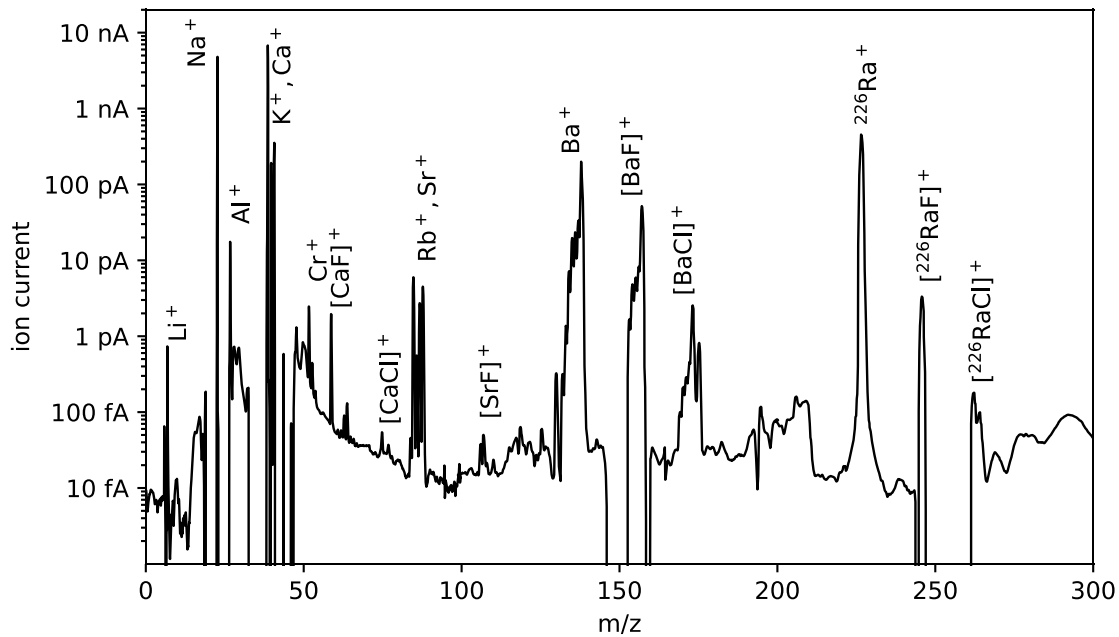


FIGURE 2.7: Mass spectrum of ions produced from the employed radium solution in the RISIKO mass separator by surface ionization at an approximate temperature of 2300 K.

referred to as physical-, rather than chemical vapor deposition (CVD). Mechanisms to generate the vapor include thermal methods, plasma and sputtering processes and laser heating or pulsed laser ablation. For thermal physical vapor deposition (thermal-PVD), which is the simplest among the PVD methods, the sample is either heated by radiative, ohmic or electron beam heating, which causes atoms or molecules of a desired species to evaporate. Process pressures range from ultra-high to medium vacuum, depending on the respective evaporation technique.

At this pressure range, the mean free path of gas-phase atoms and molecules is much longer than the geometric dimensions of the vacuum and deposition apparatus, and therefore, the deposition takes place almost exclusively in line-of-sight. This enables to confine the deposition area through shadowing with an aperture. Thermal-PVD with direct current heating (henceforth denoted as thermal-PVD) is limited to deposit substances which do not decompose before evaporation or sublimation and for which the vapor pressure is high enough at the practically reachable temperatures of about 2300 K. In the case of decomposition reactions, species different from the original sample may be condensed on the substrate, e.g., by the decomposition of carbonates, nitrates, and sulfates among others. For thermal-PVD, typically, a sample heater is used made of materials that show negligible vapor pressure at the desired temperature range, most commonly using refractory metals such as tantalum, tungsten, molybdenum, niobium or alloys thereof. Alternatively, high temperature ceramic crucibles may be used in conjunction with radiative heating. Thermal-PVD is very sensitive to the quality of the vacuum conditions and usually the lowest attainable pressure is desired.

The kinetic energy of incident particles on the substrate, assuming thermal equilibrium, follows a Maxwell-Boltzmann distribution and is on the order of few 0.1 eV in the typical

temperature range of thermal-PVD. In contrast to the previously described ion implantation, thermal-PVD does therefore not allow the deposited substance to significantly penetrate the substrate material. Conversely, sputtering yields much higher energy particles in the range of few 100 eV, which can penetrate the first few layers of the substrate material. Additionally, the thermal-PVD method does not allow to separate ^{226}Ra from the other materials in the sample and introduces additional impurities from materials in the setup of non-negligible vapor pressures. In comparison to the significantly small mass of ^{226}Ra required for the construction of emanation sources in the desired range, this even includes heated copper conductors and impurities in the refractory metal evaporation source setup. However, thermal-PVD can still suppress some of the involatile impurities, compared to, among others, simple drop-casting or electrodeposition (section 2.4.2 and Publication I). In part, this is since only very little volume of solvents are used, leading to a reduced contribution of solvent impurities in comparison with section 2.4.2. Thermal-PVD was previously reported as a high-quality tool for the production of very high resolution α -sources and high quality targets, among others, in (Jackson, 1960; Parker and Grunditz, 1963; Pommé and Sibbens, 2008; Sapundjiev et al., 2012; Sibbens et al., 2018; Sibbens et al., 2015; Sibbens and Altzitzoglou, 2007).

For radium, this technique was relatively scarcely reported before, where (Sletten, 1971) used a mixture of radium oxide and metallic lanthanum powder in stoichiometric amounts to evaporate metallic radium. This process can not be adapted for the present work, since it would require a weighable amount of radium and since it may introduce lanthanum impurities in the deposited layer, leading to an increased areal density.

Adsorbed atoms or molecules on the substrate from the vapor diffuse laterally until they occupy a position of locally minimal energy and crystallization occurs, usually, where defects, impurities or previously crystallized species are present. This leads to the formation of a distinct nano-scale structure of epitaxially grown films, depending strongly on the deposition conditions, e.g., substrate structure and temperature as well as the deposited species and, possibly, impurities. Thus, the PVD methods coat the substrate in a film consisting of nano-scale particles, which was qualitatively investigated in Publication III using scanning electron microscopy with secondary electron detection. While attempts were made, the investigation of X-Ray fluorescence (EDX) yielded unsatisfactory results considering the specifically small amount of radium deposited and considering that the strong barium and radium fluorescences can only be excited at relatively high electron energies. The relatively high penetration depth or conversely low interaction probability of these high energy electrons leads to EDX spectra which almost exclusively show the substrate (silicon) fluorescences.

Selection of a suitable ^{222}Ra -compound

The earth-alkaline metals generally have relatively low melting and boiling points, however, they are usually not encountered in their metallic form. Therefore, the thermal-PVD process does not concern metallic radium, but several of the radium salts potentially have properties that lend them to thermal-PVD, most notably the halides. While the boiling points and vapor pressure data of practically all radium salts are not well studied, the barium homologues can aid as a basis from which to estimate the respective radium salt properties due to their general similarity. Thermodynamically, the processes of evaporation and sublimation are described by the Clapeyron equation,

$$\frac{dp}{dT} = \frac{\Delta_{vap}Hp}{RT^2} \quad (2.49)$$

which allows to compute the slope of the phase boundaries and allows to estimate vapor pressures based on the knowledge of thermodynamic data approximated to be temperature and pressure independent and the melting and boiling points respectively.

BaCl_2 was thus presumed to be a suitable candidate for direct current heated thermal-PVD in Publication IV, judging from the experimental results at the RISIKO mass separator and the known thermodynamic data of BaCl_2 . The approximate vapor pressure curves calculated from literature data (retrieved from the NIST Janaf database (Thomas C. Allison, 2013)) for the barium halides and its oxide are given Figure 2.8, alongside the estimated dissipated power from the heater by radiative energy dissipation according to the Stefan-Boltzmann law for the heating geometry used in Publication IV (assumed temperature and wavelength independent emissivity of 0.35). The nitrate, carbonate and sulfate salts decompose to the respective oxides at elevated temperatures. Judging by this estimated data, the evaporation of BaCl_2 is easiest, allowing for a reduced thermal load on the substrate at the required high solid-angle deposition geometry. Alongside the good availability of this compound, it was therefore chosen as a starting material for the thermal-PVD growth of a radium containing thin film. The oxide and the salts resulting in the oxide upon thermal decomposition were found unsuitable, due to the considerable thermal load associated with the required temperature and the ultimate goal of Publication IV to coat a heat sensitive semiconductor detector with a ^{226}Ra layer.

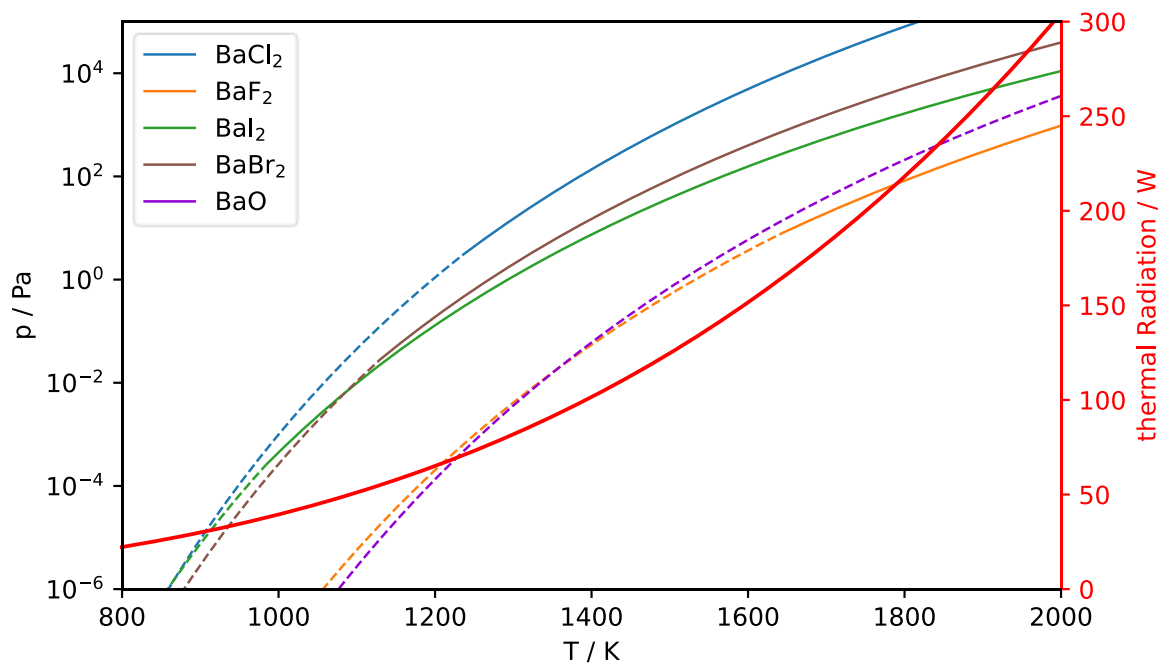


FIGURE 2.8: Estimated vapor pressure for different barium compounds and estimated heating power as a function of temperature

Choice of evaporator geometry

The choice of the deposition geometry in thermal-PVD allows to tune the process to achieve one of two properties. Either very uniform deposition at low deposition efficiency or high deposition efficiency with inhomogeneously deposited layers can be achieved. Generally, it is preferred to achieve relatively high deposition efficiency, in order to keep the ongoing

contamination of the deposition apparatus with ^{226}Ra as low as possible. Hence, a geometry which achieves non-uniform layers at relatively high geometrical efficiency was chosen concerning the following theoretical considerations.

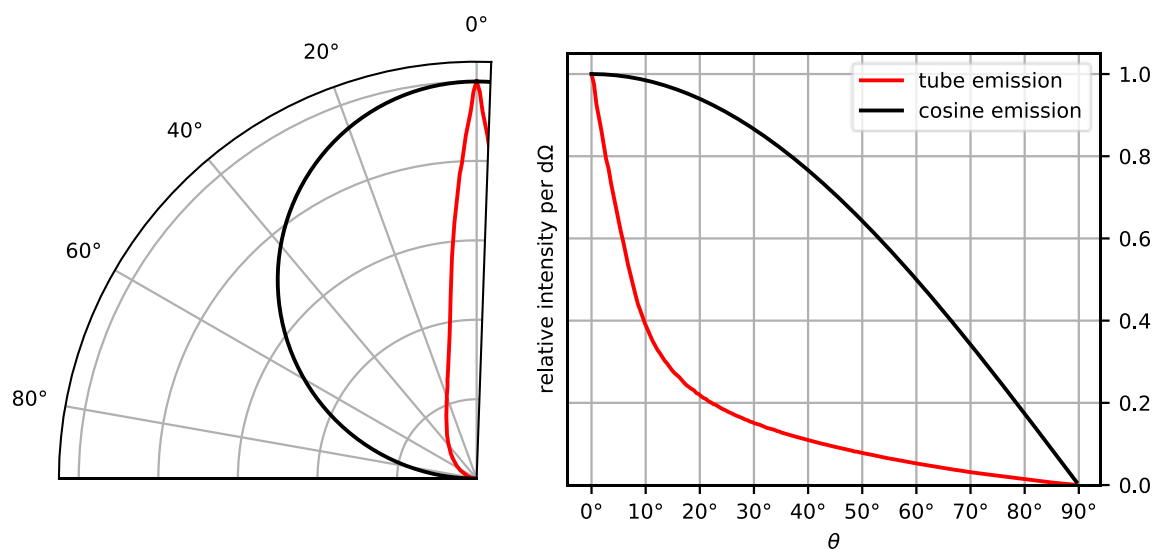


FIGURE 2.9: Monte Carlo simulated (red) polar angular distribution of vapor emerging from a thin tube (25 mm length, 4 mm diameter) in comparison with the cosine distribution for vapor emerging from a flat surface (black)

Emergence of molecules from a variety of different geometries has been modeled based on kinetic gas theory beginning in the early 20th century. At an operating pressure range lower than 10^{-3} Pa, the mean free path of molecules in the gas phase is much larger than the geometric dimensions of the evaporation setup. Therefore, the trajectories of the molecules in the gas phase evolve almost entirely by scattering on the boundaries rather than by mutual interference (e.g., collisions). Assuming a hemispherical, diffuse scattering distribution resulting from each collision with the geometrical boundaries, the vapor profile emerging from simple heater geometries can be estimated both by analytical formulas and by Monte-Carlo simulation. It is well known that effusion from a reservoir volume through a simple orifice into another, evacuated volume follows a cosine distribution, and, that the scattering of particles on boundaries generally happens diffusely according to a cosine distribution (Knudsen, 1909a; Knudsen, 1909b). As a result, the angular distribution of vapor emerging from long tubular heaters deviates from the cosine distribution with a biased emission towards the normal on the tube orifice. (Heinke et al., 2020) arrive at a similar conclusion about the effusion from comparable geometries.

In Figure 2.9, results from a Monte-Carlo simulation (custom code) considering the emission of molecules generated at the bottom of a tube with given length to radius proportions are shown, using cosine distributed re-emission (diffuse reflection) upon contact with tube boundaries and random origin points of particles on the bottom of the tube. Based on this calculation, the thermal-PVD setup designed and used in Publication IV (tube of 25 mm length, 4 mm diameter, deposition distance 35 mm, deposition diameter 20 mm) has a geometrical deposition efficiency of approximately 18 %, while the fraction of the hemispherical solid angle subtended by the substrate is only 4 % in this configuration. The inhomogeneous resultant activity distribution on the substrate from this biased emission was chosen over more homogeneous distribution with significantly reduced efficiency in order to keep the initial radium load as well as the ongoing contamination of the deposition apparatus as low

as possible. Alternatively, multiple substrates may be placed in the top hemisphere of a different evaporator design in order to increase the effective deposition efficiency for a future, improved setup with higher throughput at presumably similar overall efficiency.

2.4.5 Comparison of α -particle spectra of the differently produced sources

An overview of the differently produced sources within this work is shown in the photographs in Figure 2.10, which clearly illustrates the different amounts of total mass deposited by each method.

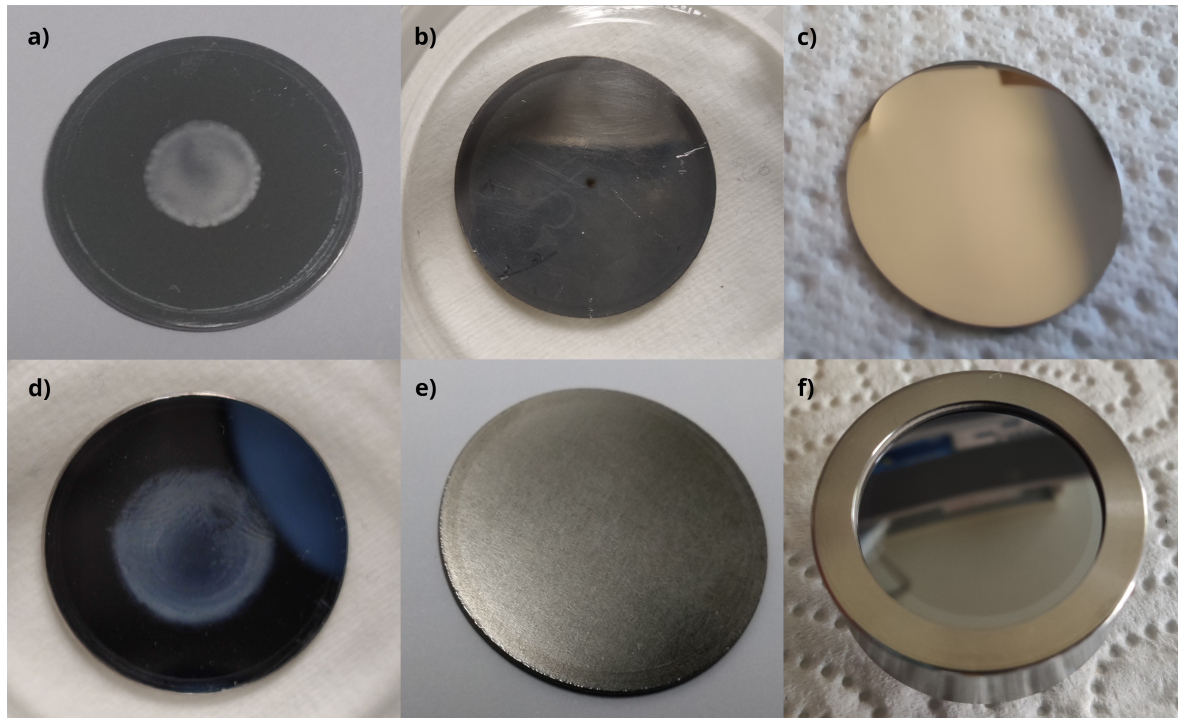


FIGURE 2.10: Photographs of different ^{222}Rn emanation sources produced in this work. a) and d) different electrodeposited sources; a) ≈ 670 Bq, d) ≈ 100 Bq. b) ≈ 840 Bq ^{226}Ra ion implanted into aluminium with visible target amorphization, e) ≈ 1140 Bq ^{226}Ra ion implanted into tungsten. c) ≈ 10 Bq ^{226}Ra on a 1" Si-wafer deposited by thermal-PVD, f) commercial PIPS detector modified by a layer of 440 Bq ^{226}Ra by thermal-PVD (IRSD)

The emanation sources produced by each of the outlined methods have each been measured in the same DSA α -particle spectrometry setup, using the same α -particle detector as a reference. A comparison of the ^{226}Ra peaks of each source production method is shown in 2.11.

It can be readily observed, that the electrodeposition method creates sources which have a much more pronounced tailing of the radium emissions, underpinning the propositions of section 2.4.2. Therefore, it is concluded that this method produces the deposits with the highest areal densities among the chosen methods. Due to the specifically small mass of ^{226}Ra deposited, this must be entirely due to chemical impurities that are co-deposited or due to electrochemical reactions leading to the deposition of electrolyte breakdown products.

In terms of chemical impurities, the ion implantation introduces practically no material into the target other than the ^{226}Ra . From SRIM calculations the mean implantation depth into the aluminium targets is around 10 nm. Interestingly, the peak shape of the thermal-PVD

radium sources matches the peak shape of the aluminium implanted ^{226}Ra . This allows to estimate that the layer thickness of the thermal-PVD method is at most equivalent in terms of the energy loss of the α -particles to approximately 10 nm of pure aluminium or less, depending on the contribution of the employed α -particle detector to the peak shape. For the implanted and the thermal-PVD sources, the peak shape is likely entirely caused by the dead-layer and the characteristics of the employed α -particle detector. Thus, the areal density of the thermal-PVD layer may even be smaller.

This is a crucial characteristic for the application of the thermal-PVD method in publication IV, where it is used to deposit ^{226}Ra directly onto the dead-layer of a silicon detector. In this configuration, the tailing of peaks is significantly pronounced in comparison to a low solid-angle configuration such that the areal density of the layer is one of the most important characteristics to obtain the well resolved spectra needed for accurate quantification of ^{226}Ra and residual ^{222}Rn . The amount of tailing directly influences the achievable uncertainty in the emanation, due to the overlap of the peaks corresponding to ^{226}Ra , ^{222}Rn , ^{218}Po , and ^{210}Po .

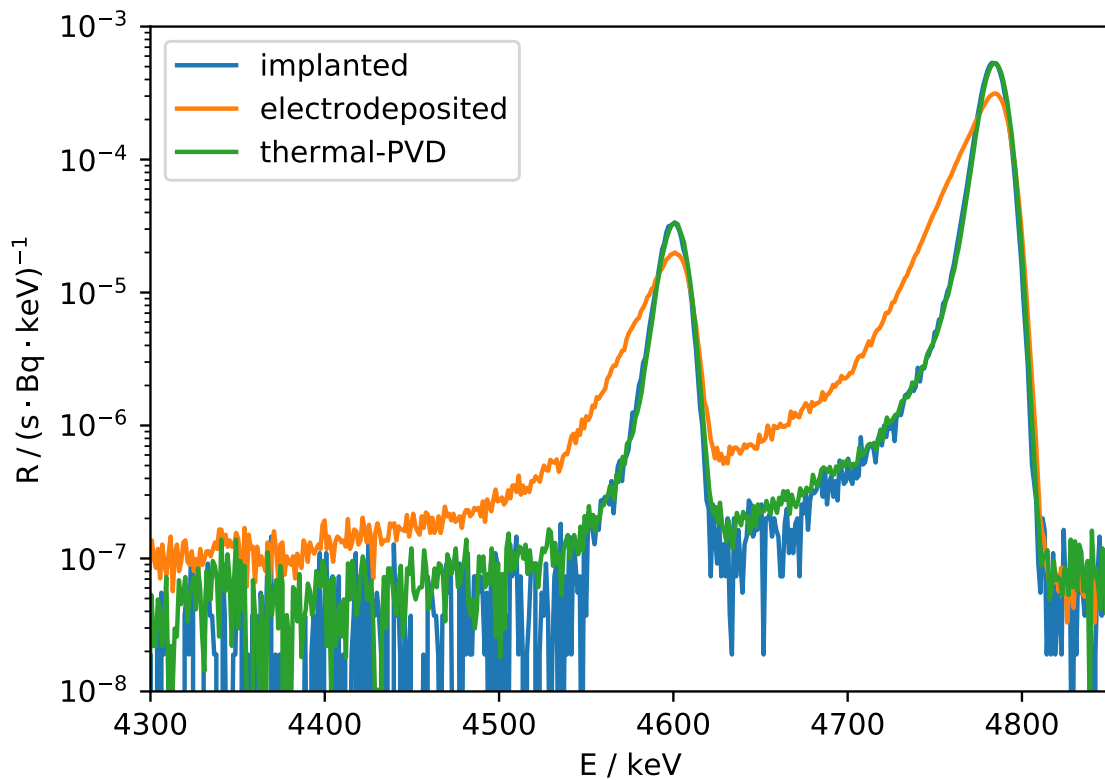


FIGURE 2.11: Comparison of the ^{226}Ra emissions in the alpha-particle spectrum of the different deposition methods, measured using the same setup: electrodeposition (orange) FWHM 23 keV, ion implantation (blue) FWHM 15.3 keV, thermal-PVD (green) FWHM 15.2 keV. Specified nominal resolution of the detector amounts to 20 keV FWHM.

Chapter 3

Publication I

A new primary Rn-222 emanation standard

Florian Mertes, Stefan Röttger, Annette Röttger

in

Applied Radiation and Isotopes, Volume 156, February 2020

DOI: 10.1016/j.apradiso.2019.108928

Received 27 March 2019

Received in revised form 24 July 2019

Accepted 7 October 2019

Author contributions

Conceptualization, methodology: **F.M.**, S.R., A.R.

Investigation/experiments, formal analysis: **F.M.**

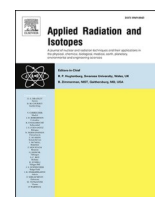
Visualization, original draft preparation: **F.M.**

Resources, supervision, project administration, funding acquisition: S.R., A.R.



Contents lists available at ScienceDirect

Applied Radiation and Isotopes

journal homepage: <http://www.elsevier.com/locate/apradiso>

A new primary emanation standard for Radon-222

Florian Mertes^{*}, Stefan Röttger, Annette Röttger

Physikalisch-Technische Bundesanstalt, Bundesallee 100, 38116, Braunschweig, Germany

ARTICLE INFO

Keywords:
Radon-222
Emanation
Primary standard
Defined solid-angle alpha-particle spectrometry

ABSTRACT

New emanation sources for Rn-222 have been developed by electrodeposition of Ra-226 onto stainless-steel discs. With a high resolution of up to 20 keV FWHM in the Ra-226 peak at 4.87 MeV, defined solid-angle alpha-particle spectrometry is the method of choice to determine the deposited Ra-226 activity. The amount of emanating Rn-222 is determined by gamma-ray spectrometry using HPGe-detectors. The measurement is based on the distorted equilibrium of the Ra-226 decay chain due to Rn-222 emanation. Comparative gamma-ray spectrometric measurements with sealed, Rn-222 tight sources of the same type and geometry make the knowledge of emission probabilities and detection efficiency unnecessary. The new emanation sources allow the production of stable reference atmospheres in the regime below 300 Bq·m⁻³ with uncertainties not exceeding 2% for k = 1.

1. Introduction

Exposure to Rn-222 and its progeny is considered to be a leading cause of lung cancer. In accordance to ICRP recommendations (ICRP, 2010), Council Directive EURATOM 2013/59 lays down basic safety standards for EU-citizens concerning residential and occupational Rn-222 levels (European Commission, 2014). Therein, it is stipulated that residential and occupational annual average Rn-222 activity concentrations should not exceed 300 Bq·m⁻³. How these basic safety standards are implemented into national law is up to the EU member states, and some countries have already implemented reference levels as low as 100 Bq·m⁻³. Consequently, government agencies are asked to measure Rn-222 activity concentrations in the regime below 300 Bq·m⁻³ by the subsequent national regulations. With increased awareness, the general public might also be encouraged to conduct measurements of low activity concentrations in their homes. This drives the need for suitable calibration procedures of radon measuring devices at low activity concentrations.

The state of the art of Rn-222 calibrations often involves gaseous Rn-222 standards to generate reference atmospheres of Rn-222. These standards are produced by freezing out Rn-222 and determining its activity by defined solid-angle alpha-particle spectrometry (Dersch, 2004; Picolo, 1996; Picolo et al., 2000). However, the use of gaseous Rn-222 standards is unsuitable for the calibration of devices at low activity concentrations since the achievable counting statistics are limited by the nature of a decaying atmosphere and the poor detection efficiency of

small volume Rn-222 detectors typically used in commercial Rn-222 measurement systems. To address this issue, an alternative method based on emanation sources was developed in the PTB in 2013 (Linzmaier and Röttger, 2013; Röttger et al., 2014). However, the described source design was based on Rn-222 diffusion through thin polymer foils covering the sources, resulting in a dependency of the sources on humidity, temperature and pressure as the diffusion coefficient is dependent on these environmental parameters.

New emanation standards for Rn-222 have been produced by electrodeposition of Ra-226 onto solid metal discs. Activity determination of deposited Ra-226 on these discs is carried out by defined solid-angle alpha-particle spectrometry as a primary measurement technique. The emanation coefficient χ is deduced from gamma-ray spectrometry comparing the measured full-energy peak count-rates in the Ra-226 decay chain of open and sealed electrodeposited Ra-226 sources. The resulting emanation sources can be used as primary standards for the Rn-222 activity concentration, since the Ra-226 activity is measured by an absolute technique and the emanation coefficient χ is determined without the need for another Rn-222 standard.

The production and characterization of these sources is described and discussed in the following.

2. Sample preparation and source production

Parker et al. investigated the suitability of electro-deposition of a wide variety of isotopes from slightly acidic organic media at high

^{*} Corresponding author.

E-mail address: florian.mertes@ptb.de (F. Mertes).

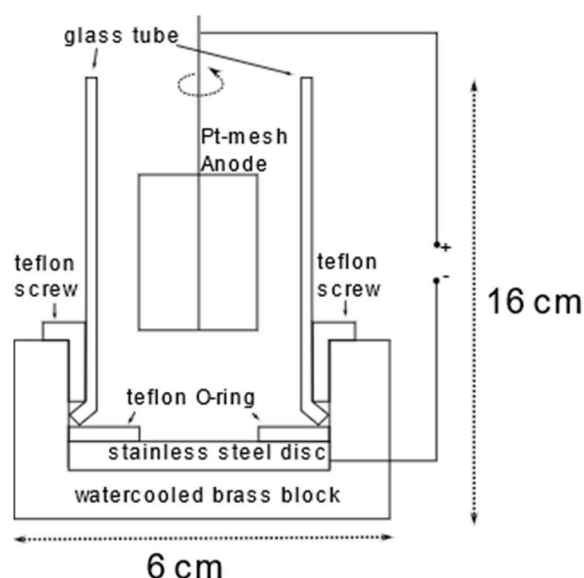


Fig. 1. Apparatus for the electrodeposition of Ra-226.

voltages, and coined the term “molecular plating” for this technique (Getoff et al., 1967; Parker et al., 1964a, 1964b). A non-metallic form of deposition was postulated since the standard reduction potentials of the deposited metals and the overall transported charge are too low to allow for reductive plate-out. With a standard reduction potential of -2.8 V this is especially true for Ra^{2+} (Bratsch, 1989).

Whitehead et al. (1992) and Hancock and Martin (1991) published comparable protocols for the molecular-plating of Ra-226 for environmental samples, which have been used for the production of sources in the range of several 100 Bq Ra-226 from a Ra-226 standard solution. Vargas and De Soto have shown that Ra-226 deposited in such a way will allow for Rn-222 emanation, the amount limited by the thickness of the resulting layer (Vargas and De Soto, 1996; Vargas, 2000). Since Ba^{2+} would co-deposit with Ra^{2+} (Vargas and De Soto, 1995) and all available Ra-226 standard solutions had Ba^{2+} carriers (3–6 orders of magnitude more Ba^{2+} than Ra^{2+}), the Ba^{2+} content was reduced by extraction chromatography prior to deposition in the present study.

The initial chemical composition of the Ra-226 solution (PTB standard Ra-226 solution) employed was nominally 71 kBq Ra-226 as RaCl_2 in $0.1 \text{ mol}\cdot\text{L}^{-1}$ HCl with $5.7 \text{ mg}\cdot\text{mL}^{-1}$ Ba^{2+} as $\text{BaCl}_2 \cdot 6 \text{ H}_2\text{O}$ and $(12.90 \pm 0.13) \text{ kBq}$ of Ba-133 with the same carrier solution added gravimetrically from a PTB Ba-133 standard solution as a radioactive tracer for inactive Ba^{2+} . The resulting solution was evaporated to dryness on a sand-bath (90°C), and 2 mL of 65% HNO_3 (Merck, EMSURE®, analysis grade) were added to the residue and subsequently removed by evaporation to convert the chlorides into the respective nitrates. The resulting residue was dissolved in 1 mL of 0.6 M HNO_3 and passed onto a pre-conditioned (30 mL of 0.6 M HNO_3) column of 3 Sr-Resin cartridges (4,4'(5')-bis(tertbutylcyclohexano)-18-crown-6 in 1-Butanol, dispersed on SiO_2 -particles, purchased from TrisKem International). While the resin was initially developed for the preparation of Sr-samples (Philip Horwitz et al., 2007), it has been shown to be an effective chromatography system for the separation of Ba^{2+} and Ra^{2+} as well (Chabaux et al., 1994). Radium was eluted from the column with 0.6 M HNO_3 at a flow rate of $1 \text{ mL}\cdot\text{min}^{-1}$. Fractions of 10 mL were taken from the eluate and were investigated using gamma-ray spectrometry with a HPGe-Detector. The detection efficiency was deduced from measuring PTB Ba-133 and Ra-226 standard solutions in the same geometry.

Since no Ba-133 could be detected in the first fraction by gamma-ray spectrometry, the Ba^{2+} content in this fraction was measured by ICP-MS and found to be $(86 \pm 5) \text{ ppb}$ (m/m). The Ra-226 content in this fraction was $(84 \pm 1) \text{ ppb}$ (m/m) or $(3.13 \pm 0.05) \text{ kBq}\cdot\text{mL}^{-1}$, as determined by

Table 1

Overview over produced sources, activity determinations and the respective emanation coefficients χ

Source ID	$A_{\text{Ra-226}}/\text{Bq}$ (recovered $A_{\text{Ra-226}}$)	χ (N)	Deposition Method/ Solvent
2017–1709	48.01 ± 0.17 (49%)	0.8260 ± 0.0013 (22)	potentiostatic 35 V/ EtOH
2017–1710	58.5 ± 1.7^a (17%)	0.7363 ± 0.0028 (9)	potentiostatic 35 V/ EtOH
2017–1074	57.5 ± 2.5^a (29%)	0.893 ± 0.003 (13)	potentiostatic 35 V/ EtOH
2018–1437	104.4 ± 0.4 (36%)	0.637 ± 0.005 (3)	galvanostatic 1 $\text{mA}\cdot\text{cm}^{-2}/\text{IPA}$
2018–1438	182.2 ± 0.7 (43%)	0.7813 ± 0.0019 (4)	galvanostatic 1 $\text{mA}\cdot\text{cm}^{-2}/\text{IPA}$
2018–1439	184.3 ± 0.5 (81%)	0.6535 ± 0.0023 (9)	potentiostatic 200 V/ IPA
2018–1440	193.9 ± 0.7 (65%)	0.6533 ± 0.0023 (10)	potentiostatic 200 V/ IPA
2018–1441	665.5 ± 1.9 (67%)	0.7645 ± 0.0009 (32)	potentiostatic 90 V/ IPA

^a comparative gamma-ray spectrometric determination with 2017–1709 as a reference.

the described gamma-ray spectrometry method. As more significant levels of Ba^{2+} were found as detectable Ba-133 in the later fractions, only the first fraction was used in the production of the sources.

To prepare each source, the deposition apparatus shown in Fig. 1 was filled with 9 mL of analytical grade ethanol (EtOH, Merck, EMSURE®) or 2-propanol (IPA, Merck, EMSURE®), respectively. A desired amount of activity of Ra-226 was transferred directly from the first fraction to the cell by means of a pipette. The amount of added Ra-226 was determined gravimetrically. A potential was applied by a Keithley Model 2410 SMU in 2-electrode operation mode. Depositions at constant current density and constant potential were both carried out. While no direct advantage of potentiostatic over galvanostatic deposition was identified, higher voltages and 2-propanol as a solvent seemed to lead to higher deposition efficiency. Deposition times were approximately 1 h for each source in an open-bench setup. The diameter of the deposit is fixed by a Teflon aperture covering the steel disc with an opening of nominally 15 mm in diameter. A total of 8 sources were produced by this method.

Table 1 shows the respective deposition parameters, the resulting activity of the produced sources and their emanation coefficients χ as determined by the measurements presented later. SEM-images of the deposit are depicted in Fig. 2 and show a highly porous deposit, offering a large surface area for Rn-222 to escape.

Digital autoradiographs of the sources are taken with a Fujifilm FLA-9000. These yield the relative activity distribution, w_{dA} , on the source per 0.04 mm^2 square pixel. A typical radiograph of the produced sources is shown in Fig. 3. The radiographs show that the method does not produce homogeneous deposits, however this is accounted for in the measurement of the Ra-226 activity and is described in more detail below.

One of the produced sources was sealed against Rn-222 emanation after alpha-particle- and gamma-ray-spectrometric measurements by gluing a stainless-steel sheet (nominally 0.05 mm thickness) onto the source disc with a 2-component epoxy resin (DELO-DUOPOX 01 rapid). Tightness of the seal against Rn-222 emanation was investigated using a calibrated AlphaGuard (Saphymo, Model PQ2000) in diffusion mode that was placed in a noble gas tight reference volume (50 L) and flushed with aged air. No significant increase in the Rn-222 level was identified after the sealed source was introduced into this reference volume. Given the statistical fluctuation of the AlphaGuard's background reading, its detection limit would allow to detect a leak in the seal down to 0.5% of emanating Rn-222.

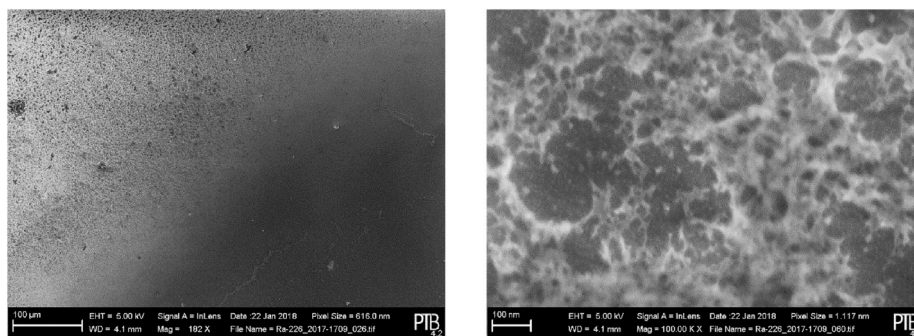


Fig. 2. SEM pictures of the deposit at different magnifications.

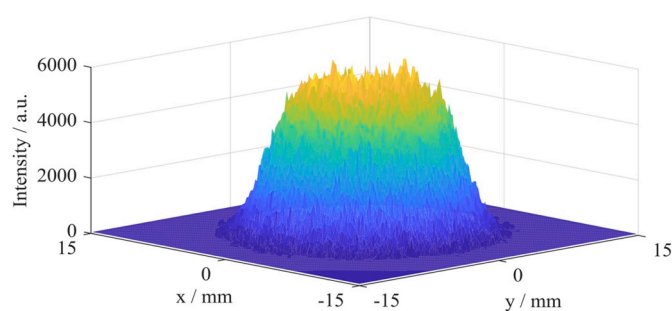


Fig. 3. Autoradiograph of source 2018–1441 with 0.04 mm^2 pixel size. The coordinate systems origin refers to the center of the circular stainless-steel disc carrying the deposit.

3. Determination of deposited Ra-226 activity

The deposited Ra-226 activity on each source was determined by defined solid-angle alpha-particle spectrometry. The setup consists of a passivated implanted planar silicon (PIPS) detector (300 mm^2 , specified at 17 keV FWHM at 5.5 MeV) and a source holder, which features two apertures that define the solid angle between source and detector. The apertures are at a fixed distance of $(50.03 \pm 0.03) \text{ mm}$ to one another and have a diameter of their openings of $(28.00 \pm 0.20) \text{ mm}$ and $(20.002 \pm 0.010) \text{ mm}$. The PIPS detector is $(2.0 \pm 0.5) \text{ mm}$ above the second aperture, whereas the source disc is pressed onto the lower aperture by a spring. All relevant geometrical parameters and assigned uncertainties of the setup are known, traceable to PTB standards. This includes a possible shift of the source against the rotational axis, the distance between the apertures, the distance between the detector and the top aperture, the diameters of the aperture openings and the tilting angles of the apertures against the rotational axis and the detector plane. Measurements are carried out at an air pressure of 10^{-3} mbar to suppress the recoil implantation of Rn-222 and decay products into the detector.

The geometry factor, G , which defines the counting efficiency of the setup is given by equation (1). G is calculated separately by Monte-Carlo integration for each source to account for the different activity distributions on each source. For this purpose, origin points (x, y) for the trajectories of alpha particles on the source are sampled directly from the associated experimental autoradiography data. Therefore, the inhomogeneity of each deposit is included in its resulting geometry factor G . This sampling is done by mapping two uniform random floats in the interval $[0,1]$ to the normalized row- or respectively column-wise cumulative density functions of the autoradiography data. Polar angles θ and azimuthal angles φ are sampled from a spherical distribution with a bias on θ towards the detector. For each pair of x, y, θ and φ , the given trajectory is checked for intersections with one of the apertures and the detector. After each 10^7 iterations, the geometrical parameters of the detector and the apertures are sampled from gaussian distributions

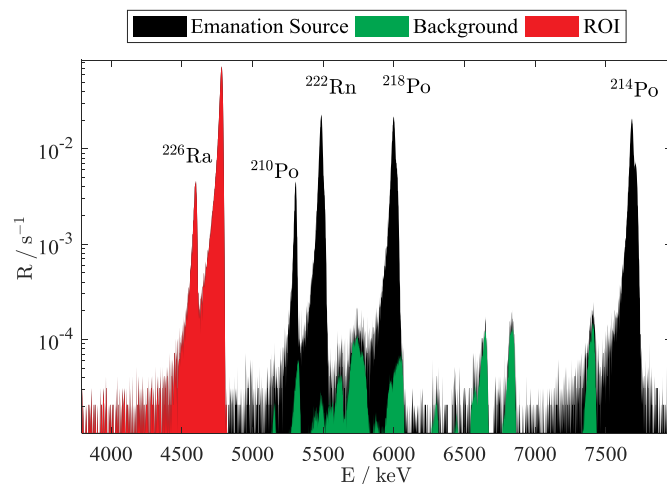


Fig. 4. Typical alpha-particle spectrum of electrodeposited sources. FWHM of the 4786 keV Ra-226 Peak is 21 keV.

given by the known geometrical parameters and associated uncertainties. G is obtained by counting the trajectories that hit the detector and calculating the fraction of detector hits and total samples and correcting for the applied bias on θ . Since the parameters of the geometry are iteratively changed, the distribution of G around its mean value is obtained by computing a histogram of the calculated values for G . The technique is in accordance with GUM Supplement 1 (Joint Committee for Guides in Metrology, 2008). A comparable approach has been described in (Arinc et al., 2016).

$$G = \frac{\int_A \Omega_{dA} \cdot w_{dA} dA}{4\pi \int_A w_{dA} dA} \quad (1)$$

where Ω_{dA} describes the solid-angle subtended between the detector and a surface element, dA , on the source, and w_{dA} describes the relative amount of activity in the surface element dA .

Dead time was corrected by a high-precision pulse generator which is connected to the detector pre-amplifier and is traceable to the PTB frequency standard. Because of the good energy resolution of the resultant alpha-particle spectra with typically 20–30 keV FWHM in the 4.87 MeV Ra-226 peak (see Fig. 4), it is assumed that self-absorption in the source and scattering of alpha particles on the source backing is negligible. A GEANT4 simulation (Allison et al., 2006) of the setup at an estimated source thickness and composition of 500 nm BaNO_3 and $5 \cdot 10^8$ alpha-particles with 5 MeV showed that these assumptions can introduce an estimated uncertainty of up to 0.3%. An extensive analysis of uncertainties in defined solid-angle alpha-particle spectrometry is given in (Pommé, 2015), where a comparable effect of scattering and self-absorption was estimated. Rotation of the source between taking the

Table 2
Uncertainty budget for Ra-226 activity determination of source 2017-1709.

Quantity	Value (k = 1)	relative contribution
N_{Ra-226}	$199.5 \cdot 10^3 \pm 6 \cdot 10^2$	66.5%
N_{Pulser}	$21.595 \cdot 10^6 \pm 5 \cdot 10^3$	0.4%
$N_{Ra-226,bg}$	$1.1 \cdot 10^3 \pm 4 \cdot 10^2$	0.9%
$N_{Pulser,bg}$	$129.5737 \cdot 10^6 \pm 1.14 \cdot 10^4$	$5 \cdot 10^{-8}$ %
f	$(49.995670 \pm 5 \cdot 10^{-6}) \cdot s^{-1}$	$1 \cdot 10^{-6}$ %
G	$9.597 \cdot 10^{-3} \pm 1.8 \cdot 10^{-5}$	28.2%
$c_{scatter}$	0.9985 ± 0.0009	6.0%
A	$(48.01 \pm 0.17) Bq$	

autoradiograph and performing alpha-particle spectrometry measurements is disregarded since the setup features a very high degree of rotational symmetry. Table 2 shows an example uncertainty budget for the determination of the Ra-226 activity. Equation (2) is used for the analysis of the resultant alpha-particle spectra.

$$A = \frac{f}{G} \cdot \left(\frac{N_{Ra-226}}{N_{Pulser}} \cdot c_{scatter} - \frac{N_{Ra-226,bg}}{N_{Pulser,bg}} \right) \quad (2)$$

where f denotes the frequency of the pulse generator, G denotes the geometrical efficiency as defined by equation (1) and N_{Ra-226} , $N_{Ra-226,bg}$, N_{Pulser} and $N_{Pulser,bg}$ denote the Ra-226 peak net area and the pulser peak net area of the measurement and the background spectra, respectively. $c_{scatter}$ denotes a correction factor for possible self-absorption in the source and scattering of alpha-particles.

4. Determination of the emanation coefficient

The emanation coefficient χ , the fraction of emanating Rn-222, is determined by assessing the distorted equilibrium in the Ra-226 decay chain due to Rn-222 emanation, as shown in equation (3). The method is adapted from (Linzmaier and Röttger, 2014).

$$\chi = 1 - \frac{A_{Rn-222}}{A_{Ra-226}} = 1 - \frac{A_{Pb-214}}{A_{Ra-226}} \quad (3)$$

where χ denotes the emanation coefficient and A_{Rn-222} , A_{Ra-226} and A_{Ra-226} denote the activity of Rn-222, Ra-226 and Pb-214 in the source respectively.

The emanation coefficient χ was then determined with equation (4), below, by comparison of the full-energy peak count rate ratios of the respective gamma-ray spectra of the emanation sources and the produced sealed source of the same type and geometry. This leads to significantly lower uncertainty in the emanation coefficient χ compared to traditional gamma-ray spectrometric measurement using detector efficiency and transition probabilities as these factors cancel out. The detection efficiency is otherwise commonly amongst the highest contributors to the combined uncertainty in gamma-ray spectrometric measurements.

The measurements of the emanation coefficient χ were carried out using 2 HPGe detectors (EG&G Ortec, GEM-F8020P4 and GXP-115220-S) inside lead castles. The sources are mounted in a noble gas tight stainless-steel source holder which is connected in a loop to a reservoir volume to prevent Rn-222 from entering the laboratory and to accumulate Rn-222 inside this volume. The use of the source holder further ensures reproducibility of the measuring geometry. Humidity, pressure and temperature are not controlled inside of the loop. Convection in the loop is forced by a circulating pump at nominally $1 L \cdot min^{-1}$. The sources are mounted inside the source holder such that the emerging gamma-rays are passing the layer of epoxy-resin and the stainless-steel sheet to reach the HPGe crystal in case of the sealed source. The possible imperfect seal and thus imperfect secular equilibrium of the sealed source is accounted for by a correction factor c_{seal} , which is estimated

Table 3
Uncertainty budget for an 86400 s measurement of source 2017-1709.

Quantity	Value/ s^{-1} (k = 1)	relative contribution
R_{sealed}^{Ra-226}	0.2869 ± 0.0026	10.2%
R_{sealed}^{Pb-214}	1.7812 ± 0.0026	0.2%
R_{open}^{Ra-226}	0.0856 ± 0.0016	58.8%
R_{open}^{Pb-214}	0.0825 ± 0.0013	25.1%
R_{bg}^{Ra-226}	0.0146 ± 0.0005	2.5%
R_{bg}^{Pb-214}	0.0023 ± 0.0004	2.1%
c_{seal}	0.9950 ± 0.0029	0.9%
c_{abs}	1.0041 ± 0.0014	0.2%
χ	0.827 ± 0.005	

between 0.995 and 1 because of the detection limit of the AlphaGuard that was used to investigate the tightness of the sealed source as described previously. c_{abs} denotes a correction factor which accounts for the absorption that occurs in the sealed source due to the layer of epoxy-resin and the stainless-steel sheet on the source, and is analytically estimated from the Lambert-Beer law and the respective mass-attenuation coefficients obtained through XCOM (Berger et al., 2019).

$$\chi = 1 - \frac{R_{open}^{Pb-214} - R_{bg}^{Pb-214}}{R_{open}^{Ra-226} - R_{bg}^{Ra-226}} \cdot \frac{R_{sealed}^{Ra-226} - R_{bg}^{Ra-226}}{R_{sealed}^{Pb-214} - R_{bg}^{Pb-214}} \cdot c_{seal} \cdot c_{abs} \quad (4)$$

where R_{open} and R_{sealed} denote the respective full-energy peak count rates of the open and the sealed sources and R_{bg} denotes the associated background count rates. As described above, c_{seal} and c_{abs} denote correction factors.

Equation (4) was applied using the Pb-214 peak at 351.9 keV and the Ra-226 peak at 186.2 keV. An example of an uncertainty budget for a day-wise measurement and evaluation of these peaks is shown in Table 3. Peak areas and associated uncertainties were determined by subtracting a linear background. Determined values for the emanation coefficient χ are given for each source in Table 1. Uncertainties of the emanation coefficient χ listed in Table 1 are calculated with the uncertainty of the mean values of the full-energy peak count rate ratios of N day-wise measurements. Background spectra were measured before measuring each source and showed stability in the Rn-222 progeny count rates. Within the measurement uncertainties, the emanation coefficient χ appeared stable over the N day-wise measurements taken for each source.

5. Conclusion

It was shown that thin-film deposition using molecular-plating techniques allows the manufacture of Ra-226 sources from which a high fraction of generated Rn-222 can emanate. Emanation coefficients between 0.6 and 0.9 were observed for the produced sources. A possible explanation for the varying emanation coefficients are the different plating conditions that were employed because these conditions impact the kinetics of particle growth of the deposit. The kinetics in turn determine the microstructure of the film, which can cause different emanation characteristics. From the amount of deposited Ra-226 and the emanation coefficient χ , a known and stable activity concentration of Rn-222 in air can be produced with the sources. The Ra-226 activity is determined with an absolute technique, and the emanation coefficient is determined without the need for another Rn-222 standard, which allows the use of these sources as primary standards for activity concentration of Rn-222 in air. The combined uncertainty of the resulting activity concentration using these sources does not exceed 2% ($k = 1$) under the assumption that a precisely known reference volume is available. Because of the thin-layer and highly porous Ra-226 deposit, with particles in the range of a couple of nm in diameter, it is suggested that the

recoil energy of Rn-222 (86 keV) is an important factor in the emanation from the sources. However, as the surface-to-volume ratio increases, humidity might readily adsorb onto the particles which can cause the emanation coefficient to change with respect to changes in humidity. Within the collected data and associated uncertainties, however, such an effect was not observed even though the humidity was uncontrolled during the measurements of the emanation coefficient. Further, up to 50% of the emerging Rn-222 nuclei are implanted into the steel backing by their recoil. Whether these Rn-222 nuclei can subsequently diffuse out of the metal is unknown. Further studies will be conducted to investigate the effect of changing humidity and temperature on the emanation characteristics from such deposits.

Acknowledgments

This work is supported by the European Metrology Programme for Innovation and Research (EMPIR) JRP-Contract 16ENV10 MetroRADON (www.euramet.org). The EMPIR initiative is co-funded by the European Union's Horizon 2020 research and innovation programme and the EMPIR Participating States. The authors thank Mrs. Stefanie Hennig, Mrs. Marion Ehlers, Mrs. Peggy Krause and Dr. Daniel Zapata-Garcia for their aid in experimental work and Mr. Fabian Köhler for performing ICP-MS measurements. The authors also thank Mr. George Winterbottom for correction of the manuscript.

Appendix A. Supplementary data

Supplementary data to this article can be found online at <https://doi.org/10.1016/j.apradiso.2019.108928>.

References

- Allison, J., et al., 2006. Geant4. Nucl. Sci. IEEE Trans. 53 (1) <https://doi.org/10.1109/TNS.2006.869826>.
- Arinc, A., Parfitt, M.J., Keightley, J.D., Wilson, A., 2016. Defined solid angle alpha counting at NPL. Appl. Radiat. Isot. 109, 198–204. <https://doi.org/10.1016/j.apradiso.2015.11.073>.
- Berger, M.J., Hubbell, J.H., Seltzer, S.M., Chang, J., Coursey, J.S., Sukumar, R., Zucker, D.S., Olsen, K., 2019. XCOM: Photon Cross Section Database Version 1.5. National Institute of Standards and Technology, Gaithersburg, MD.
- Bratsch, S.G., 1989. Standard electrode potentials and temperature coefficients in water at 298.15 K. J. Phys. Chem. Ref. Data 18, 1–21. <https://doi.org/10.1063/1.555839>.
- Chabaux, F., Othman, D. Ben, Birck, J.L., 1994. A new RaBa chromatographic separation and its application to Ra mass-spectrometric measurement in volcanic rocks. Chem. Geol. 114, 191–197. [https://doi.org/10.1016/0009-2541\(94\)90052-3](https://doi.org/10.1016/0009-2541(94)90052-3).
- Dersch, R., 2004. Primary and secondary measurements of Rn-222. Appl. Radiat. Isot. 60, 387–390. <https://doi.org/10.1016/j.apradiso.2003.11.046>.
- European Commission, 2014. Council directive 2013/59/euratom of 5 December 2013. Off. J. Eur. Union 1–73. <https://doi.org/10.3000/19770677.L.2013.124.eng>.
- Getoff, N., Bildstein, H., Proksch, E., 1967. Molecular plating. V. The influence of some experimental factors on the deposition yield. Nucl. Instrum. Methods 46, 305–308. [https://doi.org/10.1016/0029-554X\(67\)90088-2](https://doi.org/10.1016/0029-554X(67)90088-2).
- Hancock, G.J., Martin, P., 1991. Determination of Ra in environmental samples by α -particle spectrometry. Int. J. Radiat. Appl. Instrumentation. Part 42, 63–69. [https://doi.org/10.1016/0883-2889\(91\)90125-K](https://doi.org/10.1016/0883-2889(91)90125-K).
- ICRP, 2010. Lung cancer risk from radon and progeny & statement on radon. ICRP publication 115. Ann. ICRP 40, 1.
- Joint Committee for Guides in Metrology, 2008. Evaluation of Measurement Data — Supplement 1 to the JCGM, vol. 101, p. 90.
- Linzmaier, D., Röttger, A., 2014. Development of a transfer standard for the measurement of low Rn-222 activity concentration in air. Appl. Radiat. Isot. 87, 306–309. <https://doi.org/10.1016/j.apradiso.2013.11.076>.
- Linzmaier, D., Röttger, A., 2013. Development of a low-level radon reference atmosphere. Appl. Radiat. Isot. 81, 208–211. <https://doi.org/10.1016/j.apradiso.2013.03.032>.
- Parker, W., Bildstein, H., Getoff, N., 1964a. Molecular plating I, a rapid and quantitative method for the electrodeposition of thorium and uranium. Nucl. Instrum. Methods 26, 55–60. [https://doi.org/10.1016/0029-554X\(64\)90049-7](https://doi.org/10.1016/0029-554X(64)90049-7).
- Parker, W., Bildstein, H., Getoff, N., 1964b. Molecular plating III the rapid preparation of radioactive reference samples. Nucl. Instrum. Methods 26, 314–316. [https://doi.org/10.1016/0029-554X\(64\)90095-3](https://doi.org/10.1016/0029-554X(64)90095-3).
- Philip Horwitz, E., Chiarizia, R., Dietz, M.L., 2007. A novel strontium-selective extraction chromatographic resin*. Solvent Extr. Ion Exch. 10, 313–336. <https://doi.org/10.1080/07366299208918107>.
- Piccolo, J.L., 1996. Absolute measurement of radon 222 activity. Nucl. Instruments Methods Phys. Res. Sect. A Accel. Spectrometers, Detect. Assoc. Equip. 369, 452–457. [https://doi.org/10.1016/S0168-9002\(96\)80029-5](https://doi.org/10.1016/S0168-9002(96)80029-5).
- Piccolo, J.L., Pressyanov, D., Blanchis, P., Barbier, M., Michielsen, N., Grassin, D., Voisin, V., Turek, K., 2000. A radon 222 traceability chain from primary standard to field detectors. Appl. Radiat. Isot. 52, 427–434. [https://doi.org/10.1016/S0969-8043\(99\)00190-6](https://doi.org/10.1016/S0969-8043(99)00190-6).
- Pommé, S., 2015. The uncertainty of counting at a defined solid angle. Metrologia 52, S73–S85. <https://doi.org/10.1088/0026-1394/52/3/S73>.
- Röttger, A., Honig, A., Linzmaier, D., 2014. Calibration of commercial radon and thoron monitors at stable activity concentrations. Appl. Radiat. Isot. 87, 44–47. <https://doi.org/10.1016/j.apradiso.2013.11.111>.
- Vargas, M.J., 2000. Model to explain simultaneously the ^{222}Rn and ^{220}Rn emanation from thin electrodeposited sources. Nucl. Instruments Methods Phys. Res. Sect. A Accel. Spectrometers, Detect. Assoc. Equip. 447, 608–613. [https://doi.org/10.1016/S0168-9002\(99\)01289-9](https://doi.org/10.1016/S0168-9002(99)01289-9).
- Vargas, M.J., De Soto, F.F., 1995. Influence of Ba on the electrodeposition of ^{226}Ra . J. Radioanal. Nucl. Chem. Artic. 198, 143–150. <https://doi.org/10.1007/BF02038252>.
- Vargas, M.J., De Soto, F., 1996. A study of ^{222}Rn emanation in electrodeposited sources of ^{226}Ra with barium. Nucl. Instruments Methods Phys. Res. Sect. A Accel. Spectrometers, Detect. Assoc. Equip. 368, 488–491. [https://doi.org/10.1016/0168-9002\(95\)00854-3](https://doi.org/10.1016/0168-9002(95)00854-3).
- Whitehead, N.E., Ditchburn, R.G., McCabe, W.J., Van Der Raaij, R., 1992. Factors affecting the electrodeposition of ^{226}Ra . J. Radioanal. Nucl. Chem. Artic. 160, 477–485. <https://doi.org/10.1007/BF02037123>.

Chapter 4

Publication II

Ion implantation of ^{226}Ra for a primary ^{222}Rn emanation standard

Florian Mertes, Nina Kneip, Reinhard Heinke, Tom Kieck, Dominik Studer, Felix Weber, Stefan Röttger, Annette Röttger, Klaus Wendt, Clemens Walther

in

Applied Radiation and Isotopes, Volume 181, January 2022

DOI: 10.1016/j.apradiso.2021.110093

Received 22 September 2021

Received in revised form 2 December 2021

Accepted 28 December 2021

Author contributions

Conceptualization, methodology: **F.M.**, N.K., R.H., T.K., D.S., F.W., S.R., A.R., K.W., C.W.

RISIKO experiments, formal analysis: **F.M.**, N.K., R.H., T.K., D.S., F.W.

Radiometric investigation, source characterizations, formal analysis: **F.M.**

Visualization, original draft preparation: **F.M.**, N.K.

Resources, supervision, project administration, funding acquisition: S.R., A.R., K.W., C.W.



ELSEVIER

Contents lists available at ScienceDirect

Applied Radiation and Isotopes

journal homepage: www.elsevier.com/locate/apradisoIon implantation of ^{226}Ra for a primary ^{222}Rn emanation standardFlorian Mertes^{a,*}, Nina Kneip^b, Reinhard Heinke^b, Tom Kieck^b, Dominik Studer^b, Felix Weber^b, Stefan Röttger^a, Annette Röttger^a, Klaus Wendt^b, Clemens Walther^c^a Physikalisch-Technische Bundesanstalt, Bundesallee 100, 38116, Braunschweig, Germany^b Johannes Gutenberg-Universität Mainz, Institut für Physik, Staudingerweg 7, 55128, Mainz, Germany^c Leibniz Universität Hannover, Institut für Radioökologie und Strahlenschutz, 30419, Hannover, Germany

ARTICLE INFO

Keywords:

Ion implantation

 ^{222}Rn emanation

Laser ionization

Defined solid-angle alpha-particle spectrometry

ABSTRACT

Laser resonance ionization at the RISIKO 30 kV mass separator has been used to produce isotopically and isobarically pure and well quantified ^{222}Rn emanation standards. Based upon laser-spectroscopic preparation studies, ion implantation into aluminum and tungsten targets has been carried out, providing overall implantation efficiencies of 40% up to 60%. The absolute implanted activity of ^{226}Ra was determined by the technique of defined solid-angle α -particle spectrometry, where excellent energy resolution was observed. The ^{222}Rn emanation coefficient of the produced targets was studied using α -particle and γ -ray spectrometry, and yielded results between 0.23 and 0.34, with relative uncertainty on the order of 1%. No dependence exceeding a 1% change of the emanation on humidity could be identified in the range of 15 %rH to 75 %rH, whereas there were hints of a slight correlation between the emanation and temperature. Additionally, and as expected, the emanation coefficient was found to be dependent on the target material as well as the implanted dose.

1. Introduction

National and international guidelines and regulations drive the need for SI-traceable measurements of ^{222}Rn at very low activity concentrations ($<300 \text{ Bq}\cdot\text{m}^{-3}$) in air. For such low concentrations, conventional gaseous standards of ^{222}Rn are not suitable for the calibration of measurement devices because the decaying nature of reference atmospheres produced in this way results in poor counting statistics. An alternative was found relatively recently in ^{222}Rn emanation standards (Linzmaier and Röttger, 2013; Mertes et al., 2020), which are ^{226}Ra sources constructed in such a way that a known amount of ^{222}Rn is released from them per unit time. Emanation standards can thus be used to produce time-stable reference atmospheres with the potential to overcome the poor counting statistics from decaying atmospheres. However, the processes leading to the release of ^{222}Rn are usually diffusion processes, such that they correlate with the climate parameters of the environment the sources are operated in. In this work, we investigated the use of ion implantation of ^{226}Ra for the construction of ^{222}Rn emanation sources.

To ionize ^{226}Ra for this purpose, resonance ionization mass spectrometry (RIMS), which is a highly efficient tool to produce ultra-pure mono-isotopic ion beams for various applications including the collection or implantation of ultra-pure isotopic samples, is used. The

technique is commonly applied at on-line radioactive ion beam facilities such as CERN-ISOLDE (Fedosseev et al., 2017) or TRIUMF-ISAC (Lassen et al., 2017) for efficient production of exotic nuclides as well as off-line for rare isotope purification and enrichment. A suitable facility for the latter is the RISIKO mass separator at Mainz University used for ^{163}Ho purification for the ECHO neutrino mass experiment (Kieck et al., 2019b) and other similar tasks.

Resonant laser ionization involves efficient stepwise excitation of an atomic valence electron along strong optical transitions into the ionization continuum using high-power tunable pulsed laser sources. Due to the individual atomic structure of each chemical element, this process is highly selective in the suppression of initial isobaric contaminations. The combination with high transmission mass separation, e.g., in a magnetic sector field separator, adds suppression of isotopic contamination, resulting in a highly pure mono-isotopic ion beam. On the other hand, a careful choice of a suitable optical excitation ladder for each element of interest and application is of primary relevance and must be made considering the laser system at hand.

In the following, we discuss the case of RIMS on radium, specifically the isotope ^{226}Ra , in the context of the production of high quality, low-level ^{222}Rn emanation standards by ion implantation, intended for the generation of primary, time-stable, and SI-traceable ^{222}Rn reference

* Corresponding author.

E-mail address: florian.mertes@ptb.de (F. Mertes).

<https://doi.org/10.1016/j.apradiso.2021.110093>

Received 22 September 2021; Received in revised form 2 December 2021; Accepted 28 December 2021

Available online 31 December 2021

0969-8043/© 2021 Published by Elsevier Ltd.

atmospheres below $300 \text{ Bq} \cdot \text{m}^{-3}$. For such sources, the ion implantation process should provide significant metrological benefits compared to the more traditional approaches of gravimetric drop-casting of standardized solutions (Linzmaier and Röttger, 2013) or electrodeposition (Jurado Vargas and Fernández De Soto, 1996; Mertes et al., 2020). Specifically, enhanced stability concerning environmental changes and improvement in the accuracy of applied characterization techniques is expected and was checked systematically. For complete characterization of the sources, detailed measurements on the ^{222}Rn emanation coefficients, which describe the percentage of emitters that undergo exhalation, were carried out. For this purpose, the ratio of the residual ^{222}Rn and ^{226}Ra activities in the source was measured using γ -ray spectrometry of the progeny and α -particle spectrometry. Moreover, the approach of ion current measurements for implantation efficiency determination is compared with defined solid-angle α -particle spectrometry, allowing the determination of absolute ^{226}Ra activity.

1.1. Laser resonance ionization of radium

For the ionization of radium, the Mainz University Ti:sapphire (Ti:Sa) laser system is used (Mattolat et al., 2009; Rothe et al., 2011), which is pumped by a commercial frequency-doubled Nd:YAG laser (Photonics Industries DM100-532) at 532 nm, operating with a high pulse repetition rate of 10 kHz for efficient temporal overlap with a continuous evaporation source. An average output power in the range of 0.3 W–1.5 W in the blue to UV spectral range can be achieved by intra-cavity second harmonic generation (Sonnenschein et al., 2015) with a typical spectral linewidth of 7 GHz and a pulse length of 50 ns. The emission wavelength of the Ti:Sa laser used in this work, which is a modified development of the one presented in (Teigelhöfer et al., 2010), is selected by angle-tuning of a diffraction grating acting as end mirror of the resonator. This permits for rapid continuous wide range frequency tuning. Wavelengths are measured by a wavelength meter (High Finesse WSU-30).

In preparation for the radium implantation and extending earlier spectroscopic work (Wendt et al., 1987) and ionization scheme development (Day Goodacre et al., 2018; Raeder et al., 2014), different two-step ionization schemes were explored and compared at the RISIKO mass separator, which are presented in Fig. 1. The bottom panel shows the three tested two-step ionization schemes, for which the same first excitation step at 482.7 nm was used with $\approx 470 \text{ mW}$ of laser light to populate the $20\,715.7 \text{ cm}^{-1}$ level along the strong $7s^2\,^1S_0 \rightarrow 7s7p\,^1P_1$ singlet transition (Kramida et al., 2020).

A long-range scan of the second excitation step in the range of the

first ionization potential (IP) at $42\,573.36 \text{ cm}^{-1}$ and above is given in the top panel of Fig. 1. It shows a rather unstructured continuum without significant auto-ionizing states above the IP. The pronounced oscillatory structure between $43\,100$ – $43\,450 \text{ cm}^{-1}$ was caused by regular laser power fluctuations due to interference effects in the phase-matching process of the frequency doubling unit occurring during scans. Below the IP, series of Rydberg levels are clearly visible, which undergo efficient ionization by collisions, electric stray fields, black body radiation, or additional laser photons. A strong Rydberg level at $42\,492.45 \text{ cm}^{-1}$, located about 80 cm^{-1} below the IP, was populated with 459.2 nm laser radiation and was tested for ionization, denominated as scheme A. Alternatively, non-resonant ionization was performed at two different wavelengths of 452.5 nm and 432.7 nm , denoted schemes B and C. A comparable signal intensity, representing the overall ionization efficiency, was achieved with scheme C with respect to scheme A and for simplicity, this scheme with non-resonant ionization was used for the radium implantations as no control and precise readjustment of the second step laser frequency is required. Note that within ion sources with strong electric fields the Rydberg ionization rate may be significantly enhanced.

1.2. Ion implantation of ^{226}Ra at RISIKO

The mass separator facility RISIKO combines a hot cavity laser ion source with magnetic sector field mass selection at a high voltage, high transmission device to produce isotopically and isobarically pure ion beams. To obtain ^{226}Ra samples for the ion implantation process, a ^{226}Ra solution of nominally 71 kBq (RaCl_2 with $0.5\% \text{ m/m BaCl}_2 \cdot 2\text{H}_2\text{O}$ in 0.1 M HCl) was converted into the nitrate by addition and subsequent evaporation of concentrated HNO_3 . It was purified from Ba^{2+} carriers by extraction chromatography through Sr-resin (Philip Horwitz et al., 2007) consisting of 4,4'-(5')-bis(tertbutylcyclohexano)-18-crown-6 in 1-butanol, dispersed on SiO_2 -particles (TrisKem International), similar to the method reported in (Mertes et al., 2020). The Ba^{2+} extraction was monitored by gravimetric addition of nominally 13 kBq $^{133}\text{BaCl}_2$ as a radiotracer for inactive Ba^{2+} , pooling those chromatography fractions in which no ^{133}Ba could be detected in the γ -ray spectrum. This sample preparation step was chosen to reduce space-charge effects from excessive amounts of Ba^{2+} and to avoid the excessive formation of RaCl_2 gas-phase molecules and $[\text{RaCl}]^+$ ions in the evaporator. During preparatory mass scans, the formation and ionization of $[\text{RaCl}]^+$ could still be observed from residual chloride contamination of the sample, stressing the need for this preparation step.

From the resultant solution of $^{226}\text{Ra}(\text{NO}_3)_2$ in 0.6 M HNO_3 , desired

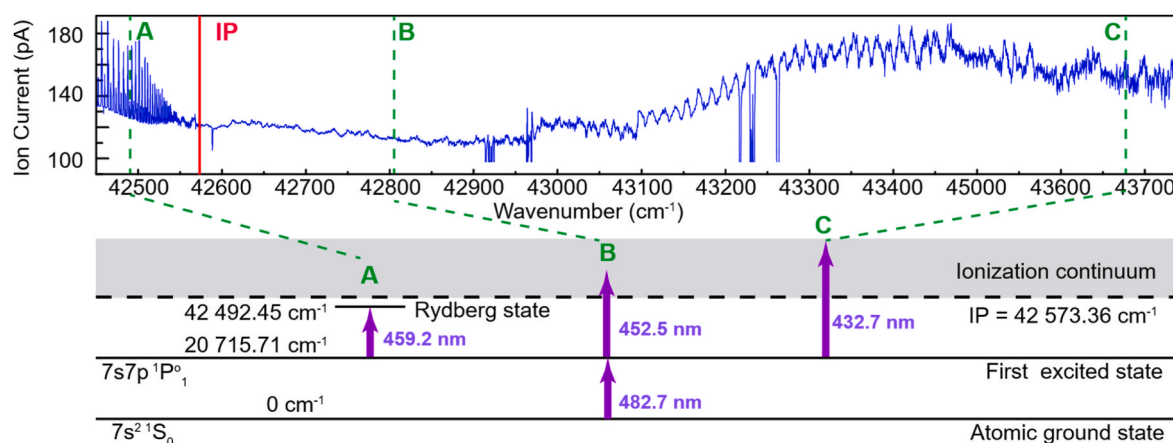


Fig. 1. Bottom: Two-step laser ionization schemes for radium ionization applied in this work. Electron configuration and level energies from (Kramida et al., 2020). Individual transitions A, B, and C are indicated at the corresponding energy positions of the spectrum above. Top: Long-range scan of the second excitation step from $42\,450 \text{ cm}^{-1}$ to $43\,750 \text{ cm}^{-1}$. Signal dips between $42\,900$ – $43\,000 \text{ cm}^{-1}$ and $43\,200$ – $43\,300 \text{ cm}^{-1}$ occurred during ongoing laser and mass separator optimizations. For further details see text.

amounts of activity were drop-cast onto $5 \times 5 \text{ mm}^2$ hafnium foils (97%, Goodfellow). The foils were folded afterward to fully enclose the sample and act as a reducing agent. The deposited ^{226}Ra activity on each foil was measured using γ -ray spectrometry with a high-purity germanium (HPGe) detector, comparing the 186 keV ^{226}Ra full-energy peak with a PTB reference ^{226}Ra point source.

For RIMS at the RISIKO facility, these ^{226}Ra samples were placed one at a time into a thin tantalum capillary (20 mm length, 1 mm inner diameter) acting as an independently heated sample reservoir. It is attached to the back of a tantalum tube furnace (34 mm length, 2.5 mm inner diameter) acting as an atomizer. A detailed schematic of the setup is given in (Kieck et al., 2019a). Both the sample reservoir and the atomizer are heated resistively. While the latter was kept at a constant temperature of about 2000 °C, as estimated from previous studies of the hot cavity setup (Kieck et al., 2019a), the sample reservoir was gradually heated slowly to allow controlled sample supply to the ion source. Ionization took place either unselectively by contact with the hot cavity walls (surface ionization), or specifically for the Ra atoms by laser resonance ionization. Due to the selectivity of the latter process, the relative contribution of unspecific background on the mass 226 was significantly reduced while in parallel the overall ionization efficiency was strongly increased in comparison to pure surface ionization. The ions were accelerated to a kinetic energy of 30 keV and shaped to form an ion beam by ion optical elements. Mass separation within the 60° dipole magnet achieved a resolving power of $m/\Delta m \approx 800$. After the separator slits at the focal plane of the magnet, the ion beam was post-focalized with an Einzel lens down to a beam size of 0.5 mm FWHM, permitting also for precise steering and spatial spot control for implantation into the different targets (Kieck et al., 2019b). The electrically conductive implantation targets were positioned one at a time within an insulated Faraday cup device (FC) including a repeller electrode put on -200 V potential for rejection of secondary electrons. This arrangement allows for permanent monitoring of the ion beam during implantation and reliable ion beam current quantification. A sketch of the overall experimental setup of the RISIKO mass separator with the laser system for resonance ionization is shown in Fig. 2.

Fig. 3 depicts the data from a typical implantation run with ion current plotted versus elapsed time. The curve progression can be separated into different phases I, II, and III. Controlled source heating enables reasonably steady evaporation and atomization of source atoms, as desirable for a proper resonance ionization process. During the initial phase I the goal of producing a radium ion beam with reasonably stable ion current was achieved and is visible in Fig. 3 by a small plateau at 1

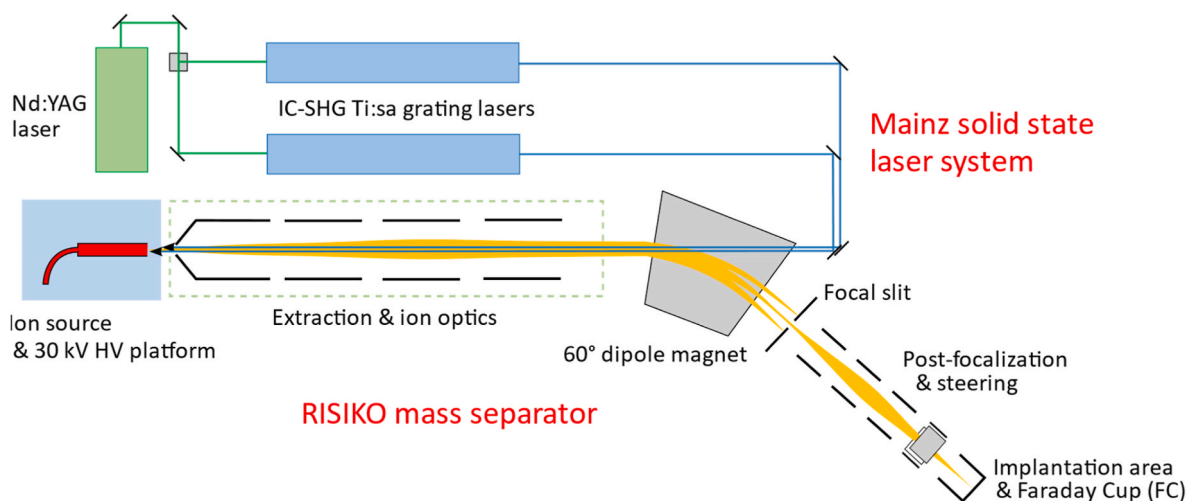


Fig. 2. Schematic sketch of the RISIKO laser mass separator facility for isotope separation and implantation. The ion beam is shown in yellow and the laser beams in blue. Details of the ion source and the implantation area including post-focalization and steering are discussed in the text. (For interpretation of the references to color in this figure legend, the reader is referred to the Web version of this article.)

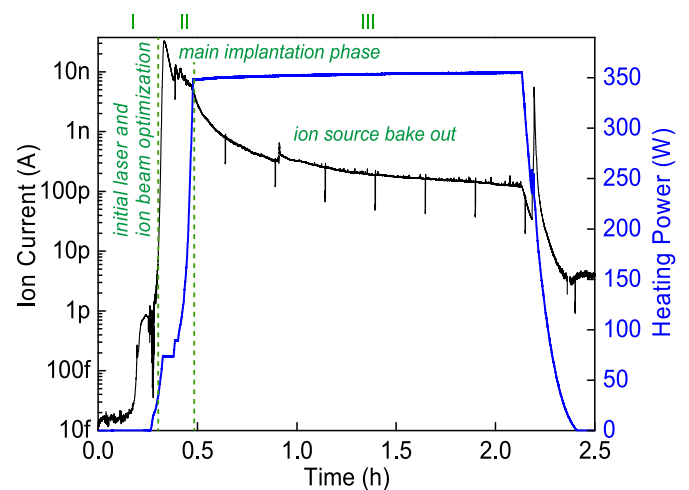


Fig. 3. Typical implantation process for the example of target 2018-1128. The black trace represents the ion current of implanted ^{226}Ra ions and the blue curve gives the heating power of the sample reservoir, which defines its temperature. The significant phases I, II, and III of the measurement are indicated, separated by the vertical dashed lines. (For interpretation of the references to color in this figure legend, the reader is referred to the Web version of this article.)

pA. The low ion current during this phase was used to optimize the ion optics and the laser ionization process. These optimizations are very important to achieve high implantation efficiency. The main implantation phase II, specified by a relatively high ion beam current in the higher nA range, and correspondingly high implantation rate, has a typical duration in the range of 10 min–30 min depending on the ratio between ion current and activity of the sample. At RISIKO a maximum ion current in the range of a few 100 nA is known to ensure optimum transmission and implantation without ion beam degradation. Correspondingly, initial sample evaporation was controlled by careful heating of the sample reservoir, as the ^{226}Ra implantation was executed with a specifically low ion current of about 10 nA. Additionally, the atomizer cavity and reservoir were regularly baked out at the end of each measurement in phase III to purge the ion source from any remainders of the sample in preparation for the next implantation run. This also reduces influences of violent evaporation processes as observed at the end of the heating phase, for example. The ^{226}Ra ions produced during phase III

were also implanted into the targets.

To quantify the targeted enhancement of laser resonance ionization over surface ionization, the lasers were blocked periodically with a shutter (signal dips in Fig. 3). Typically, an enhancement factor of significantly above 2 was demonstrated.

A total of 6 targets (3 tungsten sheets, 3 aluminum sheets) were implanted with ^{226}Ra with a total collection duration of about one to 2 h per target in a single implantation cycle. The collection duration varied corresponding to the desired implanted activity, the achieved ion current and the state of the sample in the ion source. The efficiency ε_C of the overall ^{226}Ra implantation process was defined as the ratio of activity A_C implanted into the target to the initial activity in the sample A_0 placed in the ion source, as previously determined by γ -ray spectrometry.

$$\varepsilon_C = \frac{A_C}{A_0} = \frac{\ln 2}{T_{1/2}} \frac{\int I dt}{A_0 e} \quad (1)$$

A_C is extracted from the time-integrated ion current I for singly charged ions (total charge), measured on the target during implantation, while e is the elemental charge and $T_{1/2}$ is the half-life of ^{226}Ra , 1600 a (Bé et al., 2004). The ionization efficiency ε relates the number of atoms initially placed in the ion source to the number of atoms that are ultimately implanted into the target. It is composed of several factors, i.e., sample vaporization and atomization (avoiding molecule formation), the laser ionization process itself, ion survival in the atomizer cavity, extraction, ion beam formation, and transmission through the separator. Due to potential sputtering of already implanted material, the total collected charge given by the integrated ion current does not necessarily reflect the number of atoms that reside within the target after the implantation procedure.

Four samples, denoted S1, S2, S3, and S4, containing on the order of $N_0 \approx 10^{14}$ atoms of ^{226}Ra each (corresponding to the activities A_0) were used for the implantations into six circular targets of 30 mm nominal diameter and 1 mm thickness (obtained from Goodfellow, 99.5% W and 99.999% Al respectively). Each target was manually polished and cleaned with isopropyl alcohol before implantation. Results of the implantation process are compiled in Table 1. The A_α values represent the individual activities of implanted ^{226}Ra as determined by defined solid-angle α -particle spectrometry, as discussed in detail below. The implanted ion current, continuously recorded by the insulated Faraday cup implantation foil holder, delivered the implanted atom number which was used to derive A_C . Implantation efficiencies are calculated based on the radiometric results and the ion current integration, respectively, as indicated by the index α or C. As detailed in the Discussion and Conclusions section below, they are in overall good

Table 1

Overview of the implanted targets and initial sample sizes (activity per sample A_0) together with the implanted activity A_α and A_C , measured by α -particle spectrometry and ion current integration, respectively. In addition, efficiencies ε_C , derived from ion current integration as (A_C/A_0), and ε_α , derived from α -particle spectrometry as (A_α/A_0) are given. Uncertainties and systematic errors are discussed in the text.

Target (Material)	Sample A_0 (Bq)	A_α (Bq)	A_C (Bq)	A_C/A_α	ε_α (%)	ε_C (%)
2018-1120 (W)	S1 2500 (90)	922 (4)	766 (77)	0.83	36.9 (13)	30 (3)
2018-1121 (W)	S2 1940 (70)	1139 (5)	1155 (115)	1.01	58.7 (21)	60 (6)
2018-1122 (W)	S3 3080 (100)	671 (3)	724 (72)	1.07	35.4 (9)	32 (3)
2018-1128 (Al)		842 (4)	798 (80)	0.94		
2018-1133 (Al)	S4 3400 (90)	603 (3)	513 (51)	0.85	46.3 (15)	46 (5)
2018-1134 (Al)		514.2 (21)	475 (47)	0.92		

agreement.

1.3. Defined solid angle α -particle spectrometry

As a reference method to perform absolute measurements of the implanted ^{226}Ra activity, α -particle spectrometry under defined solid angle (DSA) was applied, which is among the most accurate primary methods for activity determination for α -particle emitters, achieving standard uncertainties routinely below 1% (Arinc et al., 2016; Pommé, 2015). This technique was carried out utilizing the PTB DSA α -particle spectrometer M10 with an approximate geometrical efficiency of 1% of 4π sr. The basis of this method is the exact determination of the solid angle of the radiation source subtended by the detector, which is in practice realized by an aperture system opaque to α -particles. The knowledge of the aperture geometry allows calculating the detection efficiency employing Monte-Carlo integration of (2), i.e., through path tracing of randomly generated rays within the source area A . The geometrical efficiency G is given by

$$G = \frac{1}{4\pi} \frac{\int_A \Omega_{dA} w_{dA} dA}{\int_A w_{dA} dA} \quad (2)$$

where A denotes the total area of the radiation source, dA an area element within A , Ω_{dA} the solid angle subtended by the detector with respect to dA and w_{dA} the relative contribution of activity contained within dA to the total activity.

The geometrical parameters of the setup are known precisely and traceably to PTB standards and result in an accuracy of 0.25% in the calculated geometrical efficiency. They are given in more detail in (Mertes et al., 2020). The dead time of the system is corrected for by a high-precision pulse generator, which is connected to the system pre-amplifier operating at a nominal repetition rate of 50 Hz with negligible uncertainty. The employed ion-implanted, passivated Si-diode detector in the M10 setup is a Canberra PIPS® of 600 mm² active area and 300 μm depletion depth with a rated energy resolution (FWHM) of 20 keV at 5.5 MeV. Fig. 4 shows typical α -particle spectra of the produced Al- and W-targets, which were implanted with ^{226}Ra as given above. The spectra were obtained approximately 2 months after implantation and show a slight variation in energy resolution between the different target materials. Nevertheless, overall unmatched energy resolution is observed if compared with the 20 keV FWHM reported in (Marouli et al., 2017) and specifically in (Mertes et al., 2020), measured with the same setup for electrodeposited ^{226}Ra . In Fig. 4, the two spectra with the highest deviation in resolution are deliberately accentuated. The average observed FWHM of the higher energy ^{226}Ra peaks amount to 16.8 keV (W) and 15.6 keV (Al) respectively, obtained from a graphical method.

In order to determine the exact measurement geometry, a digital autoradiograph of each source was taken with a FUJIFILM FLA-9000, which yields intensity values on a 100×100 grid of (0.2×0.2) mm² pixels. As an example, Fig. 5 shows a radiograph obtained in this way. The targets are centered with respect to the grid by using four ^{238}Pu reference point sources placed rectangularly around the target. All resulting autoradiographs show bivariate Gaussian distributions with a variance of approximately 1 mm in both directions, i.e., a FWHM of about 2.3 mm. The obtained data is interpreted as the projected activity distribution. Thus, in the Monte-Carlo integration of (2), the autoradiography data is employed directly for the sampling of origin points of random paths to be tracked, where uniform distributions within each pixel are assumed for oversampling.

Due to the non-central installation of targets in the Faraday Cup during implantation, each radiograph shows slightly different eccentricity. Therefore, the computation of the geometrical efficiency G was carried out for each source independently. All geometrical parameters were iteratively resampled to obtain a population of G around its mean value, as similarly reported in (Arinc et al., 2016), including the

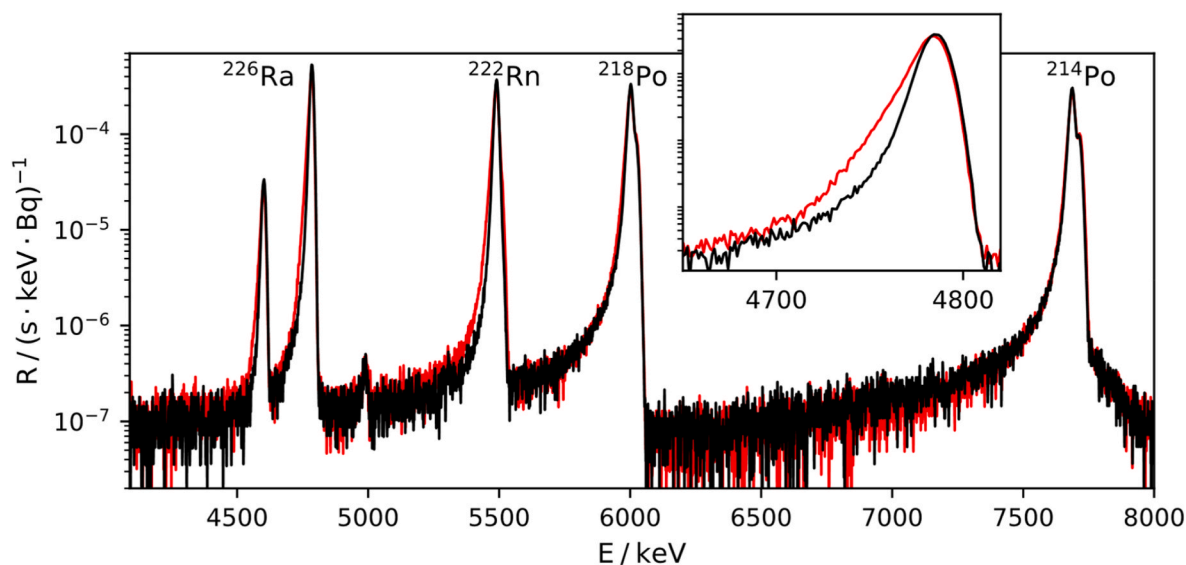


Fig. 4. Depiction of collected α -particle spectra for targets 2018-1122 (W target, red) and 2018-1133 (Al target, black), normalized to activity and measurement time with a magnified view of the higher energy ^{226}Ra emission. (For interpretation of the references to color in this figure legend, the reader is referred to the Web version of this article.)

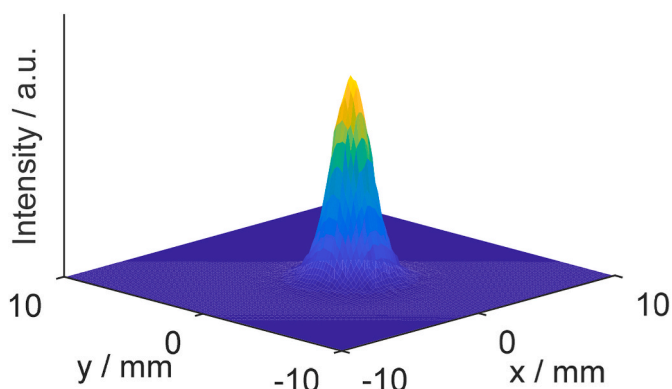


Fig. 5. Depiction of a typical digital autoradiograph of implanted ^{226}Ra activity of target 2018-1121 (W) as an example. The origin coincides with the center of the circular target.

propagation of the geometrical uncertainties in accordance with GUM supplement 1 (Joint Committee for Guides in Metrology, 2008). Since there is no control over rotations of the source between taking the radiograph and installation of the source in the spectrometer, a random rotational angle uniform in $[-\pi, \pi]$ with respect to the center of the target, as well as a Gaussian pixel-size uncertainty of 10% and a Gaussian random x,y-offset of ± 0.2 mm, were included in the analysis of G.

It should be noted that the autoradiography measures the convolution of an unknown point-spread function with the true projected activity distribution, due to the finite distance between the autoradiography film and the source surface. To account for the additional uncertainty from this effect, G was also computed for the best-case activity distribution of a bivariate Gaussian with a FWHM of 0.5 mm due to the estimated beam profile from (Kieck et al., 2019b). This approach delivered a maximum deviation of 0.3% of the resulting counting efficiency from the value obtained using the autoradiography data, and hence a rectangularly distributed correction factor within [1.000, 1.003] is included in the uncertainty analysis. Moreover, backscattering and self-absorption contributions to the uncertainty are estimated to be on the order of 0.2% (Mertes et al., 2020; Pommé, 2015).

Peak areas in the α -particle spectra were determined using a

regression model based on the sum of exponentially modified, left-handed Gaussians, as introduced in (Bortels and Collaers, 1987) and further refined in (Pommé and Caro Marroyo, 2015). Three left-handed exponential terms were used in each α -particle peak and it was required that the ^{226}Ra 4684 keV and the 4870 keV emission share the same shape parameters. For the peaks of ^{222}Rn and the short-lived progeny, a single Gaussian was added to the peak shape model to account for the high-energy satellite peaks (see Fig. 4). The computer program *Fityk* (Wojdyr, 2010) was used to regress this model onto the observed spectra by minimizing the weighted sum of squared residuals.

From the analysis of the adjacent regions to the peak, it was estimated that the remaining uncertainty for unresolved or incorrectly modeled tailing contributions to the ^{226}Ra count rate, further denoted as R_{Ra} , corresponds to a standard uncertainty of 0.2%.

A detailed uncertainty budget listing the relative standard uncertainties and their relative contributions to the combined uncertainty for the activity determination of source 2018-1121 is given in Table 2 as an example.

1.4. Emanation theory and associated measurements

The emanation of ^{222}Rn from the implanted sources is described by the emanation coefficient, χ , which is given by the percentage of exhaled versus retained ^{222}Rn activity after the initial ^{226}Ra decay. This ratio is, in this case, largely due to recoiling and thus depends on the target material, the implantation depth, and environmental parameters. After the α -decay of ^{226}Ra , the emerging ^{222}Rn nuclei experience an average

Table 2
Uncertainty budget for DSA α -particle spectrometric activity determination of target 2018-1121, where the relative standard uncertainty of the respective components and their relative contributions to the combined uncertainty σ_A of the ^{226}Ra activity are given.

Source for uncertainty	σ / %	rel. contribution
Counting statistics	0.04	1%
Peak shape	0.20	27%
Solid angle	0.25	40%
Activity distribution	0.09	5%
Self-absorption and backscattering	0.20	27%
σ_A / %	0.4	

kinetic energy of 86 keV. Since the implantation was carried out at just 30 keV, a certain fraction of ^{222}Rn nuclei is consequently and unavoidably ejected from the source body due to their recoil energy. From theoretical considerations this recoiling fraction is mainly related to the energy dependence of the stopping power of the target material, i. e., the difference in range of 30 keV ^{226}Ra and 86 keV ^{222}Rn nuclides, keeping in mind that the recoil is isotropic, while the implantation is approximately perpendicular to the target surface. To investigate the material dependency, the two very different target materials Al and W were used for comparison. While the absolute value of the stopping power (or equivalently implantation depth) initially only has a small effect, since it applies to both the implantation as well as the recoiling process, the impact of secondary effects, such as target material sputtering on the emanation coefficient, is strongly dependent on the material and the absolute implantation depth. A prior baseline value of 0.23 was estimated for the recoil emanation coefficient for both target materials using the projected range calculation from the *Stopping and Range of Ions in Matter* (SRIM) software (Ziegler et al., 2010). This calculation gives a mean projected range of 19 nm and 5 nm for 30 keV ^{226}Ra in Al and W, respectively. Nuclei that are not ejected directly from recoiling can subsequently diffuse out of the material, depending on the respective diffusion coefficients, which are unknown. Emanation through recoil is expected to lead to much more stable emanation behavior concerning changes in environmental parameters compared to source setups, which are largely based on diffusive emanation, such as the ones discussed by (Linzmaier and Röttger, 2013) among others. This is ascribed to the fact that diffusion is strongly impacted by temperature, partial pressure gradients, and ad- and absorption of humidity, while these parameters are thought to not affect recoiling as much.

For determination of the emanation coefficient χ via the amount of permanently emanating and steadily regenerated ^{222}Rn from the sources, two types of independent, absolute measurement methods were applied. After the sources reached a steady-state (approx. after 20 days), χ is given by

$$\chi = 1 - \frac{A_{Rn}}{A_{Ra}} \quad (3)$$

where A_{Rn} and A_{Ra} denote the activity of the respective nuclide in the emanation source. Firstly, the method presented in (Linzmaier and Röttger, 2013) and (Mertes et al., 2020) was considered, which is based on the equilibrium of the γ -emitting short-lived ^{222}Rn progeny ^{214}Pb and ^{214}Bi against ^{226}Ra in the source, which is distorted due to emanation of ^{222}Rn . Secondly, the emanation coefficient was also measured by a previously unreported method derived from first principles through assessing the α -particle spectra obtained for the residual ^{222}Rn within the source. Both methods have their own drawbacks and associated sources for systematic uncertainties and biases, which are discussed in the following sections.

1.5. γ -ray spectrometric determination of the emanation coefficient

The γ -ray spectrometric method as reported in (Linzmaier and Röttger, 2013; Mertes et al., 2020) was used for γ -ray spectrometric determination of the emanation coefficients. For this method, a reference source of similar type and geometry is needed, in which the natural secular equilibrium between the short-lived ^{222}Rn progeny and ^{226}Ra is fully established through sealing against ^{222}Rn emanation. In order to obtain such reference sources, one of the sources of each target material (W, Al) was closed hermetically against ^{222}Rn emanation by gluing a stainless-steel sheet (nominal 0.05 mm thickness) onto the respective target using a 2-component epoxy resin (Delo-Duopox 01 rapid). The quality of the seal was investigated for each source produced in this way in a nominal 50 L noble-gas tight volume, in which an AlphaGuard (Saphymo, Model PQ2000) measures the ^{222}Rn -concentration. Since there was no detectable increase in ^{222}Rn concentration after flushing

with aged air, the sealing was estimated to be tight to better than 0.5% loss of emanating ^{222}Rn . Conversely, previous attempts using a cyanacrylate glue yielded an unsatisfactory seal and as a result one of the sources (2018-1122) was thus cleaned from residual glue with a cotton cloth moistened in acetone. This procedure showed to remove less than 5% of the activity as investigated by subsequent α -particle spectrometry, which indicates a relatively high chemical and mechanical stability of the implanted sources.

For the determination of the emanation coefficient using γ -ray spectrometry, closely following the procedure in (Linzmaier and Röttger, 2013; Mertes et al., 2020), the full energy peak count rate ratios of the short-lived ^{222}Rn progeny ^{214}Pb and ^{226}Ra were compared with those measured for the respective sealed source. Table 4 shows results obtained by averaging data over all collected spectra and all investigated γ -ray emissions (^{214}Pb 242 keV, 295 keV, 352 keV). Since a ratio of count rates is evaluated, the effects of possible changes in geometry and differences in γ -ray attenuation between the sealed and open sources are particularly small. Slight changes in measurement geometry between the sealed and open sources resulting from potential target thickness variation on the order of 0.1 mm are assumed to introduce an uncertainty of 0.1%. Especially in the case of the W targets, measurements were only possible through the layer of epoxy-resin (as opposed to through the target material) due to the specifically high γ -ray attenuation in W. Thereby, an additional uncertainty arises from the attenuation of γ -rays within the layer of epoxy resin and stainless steel, which was analytically estimated from the Lambert-Beer law and the mass attenuation coefficients from XCOM (Berger et al., 2019) for each investigated γ -ray emission and was found to not exceed a deviation of 0.3% with respect to the count rate ratios. Due to the absolute magnitude of the emanation coefficients, relative uncertainty estimates for the count rate ratios are propagated amplified by a factor of approximately 3. An uncertainty budget for a γ -ray spectrometric determination of the emanation coefficient using the 352 keV ^{214}Pb emission for source 2018-1120 is given in Table 3 as an example.

The γ -ray spectrometric method has the drawback that it does not directly measure the ^{222}Rn within the source but progeny of ^{218}Po . Since it was assumed that the emanation of ^{222}Rn is primarily due to recoil and much less to only the diffusion of atoms, this method is potentially impacted by further recoil losses of ^{218}Po and ^{214}Pb . In addition, the necessity of the sealed reference source introduces systematic uncertainties due to potential imperfect sealing and unavoidable changes in measurement geometry. As the magnitude of these effects is partially unknown, the second method was applied to verify the results.

1.6. Absolute α -particle spectrometric determination of the emanation coefficient

The second method directly measures the α -decay of ^{222}Rn that is retained within the source. Nevertheless, it is difficult to dissect contributions of recoiling ^{222}Rn atoms that are implanted into the detector and its surroundings during α -particle spectrometric measurements, causing possible bias. The occurrence of these recoil contributions to the peaks of ^{222}Rn , ^{218}Po , and ^{214}Po in α -particle spectra was previously

Table 3

Typical uncertainty budget for the γ -ray spectrometric determination of the emanation coefficient (example for target 2018-1120 and the 352 keV ^{214}Pb emission), where the relative standard uncertainty of the respective components and their relative contributions to the propagated combined uncertainty σ_χ of χ are given.

Source for uncertainty	σ / %	rel. contribution
Counting statistics	0.3	40%
Change in geometry	0.1	5%
γ -ray attenuation	0.17	15%
Incomplete sealing	0.29	40%
σ_χ / %	1.1	

Table 4

Comparison of determined emanation coefficients of the implanted ^{226}Ra sources using α -particle spectrometry (χ_α) and γ -ray spectrometry (χ_γ) and observed FWHM in α -particle spectra of the 4784 keV ^{226}Ra emission.

Target (Material)	χ_α	χ_γ	FWHM $^{226}\text{Ra}/\text{keV}$
2018-1120(W)	0.308 (4)	0.3077 (29)	16.5
2018-1121(W)	0.340 (4)	0.341 (5)	16.8
2018-1122(W)	0.285 (4)	-	17.1
2018-1133(Al)	0.273 (4)	0.272 (4)	15.3
2018-1134(Al)	0.260 (3)	-	15.5
2018-1128(Al)	0.233 (4)	0.230 (4)	16.0

reported for electrodeposited ^{226}Ra sources in (Marouli et al., 2017), while in (Jurado Vargas et al., 1995) measurements of the emanation using α -particle spectrometry were reported, which seemingly neglected this fact. Moreover, α -particle spectra are recorded under low to medium vacuum conditions of typically few 10^{-1} Pa, which might affect the derivation of the emanation coefficient both by changing the chemical composition in the source material through drying and desorption and by the resulting pressure gradients.

As pointed out, for the determination of the emanation coefficient from the obtained α -particle spectra, the ingrowing secondary background generated by ^{222}Rn atoms recoiling into the detector must be corrected, especially in case of prolonged measurements. For illustration, Fig. 6 depicts the observed evolution of the ^{222}Rn -peak of an α -particle spectrum over time.

The approach of peak deconvolution commonly applied in α -particle spectrometry was experienced to be unreliable and unsatisfactory for the deconvolution of the strongly overlapping ^{222}Rn and recoil ^{222}Rn peaks without using temporal information.

This is due to the high degrees of freedom of the available various peak-shape models, reported in (Pommé and Caro Marroyo, 2015) among others, which lead to numerical instability, overfitting, and high sensitivity to starting parameters. Moreover, the distribution of plausible parameters is thought to be strongly correlated and multi-modal since different combinations of tailing parameters of the two contributing peaks can lead to indistinguishable likelihoods, essentially attributing either too much or too little of the peak area to the respective secondary background or source contributions, arising from the overlapping left-handed tailings. Possible strategies to resolve this are either to incorporate shape information on the secondary background peak or to use time-domain information and ingrowth modeling. Shape information could be acquired by subsequent measurements but several complications were experienced using this strategy. These arise from the

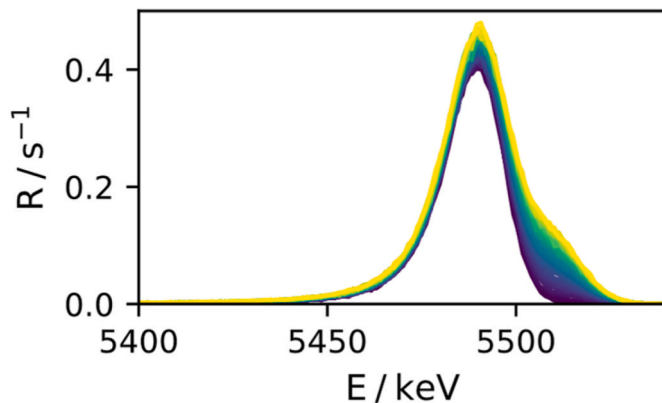


Fig. 6. Typical ingrowth of the observed α -particle peak of ^{222}Rn . Time development since installation of the source is given by color-coding from blue (start) to yellow (end) throughout approx. 7 d. The ingrowing satellite peak is due to ^{222}Rn recoil implantation into the detector. (For interpretation of the references to color in this figure legend, the reader is referred to the Web version of this article.)

limited statistics collectible during the decay and gain drifts that distort the spectra. The computation of meaningful uncertainty estimates in this case requires computationally intensive Monte-Carlo sampling, which was found to be impracticable. Therefore, in this work, the choice was made to use time-domain information to dissect the secondary background contributions to the combined peak. In order to make progress in modeling the ingrowth of the recoiled ^{222}Rn to the overall counting rate in the combined ^{222}Rn peak, a simple method was derived, as described below. As previously stated, the area of the combined peak was determined by regression of the sum of a triple-tailed, exponentially modified Gaussian and a single Gaussian for the satellite peak, intentionally not attempting to deconvolve the relative contributions but to determine the combined peak area.

The counting rate in the combined ^{222}Rn peak is assumed to be the sum of the differently weighted, time-integrated activities in the source and the detector, respectively.

$$R'(t, r) = \frac{\varepsilon_{Rn}}{r} \int_t^{t+r} A_{Rn}(\tau) d\tau + \frac{\varepsilon_i}{r} \int_t^{t+r} A_i(\tau) d\tau \quad (4)$$

where $R'(t, r)$ is the apparent, combined count rate of the ^{222}Rn peak at time instant t , observed in a spectrum obtained over the real-time interval r . A_{Rn} and A_i denote the ^{222}Rn activity in the source and the recoil implanted activity in the detector and surroundings, respectively, which are measured with counting efficiencies ε_{Rn} and ε_i .

For A_{Rn} and A_i , the following first-order continuity equations are formulated, assuming that the emanation coefficient is constant and that the source already reached the associated equilibrium state.

$$\frac{dA_{Rn}}{dt} = 0 \quad \frac{dA_i}{dt} = -\lambda_{Rn}A_i + k \quad (5)$$

where λ_{Rn} denotes the decay constant of ^{222}Rn and k denotes a latent ingrowth term in activity per unit time.

By substituting the solutions of the continuity equations and carrying out the integration, equation (6) was derived for the observed combined count rate corrected for recoil contributions present at the start of the measurements due to remaining recoiled ^{222}Rn from previous measurements, resulting in the count rate $R_{i,0}$. $R_{i,0}$ was determined by extrapolation from previous background measurements through weighted linear least squares.

$$R'(t, r) - R_{i,0}f = R_{Rn} + \frac{R_{i,0}}{r}f + R_{i,\infty}(1-f) \quad (6)$$

where $f(t, r) = \frac{e^{-\lambda_{Rn}t}}{1 - e^{-\lambda_{Rn}r}}(1 - e^{-\lambda_{Rn}r})$, $R'(t, r)$ is the apparent combined count rate at measurement start time t with the associated real-time interval r , $R_{i,0}$ is the count rate generated by the recoil implanted ^{222}Rn at the beginning of the installation of a source, $R_{i,\infty}$ is the associated equilibrium value, and R_{Rn} is the count rate due to the ^{222}Rn activity of the source. Equation (6) can be seen as a linear regression with respect to the parameters and the independent variable $1 - f(t, r)$ for pairs of t and r , which was carried out by weighted linear least squares through numerical matrix inversion. The covariance structure on the dependent variable, $R' - R_{i,0}f$, resulting from uncertain $R_{i,0}$, was taken into account by first computing its covariance matrix made up of the counting statistics and the contributions due to $R_{i,0}$ and using its inverse as the weights. This allows for direct propagation of the uncertainty associated with $R_{i,0}$. The uncertainty arising from λ_{Rn} (0.02%) was disregarded in this analysis as it was considered negligible. A typical result of this procedure is shown in Fig. 7.

The absence of ^{210}Po due to the mass-separation process was found to allow for a more precise determination of the ^{222}Rn peak area. Otherwise a slight overlap between the ^{222}Rn (5489 keV) tailing and the ^{210}Po peak (5304 keV) would have disturbed the data. For this analysis the dead-time of the system was neglected since only the ratio of count rates

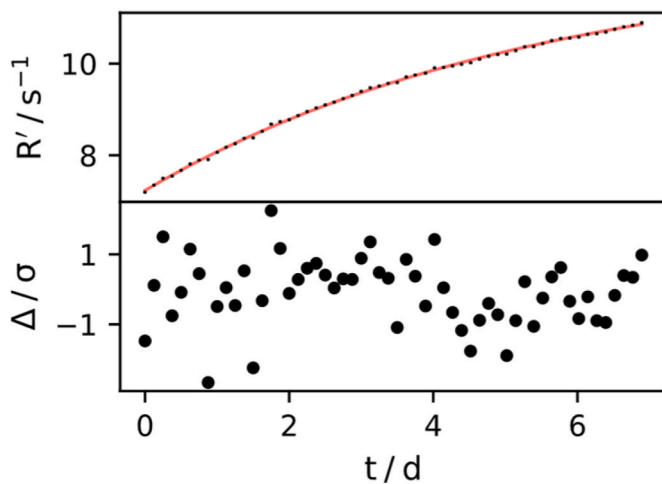


Fig. 7. Modeled ingrowth behavior of combined ^{222}Rn α -particle peak count rate (top) of source 2018-1121 and associated normalized residuals (bottom).

is needed, which is unaffected by the dead-time.

This procedure was carried out for each of the 6 produced sources and the respective emanation coefficients were calculated, extending (3) by the regression parameter R_{Rn} and the average count rate of the ^{226}Ra peak R_{Ra} , as was already evaluated previously for the ^{226}Ra activity measurements.

$$\chi = 1 - \frac{A_{Rn}}{A_{Ra}} = 1 - \frac{R_{Rn}}{R_{Ra}} \quad (7)$$

The main contribution to the combined uncertainty is due to the potential systematic anti-correlation of R_{Rn} and R_{Ra} caused by imperfect determination of contributions of the tail of the ^{222}Rn peak to the ^{226}Ra peak. Since the uncertainty of R_{Ra} is 0.2% due to remaining tailing contributions, a worst-case of 0.4% is estimated for the uncertainty of the activity ratios due to this anti-correlation, assuming pessimistically that all unresolved contributions to R_{Ra} belonged to R_{Rn} . Due to the emanation coefficients on the order of 0.3, this results in a worst-case systematic uncertainty of about 1% in the emanation coefficients, which is reflected in the uncertainty given in Table 4, where the

resulting emanation coefficients from both analyses are tabulated. Very good agreement between both approaches to better than 1% was shown, indicating their equivalence and accuracy. Similarly, both methods turned out to lead to comparable uncertainty, largely caused by the estimation of systematic contributions.

1.7. Stability of emanation coefficients with respect to environmental conditions

For a full characterization of the emanation sources, measurements of one of them (Al, 2018-1133) were carried out in a 20 m³ climate chamber at varying relative humidity in the range of 15 %rH to 70 %rH at 21 °C–32 °C using an electrically cooled HPGe detector and a 1.5" LaBr₃ detector with the implanted target mounted in the middle of both detectors. To fit both detectors, a partially open lead shield as shown in Fig. 8 was used. Detectors were operated with acquisition times of 12 h. Temperature and relative humidity were recorded in proximity to the implanted target with a SHT-35 sensor.

Fig. 9 shows the evolution of the normalized count rate ratio of the full-energy peaks of the 352 keV ^{214}Pb and 186 keV ^{226}Ra emissions to a steep change in humidity from 15 %rH to 70 %rH. No significant (two-sided, unequal variance T-test, $p = 0.60$) deviation could be found in the mean values before and after the change. The detection limit was estimated by calculating the critical value of change, for which this statistical test would yield $p < 0.05$, which corresponds to a change in the emanation of approximately 1% at a 95% significance level.

Fig. 10 shows the change of this count rate ratio for a temperature increase from 21 °C to 32 °C. It was found that within the time and the uncertainty of the measurements, the mean value of the ratio decreased by 0.8% in conjunction with increasing temperature, which is significant ($p < 0.002$). This change corresponds to an increase in the emanation of approximately 2%. Gain drifts with respect to temperature were corrected by calculating a distinct energy calibration for each spectrum, however, drift within the integration time could not be corrected, which potentially contributes to the observed deviation due to inaccuracies in peak area determination, especially in the case of the strongly temperature-dependent LaBr₃ detector. Changes in the counting efficiency due to temperature expansion were not corrected, since they were considered negligible in this temperature range. The observed decrease in the count rate ratio is likely caused by the source itself

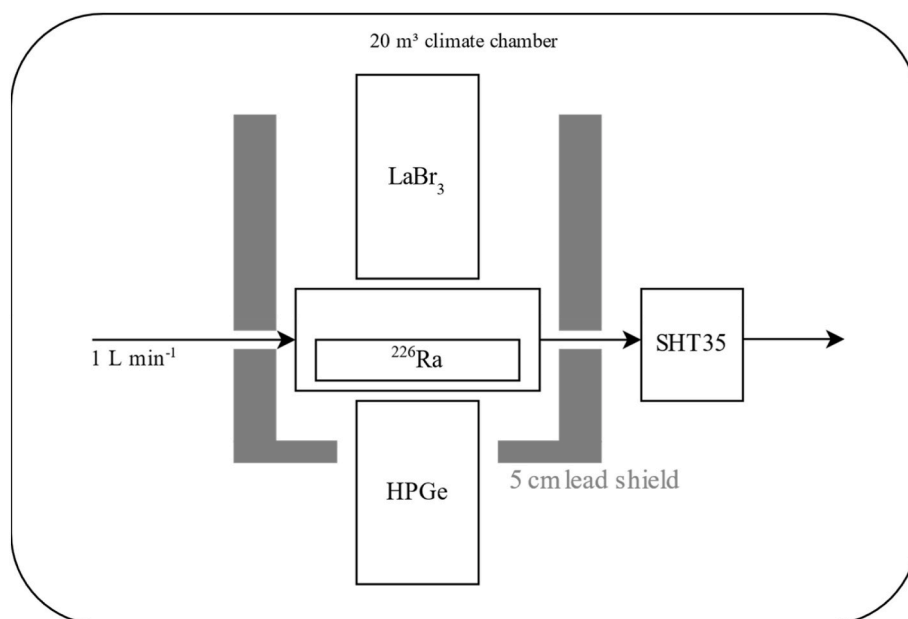


Fig. 8. Schematic of the γ -ray spectrometry setup in a 20 m³ climate chamber used in this work.

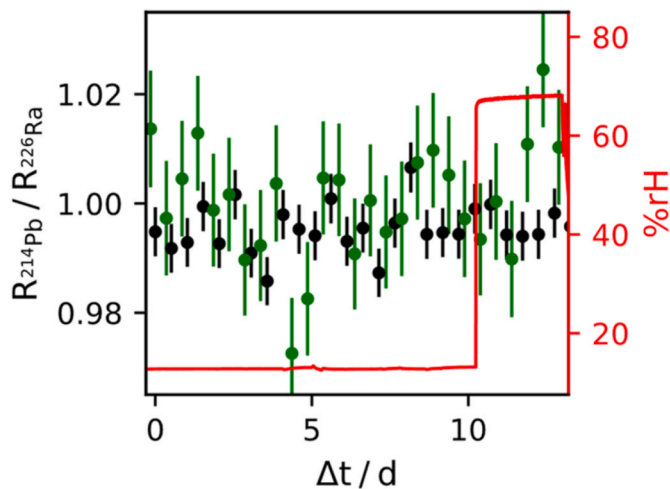


Fig. 9. Normalized count rate ratios of the 352 keV ^{214}Pb and 186 keV ^{226}Ra emission measured with a 1.5'' LaBr_3 (green) detector and a HPGe (black) detector at varying relative humidity from 15 %rH to 70 %rH (red). (For interpretation of the references to color in this figure legend, the reader is referred to the Web version of this article.)

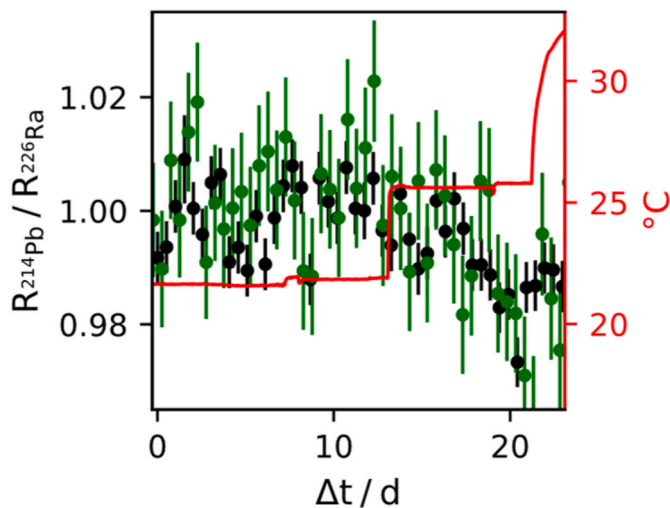


Fig. 10. Normalized count rate ratios of the 352 keV ^{214}Pb and 186 keV ^{226}Ra emission measured with a 1.5'' LaBr_3 (green) detector and a HPGe (black) detector at varying temperature (red). (For interpretation of the references to color in this figure legend, the reader is referred to the Web version of this article.)

because both detectors yielded comparable results, while a change of counting efficiency at different energies and gain drift is expected to have different effects on each detector.

2. Discussion and conclusions

Ion implantation of ^{226}Ra at high isobaric and isotopic purity was successfully carried out at the RISIKO laser mass separator of Mainz University to create high quality, radiometrically and chemically pure ^{222}Rn emanation sources. The comparison of α -particle spectrometry for the determination of the implantation efficiency exhibits overall good agreement with the ion current measurements, considering that an uncertainty of 10% was assumed for the ion current measurements due to sputtering effects in the detector system. This validates the ion current and implantation efficiency measurements of the mass separator facility to within this uncertainty and indicates the isotopic and isobaric purity

since the method applies only when all ions are indeed $^{226}\text{Ra}^+$. When comparing the ion current measurements, and keeping in mind that target 2018-1120 was implanted under unfavorable conditions during initial beamline optimizations, a slight target material dependency can be hypothesized. This might be related to the different sputtering yields and charge distributions of sputtered ions related to the different target materials. Due to the negative potential of the Faraday cup repeller electrode, secondary electron emission is suppressed and the probable loss of charge from escaping positively charged sputtered ions generally leads to underestimation of the implanted activity. However, the prolonged implantation results in the sputtering of already implanted ^{226}Ra , which distorts the ion current measurements in the opposite direction, especially in the case of the shallow implantation depth of the W targets.

Nonetheless, a good implantation efficiency on the order of 50% was achieved by employing a two-step laser ionization scheme on top of surface ionization in a hot tantalum cavity. The high quality of the resulting emanation sources is highlighted by the unusually high resolution in the obtained α -particle spectra.

Moreover, it was observed that emanation coefficients in the range of 0.23–0.34 are achievable using ion implantation at 30 keV depending on the target material, which is relatively close to our rough theoretical estimate of the recoil-loss probability for ^{222}Rn from the calculation of the projected transmission ranges through SRIM. In the case of tungsten targets the deviation from the predicted recoil emanation coefficient was found to be more pronounced than for aluminum, and it was found that this deviation increased with increasing amounts of implanted ^{226}Ra . This effect is clearly related to target material sputtering having a greater effect in the case of W target due to the shallow depth profile of implanted ^{226}Ra . The sole exception of this trend is target 2018-1128, in which experimental difficulties potentially caused by a vacuum breakdown changed the structure of the target, resulting in a clearly visible amorphization of the target, unlike the other targets. During the measurements in the climate chamber, the temperature dependence of the emanation was apparent. We hypothesize from this that there is indeed a non-negligible contribution of diffusing ^{222}Rn to the overall emanation and that the higher emanation in the case of tungsten targets might thus also be explained by different diffusion properties. While it is well known that the emanation of ^{222}Rn shows a strong humidity dependence for many materials, especially porous ones, (e.g., Janik et al., 2015; Stranden et al., 1984; Zhou et al., 2020), a correlation between humidity and emanation for implanted ^{226}Ra sources, remarkably, could not be identified in this study, which is in line with our prior assumptions.

To account for possible recoil losses of short-lived progeny, which might invalidate previously reported measurement techniques, a new absolute method to determine the emanation coefficient of such sources using α -particle spectrometry was developed. Exceptionally good agreement to the previously established γ -ray spectrometric methods was found, giving strong confidence to both techniques. For statistical reasons and lower sensitivity coefficients for systematic uncertainties, higher emanation coefficients and especially their variations are easier and more accurately measurable. This in turn means that conservative estimation of systematic uncertainties leads to potentially strongly overestimated uncertainties in the emanation coefficients, indicated by the excellent agreement between both methods for its determination, whereas observed deviations were below these conservative uncertainty estimates. Moreover, the agreement between the different methods underpins the findings of high stability of the emanation coefficient with respect to humidity, since the α -particle spectra are recorded in vacuum conditions.

For the determination of the implanted activity, the DSA α -particle spectrometry method yielded relative uncertainties down to 0.4%. The emanation coefficients were determined with combined relative uncertainty on the order of 1%, with potential for improvement by prolonged measurement times and more elaborate peak deconvolution in case of the α -particle spectrometric method. A method to simultaneously regress the ingrowth of the recoil ^{222}Rn peak and the observed time

series of α -particle spectra could potentially improve the estimation of systematic uncertainty. Unfortunately, that is beyond the scope of this study due to the vast computational complexity.

The produced emanation sources can be used to establish time-stable, SI-traceable ^{222}Rn reference atmospheres at a combined uncertainty below 2% with ^{222}Rn source terms between $340 \mu\text{Bq s}^{-1}$ and $820 \mu\text{Bq s}^{-1}$, even at variable humidity. A possible path for improvement, especially concerning the determination of emanation coefficients, is to change the implantation depth profile either by adjustment of the implantation energy or by mounting the target at an angle with respect to the ion beam, which is expected to increase the emanation coefficients and thus result in even higher accuracy of the presented measurement techniques.

Overall, the ion implantation process was found to be a very promising technique for the production of stable, low-level ^{222}Rn emanation standards of highest metrological quality. This was due to the high degree of control manifested in the achievable accuracy of characterization techniques, with clear paths for further improvement and without the need for standardized ^{226}Ra solutions.

Declaration of competing interest

The authors declare that they have no known competing financial interests or personal relationships that could have appeared to influence the work reported in this paper.

Acknowledgment

This project 19ENV01 traceRadon has received funding from the European Metrology Programme for Innovation and Research (EMPIR) programme co-financed by the Participating States and from the European Union's Horizon 2020 research and innovation programme. 19ENV01 traceRadon denotes the EMPIR project reference.

References

- Arinc, A., Parfitt, M.J., Keightley, J.D., Wilson, A., 2016. Defined solid angle alpha counting at NPL. *Appl. Radiat. Isot.* 109, 198–204. <https://doi.org/10.1016/j.apradiso.2015.11.073>.
- Bé, M.-M., Chisté, V., Dulieu, C., Browne, E., Chechev, V., Kuzmenko, N., Helmer, R., Nichols, A., Schönfeld, E., Dersch, R., 2004. Table of Radionuclides, Monographie BIPM-5. Bureau International des Poids et Mesures, Pavillon de Breteuil, F-92310 Sèvres, France.
- Berger, M.J., Hubbell, J.H., Seltzer, S.M., Chang, J., Coursey, J.S., Sukumar, R., Zucker, D.S., Olsen, K., 2019. XCOM: Photon Cross Section Database Version 1.5. National Institute of Standards and Technology, Gaithersburg, MD.
- Bortels, G., Collaers, P., 1987. Analytical function for fitting peaks in alpha-particle spectra from Si detectors. *Int. J. Radiat. Appl. Instrumentation Part 38*, 831–837. [https://doi.org/10.1016/0883-2889\(87\)90180-8](https://doi.org/10.1016/0883-2889(87)90180-8).
- Day Goodacre, T., Billowes, J., Binnersley, C.L., Bissell, M.L., Chrysalidis, K., Cocolios, T. E., de Groote, R.P., Farooq-Smith, G.J., Fedorov, D.V., Fedosseev, V.N., Flanagan, K. T., Franchoo, S., Garcia Ruiz, R.F., Gins, W., Heinke, R., Koszorús, Á., Lynch, K.M., Marsh, B.A., Molkanov, P.L., Naubereit, P., Neyens, G., Ricketts, C.M., Rothe, S., Seiffert, C., Seliverstov, M.D., Stroke, H.H., Studer, D., Vernon, A.R., Wilkins, S.G., Wendt, K.D.A., Yang, X.F., 2018. Radium ionization scheme development: the first observed autoionizing states and optical pumping effects in the hot cavity environment. *Spectrochim. Acta Part B At. Spectrosc.* 150, 99–104. <https://doi.org/10.1016/j.sab.2018.10.002>.
- Fedosseev, V., Chrysalidis, K., Goodacre, T.D., Marsh, B., Rothe, S., Seiffert, C., Wendt, K., 2017. Ion beam production and study of radioactive isotopes with the laser ion source at ISOLDE. *J. Phys. G Nucl. Part. Phys.* 44, 084006 <https://doi.org/10.1088/1361-6471/aa78e0>.
- Janik, M., Omori, Y., Yonehara, H., 2015. Influence of humidity on radon and thoron exhalation rates from building materials. *Appl. Radiat. Isot.* 95, 102–107. <https://doi.org/10.1016/j.apradiso.2014.10.007>.
- Joint Committee for Guides in Metrology, 2008. *Evaluation of Measurement Data — Supplement 1 to the JCGM*, vol. 101, p. 90.
- Jurado Vargas, M., de Soto, F.F., Sánchez, A.M., 1995. Energy resolution, yield and radon diffusion in the electrodeposition of radium. *Nucl. Instrum. Methods Phys. Res. A* 364, 349–353. [https://doi.org/10.1016/0168-9002\(95\)00393-2](https://doi.org/10.1016/0168-9002(95)00393-2).
- Jurado Vargas, M., Fernández De Soto, F., 1996. A study of ^{222}Rn emanation in electrodeposited sources of ^{226}Ra with barium. *Nucl. Instruments Methods Phys. Res. Sect. A Accel. Spectrometers, Detect. Assoc. Equip.* 368, 488–491. [https://doi.org/10.1016/0168-9002\(95\)00854-3](https://doi.org/10.1016/0168-9002(95)00854-3).
- Kieck, T., Biebricher, S., Düllmann, C.E., Wendt, K., 2019a. Optimization of a laser ion source for ^{163}Ho isotope separation. *Rev. Sci. Instrum.* 90, 053304 <https://doi.org/10.1063/1.5081094>.
- Kieck, T., Dorrer, H., Düllmann, C.E., Gadelshin, V., Schneider, F., Wendt, K., 2019b. Highly efficient isotope separation and ion implantation of ^{163}Ho for the ECHO project. *Nucl. Instruments Methods Phys. Res. Sect. A Accel. Spectrometers, Detect. Assoc. Equip.* 945, 162602 <https://doi.org/10.1016/j.nima.2019.162602>.
- Kramida, A., Ralachenko, Y., Reader, J., 2020. NIST atomic spectra database [WWW Document]. <https://doi.org/10.18434/T4W30F>.
- Lassen, J., Li, R., Raeder, S., Zhao, X., Dekker, T., Heggen, H., Kunz, P., Levy, C.D.P., Mostanmand, M., Teigelhöfer, A., Ames, F., 2017. Current developments with TRIUMF's titanium-sapphire laser based resonance ionization laser ion source. *Hyperfine Interact.* 238, 33. <https://doi.org/10.1007/s10751-017-1407-9>.
- Linzmaier, D., Röttger, A., 2013. Development of a low-level radon reference atmosphere. *Appl. Radiat. Isot.* 81, 208–211. <https://doi.org/10.1016/j.apradiso.2013.03.032>.
- Marouli, M., Pommé, S., Van Ammel, R., García-Toraño, E., Crespo, T., Pierre, S., 2017. Direct measurement of alpha emission probabilities in the decay of ^{226}Ra . *Appl. Radiat. Isot.* 125, 196–202. <https://doi.org/10.1016/j.apradiso.2017.04.029>.
- Mattolat, C., Rothe, S., Schwellnus, F., Gottwald, T., Raeder, S., Wendt, K., Iguchi, T., Watanabe, K., 2009. An all-solid-state high repetition rate titanium:sapphire laser system for resonance ionization laser ion sources. In: *AIP Conference Proceedings*. AIP, pp. 114–119. <https://doi.org/10.1063/1.3115586>.
- Mertes, F., Röttger, S., Röttger, A., 2020. A new primary emanation standard for Radon-222. *Appl. Radiat. Isot.* 156, 108928. <https://doi.org/10.1016/j.apradiso.2019.108928>.
- Philip Horwitz, E., Chiarizia, R., Dietz, M.L., 2007. A novel strontium-selective extraction chromatographic resin. *Solvent Extr. Ion Exch.* 10, 313–336. <https://doi.org/10.1080/07366299208918107>.
- Pommé, S., 2015. The uncertainty of counting at a defined solid angle. *Metrologia* 52, S73–S85. <https://doi.org/10.1088/0026-1394/52/3/S73>.
- Pommé, S., Caro Marroyo, B., 2015. Improved peak shape fitting in alpha spectra. *Appl. Radiat. Isot.* 96, 148–153. <https://doi.org/10.1016/j.apradiso.2014.11.023>.
- Raeder, S., Lassen, J., Heggen, H., Teigelhöfer, A., 2014. In-source spectroscopy on astatine and radium for resonant laser ionization. *Hyperfine Interact.* 227, 77–83. <https://doi.org/10.1007/s10751-014-1040-9>.
- Rothe, S., Marsh, B.A., Mattolat, C., Fedosseev, V.N., Wendt, K., 2011. A complementary laser system for ISOLDE RILIS. *J. Phys. Conf. Ser.* 312, 052020 <https://doi.org/10.1088/1742-6596/312/5/052020>.
- Sonnenschein, V., Moore, I.D., Pohjalainen, I., Reponen, M., Rothe, S., Wendt, K., 2015. Intracavity frequency doubling and difference frequency mixing for pulsed ns Ti:sapphire laser systems at on-line radioactive ion beam facilities. In: *Proceedings of the Conference on Advances in Radioactive Isotope Science (ARIS2014)*. Journal of the Physical Society of Japan. <https://doi.org/10.7566/JPSCP.6.030126>.
- Stranden, E., Kolstad, A.K., Lind, B., 1984. The influence of moisture and temperature on radon exhalation. *Radiat. Protect. Dosim.* 7, 55–58. <https://doi.org/10.1093/oxfordjournals.rpd.a082962>.
- Teigelhöfer, A., Bricault, P., Chachkova, O., Gillner, M., Lassen, J., Lavoie, J.P., Li, R., Meißner, J., Neu, W., Wendt, K.D.A., 2010. Grating tuned Ti:Sa laser for in-source spectroscopy of Rydberg and autoionizing states. *Hyperfine Interact.* 196, 161–168. <https://doi.org/10.1007/s10751-010-0171-x>.
- Wendt, K., Ahmad, S.A., Klempt, W., Neugart, R., Otten, E.W., Stroke, H.H., 1987. On the hyperfine structure and isotope shift of radium. *Z. Physik D Atoms, Mol. Clust.* 4, 227–241. <https://doi.org/10.1007/BF01436633>.
- Wojdyr, M., 2010. Fityk : a general-purpose peak fitting program. *J. Appl. Crystallogr.* 43, 1126–1128. <https://doi.org/10.1107/S0021889810030499>.
- Zhou, Q., Shubayr, N., Carmona, M., Standen, T.M., Kearfott, K.J., 2020. Experimental study of dependence on humidity and flow rate for a modified flowthrough radon source. *J. Radioanal. Nucl. Chem.* 324, 673–680. <https://doi.org/10.1007/s10967-020-07081-0>.
- Ziegler, J.F., Ziegler, M.D., Biersack, J.P., 2010. SRIM – the stopping and range of ions in matter (2010). *Nucl. Instrum. Methods Phys. Res. Sect. B Beam Interact. Mater. Atoms* 268, 1818–1823. <https://doi.org/10.1016/j.nimb.2010.02.091>.

Chapter 5

Publication III: Approximate sequential Bayesian inference to estimate ^{222}Rn emanation from ^{226}Ra sources from spectral time-series

Florian Mertes, Stefan Röttger, Annette Röttger

in

Journal of Sensors and Sensor Systems, 12, 2023

DOI: 10.5194/jsss-12-147-2023

Received 23 September 2021

Received in revised form 27 December 2022

Accepted 9 March 2023

Author contributions

Conceptualization, funding acquisition, supervision, draft review: S.R., A.R.

Methodology, model design: **F.M.**

Data acquisition, formal analysis, software implementation, original draft preparation: **F.M.**

J. Sens. Sens. Syst., 12, 147–161, 2023
<https://doi.org/10.5194/jsss-12-147-2023>
© Author(s) 2023. This work is distributed under the Creative Commons Attribution 4.0 License.



Approximate sequential Bayesian filtering to estimate ^{222}Rn emanation from ^{226}Ra sources using spectral time series

Florian Mertes, Stefan Röttger, and Annette Röttger

Division 6 – Ionizing Radiation, Physikalisch-Technische Bundesanstalt,
38116 Braunschweig, Germany

Correspondence: Florian Mertes (florian.mertes@ptb.de)

Received: 23 September 2021 – Revised: 27 December 2022 – Accepted: 9 March 2023 – Published: 25 April 2023

Abstract. A new approach to assess the emanation of ^{222}Rn from ^{226}Ra sources based on γ -ray spectrometric measurements is presented. While previous methods have resorted to steady-state treatment of the system, the method presented incorporates well-known radioactive decay kinetics into the inference procedure through the formulation of a theoretically motivated system model. The validity of the ^{222}Rn emanation estimate is thereby extended to regimes of changing source behavior, potentially enabling the development of source surveillance systems in the future. The inference algorithms are based on approximate recursive Bayesian estimation in a switching linear dynamical system, allowing regimes of changing emanation to be identified from the spectral time series while providing reasonable filtering and smoothing performance in steady-state regimes. The derived method is applied to an empirical γ -ray spectrometric time series obtained over 85 d and is able to provide a time series of emanation estimates consistent with the physics of the emanation process.

1 Introduction

^{222}Rn is an odorless, colorless, radioactive noble gas, occurring naturally in the environment as part of the primordial ^{238}U decay chain. Due to its high mobility in the environment, radon can accumulate inside buildings where, in conjunction with its decay products (short-lived progeny; SLP), it is responsible for the most significant natural exposure of the general public to ionizing radiation, which is an important consideration for incidents of lung cancer (Darby et al., 2005). In the 2013/59/EURATOM treaty, 300 Bq m^{-3} was stipulated as the action level for indoor ^{222}Rn activity concentrations, beyond which mitigation is required. On the other hand, however, measurements of outdoor ^{222}Rn activity concentration at environmental levels have numerous beneficial applications in environmental sciences, including (but not limited to): as a tracer of terrestrial influence on air masses (Chambers et al., 2016, 2018); as a tool for classifying the atmospheric mixing state (e.g., Perrino et al., 2001; Williams et al., 2013, 2016; Chambers et al., 2019b, a); and as a tool for estimating integrated local- to regional-scale

emissions of trace gases with similarly distributed sources, such as CH_4 , N_2O , or CO_2 (Levin, 1987; Biraud et al., 2002; Laan et al., 2010; Levin et al., 2021). For these reasons, there is an interdisciplinary need for SI-traceable calibration procedures at low activity concentrations for atmospheric radon monitors, and the associated realization and dissemination of the unit Bq m^{-3} , which can only be feasibly realized through emanation sources rather than gaseous standards (Mertes et al., 2020; Linzmaier and Röttger, 2013; Röttger et al., 2014). In these prior studies, a method was presented that enabled γ -ray spectrometric data from an open ^{226}Ra source (i.e. emitting ^{222}Rn) to be used to estimate the resulting activity concentration of ^{222}Rn in a closed volume, by measuring the activity of residual SLP in the source to quantify the ^{222}Rn emanation. In recent years, there has been a trend towards the use of dynamic calibration conditions for ^{222}Rn (e.g., Fialova et al., 2020), eliminating the need for the long build-up period associated with static conditions. However, it has been demonstrated that emanation from most materials demonstrates a strong dependence on humidity and temperature as a result of changes in diffusion properties (Janik et al., 2015;

Stranden et al., 1984; Zhou et al., 2020), which generally results in a correlation between emanation and environmental parameters. In these cases, previously established methods to determine the amount of emanating ^{222}Rn fail over a considerable time span, since the dynamical processes taking place in the source are not accounted for. Hence, experimental investigations of source behavior under different environmental conditions are hardly possible using established methods. Yet, this capability is particularly important for the realization of in situ field calibrations of large volume atmospheric ^{222}Rn monitors, since dynamic methods would simplify the technical aspects of in situ field calibrations considerably. Said limitations are pointed out and discussed in the theoretical section of this work and have not been stated nor addressed elsewhere. A possible way to correct for such environmental influences, however, lies in determining the amount of emanating ^{222}Rn in near real time. We present herein that this can be achieved through continuous measurement of spectrometric time series of the ^{222}Rn emanation sources and a suitable method for data analysis that addresses the dynamic behavior of the system. The main contributions of the present work are the discussion of the limitations of established methods and the derivation and implementation of an alternative method, based on the well established computational techniques of recursive Bayesian estimation. First results obtained by application of the proposed method to experimental data are presented, which illustrate the theoretically motivated limitations and which can be well explained on the basis of the physical processes taking place in the emanation source, justifying the correctness and superiority of the presented method.

2 Theory and derivations

2.1 Radioactive decay kinetics

Radioactive decay chain kinetics are described by a linear time invariant (LTI) system of ordinary differential equations. Historically, this has been expressed in terms of the Bateman equations (Bateman, 1910), but recently this has been more conveniently written in matrix form (Pressyanov, 2002; Levy, 2019; Amaku et al., 2010). Undistorted radioactive decay kinetics of a decay chain of n nuclides without, or with only negligible, branching, as in the case of the ^{226}Ra decay chain, can thus be written concisely as Eq. (1). The fundamental matrix \mathbf{K} can be constructed such that it consists of the respective decay constants λ_i on its diagonal and generally on its first superdiagonal, while all other entries are 0. \mathbf{A} denotes a vector consisting of the activities of the respective nuclides in the decay chain. Equation (1) can readily be discretized using the matrix exponential of \mathbf{K} , which is in a form that can be conveniently computed by diagonalization of \mathbf{K} , e.g., through its (symbolically accessible) Jordan

canonical form or its Eigen decomposition.

$$\begin{aligned} d\mathbf{A} &= d \begin{bmatrix} A_0 \\ A_1 \\ \dots \\ A_n \end{bmatrix} \\ &= \begin{bmatrix} -\lambda_0 & \lambda_0 & 0 & \vdots \\ 0 & -\lambda_1 & \lambda_1 & \vdots \\ \dots & \dots & \dots & \vdots \\ 0 & 0 & 0 & -\lambda_n \end{bmatrix} \begin{bmatrix} A_0 \\ A_1 \\ \dots \\ A_n \end{bmatrix} dt \\ &= \mathbf{K}\mathbf{A}dt \end{aligned} \quad (1)$$

2.2 ^{222}Rn emanation

The release of ^{222}Rn from a ^{226}Ra source distorts the dynamics described above, due to the introduction of an additional sink-term η (^{222}Rn atoms released per unit time), which is not directly quantifiable experimentally. Previously, a method was presented to measure a steady-state emanation coefficient, previously understood to be the ratio of exhaled and generated ^{222}Rn atoms (Mertes et al., 2020; Linzmaier and Röttger, 2013) at any instant in time.

$$\chi = \frac{\eta}{A_{\text{Ra-226}}^{\text{S}}}, \quad (2)$$

where χ is the emanation coefficient, η is the release of ^{222}Rn atoms per unit time, and $A_{\text{Ra-226}}^{\text{S}}$ is the ^{226}Ra activity of the source.

By first principles, however, the ^{222}Rn activity $A_{\text{Rn-222}}^{\text{S}}$ must follow first-order continuity as in Eq. (3).

$$dA_{\text{Rn-222}}^{\text{S}} = -\lambda_{\text{Rn-222}}A_{\text{Rn-222}}^{\text{S}}dt + \lambda_{\text{Ra-226}}A_{\text{Ra-226}}^{\text{S}}dt - \lambda_{\text{Rn-222}}\eta dt, \quad (3)$$

where $A_{\text{Rn-222}}^{\text{S}}$ and $A_{\text{Ra-226}}^{\text{S}}$ are the activities of the respective nuclides in the source material.

To this point, the best method to derive χ has been by measuring the ratio of SLP and ^{226}Ra activities within the source, most commonly by γ -ray spectrometry, where χ is defined as

$$\chi = 1 - \frac{A_{\text{Rn-222}}^{\text{S}}}{A_{\text{Ra-226}}^{\text{S}}} = 1 - \frac{A_{\text{Pb-214}}^{\text{S}}}{A_{\text{Ra-226}}^{\text{S}}}. \quad (4)$$

According to Eqs. (2) and (3) however, this is only applicable under steady-state conditions. This limitation was not acknowledged or discussed in earlier work. Consequently, application of this simple method is restricted either to regimes of a completely stabilized source, or a closed accumulation volume for the emitted ^{222}Rn . In closed volumes, the errors associated with neglecting the dynamics in the source are negligible, since the volumetric ^{222}Rn follows the same

dynamics. As such, after initial equilibration, Eq. (4) holds, even with changing χ . However, in this case χ is more accurately understood to be a partitioning coefficient of ^{222}Rn between the source and the closed volume, rather than the definition given in Eq. (2). The result of Eq. (3) is that the measurable $A_{\text{Rn-222}}^{\text{S}}(t)$ is given by the convolution of the latent $\eta(t)$ with an impulse response function that is defined by the radioactive decay kinetics. Thus, the estimation of $\eta(t)$, or equivalently $\chi(t)$, based on measurements of $A_{\text{Rn-222}}^{\text{S}}(t)$ is an inverse problem and cannot be carried out feasibly by simple numerical estimation of the gradient (cf. Eq. 3) due to the ubiquitous Poisson noise associated with radioactivity measurements. Moreover, in dynamic calibrations, $\eta(t)$ must be expected to vary with changes in the environmental conditions. It is also expected that this dependency will be strongly related to the source design and its specific production parameters. A further consideration is that, when using this method, it is not readily possible to accurately measure correlations of $\chi(t)$ with environmental conditions on timescales smaller than at least five half-lives of ^{222}Rn without considering the decay kinetics. These limitations make it infeasible to use the existing direct approach to continuously estimate ^{222}Rn release as required in dynamic calibration procedures, or to derive correction factors for different environmental conditions, since the time required would be far too long for such measurements due to the half-life of ^{222}Rn of approximately 3.8 d. Here we present and discuss a new approach that embraces the described behavior and enables the release of ^{222}Rn from sources to be estimated more accurately using continuous spectrometric measurements with the generalization to non-steady-state situations. The algorithms and assumptions presented have been chosen such that, in the future, the necessary computations would be feasible on relatively low-power devices (e.g., current single-board computers) in an online fashion.

2.3 Recursive Bayesian estimation and model formulation

Recursive Bayesian estimation describes a class of algorithms to perform statistical inference in dynamical systems that can be modeled by a (first-order) Markov process. The general idea of these methods is to sequentially form priors for a state vector \mathbf{x} and a dynamical model of the system, and use noisy measurements \mathbf{y} related to \mathbf{x} to correct them through a measurement model and Bayes theorem (Särkkä, 2013). This method can be used to perform statistical inversion, in that it enables the estimation of latent terms whose values in a specific dynamical system are only partly measured. This is closely related to the case described in the previous section, given that the state vector, the dynamics, and the measurements can all be suitably modeled. In this setting, two collections of conditional probability distributions are of interest, which are commonly called the filtering distributions $p(\mathbf{x}_n | \mathbf{y}_{1:n})$ and the smoothing distributions

$p(\mathbf{x}_n | \mathbf{y}_{1:N})$, where the notations $1:n$ and $1:N$ denote the collection of all data observed up to time t_n and the collection of all data, respectively, and t specifies an instant in time in the set of measurement times, T , indexed by n . In cases where \mathbf{x} follows a first-order Markov process, and under certain conditional independence assumptions, the definition of $p(\mathbf{x}_n | \mathbf{y}_{1:n})$ and $p(\mathbf{x}_n | \mathbf{y}_{1:N})$ can be expressed recursively (Särkkä, 2013; Särkkä and Solin, 2019). Prediction of the state vector \mathbf{x}_n at time t_n given a collection of measurements $\mathbf{y}_{1:n-1}$ up to time t_{n-1} and the filtering density of the state at time t_{n-1} , $p(\mathbf{x}_{n-1} | \mathbf{y}_{1:n-1})$ is given by the Chapman–Kolmogorov Eq. (5) (Särkkä and Solin, 2019).

$$p(\mathbf{x}_n | \mathbf{y}_{1:n-1}) = \int p(\mathbf{x}_n | \mathbf{x}_{n-1}) p(\mathbf{x}_{n-1} | \mathbf{y}_{1:n-1}) d\mathbf{x}_{n-1} \quad (5)$$

Upon observation of \mathbf{y}_n , the density predicted by Eq. (5) is corrected into a filtered posterior using Bayes theorem with the measurement likelihood $p(\mathbf{y}_n | \mathbf{x}_n)$, assumed to be conditionally independent of the past states and measurements, i.e. $p(\mathbf{y}_n | \mathbf{x}_{1:n}, \mathbf{y}_{1:n-1}) = p(\mathbf{y}_n | \mathbf{x}_n)$ (Särkkä, 2013).

Conversely, smoothing refers to computing the density of the state given all measurements in a specific time interval, or the complete collection. In most cases, smoothing can be defined recursively using information inferred from the filtering and starting a backward recursion at the last time instant at which the smoothing and filtering densities are equal. Formally, the smoothing density is recursively defined by Eq. (6) for the above conditional independence assumptions.

$$p(\mathbf{x}_n | \mathbf{y}_{1:N}) = p(\mathbf{x}_n | \mathbf{y}_{1:n}) \int \frac{p(\mathbf{x}_{n+1} | \mathbf{x}_n)}{p(\mathbf{x}_{n+1} | \mathbf{y}_{1:n})} p(\mathbf{x}_{n+1} | \mathbf{y}_{1:N}) d\mathbf{x}_{n+1} \quad (6)$$

The most notable examples of these types of algorithms are the Kalman filter (Kalman, 1960) and the Rauch–Tung–Striebel smoother (Rauch et al., 1965), which yield the optimal estimators for discrete systems of linear dynamics and independent Gaussian noise, where the filtering and smoothing can be carried out in $O(T)$ time.

For the problem at hand, a stochastic differential equation (SDE) is needed to express the (time-varying) uncertainty associated with the latent continuous variable $\eta(t)$. This can be seen as an application of the latent-force models introduced in Alvarez et al. (2009), whose link with Bayesian filtering was previously established in Särkkä et al. (2019) and Hartikainen and Särkkä (2012). The specific choice of SDE is subjective but allows the properties of the resultant functions to be constrained, and can be used to encode prior knowledge (Särkkä and Solin, 2019). In this work, without any claims of optimality, the choice was made to use the zero-mean, mean-reverting Ornstein–Uhlenbeck process for the first derivative of η , i.e., Eq. (7), resulting in constraining η to somewhat smooth functions of certain autocorrelation.

$$\frac{d^2\eta}{dt^2} = -\gamma \frac{d\eta}{dt} + \sigma d\beta_t, \quad (7)$$

where $d\beta_t$ describes the increments of a scalar standard Brownian motion.

While this choice is not entirely representative of the physical mechanisms related to η , in that, for example, it allows for negative values of η , it results in a Gaussian process for which the inference procedure has convenient conjugacy and thus a closed-form solution, such that the resultant algorithms are suitable for online operation on low-power computational hardware that can be reasonably used to monitor an emanation source during its operation. It should also be noted that Eq. (2) was formulated with this in mind, in the sense that η is modeled as state-independent, rather than state-dependent, as would likely be more realistic for a diffusive process like ^{222}Rn emanation. However, these theoretical inaccuracies did not manifest in practice with the experimental data presented in Sect. 3, given that η is far enough from 0 and the collected data are strong enough, while only approximate inference is of interest. The system is thus modeled to follow the combined SDE given in Eqs. (8)–(11) in terms of the Itô stochastic integral (Särkkä and Solin, 2019; Hartikainen and Särkkä, 2012).

$$dx = \mathbf{K}xdt + \mathbf{L}d\beta_t \quad (8)$$

$$x = \begin{bmatrix} A_{\text{Rn-222}}^{\text{S}} \\ A_{\text{Ra-226}}^{\text{S}} \\ \eta \\ \frac{d\eta}{dt} \end{bmatrix}; \quad \mathbf{K} = \begin{bmatrix} -\lambda_{\text{Rn-222}} & \lambda_{\text{Rn-222}} & -\lambda_{\text{Rn-222}} & 0 \\ 0 & -\lambda_{\text{Ra-226}} & 0 & 0 \\ 0 & 0 & 0 & 1 \\ 0 & 0 & 0 & -\gamma \end{bmatrix}; \quad \mathbf{L} = \begin{bmatrix} 0 \\ 0 \\ 0 \\ \sigma \end{bmatrix} \quad (9)$$

$$x_t = e^{\mathbf{K}(t-t_0)}x_0 + \int_{t_0}^t e^{\mathbf{K}(t-\tau)}\mathbf{L}d\beta_\tau \quad (10)$$

$$p(x_n|x_{n-1}) \propto \mathcal{N}\left(e^{\mathbf{K}(t_n-t_{n-1})}x_{n-1}, \int_{t_{n-1}}^{t_n} e^{\mathbf{K}(t_n-\tau)}\mathbf{L}\mathbf{L}^T e^{\mathbf{K}^T(t_n-\tau)}d\tau\right) \quad (11)$$

2.4 Measurement model for integrating spectrometric data

Unlike most applications of such filtering algorithms for discretized LTI systems, here the supporting measurements cannot be made at instantaneous moments in time because disintegrations of a specific nuclide can only be recorded over a finite time interval, r_n , indexed by n . In routine radioactivity analysis, this behavior results in decay or ingrowth during measurement corrections. However, in the present case, an additional contribution to the uncertainty results from unknown changes of η over the integration time.

The way we have chosen to model this behavior in the present study is to start by stating that the uncorrupted (i.e., noise-free) measurements are given by Eq. (12), where, for

now, we assume that \mathbf{H} is known deterministically.

$$y(t, r) = \mathbf{H} \int_0^r x(t + \tau) d\tau, \quad (12)$$

where \mathbf{H} is a matrix that maps the state integral to the measurement space.

The elements of \mathbf{H} are related to the counting efficiency of the setup and/or nuclide. Note that, in principle, it would be possible to choose \mathbf{H} to directly model some region of the spectrum, but we chose to use derived peak areas or even spectrum integrals as the input data such that the elements of \mathbf{H} are just the counting efficiencies. More elaborate modeling in the spectrum space was not attempted, since the filtering algorithms generally require inversion of the residual covariance matrix in the measurement space, and thus scale approximately with $O(k^3)$ where k is the dimensionality of the measurements.

Since integration is a linear operator, the joint distribution of x_{n-1} , x_n , and y_n clearly has a Gaussian density, and hence $p(x_n, y_n | y_{1:n-1})$ is readily found by marginalizing over x_{n-1} , given that the previous time step posterior filtering distribution $p(x_{n-1} | y_{1:n-1})$ is already known (and Gaussian). This joint density is derived in Appendix A1. It is assumed that the measurement y_n is related to the state x_n by integrating from $t_{n-1} + \delta_n$ to $t_n = t_{n-1} + \delta_n + r_n$, such that arbitrary integration intervals r_n and arbitrary time offsets δ_n are possible (e.g., if measurements are skipped or delayed). In other words, each time instant where the density of x is inferred coincides with the endpoint of each spectrum acquisition. This approach intrinsically accounts for the ingrowth and decay during the finite integration time, but more importantly, additionally estimates the uncertainty arising from the possible change of η within the integration time. Given that $p(x_n, y_n | y_{1:n-1})$ under the present model is thus accessible, the posterior filtering distribution $p(x_n | y_{1:n})$ is found by conditioning onto the observed value for y_n using the well-known conditioning formula for multivariate Gaussians.

Radioactivity measurements generally follow Poisson statistics. In the framework of Bayesian inference and recursive Bayesian estimation, non-Gaussian noise considerably complicates the inference procedure, since the measurements are then no longer a Gaussian process and thus no longer conjugate with the state. For this reason, there is no exact closed-form solution for the filtering recursions in the case of non-Gaussian noise. Considerable work has been done to address this, including sampling procedures like Markov chain Monte Carlo, particle filtering, or expectation propagation (Minka, 2013), or by assuming that all arising probability density functions (PDFs) are Gaussian combined with an estimation strategy for the moments (e.g., unscented Kalman filter; Julier et al., 2000). Generally, we found such approaches unsuitable due to their computational complexity but also because the measurements can be well approximated as Gaussian (due to the high number of counts that are being

observed). Instead, we approximate the measurement likelihood as Gaussian where the moments are evaluated from the previous time step filtering distribution of \mathbf{x} . Ebeigbe et al. (2020) proposed that the covariance matrix could be estimated from the mean of the filtered state in a different context, which we adopted. Combining this with the results of Appendix A1, we obtain Eq. (13) as an approximation of the joint density $p(\mathbf{x}_n, \mathbf{y}_n | \mathbf{y}_{1:n-1})$.

$$p(\mathbf{x}_n, \mathbf{y}_n | \mathbf{y}_{1:n-1}) \propto \mathcal{N} \left(\begin{bmatrix} \mathbf{F}_r \mathbf{F}_\delta \boldsymbol{\mu}_{n-1} \\ \mathbf{H} \mathbf{M} \mathbf{F}_\delta \boldsymbol{\mu}_{n-1} \end{bmatrix}, \begin{bmatrix} \boldsymbol{\Sigma}^{\mathbf{x}\mathbf{x}} & \boldsymbol{\Sigma}^{\mathbf{x}\mathbf{y}} \\ \boldsymbol{\Sigma}^{\mathbf{x}\mathbf{y}\mathbf{T}} & \boldsymbol{\Sigma}^{\mathbf{y}\mathbf{y}} \end{bmatrix} \right), \quad (13)$$

where

$$\boldsymbol{\Sigma}^{\mathbf{x}\mathbf{x}} = \mathbf{F}_r \left(\mathbf{F}_\delta \boldsymbol{\Sigma}_{n-1} \mathbf{F}_\delta^{\mathbf{T}} + \mathbf{U}_\delta \right) \mathbf{F}_r^{\mathbf{T}} + \mathbf{U}_r,$$

$$\boldsymbol{\Sigma}^{\mathbf{x}\mathbf{y}} = \mathbf{F}_r \left(\mathbf{F}_\delta \boldsymbol{\Sigma}_{n-1} \mathbf{F}_\delta^{\mathbf{T}} + \mathbf{U}_\delta \right) \mathbf{M}^{\mathbf{T}} \mathbf{H}^{\mathbf{T}} + \mathbf{C} \mathbf{H}^{\mathbf{T}},$$

$$\boldsymbol{\Sigma}^{\mathbf{y}\mathbf{y}} = \mathbf{H} \mathbf{M} \left(\mathbf{F}_\delta \boldsymbol{\Sigma}_{n-1} \mathbf{F}_\delta^{\mathbf{T}} + \mathbf{U}_\delta \right) \mathbf{M}^{\mathbf{T}} \mathbf{H}^{\mathbf{T}} + \mathbf{H} \mathbf{B} \mathbf{H}^{\mathbf{T}} + \mathbf{O} + \mathbf{R}$$

and where the index n has been dropped on r and δ for notational brevity and the included matrices are given as follows: \mathbf{R} is a variance term that accounts for the variance contribution of the background count rate, which is estimated from prior background measurements and is assumed constant over time, and $\boldsymbol{\mu}_{n-1}$ and $\boldsymbol{\Sigma}_{n-1}$ denote the mean and covariance matrix of the filtering distribution at the previous time step.

$$\begin{aligned} \mathbf{F}_a &= e^{\mathbf{K}a} & \mathbf{U}_a &= \int_0^a e^{\mathbf{K}(a-\tau)} \mathbf{L} \mathbf{L}^{\mathbf{T}} e^{\mathbf{K}^{\mathbf{T}}(a-\tau)} d\tau \\ \mathbf{M}_r &= \int_0^r e^{\mathbf{K}\tau} d\tau & \mathbf{C}_r &= \int_0^r \int_\tau^r e^{\mathbf{K}(r-\tau)} \mathbf{L} \mathbf{L}^{\mathbf{T}} e^{\mathbf{K}^{\mathbf{T}}(a-\tau)} da d\tau \\ \mathbf{B}_r &= \int_0^r \int_\tau^r \int_\tau^r e^{\mathbf{K}(a-\tau)} \mathbf{L} \mathbf{L}^{\mathbf{T}} e^{\mathbf{K}^{\mathbf{T}}(b-\tau)} da db d\tau \\ \mathbf{O} &= \text{diag}(\min(1, \mathbf{H} \mathbf{M} \mathbf{F}_\delta \boldsymbol{\mu}_{n-1})) \end{aligned}$$

2.5 Extension for strong variations in emanation characteristics or discontinuities

The variance σ of the Brownian motion process in Eq. (7) allows a linear dynamical model as shown in Sect. 2.3 and 2.4 to be tuned in a trade-off-like fashion for one of two properties. Predictions are good in times of relatively constant η and low σ , such that the measurement noise is well filtered at the expense of fidelity in response to steep changes in η , or vice versa. In practical situations however, where the humidity can change rapidly and is known to affect the emanation, a period of re-equilibration is induced in the source, before it returns to somewhat stable behavior. Therefore, experimental time series of the radon source spectra typically show properties that are not well addressed by a single such model of

linear dynamics due to the described distinct regimes. This kind of situation is strongly related to the tracking of maneuvering targets, a field in which Bayesian recursive estimation is well established. To obtain good filtering performance in the sense of providing relatively smooth estimates with small uncertainty in case of constant η while retaining the ability to quickly react to steep gradients with associated larger estimation uncertainty, one approach suggested by Nadarajah et al. (2012) and Mazar et al. (1998), among others, is to use the interacting multiple model (IMM) recursive estimator. This is commonly used for object tracking and in this work was adopted to refine the procedure outlined in the previous sections. In the IMM, multiple filters operate on the data at the same time, and their output is mixed based on the likelihood of their measurement predictions. In this way a second, discrete, first-order Markov process describing a discrete random variable s_n that indexes into the several applicable and differently parameterized linear dynamical models is formally introduced and evolves according to some, potentially parameterized, transition matrix $\boldsymbol{\Pi}$. As a result, the filtering and smoothing distributions become the compound distributions $p(s_n, \mathbf{x}_n | \mathbf{y}_{1:n})$ and $p(s_n, \mathbf{x}_n | \mathbf{y}_{1:N})$, respectively, which now also carry probabilistic information regarding the active model index s_n .

These compound distributions can be decomposed into discrete and continuous components which are approximately represented as mixtures of Gaussians. This kind of system is also called a switching linear dynamical system (SLDS). In the SLDS, exact filtering is not computationally feasible (Barber, 2006; Hartikainen and Särkkä, 2012), since the filtering distribution is a mixture of Gaussians whose components are being multiplied by the number of models at each time step resulting in the exponential growth of components. Most approaches for approximation, like the one employed here, replace the resultant mixture at each step of filtering and smoothing with a smaller one, limiting the number of kept components in the Gaussian mixtures to some fixed upper value I . In case of filtering, these types of algorithms are referred to as Gaussian sum filtering (GSF). Figure 1 gives an outline, both in terms of a component-wise (i.e., marginalized only over the mixture component indices i_n) and a marginal view (i.e., marginalized over both the model indices s_n and the component indices i_n) of the applied GSF method for the final SLDS model for the example of two Gaussian components per mixture. The basis of the prediction and correction steps for each combination of active model and prior components, jointly indexed by s_n, s_{n-1} , and i_{n-1} , is detailed in Sect. 2.3 and 2.4. By the discretizations carried out in Sect. 2.3 and 2.4, it is thus implicitly assumed that the active model index can only switch after the observation of each spectrum but not during the integration time of each spectrum. The probabilities $p(s_n | \mathbf{y}_{1:n})$ are also estimated by the algorithm by evaluation of the likelihood of measuring \mathbf{y}_n in each component of the prediction step density and marginalization over \mathbf{x}_n and associated i_n , re-

spectively. For further details on the GSF method, the reader is directed to Barber (2006). The results of the GSF algorithm are the (unsummed) factors on the right hand side of the following approximation of the decomposed filtering distribution, which consist of said Gaussian mixtures:

$$p(\mathbf{x}_n | \mathbf{y}_{1:n}) \approx \sum_{s_n} p(s_n | \mathbf{y}_{1:n}) \sum_{i_n} w_{s_n, i_n} p(\mathbf{x}_n | s_n, i_n, \mathbf{y}_{1:n}), \quad (14)$$

where s_n is the model index at time step t_n , i_n is the component index of the approximating Gaussian mixtures, and w_{s_n, i_n} are the associated Gaussian mixture weights.

In this setting, the smoothing distribution is also a compound distribution in which the components of each mixture are multiplied within each smoothing step in a backwards recursive formulation by the number of linear dynamical models. Therefore, smoothing is also only possible approximately, once again, on the basis of approximating each arising Gaussian mixture with a smaller one. One way to approximately obtain smoothed results in the SLDS setting is thus given by the expectation correction (EC) algorithm introduced in Barber (2006) and shown therein to provide state-of-the-art results, both in terms of computational efficiency and accuracy, using the results of the GSF forward pass and performing a backwards recursion through the time series. The EC algorithm requires, analogous to the GSF forward pass, the propagation and correction methods, in the form of the filtering and smoothing steps, for the parameterized linear dynamical system outlined in Sect. 2.3 and 2.4 acting on each Gaussian mixture component. In this case, however, the integrating behavior of the measurements does not lead to any required adjustments, and the applied equations are thus exactly analogous to the classical Rauch–Tung–Striebel smoother that represent a formal reversal of the dynamics. These have also been used in the original presentation of the EC algorithm (Algorithm 5 in Barber, 2006). Figure 2 provides a graphical illustration similar to the filtering method in Fig. 1 of the EC smoothing backward pass. The EC algorithm provided in Barber (2006) was used without further modifications, and for more information on this algorithm, the reader is directed to this work.

While not a main contribution to this paper, for completeness sake and to facilitate possible re-implementation, both the GSF forward pass and the EC backward pass are outlined in pseudo-code in Appendix A2 in the way they have been implemented here.

To model the two distinct regimes outlined before, two linear dynamical models are used that share their γ values, but for one (cf. Eq. 8), σ is constrained to a small value. Consequently, one of the models corresponds to regimes of changing η and the other to near constant η . This approach allows us via the model index probabilities $p(s_n | \mathbf{y}_{1:n})$ and $p(s_n | \mathbf{y}_{1:N})$ obtained from the GSF and the EC algorithms to also probabilistically identify regimes of constant radon emanation within a time series of recorded spectra, even when the retained activity of ^{222}Rn is still in a re-equilibration period, as will be illustrated in the experimental results pre-

sented later. In that sense, and by construction of the two models, the model index probabilities can be physically interpreted as the probability of the source to currently have stable emanation characteristics. A non-zero σ acting as a regularization term is, however, still needed in the case of the model corresponding to the constant regimes because otherwise the approximations used within both the GSF and the EC algorithm become numerically unstable. The final model contains four unknown parameters, σ , γ , and the components of $\mathbf{\Pi}$, which is row-wise normalized and whose components are thus parameterized by two parameters. These four parameters are tuned by minimizing the (approximate) negative marginal log likelihood of the measurement series, $-\sum_n \ln p(\mathbf{y}_n | \mathbf{y}_{1:n-1}, \sigma, \gamma, \mathbf{\Pi})$, that is accessible in the GSF forward pass (see Algorithm 1 in Appendix A2). For the purposes of this initial investigation, we assume the uncertainty arising from uncertain parameters is negligible in light of the counting statistics, the uncertainty encoded in the prior of the initial state, $p(\mathbf{x}_0)$, and the components of \mathbf{H} .

2.6 Propagation of the detection efficiency uncertainty

In practice, the components of \mathbf{H} are not known without uncertainty, and the uncertainty associated with \mathbf{H} is the most significant contribution to the combined uncertainty of η in most practical cases. The outlined formalism above is a way to obtain estimates for $p(\mathbf{x}_n | \mathbf{y}_{1:n}, \mathbf{H})$ and $p(\mathbf{x}_n | \mathbf{y}_{1:N}, \mathbf{H})$ or the extended compound distributions $p(s_n, \mathbf{x}_n | \mathbf{y}_{1:n}, \mathbf{H})$ and $p(s_n, \mathbf{x}_n | \mathbf{y}_{1:N}, \mathbf{H})$ detailed in the previous section, respectively. For notational simplicity, the following is formulated with respect to the single-model case but applies analogously to the SLDS model. Formally, the inclusion of this systematic measurement uncertainty into the filtering or smoothing result, respectively, is given by Eq. (15), which is not tractable.

$$p(\mathbf{x}_n | \mathbf{y}_{1:n}) = \int_{\mathbf{H}} p(\mathbf{x}_n | \mathbf{y}_{1:n}, \mathbf{H}) p(\mathbf{H} | \mathbf{y}_{1:n}) d\mathbf{H} \quad (15)$$

In the present case, we assume \mathbf{H} to be constant with respect to time and that its distribution is known from previous measurements, independent of the collection $\mathbf{y}_{1:N}$. Generally, the uncertainty in \mathbf{H} associated with, for example, a prior calibration procedure, can reasonably be described by this approximation, if $\frac{d\mathbf{H}}{dt} = 0$. This allows rewriting Eq. (15) to obtain Eq. (16); however, the result remains computationally infeasible, since it would require an infinite amount of filtering and smoothing passes.

$$p(\mathbf{x}_n | \mathbf{y}_{1:n}) = \int_{\mathbf{H}} p(\mathbf{x}_n | \mathbf{y}_{1:n}, \mathbf{H}) p(\mathbf{H}) d\mathbf{H} \quad (16)$$

Thus, in the setting at hand, $p(\mathbf{x}_n | \mathbf{y}_{1:n})$, the result of Eq. (16) is given as an infinite mixture of Gaussian mixtures with weights proportional to $p(\mathbf{H})$. Our strategy of choice to approximately include the systematic uncertainty associated with \mathbf{H} is to replace the infinite mixture by a finite version, i.e., to compute the filtering and smoothing densities for

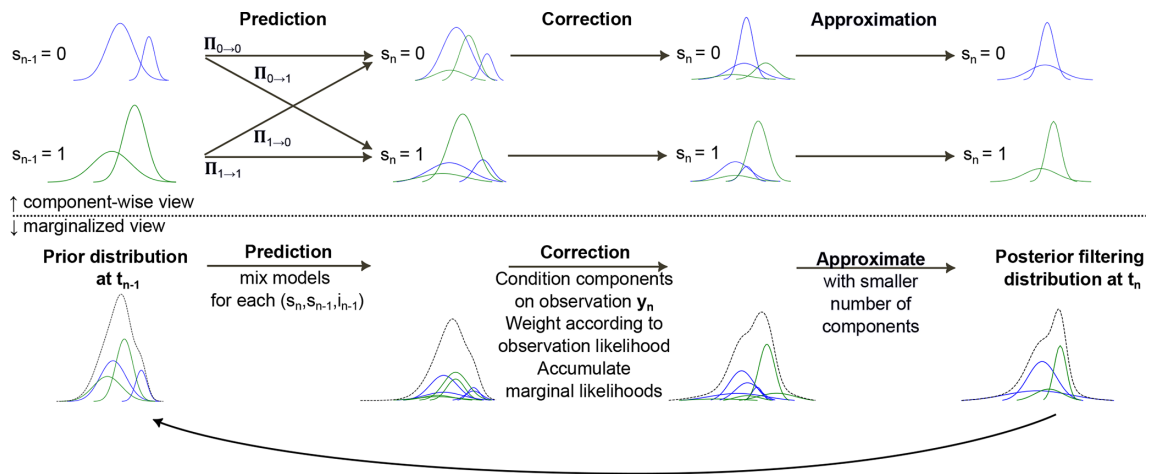


Figure 1. Illustration of the iterative computational methods applied in the Gaussian sum filtering (GSF). The filtering distributions (prior and posterior at time steps t_{n-1} and t_n , respectively) are displayed as Gaussian mixtures indexed by i_n for each of the models indexed by s_n . The top panel shows a component-wise view, and the bottom panel shows a marginalized (over s_n and i_n) view of the respective compound distributions. The algorithm can be formally divided into the prediction, correction, and approximation steps. The illustrated iteration starts at some specified prior for t_0 . For further details, see text and Appendix A2. The output of the algorithm is the approximated decomposed filtering distribution $\sum_{s_n} p(s_n | y_{1:n}) \sum_{i_n} w_{s_n, i_n} p(x_n | s_n, i_n, y_{1:n})$, the input is a prior and a collection of measurements $y_{1:N}$ with associated time stamps, measurement times, and values for all parameters (see text). The approximate marginal likelihood of the measurement sequence can be computed alongside the filtering.

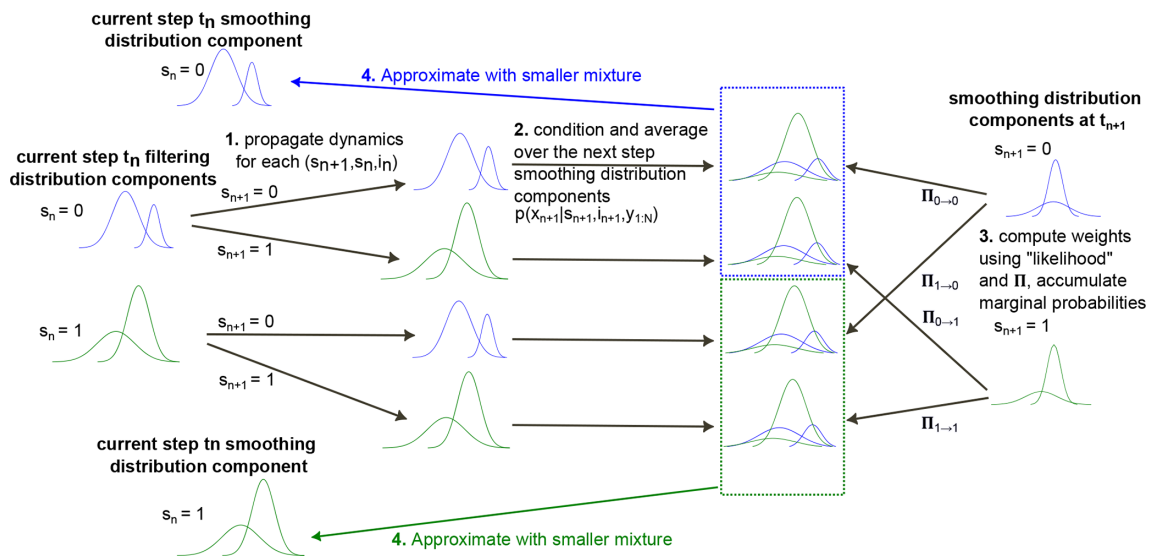


Figure 2. Illustration of the backward iterative computational steps (1)–(4) in the expectation correction algorithm applied for correcting the results from the Gaussian sum filtering (GSF) outlined in Fig. 1 to the approximate smoothing solution in the switching linear dynamical system. Input to the algorithm are the results from the GSF and associated time stamps and values for all parameters. Output is the decomposed smoothing distribution $\sum_{s_n} p(s_n | y_{1:N}) \sum_{i_n} w_{s_n, i_n} p(x_n | s_n, i_n, y_{1:N})$ as a Gaussian mixture approximation.

specific realizations of \mathbf{H} and combine them into mixtures weighted with the likelihood of said realization under the density $p(\mathbf{H})$ known from prior calibration measurements. In practice, this is closely related to the selection of sigma points of \mathbf{H} within some prior density and using the associated normalized likelihoods as multiplicative weights with the respective filtering and smoothing mixture weights to ob-

tain extended mixtures that approximately reflect the uncertainty associated with \mathbf{H} , a method inspired by the unscented Kalman filter (Julier et al., 2000) for approximate filtering in non-linear systems.

2.7 Implementation details

Implementation of the presented algorithms was carried out in Python using the JAX framework (Bradburry et al., 2018), which provides automatic batching and vectorization, just-in-time compilation, and automatic forward- and reverse-mode differentiation. This allows the optimization of the hyperparameters γ , σ , and $\mathbf{\Pi}$ using the ADAM gradient descent minimization (Kingma and Ba, 2014) routine from JAX together with the automatically computed batch gradient of the negative log likelihood, $-\sum_n \ln(y_n | y_{1:n-1}, \sigma, \gamma, \mathbf{\Pi})$, of the GSF forward pass on the entire dataset (Algorithm 1 in Appendix A2). The number of components retained in the arising Gaussian mixtures in GSF and EC is chosen according to available computational resources. Forward and backward step routines for the linear dynamical system given in Eq. (2) (cf. Appendix A1) were implemented as shown in the auxiliary functions for Algorithms 1 and 2 in Appendix A2, respectively. Gaussian mixture reduction as necessary in the GSF forward and EC backward passes (i.e., the approximation steps in the charts in Figs. 1 and 2) was implemented according to a greedy algorithm (based on Kullback–Leibler divergence (Runnalls, 2007)). The mean approximation in the EC backward pass, and implementation of the EC backward and GSF forward passes, were directly adopted as presented in Barber (2006). Gaussian mixture weights and model index probabilities are stored and operated on in ln-space (using the log-sum-exp operation for normalization) for improved numerical stability. Routines for the computation of the Matrices \mathbf{F} , \mathbf{U} , \mathbf{M} , \mathbf{C} , and \mathbf{B} in Eq. (13) were obtained from symbolic computation using SymPy (Meurer et al., 2017), and the symbolic Jordan canonical form of \mathbf{F} and were hard-coded afterward.

3 Application to experimental data

Data for this experiment were generated using an electroplated ^{226}Ra (104.4 ± 0.4) Bq source (Mertes et al., 2020) mounted on an electrically cooled high-purity germanium (HPGe) detector placed inside a 20 m^3 climate chamber. γ -ray spectra were recorded over approximately 85 d at intervals of 10 800 s real time. Within the time series, regions of missing measurements are present, i.e., δ values varied. At specific times the relative humidity inside the climate chamber was varied with the intention of inducing changes in the emanation characteristics of the ^{226}Ra source. Inside the chamber, relative humidity and temperature were measured in close proximity to the source with a SHT-35 sensor (Sensirion).

For each spectrum, counts above 200 keV were summed, a lifetime scaled background count rate (with associated uncertainty that defines \mathbf{R}) was subtracted, and the final algorithms described above (as given in Appendix A2) were applied to the resultant time series of count values (i.e., 1D measurement series) as the input data $y_{1:N}$, with five Gaus-

sian components per filter in the GSF forward and EC backward passes. Results are illustrated for the filtering in Fig. 1a and for the smoothing in Fig. 1b. Each r was chosen to reflect the real time of each spectrum as provided by the manufacturer's data-acquisition software (Genie 2000, Mirion Technologies), and each δ was computed from the recorded time stamps of acquisition start points. The dead time of the system was accounted for by correcting the derived count values using the dead-time data as provided by the data-acquisition software. The value of \mathbf{H} was determined by measurements of a sealed source of similar type and geometry as presented in Mertes et al. (2020). The uncertainty associated with the ^{226}Ra activity known from previous measurements detailed in Mertes et al. (2020) was encoded in the density of the prior for the state provided to the algorithm. Apart from the ^{226}Ra activity, a vague Gaussian prior with a diagonal covariance matrix was chosen for $p(\mathbf{x}_0)$. Inherently, the model formulation assumes perfect equilibrium between the SLP and ^{222}Rn in the source, which is a small approximation on the timescales at hand. The threshold of 200 keV was chosen because ^{226}Ra emits γ radiation almost entirely below this energy level, such that the spectrum beyond is almost entirely made up of events associated with the SLP in the source and the background radiation. We chose to neglect the information gained from the spectra regarding the ^{226}Ra activity because it was not found to substantially improve the prior. The summation of spectra is the most straightforward way to utilize the information contained within each spectrum while keeping the dimensionality of \mathbf{y} as small as possible. As a result, the prior density for the ^{226}Ra activity component of the state is retained over the entire dataset, which is why this component of the state is not shown in Fig. 3. The last component of the state vectors, $\frac{d\eta}{dt}$, is also not shown in Fig. 3 for visual clarity, since it carries no important information and is merely used as a mathematical tool to specify the properties of the stochastic process of η , the main estimation target of this work. The component $\frac{d\eta}{dt}$ is therefore not of any practical meaning.

Both the confidence intervals and the median in Fig. 3 were computed from the marginal cumulative density of the Gaussian mixtures using numerical root finding. Additionally, the confidence intervals include a systematic, Gaussian 1 % uncertainty on the specific value of \mathbf{H} which was approximately propagated using the derivation in Sect. 2.6 for five distinct realizations of \mathbf{H} ($\mu_{\mathbf{H}}, \mu_{\mathbf{H}} \pm \sigma_{\mathbf{H}}, \mu_{\mathbf{H}} \pm 2\sigma_{\mathbf{H}}$).

4 Discussion and conclusion

In the present work, we have summarized and explained the limitations of previously available approaches to estimate ^{222}Rn emanation through measurements of the short-lived progeny (SLP) retained within the source. As was derived from first principles, those methods to standardize ^{222}Rn emanation are limited to sources with stable characteristics

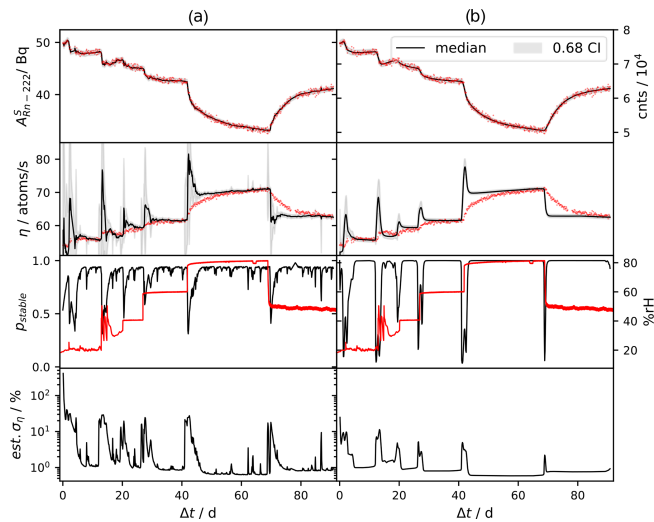


Figure 3. Column (a) shows the filtering and column (b) the smoothing results. Input data (red dots in the top-most row; right scale) and estimated residual ^{222}Rn activity (left scale) are depicted in the first row. The second row shows the estimated emanating ^{222}Rn given by the SLDS deconvolution approach outlined in Sect. 2.5 (black line; deconvolution result) and erroneously calculated from Eq. (4) (red dots). Deviations between the red dots and the filtering and smoothing results in row two are due to the inability of Eq. (4) to account for dynamic behavior. In the third row, the probability for stable regimes under the model, $p(s_n | y_{1:n})$ (column a), and $p(s_n | y_{1:N})$ (column b), where s_n equals the index of the model for the stable regime (black; i.e., inferred switch points; see Sect. 2.7) and the relative humidity (red; not used as input data) are shown. The fourth row shows the estimated relative standard uncertainty (calculated from the median and the shown confidence interval) of inferred ^{222}Rn emanation.

within the operational time and, as such, are generally restricted to use in stable environmental conditions. To alleviate this shortcoming, here we developed an alternative approach that directly infers the conditional probability density for the latent ^{222}Rn emanation term from spectral time series of the SLP that remains within the source.

During the application of the resultant algorithms to real-world data, the deviations of the steady-state approximation of the previous method (red dots in the second row of Fig. 3) from the estimated true values (black lines in the second row of Fig. 3) become apparent, underpinning the theoretical derivations. In turn, this means that a thorough analysis of data obtained in this way is restricted to models that account for the dynamic nature of the system, which has not previously been reported.

The specific structure of the filtering and smoothing results in the second row of Fig. 3, showing peaked emanation upon increases in humidity, can easily be explained physically as follows, which justifies the results of the applied method. Considering the time series of count data of the SLP within the source (input data; red dots in the first row of Fig. 3), re-

gions can be seen where changes are occurring much more quickly than would be possible based on the well-known radioactive decay kinetics. As was discussed in Sect. 2.2, the time series of counts is theoretically given by a discretely sampled convolved version of the emanation. Hence, peaked emanation must be occurring, such that the observed time series is possible within the theoretically known decay kinetics. Conversely, the drop in humidity and thus emanation at approximately 70 d does not show this behavior, and the observed ingrowth of the counts directly follows the decay kinetics. Apparently, the behavior depends on the direction of change in the emanation characteristics. This is explained by the fact that upon an increase of the effective diffusion coefficient, the source retains more ^{222}Rn atoms than the associated equilibrium value, at which point increased outflow can occur for quick re-equilibration. With the realistic assumption of zero back diffusion from the volume into the source, for a change in the opposite direction, the only way to achieve progeny equilibrium is the typical ingrowth of ^{222}Rn , which is the exact behavior shown by the deconvolution result but not by the previous method. Upon fresh preparation of an emanation source, at which point no SLP is present in the source but emanation is still considered to be happening, similar count data to the one past 70 d in Fig. 3 may be observed. This behavior was not previously discussed in Linzmaier and Röttger (2013), where the apparent initial drop in emanation (as computed by Eq. 4) resulting from the initial ingrowth of residual ^{222}Rn and SLP was seemingly considered to be its true temporal characteristic, implying that Eq. (4) may be applied in such a case.

In constant regimes, results obtained from previously reported methods converge to the values obtained using the deconvolution approach presented here, as illustrated at approximately days 60 to 70 and past 90 d of the data shown in Fig. 3. While the method we present might not seem beneficial in such constant regimes, the recursive Bayesian approach provides a computationally convenient, mathematically coherent, and flexible way to refine the uncertainty upon observation of streaming data (e.g., obtained by continuous operation of spectrometers) also within constant regimes. As such, here we report for the first time the application of a method whereby time series data of an emanation source can be used to derive correct (near) real time values of the emanation, irrespective of the state of the source. Specifically, the use case of this method and our initial motivation is the implementation of surveillance systems for emanation sources based on spectrometric measurements to improve current state-of-the-art realization, and especially the dissemination of the unit Bq m^{-3} for ^{222}Rn in the low-level activity concentration regime. With our contribution, and potential extensions thereof, these types of systems will be enabled in the future. Moreover, experimental investigations of the emanation behavior in response to different environmental conditions are drastically improved by our contribution.

To obtain approximate filtering and smoothing algorithms in the context of radioactivity measurements, we extended the well-known computational methods for inference in linear dynamical systems (i.e., Kalman filter and Rauch–Tung–Striebel smoother) with a computationally convenient approximation for the observed Poisson statistics and the integrating behavior of the measurements in Sect. 2.3 and 2.4. In doing so, we demonstrated that integrating measurements results in a Gaussian process with certain covariance with the latent continuous state which retains the convenient closed form of filtering and smoothing through conjugacy in such linear dynamical models. As was shown, the integrating measurements lead to additional additive uncertainty depending on the variance of the Brownian motion which we consider an intuitive result. These results were used in order to construct the final switching linear dynamical system inference algorithms applied during the experiments.

Within the recorded time series, distinct domains were observed in response to the way the humidity in the chamber was modified, which lends itself to the applied switching dynamical system model, differentiating between stable and non-stable regimes. This approach allows smaller uncertainty to be achieved and smoother functional realizations of η in the somewhat stable regimes, but at the same time gives reasonably high uncertainty for the unstable regimes where the deconvolution result relies on only a few data points. A simpler modeling approach relying only on a single linear dynamical system, such as a more classical version of the Kalman filter, cannot produce smooth results for the constant regimes while retaining the ability to react to steep gradients, since both properties are controlled by the variance of the Brownian motion. While all obvious switching points (induced by changes in the relative humidity) within the time series were captured by the algorithm (third row of Fig. 3), the specific autocorrelation we chose to regularize η leads to smearing of the switching point in the backward (i.e., the smoothing) pass. This is indicated by the fact that the model proposes an unstable state of the source even for times before the humidity has undergone the step changes (i.e., in times before a known change in the source properties has occurred). Note that this is not the case for the filtering results. This is can be attributed to the applied symmetric autocorrelation of η (Eq. 7) and its independency from the residual radon activity, and it may be alleviated by asymmetric autocorrelation or non-linear models but at a substantially higher computational cost. Whether our approach translates well to time series of different characteristics (e.g., drift, smooth changes) is as yet unclear and subject to further studies. Nonetheless, the model parameters provide a way to tune the algorithm for different scenarios.

For an approach like the present one to be applicable in metrology, uncertainty estimates closely related to the guide to the expression of uncertainty in measurement (GUM; Joint Committee for Guides in Metrology, 2008) are needed. At this point, the GUM is restricted to static measurements and

first steps are being taken for an extension to dynamic scenarios (e.g., in Eichstädt and Elster, 2012; Elster and Link, 2008; Link and Elster, 2009), where a slightly different formulation for error propagation has been carried out. In the present case, systematic contributions to the uncertainty are dominated by the uncertainty of the measurement mapping through matrix \mathbf{H} . We provided a computationally simple approach to approximately propagate this uncertainty across the filtering and smoothing algorithms with arbitrary precision, given that enough computational resources are available and the detection system can reasonably be assumed to be stable in time. Dropping this assumption would require the approximation of the intractable integration in Eq. (15), e.g., through Monte Carlo integration, which was found unnecessary and would have made the algorithm unsuitable for implementation on low-power, portable devices.

Appendix A: Joint density – derivation of discrete forward step for integrating measurement

Assuming that the density $p(\mathbf{x}_{n-1}|\mathbf{y}_{1:n-1})$ is given as $\mathcal{N}(\boldsymbol{\mu}_{n-1}, \boldsymbol{\Sigma}_{n-1})$, we define the state at the intermediate time point $t_{n-1} + \delta_n$ as \mathbf{x}_δ for which the following statistics are readily available through the Chapman–Kolmogorov equation (Särkkä and Solin, 2019).

$$p(\mathbf{x}_\delta|\mathbf{y}_{1:n-1}) \propto \mathcal{N}(\boldsymbol{\mu}_\delta, \boldsymbol{\Sigma}_\delta) = \mathcal{N}(\mathbf{F}_\delta \boldsymbol{\mu}_{n-1}, \mathbf{F}_\delta \boldsymbol{\Sigma}_{n-1} \mathbf{F}_\delta^T + \mathbf{U}_\delta),$$

where $\mathbf{F}_\delta = e^{\mathbf{K}\delta}$ and $\mathbf{U}_\delta = \int_0^\delta e^{\mathbf{K}(\delta-\tau)} \mathbf{L} \mathbf{L}^T e^{\mathbf{K}^T(\delta-\tau)} d\tau$, as follows from Eqs. (5) and (11).

By combination of the definition for $\mathbf{x}(t)$ in Eq. (10) and the definition of the measurement process for \mathbf{y} in Eq. (12), the measurement at t_n is given by the following integration. While the integral in Eq. (12) is an ordinary integral (e.g., in the Riemann sense), the integral in Eq. (10) is a stochastic integral in the Itô sense; i.e., the following double integral is the ordinary integral over an Itô integral, for which we assume that $\mathbf{x}(t)$ has continuous sample paths and is square integrable.

$$\begin{aligned} y_{t_n} &= \mathbf{H} \int_{t_{n-1}+\delta}^{t_n} \mathbf{x}(\tau) d\tau = \mathbf{H} \int_0^r \mathbf{x}(t_{n-1} + \delta + \tau) d\tau \\ &= \mathbf{H} \int_0^r e^{\mathbf{K}s} \mathbf{x}_{t_{n-1}+\delta} ds + \mathbf{H} \int_0^r \int_0^s e^{\mathbf{K}(s-\tau)} \mathbf{L} d\beta_\tau ds \end{aligned}$$

The triangular domain of the double integral is swapped to find

$$y_{t_n} = \mathbf{H} \int_0^r e^{\mathbf{K}s} \mathbf{x}_{t_{n-1}+\delta} ds + \mathbf{H} \int_0^r \int_\tau^r e^{\mathbf{K}(s-\tau)} \mathbf{L} ds d\beta_\tau,$$

from which the full density $p(\mathbf{x}_{n-1}, \mathbf{x}_\delta, \mathbf{x}_n, \mathbf{y}_n|\mathbf{y}_{1:n-1})$ can be computed using the expectation operator and the definition of the variance, where $\langle \cdot \rangle$ denotes the expectation oper-

ator. Moreover, by definition, $\langle \int d\beta \rangle = 0$ and thus

$$\begin{aligned} \Sigma_n^{yy} &= \langle (y_n - \langle y_n \rangle)(y_n - \langle y_n \rangle)^T \rangle \\ &= \left\langle \mathbf{H} \left(\int_0^r e^{\mathbf{K}s} ds \mathbf{x}_\delta - \int_0^r e^{\mathbf{K}s} ds \langle \mathbf{x}_\delta \rangle + \int_0^r \int_\tau^r e^{\mathbf{K}(s-\tau)} \mathbf{L} ds d\beta_\tau \right) \right. \\ &\quad \left. \left(\int_0^r e^{\mathbf{K}s} ds \mathbf{x}_\delta - \int_0^r e^{\mathbf{K}s} ds \langle \mathbf{x}_\delta \rangle + \int_0^r \int_\tau^r e^{\mathbf{K}(s-\tau)} \mathbf{L} ds d\beta_\tau \right)^T \mathbf{H}^T \right\rangle. \end{aligned}$$

Under the assumption of independence of the Brownian motion and \mathbf{x}_δ , using Itô isometry and Fubini's theorem, it follows that

$$\Sigma_n^{yy} = \langle (y_n - \langle y_n \rangle)(y_n - \langle y_n \rangle)^T \rangle = \mathbf{H} \mathbf{M} \Sigma_\delta \mathbf{M}^T \mathbf{H}^T + \mathbf{H} \mathbf{B} \mathbf{H}^T,$$

where $\mathbf{M} = \int_0^r e^{\mathbf{K}s} ds$ and $\mathbf{B} = \int_0^r \int_\tau^r \int_\tau^r e^{\mathbf{K}(a-\tau)} \mathbf{L} \mathbf{L}^T e^{\mathbf{K}^T(b-\tau)} da db d\tau$.

Analogously, the cross-covariance between \mathbf{x}_n and y_n is given as

$$\begin{aligned} \Sigma_n^{xy} &= \langle (\mathbf{x}_n - \langle \mathbf{x}_n \rangle)(y_n - \langle y_n \rangle)^T \rangle = \\ &= \left\langle \left(e^{\mathbf{K}r} \mathbf{x}_\delta - e^{\mathbf{K}r} \langle \mathbf{x}_\delta \rangle + \int_0^r e^{\mathbf{K}(r-\tau)} \mathbf{L} d\beta_\tau \right) \right. \\ &\quad \left. \left(\int_0^r e^{\mathbf{K}s} ds \mathbf{x}_\delta - \int_0^r e^{\mathbf{K}s} ds \langle \mathbf{x}_\delta \rangle + \int_0^r \int_\tau^r e^{\mathbf{K}(s-\tau)} \mathbf{L} ds d\beta_\tau \right)^T \mathbf{H}^T \right\rangle = \\ &= \mathbf{F}_r \Sigma_\delta \mathbf{M}^T \mathbf{H}^T + \mathbf{C} \mathbf{H}^T, \end{aligned}$$

with $\mathbf{C} = \int_0^r \int_\tau^r e^{\mathbf{K}(r-\tau)} \mathbf{L} \mathbf{L}^T e^{\mathbf{K}^T(a-\tau)} da d\tau$. The result in Eq. (13) is then obtained by marginalizing the full density over \mathbf{x}_{n-1} and \mathbf{x}_δ , which for the Gaussian density means to simply drop the respective columns and rows. Additionally, the forward filtering step is obtained by conditioning the resultant $p(\mathbf{x}_n, y_n | y_{1:n-1})$, Eq. (13), onto the observation of y_n using the well-known conditioning formula for the Gaussian distribution. An implementation for such computation is given by the function *FWD_STEP* in Appendix A2.

Appendix B: Applied algorithms in pseudo-code

Algorithm 1. Gaussian Sum Filtering, Filtering in SLDS

```

function FWD_STEP( $r, \delta, \mathbf{m}, \Sigma, \mathbf{H}, \mathbf{y}, \mathbf{R}, \theta$ )
     $\mathbf{F}_\delta, \mathbf{U}_\delta, \mathbf{M}_\delta, \mathbf{C}_\delta, \mathbf{B}_\delta := \text{DISCRETIZE}(\delta, \theta)$ 
    // DISCRETIZE( $t, \theta$ ) is a function that computes the matrices defined in sections 2.3 and 2.4 using  $t$  as the integration time
    // where  $\theta$  specifies a vector containing necessary model parameters, e.g.  $\gamma$  and  $\sigma$  in Eq. (9)
     $\mathbf{m}_\delta := \mathbf{F}_\delta \mathbf{m}; \Sigma_\delta := \mathbf{F}_\delta \Sigma \mathbf{F}_\delta^T + \mathbf{U}_\delta$ 
     $\mathbf{F}_r, \mathbf{U}_r, \mathbf{M}_r, \mathbf{C}_r, \mathbf{B}_r := \text{DISCRETIZE}(r, \theta)$ 
     $\mathbf{y}^- := \mathbf{H} \mathbf{M}_r \mathbf{m}_\delta$ 
     $\Sigma_{yy} := \mathbf{H} \mathbf{M}_r \Sigma_\delta \mathbf{M}_r^T \mathbf{H}^T + \mathbf{H} \mathbf{B}_r \mathbf{H}^T + \text{MIN}(1, \text{DIAG}(\mathbf{y}^-)) + \mathbf{R}$ 
    // DIAG() constructs a square-matrix of appropriate size for a vector input or returns the diagonal for a matrix input
     $\Sigma_{yx} := \mathbf{H} \mathbf{M}_r \Sigma_\delta \mathbf{F}_r^T + \mathbf{H} \mathbf{C}_r^T$ 
     $\mathbf{L} := \text{CHOLESKY}(\Sigma_{yy}); \text{SOLVE}(\mathbf{L} \mathbf{L}^T \mathbf{G} = \Sigma_{yx})$  // solves for  $\mathbf{G}$  using the computed Cholesky factorization
     $\mathbf{m}_r := \mathbf{F}_r \mathbf{m}_\delta + \mathbf{G}^T (\mathbf{y} - \mathbf{y}^-); \Sigma_r := \mathbf{F}_r \Sigma_\delta \mathbf{F}_r^T + \mathbf{U}_r - \mathbf{G}^T \Sigma_{yx}$ 
     $n := \text{SIZE}(\mathbf{y}); \ell := -\frac{n}{2} \ln(2\pi) - \sum \ln(\text{DIAG}(\mathbf{L})) - \frac{1}{2} (\mathbf{y} - \mathbf{y}^-)^T (\mathbf{L} \mathbf{L}^T)^{-1} (\mathbf{y} - \mathbf{y}^-)$  // use Cholesky factors to compute the inverse
    return  $\ell, \mathbf{m}_r, \Sigma_r$ 

function GAUSSIAN_SUM_FILTER( $N, r_{1:N}, \delta_{1:N}, \mathbf{y}_{1:N}, \mathbf{R}_{1:N}, \theta_{1:S}, \Pi, \mathbf{H}, \mathbf{m}_0, \Sigma_0, S, l$ )
    //  $\mathbf{m}_0, \Sigma_0$  refer to the prior mean vector and prior covariance matrix,  $\theta_{1:S}$  specifies vectors of required model parameters for all  $S$  models,  $l$  specifies the
    // number of kept components in arising Gaussian mixture approximations. For other symbols, see main text.
     $l_0 := 1; \rho := 0; i := 0$ 
    for  $s \in [0, \dots, S]$ 
         $\mathbf{m}_{0,s,i} := \mathbf{m}_0, \Sigma_{0,s,i} := \Sigma_0, w_{0,s,i} := 0$  // broadcast specified prior to all models/mixture components
         $\rho_{0,s} := \ln(\frac{1}{S})$  // initialize model probabilities to equal and normalized values
    end for
    for  $n \in [1, \dots, N]$  // main loop over time-steps
        for  $s_n \in [0, \dots, S]$ 
            for  $i \in [0, \dots, l_{n-1}]$  and  $s \in [0, \dots, S]$ 
                 $\ell_{s_n,s,i}, \mu_{s_n,s,i}, \mathbf{P}_{s_n,s,i} := \text{FWD\_STEP}(r_n, \delta_n, \mathbf{m}_{n-1,s,i}, \Sigma_{n-1,s,i}, \mathbf{H}, \mathbf{y}_n, \mathbf{R}_n, \theta_{s_n})$ 
                 $l_{s_n,s,i} := w_{n-1,s,i} + \ln(\Pi_{s \rightarrow s_n}) + \ell_{s_n,s,i} + \rho_{n-1,s}$ 
            end for
             $\rho_{n,s_n} := \ln(\sum_{i,s} e^{\ell_{s_n,s,i}})$ 
            if  $S * l_{n-1} \leq l$  then  $l_n := S * l_{n-1}$  else  $l_n := l$ 
             $w_{n,s_n}, \mathbf{m}_{n,s_n}, \Sigma_{n,s_n} := \text{MIXTURE\_REDUCTION}(l_{s_n}, \mu_{s_n}, \mathbf{P}_{s_n}, S * l_{n-1}, l_n)$ 
            // MIXTURE_REDUCTION( $\mathbf{p}_{1:a}, \mathbf{m}_{1:a}, \Sigma_{1:a}, a, b$ ) is a function that approximates the a component Gaussian mixture described by mean
            // vectors  $\mathbf{m}_{1:a}$ , covariance matrices  $\Sigma_{1:a}$  and (unnormalized) log-weights  $\mathbf{p}_{1:a}$  with a smaller mixture of  $b$  components. Returns new
            // (normalized) log-weights, mean vectors and covariance matrices of the approximated mixture. For reference of the method used
            // herein, see (Runnalls, 2007). This defines the Gaussian mixture filtering distributions  $p(\mathbf{x}_n | s_n, \mathbf{y}_{1:n}) \approx \sum_i w_{n,s_n,i} \mathcal{N}(\mathbf{m}_{n,s_n,i}, \Sigma_{n,s_n,i})$ 
            end for
             $\rho_n := \rho_n - \ln(\sum_{s_n} e^{\rho_{n,s_n}})$  // normalize model index log-probabilities  $\ln p(s_n | \mathbf{y}_{1:n})$ 
             $\mathcal{L} += \ln(\sum_{s_n,i} e^{\ell_{s_n,s,i}})$  // accumulate marginal log-likelihood  $\sum_n \ln p(\mathbf{y}_n | \mathbf{y}_{1:n-1})$ 
        end for
    return  $\mathcal{L}, \rho_{1:N}, w_{1:N}, \mathbf{m}_{1:N}, \Sigma_{1:N}, I_{1:N}$ 
    // returns marginal log-likelihood  $\mathcal{L}$ , and the decomposed filtering distribution
    //  $p(\mathbf{x}_n | \mathbf{y}_{1:n}) \approx \sum_{s_n} p(s_n | \mathbf{y}_{1:n}) \sum_i \bar{w}_{s_n,i} p(\mathbf{x}_n | s_n, i_n, \mathbf{y}_{1:n}) = \sum_{s_n} e^{\rho_{n,s_n}} \sum_i e^{w_{n,s_n,i} n} \mathcal{N}(\mathbf{m}_{n,s_n,i}, \Sigma_{n,s_n,i})$ 
    // specified by the model index log-probabilities  $\rho_{1:N}$ , component log-weights  $w_{1:N}$ , the mean vectors  $\mathbf{m}_{1:N}$ , the covariance matrices  $\Sigma_{1:N}$  and the number of
    // kept Gaussian mixture components for each time-step  $I_{1:N}$ 

    // Tuning of parameter vectors  $\theta_{1:S}$  and parametrization of  $\Pi$  is carried out by minimization of  $-\mathcal{L}$  by a gradient-descent method, using automatic
    // differentiation (see main text) to compute  $\frac{d\mathcal{L}}{d\theta_{1:S}}$  and  $\frac{d\mathcal{L}}{d\Pi}$ 

```

Algorithm 2. Expectation Correction, Smoothing in SLDS

```

function BKWD_STEP(r, δ, m, P, μ, Σ, θ)
    Fδ+r, Uδ+r, Mδ+r, Cδ+r, Bδ+r := DISCRETIZE(δ + r, θ)
    // DISCRETIZE(t, θ) is a function that computes the matrices defined in section 2.3 and 2.4 using t as the integration time
    // where θ specifies a vector containing necessary model parameters, e.g. γ and σ in Eq. (9)
    μδ+r+ := Fδ+rm + Σδ+r+; Σδ+r+ := Fδ+rP Fδ+rT + Uδ+r
    L := CHOLESKY(Σδ+r+); SOLVE(LLTG = Fδ+rP) // solves for G using the computed Cholesky factorization
    μδ+r+ := m + GT(μ - μδ+r+); Σδ+r+ := (J - GTFδ+r)P(J - GTFδ+r)T + GT(Uδ+r + Σ)G // J denotes the identity matrix; Joseph-form covariance update
    n := SIZE(m); ℓ := - $\frac{n}{2} \ln(2\pi) - \sum \ln(\text{DIAG}(L)) - \frac{1}{2}(\mu - \mu_{\delta+r}^+)^T (LL^T)^{-1} (\mu - \mu_{\delta+r}^+)$  // use Cholesky factors to compute the inverse
    return ℓ, μδ+r+, Σδ+r+

function EXPECTATION_CORRECTION_SMOOTHER(N, r1:N, δ1:N, θ1:S, Π, ρ1:N, w1:N, m1:N, Σ1:N, S, I1:N)
    // Uses the results from Algorithm 1, notation as defined therein
    μN,S,i+ := mN,S,i; ΣN,S,i+ := ΣN,S,i; ρN,S,i}^+ := ρN,S,i; wN,S,i}^+ := wN,S,i ∀ s ∈ [0, ..., S]; i ∈ [0, ..., IN]
    for n ∈ ]N - 1, ..., 0[
        for sn ∈ [0, ..., S], sn+1 ∈ [0, ..., S], in ∈ [0, ..., In], in+1 ∈ [0, ..., In+1]
            ℓsnsn+1, in, in+1, μsnsn+1, in, in+1+, Σsnsn+1, in, in+1+ := BKWD_STEP(rn, δn, mn, sn, in, Σn, sn, in, μn+1, sn+1, in+1+, Σn+1, sn+1, in+1+, θsn)
            ℓsnsn+1, in, in+1 := ℓsnsn+1, in, in+1 + wn, sn, in + ρn, sn, in + ln(Πsn-sn+1)
        end for
        for sn ∈ [0, ..., S[
            for sn+1 ∈ [0, ..., S], in ∈ [0, ..., In], in+1 ∈ [0, ..., In+1]
                ℓsnsn+1, in, in+1 := ℓsnsn+1, in, in+1 - ln(Σsn, in eℓsnsn+1, in, in+1) + ρn+1, sn+1, in+1 + wn+1, sn+1, in+1
            end for
            ρn, sn+ := ln(Σsn+1, in+1 eℓsnsn+1, in, in+1)
            wn, sn+, μn, sn+, Σn, sn+ := MIXTURE_REDUCTION(ℓsn, μsn+, Σsn+, In * S * In+1, In)
            // Collapse mixture defined for each sn that has In * S * In+1 components to a In component mixture, which defines the collection of
            // log-weights wn, sn+, component mean-vectors μn, sn+ and covariance matrices Σn, sn+ for the current step smoothing posterior. Same
            // function as in Algorithm 1.
        end for
    end for
    return ρ0:N}^+, w0:N}^+, μ0:N}^+, Σ0:N}^+
    // returns the decomposed smoothing distribution as the Gaussian mixture
    // p(xn|y1:N) ≈ Σsn p(sn|y1:N) Σin wsn, in p(xn|sn, in, y1:N) = Σsn eρn, sn+ Σin ewn, sn, in+ N(μn, sn, in+, Σn, sn, in+)

```

Code and data availability. Gamma-ray spectra and environmental data obtained for the experimental section as well as the implementation of the presented algorithms and processing software are available at <https://doi.org/10.5281/zenodo.7798458> (Mertes, 2023).

Author contributions. AR and SR acquired funding, supervised and conceptualized this work, and reviewed the draft. FM derived the methodology, designed the models, implemented the software, acquired the experimental data, and prepared the original draft.

Competing interests. The contact author has declared that none of the authors has any competing interests.

Disclaimer. Publisher’s note: Copernicus Publications remains neutral with regard to jurisdictional claims in published maps and institutional affiliations.

Special issue statement. This article is part of the special issue “Sensors and Measurement Science International SMSI 2021”. It is a result of the Sensor and Measurement Science International, 3–6 May 2021.

Acknowledgements. The authors thank Alan Griffiths (ANSTO) and Scott D. Chambers (ANSTO) for their comments on the paper.

Financial support. This project has received funding from the EMPIR programme co-financed by the Participating States and from the European Union’s Horizon 2020 research and innovation programme. 19ENV01 traceRadon denotes the EMPIR project reference.

This open-access publication was funded by the Physikalisch-Technische Bundesanstalt.

Review statement. This paper was edited by Alexander Bergmann and reviewed by two anonymous referees.

References

- Alvarez, M., Luengo, D., and Lawrence, N. D.: Latent force models, *J. Mach. Learn. Res.*, 5, 9–16, 2009.
- Amaku, M., Pascholati, P. R., and Vanin, V. R.: Decay chain differential equations: Solution through matrix algebra, *Comput. Phys. Commun.*, 181, 21–23, <https://doi.org/10.1016/j.cpc.2009.08.011>, 2010.
- Barber, D.: Expectation Correction for Smoothed Inference in Switching Linear Dynamical Systems, *J. Mach. Learn. Res.*, 2, 2515–2540, 2006.
- Bateman, H.: Solution of a system of differential equations occurring in the theory of radioactive transformations, *P. Cam. Philos. Soc.*, 15, 423–427, 1910.
- Biraud, S., Ciais, P., Ramonet, M., Simmonds, P., Kazan, V., Monfray, P., O’Doherty, S., Spain, G., and Jennings, S. G.: Quantification of carbon dioxide, methane, nitrous oxide and chloroform emissions over Ireland from atmospheric observations at Mace Head, *Tellus B*, 54, 41–60, <https://doi.org/10.3402/tellusb.v54i1.16647>, 2002.
- Bradburry, J., Frostig, R., Hawkins, P., Johnson, M. J., Maclaurin, D., Necula, G., Paszke, A., van der Plas, J., Wanderman-Milne, S., and Zhang, Q.: JAX: composable transformations of Python+NumPy programs, GitHub [code], <https://github.com/google/jax> (last access: 1 April 2023), 2018.
- Chambers, S., Podstawczyńska, A., Pawlak, W., Fortuniak, K., Williams, A. G., and Griffiths, A. D.: Characterizing the State of the Urban Surface Layer Using Radon-222, *J. Geophys. Res.-Atmos.*, 124, 770–788, <https://doi.org/10.1029/2018JD029507>, 2019a.
- Chambers, S., Guérette, E.-A., Monk, K., Griffiths, A., Zhang, Y., Duc, H., Cope, M., Emmerson, K., Chang, L., Silver, J., Utembe, S., Crawford, J., Williams, A., and Keywood, M.: Skill-Testing Chemical Transport Models across Contrasting Atmospheric Mixing States Using Radon-222, *Atmosphere*, 10, 25, <https://doi.org/10.3390/atmos10010025>, 2019b.
- Chambers, S. D., Williams, A. G., Conen, F., Griffiths, A. D., Reimann, S., Steinbacher, M., Krummel, P. B., Steele, L. P., van der Schoot, M. V., Galbally, I. E., Molloy, S. B., and Barnes, J. E.: Towards a Universal “Baseline” Characterisation of Air Masses for High- and Low-Altitude Observing Stations Using Radon-222, *Aerosol. Air Qual. Res.*, 16, 885–899, <https://doi.org/10.4209/aaqr.2015.06.0391>, 2016.
- Chambers, S. D., Preunkert, S., Weller, R., Hong, S.-B., Humphries, R. S., Tositti, L., Angot, H., Legrand, M., Williams, A. G., Griffiths, A. D., Crawford, J., Simmons, J., Choi, T. J., Krummel, P. B., Molloy, S., Loh, Z., Galbally, I., Wilson, S., Magand, O., Sprovieri, F., Pirrone, N., and Dommergue, A.: Characterizing Atmospheric Transport Pathways to Antarctica and the Remote Southern Ocean Using Radon-222, *Front. Earth Sci.*, 6, 190, <https://doi.org/10.3389/feart.2018.00190>, 2018.
- Darby, S., Hill, D., Auvinen, A., Barros-Dios, J. M., Baysson, H., Bochicchio, F., Deo, H., Falk, R., Forastiere, F., Hakama, M., Heid, I., Kreienbrock, L., Kreuzer, M., Lagarde, F., Mäkeläinen, I., Muirhead, C., Oberaigner, W., Pershagen, G., Ruano-Ravina, A., Ruostenoja, E., Rosario, A. S., Tirmarche, M., Tomáscaron,ek, L., Whitley, E., Wichmann, H.-E., and Doll, R.: Radon in homes and risk of lung cancer: collaborative analysis of individual data from 13 European case-control studies, *BMJ*, 330, 223, <https://doi.org/10.1136/bmj.38308.477650.63>, 2005.
- Ebeigbe, D., Berry, T., Schiff, S. J., and Sauer, T.: Poisson Kalman filter for disease surveillance, *Phys. Rev. Res.*, 2, 043028, <https://doi.org/10.1103/PhysRevResearch.2.043028>, 2020.
- Eichstädt, S. and Elster, C.: Advanced Mathematical and Computational Tools in Metrology and Testing IX, 84, 126–135, https://doi.org/10.1142/9789814397957_0016, 2012.
- Elster, C. and Link, A.: Uncertainty evaluation for dynamic measurements modelled by a linear time-invariant system, *Metrologia*, 45, 464–473, <https://doi.org/10.1088/0026-1394/45/4/013>, 2008.
- Fialova, E., Otahal, P. P. S., Vosahlik, J., and Mazanova, M.: Equipment for Testing Measuring Devices at a Low-Level Radon Activity Concentration, *Int. J. Environ. Res. Pub. He.*, 17, 1904, <https://doi.org/10.3390/ijerph17061904>, 2020.
- Hartikainen, J. and Särkkä, S.: Sequential Inference for Latent Force Models, arXiv [preprint], <https://doi.org/10.48550/arXiv.1202.3730>, 2012.
- Janik, M., Omori, Y., and Yonehara, H.: Influence of humidity on radon and thoron exhalation rates from building materials, *Appl. Radiat. Isotopes*, 95, 102–107, <https://doi.org/10.1016/j.apradiso.2014.10.007>, 2015.
- Joint Committee for Guides in Metrology: Evaluation of measurement data – Supplement 1 to the, JCGM 101, 90, https://www.bipm.org/documents/20126/2071204/JCGM_101_2008_E.pdf/325dcaad-c15a-407c-1105-8b7f322d651c (last access: 1 April 2023), 2008.
- Julier, S., Uhlmann, J., and Durrant-Whyte, H. F.: A new method for the nonlinear transformation of means and covariances in filters and estimators, *IEEE T. Automat. Contr.*, 45, 477–482, <https://doi.org/10.1109/9.847726>, 2000.
- Kalman, R. E.: A New Approach to Linear Filtering and Prediction Problems, *J. Basic Eng.-T. ASME*, 82, 35–45, <https://doi.org/10.1115/1.3662552>, 1960.
- Kingma, D. P. and Ba, J.: Adam: A Method for Stochastic Optimization, arXiv [preprint], <https://doi.org/10.48550/arXiv.1412.6980>, 2014.
- Laan, V. Der, Karstens, U., Neubert, R. E. M., Laan-Luijckx, V. Der, and Meijer, H. A. J.: Observation-based estimates of fossil fuel-derived CO₂ emissions in the Netherlands using $\Delta 14\text{C}$, CO and ^{222}Rn , *Tellus B*, 62, 389–402, <https://doi.org/10.1111/j.1600-0889.2010.00493.x>, 2010.
- Levin, I.: Atmospheric CO₂ in continental Europe—an alternative approach to clean air CO₂ data, *Tellus B*, 39, 21–28, <https://doi.org/10.1111/j.1600-0889.1987.tb00267.x>, 1987.
- Levin, I., Karstens, U., Hammer, S., DellaColetta, J., Maier, F., and Gachkivskyi, M.: Limitations of the radon tracer method (RTM) to estimate regional greenhouse gas (GHG) emissions – a case study for methane in Heidelberg, *Atmos. Chem. Phys.*, 21, 17907–17926, <https://doi.org/10.5194/acp-21-17907-2021>, 2021.
- Levy, E.: Decay chain differential equations: Solutions through matrix analysis, *Comput. Phys. Commun.*, 234, 188–194, <https://doi.org/10.1016/j.cpc.2018.07.011>, 2019.
- Link, A. and Elster, C.: Uncertainty evaluation for IIR (infinite impulse response) filtering using a state-space approach, *Meas. Sci. Technol.*, 20, 055104, <https://doi.org/10.1088/0957-0233/20/5/055104>, 2009.

- Linzaier, D. and Röttger, A.: Development of a low-level radon reference atmosphere, *Appl. Radiat. Isotopes*, 81, 208–211, <https://doi.org/10.1016/j.apradiso.2013.03.032>, 2013.
- Mazor, E., Averbuch, A., Bar-Shalom, Y., and Dayan, J.: Interacting multiple model methods in target tracking: a survey, *IEEE T. Aerospace Elec. Sys.*, 34, 103–123, <https://doi.org/10.1109/7.640267>, 1998.
- Mertes, F.: FlorianMertes/RadonDeconvolution: Version 1.0 (Release), Zenodo [code] and [data set], <https://doi.org/10.5281/zenodo.7798458>, 2023.
- Mertes, F., Röttger, S., and Röttger, A.: A new primary emanation standard for Radon-222, *Appl. Radiat. Isotopes*, 156, 108928, <https://doi.org/10.1016/j.apradiso.2019.108928>, 2020.
- Meurer, A., Smith, C. P., Paprocki, M., Čertík, O., Kirpichev, S. B., Rocklin, M., Kumar, Am., Ivanov, S., Moore, J. K., Singh, S., Rathnayake, T., Vig, S., Granger, B. E., Muller, R. P., Bonazzi, F., Gupta, H., Vats, S., Johansson, F., Pedregosa, F., Curry, M. J., Terrel, A. R., Roučka, Š., Saboo, A., Fernando, I., Kulal, S., Cimrman, R., and Scopatz, A.: SymPy: symbolic computing in Python, *PeerJ Computer Science*, 3, e103, <https://doi.org/10.7717/peerj-cs.103>, 2017.
- Minka, T. P.: Expectation Propagation for approximate Bayesian inference, *arXiv [preprint]*, <https://doi.org/10.48550/arXiv.1301.2294>, 2013.
- Nadarajah, N., Tharmarasa, R., McDonald, M., and Kirubarajan, T.: IMM Forward Filtering and Backward Smoothing for Maneuvering Target Tracking, *IEEE T. Aero. Elec. Sys.*, 48, 2673–2678, <https://doi.org/10.1109/TAES.2012.6237617>, 2012.
- Perrino, C., Pietrodangelo, A., and Febo, A.: An atmospheric stability index based on radon progeny measurements for the evaluation of primary urban pollution, *Atmos. Environ.*, 35, 5235–5244, [https://doi.org/10.1016/S1352-2310\(01\)00349-1](https://doi.org/10.1016/S1352-2310(01)00349-1), 2001.
- Pressyanov, D. S.: Short solution of the radioactive decay chain equations, *Am. J. Phys.*, 70, 444–445, <https://doi.org/10.1119/1.1427084>, 2002.
- Rauch, H. E., Tung, F., and Striebel, C. T.: Maximum likelihood estimates of linear dynamic systems, *AIAA J.*, 3, 1445–1450, <https://doi.org/10.2514/3.3166>, 1965.
- Röttger, A., Honig, A., and Linzaier, D.: Calibration of commercial radon and thoron monitors at stable activity concentrations, *Appl. Radiat. Isotopes*, 87, 44–47, <https://doi.org/10.1016/j.apradiso.2013.11.111>, 2014.
- Runnalls, A. R.: Kullback-Leibler Approach to Gaussian Mixture Reduction, *IEEE T. Aero. Elec. Sys.*, 43, 989–999, <https://doi.org/10.1109/TAES.2007.4383588>, 2007.
- Särkkä, S.: Bayesian filtering and smoothing, Cambridge University Press, <https://doi.org/10.1017/CBO9781139344203>, 2013.
- Särkkä, S. and Solin, A.: Applied Stochastic Differential Equations, Cambridge University Press, <https://doi.org/10.1017/9781108186735>, 2019.
- Särkkä, S., Alvarez, M. A., and Lawrence, N. D.: Gaussian Process Latent Force Models for Learning and Stochastic Control of Physical Systems, *IEEE T. Automat. Contr.*, 64, 2953–2960, <https://doi.org/10.1109/TAC.2018.2874749>, 2019.
- Stranden, E., Kolstad, A. K., and Lind, B.: The Influence of Moisture and Temperature on Radon Exhalation, *Radiat. Prot. Dosim.*, 7, 55–58, <https://doi.org/10.1093/oxfordjournals.rpd.a082962>, 1984.
- Williams, A. G., Chambers, S., and Griffiths, A.: Bulk Mixing and Decoupling of the Nocturnal Stable Boundary Layer Characterized Using a Ubiquitous Natural Tracer, *Bound.-Lay. Meteorol.*, 149, 381–402, <https://doi.org/10.1007/s10546-013-9849-3>, 2013.
- Williams, A. G., Chambers, S. D., Conen, F., Reimann, S., Hill, M., Griffiths, A. D., and Crawford, J.: Radon as a tracer of atmospheric influences on traffic-related air pollution in a small inland city, *Tellus B*, 68, 30967, <https://doi.org/10.3402/tellusb.v68.30967>, 2016.
- Zhou, Q., Shubayr, N., Carmona, M., Standen, T. M., and Kearfott, K. J.: Experimental study of dependence on humidity and flow rate for a modified flowthrough radon source, *J. Radioanal. Nucl. Ch.*, 324, 673–680, <https://doi.org/10.1007/s10967-020-07081-0>, 2020.

Chapter 6

Publication IV: Development of ^{222}Rn emanation sources with integrated quasi 2π active monitoring

Florian Mertes, Stefan Röttger, Annette Röttger

in

International Journal of Environmental Research and Public Health, 19, 2022

DOI: 10.3390/ijerph19020840

Received 26 November 2021

Accepted 7 January 2022

Author contributions

Resources, supervision, project administration, funding acquisition: S.R., A.R.

Conceptualization, methodology, software, formal analysis, investigation, visualization, original draft preparation: F.M.



Article

Development of ^{222}Rn Emanation Sources with Integrated Quasi 2π Active Monitoring

Florian Mertes * , Stefan Röttger and Annette Röttger 

Physikalisch-Technische Bundesanstalt, National Metrology Institute, 38116 Braunschweig, Germany; stefan.roettger@ptb.de (S.R.); annette.roettger@ptb.de (A.R.)

* Correspondence: florian.mertes@ptb.de

Abstract: In this work, a novel approach for the standardization of low-level ^{222}Rn emanation is presented. The technique is based on the integration of a ^{222}Rn source, directly, with an α -particle detector, which allows the residual ^{222}Rn to be continuously monitored. Preparation of the device entails thermal physical vapor deposition of $^{226}\text{RaCl}_2$ directly onto the surface of a commercially available ion implanted Si-diode detector, resulting in a thin-layer geometry. This enables continuous collection of well resolved α -particle spectra of the nuclei, decaying within the deposited layer, with a detection efficiency of approximately 0.5 in a quasi 2π geometry. The continuously sampled α -particle spectra are used to derive the emanation by statistical inversion. It is possible to achieve this with high temporal resolution due to the small background and the high counting efficiency of the presented technique. The emanation derived in this way exhibits a dependence on the relative humidity of up to 15% in the range from 20% rH to 90% rH. Traceability to the SI is provided by employing defined solid-angle α -particle spectrometry to characterize the counting efficiency of the modified detectors. The presented technique is demonstrated to apply to a range covering the release of at least 1 to 210 ^{222}Rn atoms per second, and it results in SI-traceable emanation values with a combined standard uncertainty not exceeding 2%. This provides a pathway for the realization of reference atmospheres covering typical environmental ^{222}Rn levels and thus drastically improves the realization and the dissemination of the derived unit of the activity concentration concerning ^{222}Rn in air.

Keywords: ^{222}Rn emanation; physical vapor deposition; silicon detectors



Citation: Mertes, F.; Röttger, S.; Röttger, A. Development of ^{222}Rn Emanation Sources with Integrated Quasi 2π Active Monitoring. *Int. J. Environ. Res. Public Health* **2022**, *19*, 840. <https://doi.org/10.3390/ijerph19020840>

Academic Editor: Miroslaw Janik

Received: 26 November 2021

Accepted: 7 January 2022

Published: 12 January 2022

Publisher's Note: MDPI stays neutral with regard to jurisdictional claims in published maps and institutional affiliations.



Copyright: © 2022 by the authors. Licensee MDPI, Basel, Switzerland. This article is an open access article distributed under the terms and conditions of the Creative Commons Attribution (CC BY) license (<https://creativecommons.org/licenses/by/4.0/>).

1. Introduction

1.1. Background and Motivation

^{222}Rn is a naturally occurring radioactive noble gas, generated in the decay chain of primordial ^{238}U , and is thus released from soil to the atmosphere through diffusion processes. ^{222}Rn can be accumulated inside buildings and has been estimated to be the second most important cause of lung cancer. It is also the most relevant contributor to the average effective dose from natural sources experienced by the general public [1–3], which is why radon measurements are of interest for public health, radiation protection, and associated legislation. Moreover, in the environmental sciences, ^{222}Rn , in ambient air, was found to be an interesting proxy for mixing processes and terrestrial influence, so the measurement of its concentration finds a multitude of applications [4–13]. Activity concentrations of ^{222}Rn in outdoor air are in the order of a few $\text{Bq}\cdot\text{m}^{-3}$. The implementation of large-scale ^{222}Rn monitoring networks, to provide concentration data for the environmental sciences, and ensuring their comparability requires calibration techniques, for radon monitors in this concentration range, that are traceable to the international system of units (SI), as addressed in the project 19ENV01 traceRadon [14].

For this purpose, it will be necessary to realize and disseminate the unit $\text{Bq}\cdot\text{m}^{-3}$ for ^{222}Rn in air, with a small uncertainty over the required range, in a way that is traceable to the SI. For calibrations at such remarkably low activity concentrations, decaying reference

atmospheres of ^{222}Rn , e.g., produced by the method of Picolo et al. [15], are generally unsuitable for statistical reasons. Relatively recently, an alternative was found in the use of so-called ^{222}Rn emanation sources [16–18], which are ^{226}Ra sources constructed with such physicochemical properties that a known or measurable amount of ^{222}Rn is released per unit time, which enables calibration at static or even dynamic activity concentrations. Since the processes resulting in this release are generally linked to the physicochemical properties of the source material, the ^{222}Rn emanation from such sources must be expected to vary with environmental parameters such as humidity, temperature, and pressure. The correlation of emanation with these parameters has previously been reported for a variety of different materials, e.g., in [19–21]. It is, therefore, of interest to construct ^{222}Rn sources whose emanation can be monitored during operation to account for these factors, especially in the case of in-field calibrations of ambient level ^{222}Rn monitors, where the exact control of all relevant climatic parameters is not feasible. In the following we present a new method of construction of such sources, specifically designed to overcome the challenges that result from the considerably low activity range of ^{226}Ra that is needed to realize reference atmospheres in the outdoor concentration range by combining the ^{222}Rn source and detector into one system. The full traceability chain to the SI, regarding determination of the ^{222}Rn delivery by this system, is laid down, along with a discussion of possible causes for systematic bias and the limits of the presented technique. Additionally, a data analysis method, enabling the estimation of near real-time values of ^{222}Rn released from the system (in terms of atoms per unit time) through statistical inversion, is briefly presented, which is tightly coupled with its design and is applied to provide emanation estimates in times of non-steady-state situations.

1.2. Theoretical Considerations for ^{222}Rn Emanation Standards for Outdoor Activity Concentrations

Generally, state-of-the-art methods to quantify the ^{222}Rn emanation from solid sources (in a primary way, i.e., not using ^{222}Rn concentration measurement devices that require calibration) rely on measuring activity ratios of ^{226}Ra and the residual γ -ray emitting ^{222}Rn progeny, ^{214}Pb and ^{214}Bi , inside an emanation source to deduce the steady-state release of ^{222}Rn or, equivalently, a partitioning coefficient of ^{222}Rn between the free volume and the source volume [16,18,22]. The basis of this method is the conservation of the total amount of ^{222}Rn nuclei that are generated by the source, which can either emanate from the source or decay within the source, which is expressed by the following first order kinetics.

$$\frac{dA_{\text{Rn}-222}}{dt} = -\lambda_{\text{Rn}-222}A_{\text{Rn}-222} + \lambda_{\text{Rn}-222}A_{\text{Ra}-226} - \lambda_{\text{Rn}-222}\eta \quad (1)$$

where η describes the number of released ^{222}Rn atoms per unit time and A denote the activities of the respective nuclides in the emanation source.

Therefore, time-resolved measurements of the ^{222}Rn and ^{226}Ra activity of an emanation source allows one to estimate η , e.g., trivially in the steady-state of $\frac{dA_{\text{Rn}-222}}{dt} = 0$.

However, at the low activities needed to realize reference atmospheres at the ambient levels, γ -ray measurements of the equilibrated ^{222}Rn progeny ^{214}Pb and ^{214}Bi are not readily efficient enough to provide good temporal resolution of this method, especially regarding the real-time monitoring and considering the ubiquitous Poisson noise. A more direct, and much more sensitive, method entails the direct measurement of ^{222}Rn that remains in the emanation source, henceforth referred to as residual ^{222}Rn , through detection of its α -particles. However, with conventional α -particle spectrometry techniques, this is only possible in vacuo, e.g., [23], and thus, it is generally not useful to investigate emanation behavior directly under ambient conditions. This is due to the rapid energy loss of α -particles in any type of material, which leads to the significant distortion of α -particle spectra, recorded at a finite distance between the source and the detector, at ambient pressure. In such a spectrum, the contributions of ^{226}Ra and ^{222}Rn would no longer be well resolved, at which point the measurement of residual ^{222}Rn is not reliable.

The main aim of this work is to establish a method to use α -particle spectrometry to realize the supporting measurements needed to apply Equation (1) for standardization of η , which will allow for a reduction of statistical uncertainties associated with the inference of η and hence, to realize reference atmospheres at the ambient levels, even at changing environmental conditions.

One way to realize the direct α -particle spectrometry of the residual ^{222}Rn is to minimize the source-detector distance, i.e., ultimately, by direct construction of the source on, or even within, an α -particle spectrometric detector. Such a setup will henceforth be referred to as the Integrated ^{222}Rn Source/Detector (IRSD) and is proposed, discussed, and implemented within this work for the first time. It is schematically depicted in Figure 1. Typically, an α -particle spectrometer, such as the one used for the IRSD, is made up of an n-type silicon wafer that is p-doped at its entrance window, nowadays commonly through ion implantation, which results in entrance windows on the order of 50 nm thickness. To operate such a detector, the resultant p/n-junction is reversely biased from a backside ohmic contact to form a depletion layer of minimal free charge carriers. Due to their high interaction probability with matter, α -particles, which enter this layer of few 0.1 mm in thickness, are detected with practically unity probability, resulting in an electrical impulse that is proportional to the incident α -particle energy. Therefore, the theoretical detection probability in this configuration is 50% resulting from the 2π sr solid-angle subtended by the detector. Moreover, the typical background in α -particle spectrometry is orders of magnitude smaller than in any γ -ray spectrometric setup, and considering that the latter requires bulky lead shielding, emanation sources monitored by α -particle spectrometry are strongly preferred for the realization of in-field calibration procedures. In addition, α -particle spectrometers are typically a factor of 10 to 100 cheaper than γ -ray spectrometers. For these reasons, α -particle spectrometry is the superior choice for the purpose of monitoring the amount of residual ^{222}Rn .

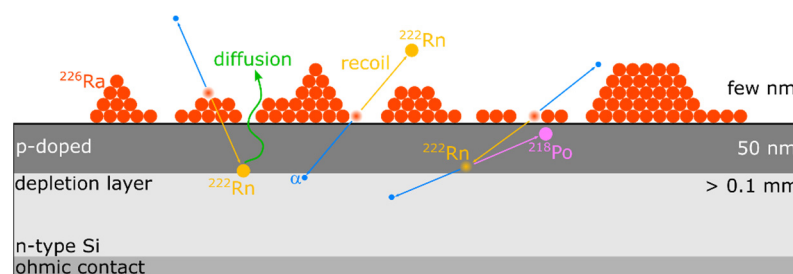


Figure 1. Schematic of silicon detector, modified with a thin layer of ^{226}Ra (IRSD). The silicon detector is made up of n-type silicon and a p-doped front side contact. Reverse biasing of the p/n-junction results in a depletion layer of several 0.1 mm thickness, which is the sensitive detection volume. The ^{222}Rn emanation mechanisms of recoiling and diffusion are depicted, as well as the spatial displacement of progeny along the decay chain. Details are given in the text.

However, in the hypothesized configuration, as shown in Figure 1, the IRSD, the p-doped entrance window and the deposited ^{226}Ra layer must be as thin as possible to minimize the variance in the energy loss of traversing α -particles. As a result of the variance in the energy loss, peaks in α -particle spectra generally show a left-handed (low energy) tailing that can lead to considerable overlap in the spectra and, thus, to significant difficulty of their analysis. Especially at such an infinitesimally small source-detector distance, the variance in the path length of α -particles entering the depletion layer through absorbing intermediate matter is high. Thus, pronounced low energy tailing of peaks in spectra, recorded in such a configuration results and methods to construct such a device must be chosen considering the mass of deposited impurities. Correspondingly, the analysis of α -particle spectra, which entails the determination of peak areas, must be carried out considering both the significance of the tailing and the specific nuclide composition at hand.

From the necessary thin layer of ^{226}Ra for the construction of the IRSD, the ^{222}Rn nuclei are released by two distinct processes. After the α -decay of ^{226}Ra , the ^{222}Rn nucleus carries a recoil energy of 86 keV on average, which is enough to overcome the binding energy of chemical bonds, electrostatic attraction, and other adsorption forces and to penetrate few nm of a solid material and several 10 μm of ambient pressure air [24]. Hence, the generated ^{222}Rn is, in part, released directly as a result of this recoil energy. Since the recoiling takes place isotropically, in a random direction, a fraction of up to 50% of the generated ^{222}Rn nuclei are implanted into the first few nm of the silicon detector. These ^{222}Rn nuclei may be subsequently released through a diffusion process, which supposedly depends strongly on the chemical composition of the radium layer and the temperature. Analogous displacement occurs for ^{218}Po and ^{214}Po , both of which are nuclei that result directly, and indirectly, from an α -decay within the decay chain of ^{226}Ra .

In this work, we investigate the feasibility and resultant performance of an IRSD system, produced by physical vapor deposition of ^{226}Ra , onto commercially available Si-detectors. Specific analytical techniques, which are detailed in Section 2, have been developed to best utilize the data that can be obtained by operation of the resultant IRSD to measure and, hence, to standardize the amount of emanating ^{222}Rn , even in non-steady state situations.

2. Materials and Methods

2.1. Construction of ^{226}Ra Modified Ion-Implanted Si-Diode Detectors

A specifically designed thermal physical vapor deposition (thermal-PVD) unit, depicted schematically in Figure 2, was implemented for the procedure of depositing a ^{226}Ra containing thin-layer directly onto commercially available implanted Si-diode detectors (e.g., Mirion PIPS[®] series, Ametek Ortec ULTRA[®] series) to implement the IRSD. It was built from standard conflat-flange components (316L stainless steel) with copper seals. The unit is equipped with a sample holder for mounting the detector to be modified with a ^{226}Ra layer (the future IRSD) at a nominal distance of 35 mm from the opening of a tantalum tube (EVOCHEM Advanced Materials) of approximately 25 mm length and 4 mm inner diameter. The tantalum tube was heated resistively, using powers up to 120 W DC, estimated (Stefan–Boltzmann law) to roughly correspond to a temperature of 1500 K in steady-state. The sample holder features a stainless-steel aperture system to confine the deposited ^{226}Ra layer by shadowing with a diameter of (20.0 ± 0.1) mm to minimize possible edge effects on the approx. 25 mm active diameter of the Si detectors. The aperture is tubular and elongated to the level of the opening of the tantalum tube to avoid contamination of the vacuum chamber as much as possible, presuming molecular flow and line-of-sight deposition. The aperture system was cleaned of ^{226}Ra with diluted HCl when the built-up contamination was found to be too large. Chamber pressure was maintained at around 10^{-4} Pa when the unit was operating using a membrane- and a turbomolecular pump (Pfeiffer vacuum HiPace80), while at ambient temperature, pressures as low as 5×10^{-6} Pa were attained.

As radium compounds are generally comparable to their barium homologues, it was presumed that RaCl_2 would show reasonably high vapor pressure at 1300 K, similar to BaCl_2 , with reportedly around 1 Pa to 10 Pa in this range [25,26], making it very feasible to evaporate, or even sublime, this radium compound at pressures in the order of 10^{-4} Pa to 10^{-3} Pa. Supposedly, RaCl_2 exists as a gas-phase molecule, and therefore, the species deposited using the present method is presumed to be RaCl_2 , which is thought to form its dihydrate upon contact with ambient moisture. Nonetheless, the sub-halide RaF of radium has been reported and investigated for radium recently [27], and the sub-halides are well known to exist for barium in the form of BaF and BaCl , which is why a mixture of radium from decomposition, radium chloride, and radium subchloride might be deposited using this method. Due to the chemical reactivity of some of the deposited species, it is expected that the chemical composition changes upon first exposure to the atmosphere.

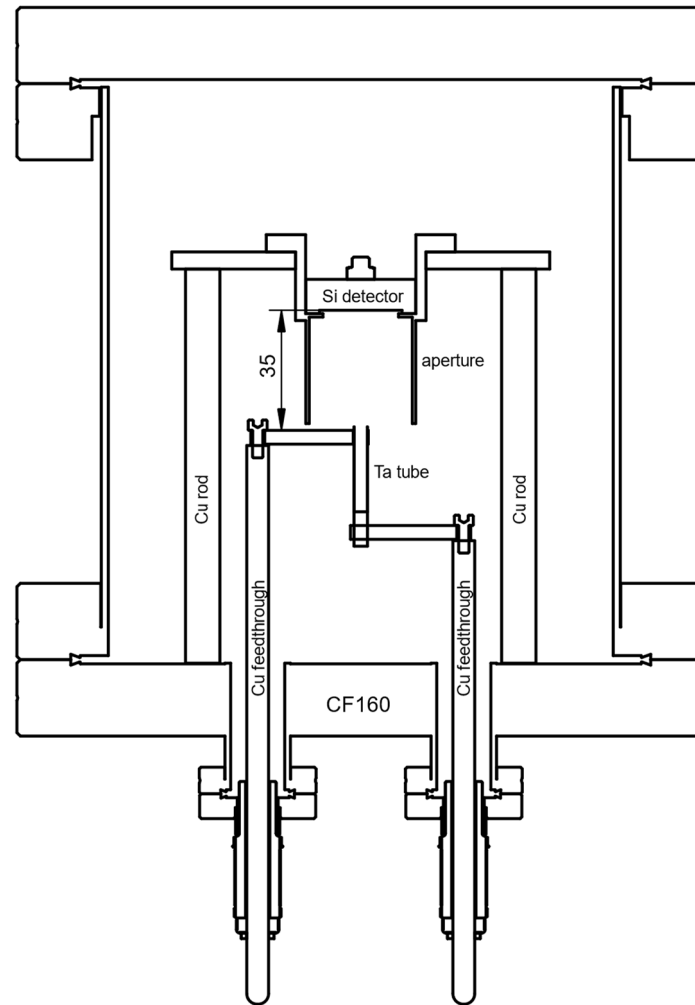


Figure 2. Schematic drawing of the custom thermal-PVD setup used in this work. Drawing not to scale. Details of the setup are described in Section 2.1.

As a source of $^{226}\text{RaCl}_2$ for the outlined thermal-PVD process, a PTB standard solution, nominally 71 kBq RaCl_2 ($^{226}\text{RaCl}_2$ in 0.1 HCl with 0.5% m/m BaCl_2), was converted into the nitrate and purified from its Ba^{2+} carrier through extraction chromatography with Sr-Resin[®] [28] (4,4'(5'')-di-tertbutyl-di-cyclohexano-18-crown-6 in 1-butanol dispersed on SiO_2 -particles). This step was deemed necessary to reduce the amount of BaCl_2 present and, hence, to minimize the amount of deposited material on the future IRSDs. The chromatography was monitored by the addition of nominally 13 kBq ^{133}Ba as a radiotracer. Resultant ^{133}Ba -free fractions were pooled and converted back into the chloride by addition, and subsequent evaporation, of conc. HCl and aliquoted for later use. This method was previously used in the production of reduced carrier ^{226}Ra solutions in [16], with optimized conditions based on [29]. ICP-MS was used to determine that the residual amount of Ba^{2+} was on the same order as the content of $^{226}\text{Ra}^{2+}$ (concerning atom numbers). For each deposition, an aliquot of this solution was transferred to a 0.5 mL conical bottom polyethylene flask, evaporated to dryness, and taken up in a suitably small volume (e.g., 0.1 mL) of 0.5 M HCl (Methanol was also tested, but it was found to lead to considerable losses by wall-attached or undissolved ^{226}Ra) to allow for transfer into the tubular tantalum evaporation source in which the solution was allowed to dry. For the removal of crystal water from the resultant $^{226}\text{RaCl}_2$ -dihydrate in the tube, the heating power was maintained at 20 W for the first 30 min of each deposition. Power was subsequently increased to a maximum of 120 W over 20 min. Deposition efficiencies, on the order of 15%, were experienced for this specific setup (including losses from solution transfer), mainly caused

by the specific deposition geometry. However, a non-negligible gross-alpha count rate was observed in close proximity to the tantalum tube orifice, likely attributable to the ^{226}Ra that did not make its way out of the tube. This might be due to the formation of highly non-volatile tantalates or chloro-tantalates.

A total of four IRSD were constructed in this way, and results are compiled in Table 1, where the deposited ^{226}Ra activity and the counting efficiency for ^{226}Ra were determined, as presented, in Section 2.4. Before the deposition onto detectors was carried out, bare prime-grade polished 1" p-type Si-wafers were modified with $^{226}\text{RaCl}_2$ on the order of 10 Bq to be investigated by scanning electron microscopy (SEM, Thermo Fisher Scientific Verios G4, through-lens secondary electron detector).

Table 1. Overview over produced IRSD.

Detector Type	Active Area/Depletion Depth	A(^{226}Ra)/Bq	$\epsilon_{\text{Ra-226}}$ /cps Bq $^{-1}$	Observed Mean η
Mirion PIPS [®]	450 mm ² /300 μm	1.91 \pm 0.02	0.502 \pm 0.006	0.999 \pm 0.017
Ametek Ortec ULTRA [®]	450 mm ² /300 μm	66.4 \pm 0.5	0.494 \pm 0.004	Figure 8
Mirion PIPS [®]	450 mm ² /300 μm	158.6 \pm 1.7	0.494 \pm 0.005	Figure 7
Mirion PIPS [®]	450 mm ² /100 μm	442 \pm 4	0.492 \pm 0.005	209 \pm 4

/ represents division by a unit.

The thin-film production method must be gentle enough not to damage the p/n-junction characteristics of the detector, which could potentially result from knock-ons during ion implantation or sputter deposition, temperature-induced diffusion of junction dopants, or excessive contamination. Thermal stress in the form of rapid or excessive heating and cooling of the detectors, along with the associated force exerted from the expanding housing and backside contact, can easily shatter the Si-wafer.

In spite of potential thermal stress, thermal physical vapor deposition (thermal-PVD) was employed in this study due to its relative simplicity and ability to provide relatively clean deposits, compared with, e.g., electrodeposition.

A tubular geometry was chosen for the vaporization unit, since it was expected to provide a somewhat directional effusion of the emerging gas-phase molecules as a function of the diameter to length ratio, favoring the fraction of ^{226}Ra , released into the solid-angle subtended by the future IRSD. This geometry is, thus, presumed to result in increased deposition efficiency at the cost of reduced uniformity.

2.2. Operation of Integrated ^{222}Rn Sources/Detectors

IRSDs constructed as described above were operated using standard pre-amplifiers (Mirion, Model 2018EB, and Ametek Ortec, Model 142B, respectively) in a light-tight environment at ambient and reduced pressures. Pulse height spectrum acquisition was carried out using a labZy nanoMCA-II and a Mirion Lynx, using integration times between 600 s and 3600 s, adjusted to the ^{226}Ra activity of the respective IRSD. The bias voltage was chosen according to the manufacturer's specifications. For general spectrum acquisition, the humidity and temperature of the environment were not controlled. However, two IRSDs were also operated in a nominal 50 L closed volume in which the temperature, relative humidity, and pressure were recorded. At specific times, the relative humidity in this volume was changed by the introduction of warm water or by flushing with laboratory air to investigate the dependence of the emanation of each IRSD on the relative humidity. In this case, the method described in Section 2.5 was used to calculate the emanation based on time-series of collected α -particle spectra.

2.3. Autoradiography

To investigate the spatial distribution of radioactivity on each of the produced IRSDs, autoradiographs were recorded using a FUJIFILM FLA-9000 readout device and digital

radiography films. Four ^{238}Pu reference point sources and a 3d printed holder were used to place the ^{238}Pu sources rectangularly around the respective IRSD. The images of the ^{238}Pu sources created on the radiography film were used to position a 140×140 grid of $(0.2 \cdot 0.2) \text{ mm}^2$ pixels over which the readout was conducted. The grid was placed in such a way that it was centered with respect to the ^{238}Pu sources and, due to the sample holder, also with respect to the outer diameter of the IRSD housing. The IRSDs were placed directly on top of the film, resulting in a displacement of the active surface of the detectors of approximately 1 mm from the radiography film because of the recess in the detector housing (Figure 3a).

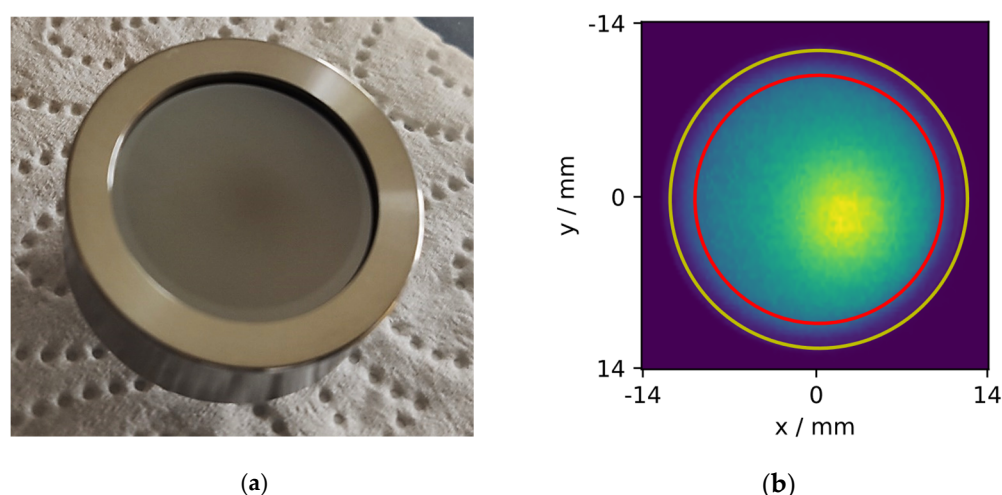


Figure 3. (a) shows a photograph of an IRSD based on a 450 mm^2 Canberra PIPS[®] detector, modified with a layer containing $440 \text{ Bq } ^{226}\text{RaCl}_2$. (b) shows a digital autoradiograph obtained from such a deposit where the inner diameter of the recessed Si-surface is given in yellow and the diameter of the shadowing aperture is given in red.

2.4. Alpha-Particle Spectrometry under Defined Solid-Angle

2.4.1. General Defined Solid-Angle Setup

The PTB primary defined-solid angle (DSA) α -particle spectrometry system was used to perform DSA α -particle spectrometry of the produced IRSDs, with an approximate geometrical efficiency of 1%, as similarly used in [16,23]. DSA α -particle spectrometry is among the most accurate tools for the standardization of activity of α -emitting nuclides, routinely achieving uncertainties below 1% [30,31]. The basis of this method is the calculation of the solid-angle, subtended by an α -particle detector, and hence, its counting efficiency through precise knowledge of the measurement geometry, defined by an aperture system. This absolute measurement technique was used to determine the deposited ^{226}Ra activity, traceably to the SI, which was subsequently used to calibrate the counting efficiency of each IRSD by comparison of the IRSD α -particle spectrum with the determined value of its ^{226}Ra activity. In this way, traceability to the SI is established.

IRSDs were mounted in the DSA spectrometer using a 3d printed holder and a spring-loaded screw to push the housing against the bottom aperture of the DSA setup. All geometrical parameters of the reference DSA setup are known, traceably, to PTB standards and, with little uncertainty, are given in more detail in [16]. However, the recess depth of the Si-surface in the IRSD was unknown. The effective distance of the active IRSD surface to the top aperture was determined for each measurement using a calibrated, digital depth micrometer screw (Mitutoyo, resolution 0.001 mm), relative to the standard sample holder, of which distance from the top aperture is known. Each depth measurement was repeated for a total of eight positions on the IRSD wafer, results were averaged, and their standard deviation was used as the uncertainty (generally $> 0.03 \text{ mm}$) of the source to aperture distance since it was higher than the uncertainty of the micrometer screw

measurement, likely due to tilting and/or warping introduced by the wafer mounting mechanism (frontside contact) in the housing and the IRSD holder. The system was operated at chamber pressures of approx. 10^{-1} Pa. Spectra of the reference DSA detector, as well as the IRSDs, were each recorded over integration times that were chosen concerning each IRSD's ^{226}Ra activity. However, spectra obtained were summed up for data analysis, neglecting possible gain-shifts. Total measurement times were adjusted concerning each deposited activity.

2.4.2. Calculation of Geometrical Efficiency

The geometrical efficiency G of the DSA setup was calculated separately for each measurement by evaluating the following relation through Monte–Carlo integration,

$$G = \frac{1}{4\pi} \frac{\int_A w_{dA} \Omega_{dA} dA}{\int_A w_{dA} dA} \quad (2)$$

where Ω_{dA} denotes the solid angle of the area element dA subtended by the detector, w_{dA} denotes the relative activity weight of the area element, and A denotes the total source area.

The uncertainty of G was estimated by resampling the geometrical parameters within their experimentally determined probability distributions, similar to [16,32]. As reported therein, the computation of G was carried out for each specific realization of the geometry through tracking randomly generated paths through the geometry and counting the detector hits. The sampling of origin points was carried out by using the experimentally determined, uniformly oversampled activity distribution from the autoradiographs from Section 2.2. A randomly distributed rotational angle uniform in the circle, a normally distributed pixel size uncertainty of 10%, and normally distributed x, y -offsets, with a standard deviation of 0.5 mm each, are included in the analysis of the geometrical uncertainty.

2.4.3. Peak Area Analysis

To derive the activity from α -particle spectra, peak areas are to be determined accurately. As discussed in Section 1.2, the peaks in the α -particle spectra, recorded with the IRSDs, show a slight overlap due to their left-handed tailing. To account for this, the peak areas in all recorded α -particle spectra were determined using non-linear regression based on a refined version of the models introduced in [33] and further improved by [34]. In these modeling procedures, each peak is represented as a mixture of exponentially modified Gaussians (ExGaussian), often with shared tailing parameters.

Due to the slight difference of the distance of each α -emitting nuclide (^{226}Ra , ^{222}Rn , ^{218}Po , and ^{214}Po) to the depletion layer (Figure 1) and their respective decay characteristics, each peak was found to be slightly differently tailed, and hence, a simple restriction to shared tailing parameters, commonly applied in α -particle spectrometry, was found to lead to insufficiently well modeled tailing. To account for this, a special regression technique was developed that allows for differently tailed peaks, while maintaining reasonable convergence speed and robustness, considering the high number of required parameters. This is achieved by ℓ^2 -regularization of the tailing parameters, keeping them somewhat similar but not entirely shared among the peaks of each nuclide in the decay chain. Physically, this is motivated by the fact that the tailing is supposed to be similar, due to the relative similarity of the α -particle energies and the relatively small deviation in the effective path length through all absorbing layers. Specific details of this modeling procedure are given in Appendix A.

2.5. Estimation of ^{222}Rn Emanation from Spectral Time-Series

As stated in Section 1.2, Equation (1), the evolution of the ^{222}Rn activity retained in the IRSDs must follow first-order continuity, accounting for the emanation of ^{222}Rn from the deposited layer, η , in terms of emanating ^{222}Rn atoms per unit time.

From the analysis of IRSD spectrometric time-series, a discretized version of the potentially time varying ^{222}Rn activity, $A_{Rn-222}(t)$, and the ^{226}Ra activity, $A_{Ra-226}(t)$, are accessible through the analysis of the peak areas. The estimation of η (or derived quantities such as the emanation coefficient), based on those time-series, is an inverse problem unless a steady-state of $\frac{dA_{Rn-222}}{dt} = 0$ has been reached. The observed version of $A_{Rn-222}(t)$ is given by the discretized convolution of η , with the impulse-response defined by the radioactive kinetics. In previous work [35,36], we developed and presented a deconvolution technique that allows the probability density function (PDF) of a discretized version of $\eta(t)$ to be estimated, including the propagation of systematic uncertainty, using the supporting measurements of the residual ^{222}Rn activity in the source.

This technique is based on recursive Bayesian inference, using a switching linear dynamical system model to estimate collections of multivariate PDFs for a state variable $x = \left[A_{Rn-222} \quad A_{Ra-226} \quad \eta \quad \frac{\partial \eta}{\partial t} \right]^T$, given a collection of peak-areas derived from a collection of spectra $S_{1\dots n}$ indexed by n , obtained at the measurement times t_n in the set of all measurement times T , while t_N describes the last measurement time instant. This includes inference of the filtering densities $p(x_n | S_{1\dots n})$, i.e., using, for each x_n , the information contained in all spectra, up to the time t_n , and their recursive correction into the smoothing densities $p(x_n | S_{1\dots N})$, using the information in all spectra, respectively. The algorithm accounts for potential changes of η during the integration time of the spectrum collection by integrating the forward propagation equations and using a certain Gaussian process autoregressive regularization on η with tunable parameters, which are optimized with respect to the marginal likelihood of the time-series. To improve fidelity during steep changes in η , as well as improving results in stable or slowly drifting regimes, the algorithm additionally estimates the probability for being in reasonably stable regimes along the time-series, with a process model for both the unstable and stable regimes. However, the uncertainty arising from the specifically chosen Gaussian process and their tuned parameters is not propagated, as this would require the evaluation of intractable integrals through computationally infeasible Markov-Chain Monte-Carlo and is considered negligible in comparison with the systematic uncertainty of the counting efficiency.

To estimate the IRSD emanation time-series in this work, this approach was modified to include the information on A_{Ra-226} acquired in each spectrum, which was unused in the initial development for γ -ray spectrometry [35,36]. The input quantities to the algorithm, which, in the following, we refer to by the *SLDS-deconvolution*, are the peak-areas of ^{222}Rn and ^{226}Ra , the time-offset between each spectrum and their live times, a prior of the initial state, as well as an estimate of the PDF of the counting efficiency vector $\varepsilon = \begin{bmatrix} \varepsilon_{Rn-222} \\ \varepsilon_{Ra-226} \end{bmatrix}$. Necessary inference equations are given in Appendix B, and for a detailed presentation of the algorithm, the reader is directed to [35,36]. The uncertainty in ε is propagated across the model using a sigma point method, as described in Appendix B. In steady-state situations, where $\frac{dA_{Rn-222}}{dt} = 0$, η is simply given by the solution of Equation (1), using the components of the counting efficiency vector ε and the count rates of the respective nuclides as

$$\eta = \frac{N_{Ra-226}}{\varepsilon_{Rn-226}t} - \frac{N_{Rn-222}}{\varepsilon_{Rn-222}t} \tag{3}$$

3. Results and Discussion

3.1. Morphological Characterization

The experimental procedure to construct the IRSD is demonstrated to form nano-crystalline deposits with typical particle sizes on the order of 10 nm and larger agglomerates of 100 nm, as shown in the SEM micrographs of a similarly manufactured modified Si-wafer (Figure 4a,b). At low magnification (Figure 4c), only a small number of larger impurities and defects can be identified. However, bright particles, of about 300 nm in size, in Figure 4a are most likely foreign particles, since they could also be observed on the shadowed portion of the wafer. The morphology of the surface appears to be considerably

different than in our previously published work with electrodeposited ^{226}Ra [16], where much more voluminous deposits were observed. Given that similar amounts of ^{226}Ra were deposited in both studies, it is suggested that the present method produces considerably cleaner deposits.

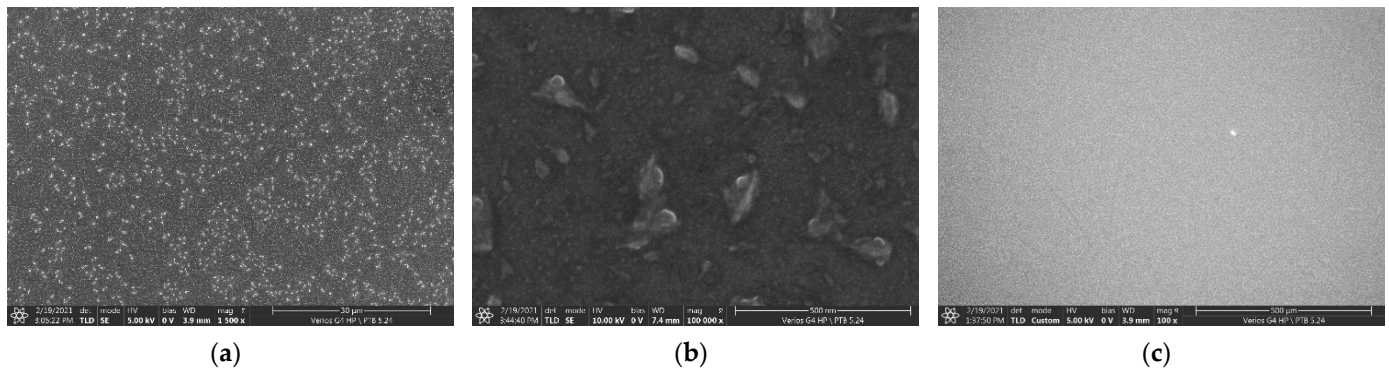


Figure 4. Secondary-electron SEM Images (through-lens detector) of thermal-PVD $^{226}\text{RaCl}_2$ on a bare 1'' prime Si-wafer at different magnifications: (a) 1500 \times , (b) 100,000 \times , (c) 100 \times . Length of bar: (a) 30 μm (b) 500 nm, (c) 500 μm .

However, since the layer is still visible to the naked eye at approx. 440 Bq (corresponding to approx. 15 ng of $^{226}\text{RaCl}_2$, Figure 3a), most likely, it is composed almost entirely of other materials. This includes impurities present in the obtained $^{226}\text{RaCl}_2$ solution, impurities introduced by all the solvents used, and impurities from the chamber materials at the respective deposition conditions. In the future, some of these impurities could potentially be avoided by a refined process, involving a mechanical shutter and feedback temperature control, to avoid contamination with readily volatile species. Nonetheless, the DSA α -particle setup showed a FWHM of only around 15 keV for the 4.78 MeV emission of ^{226}Ra , where, previously, around 20 keV was measured for electrodeposited and around 16 keV for ion implanted ^{226}Ra with the same setup [16,23], indicating relatively small α -particle energy loss within the deposited layer.

Figure 3a shows a photograph of a freshly prepared IRSD with approx. 440 Bq of $^{226}\text{RaCl}_2$, hinting at the inhomogeneity of the deposit. This is more clearly evident in Figure 3b, a typical digital autoradiograph, obtained as explained in Section 2.3. The deposits of smaller activities, shown in Table 1, were initially not visible to the naked eye. However, they turned irreversibly slightly pale white upon exposure to very humid air. The deposits were found to be soluble in water, which means that IRSDs formed in this way should not be operated in condensing atmospheres.

The eccentrically peaked activity distribution is likely due to eccentric and/or non-perpendicular manual installation of the evaporation source. Nonetheless, the radiography image shows that effusion from the tantalum tube is quite directional, which is in line with our presumptions. Since part of the high deposition density area is shadowed by the aperture due to this eccentricity, the deposition efficiency could, potentially, be improved by optimization of the evaporator position and orientation.

3.2. Typical α -Particle Spectrum Features of the IRSD

Typically, and dependent on the characteristics of interfering electronic noise from the experimental setup, the FWHM of the higher energy ^{226}Ra emission was found to be between 21 keV and 40 keV in the IRSD α -particle spectrum. While the observed FWHM are close to the manufacturer's specifications (between 17 keV and 20 keV), pronounced low-energy tailing of the peaks can be identified that results from the high variability of the α -particle energy loss in the dead-layer (p-doped region) and deposited layers, as stated in Section 1.2.

The deconvolution procedure, outlined in Section 2.4.3 and Appendix A, a typical result shown in Figure 5, yields that approximately 1.4%, 1.2%, 0.8%, and 0.5% of the total counts of the emissions related to the isotopes ^{210}Po , ^{222}Rn , ^{218}Po , and ^{214}Po , respectively, appear below a threshold of 4.8 MeV in the spectrum, i.e., the ^{226}Ra region. Considering that, due to emanation, the amount of ^{222}Rn and progeny present in the layers is around 50% of the amount of ^{226}Ra , while ^{210}Po is not present in significant quantities, this yields a maximum deviation of only 1.25% in the ^{226}Ra area determination if the tailing contributions were entirely ignored.

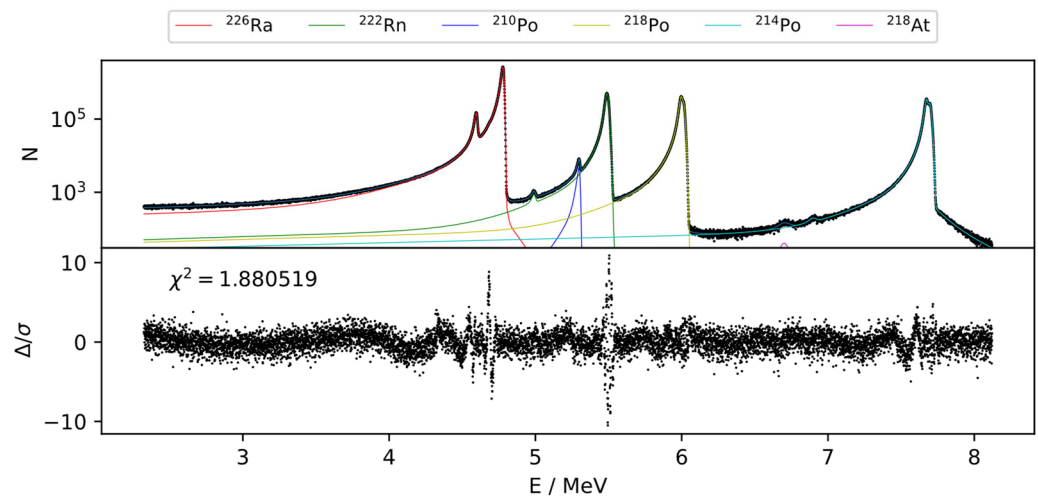


Figure 5. Typical α -particle spectrum obtained with a 442 Bq ^{226}Ra IRSD (modified Canberra PIPS[®] detector of nominal 100 μm depletion depth, 450 mm^2 active area), over the first $6 \cdot 10^5$ s after modification and regression results, according to Section 2.4.3. The 4.8 MeV ^{226}Ra emission shows a FWHM of approx. 21 keV and a FWTM of approx. 48 keV. Progeny peaks appear slightly shifted to higher energies (wrt. the energy calibration obtained from the ^{226}Ra emissions).

In all recorded spectra, the tailing properties were found to be very similar, indicating that the main contribution to the energy loss is due to the dead-layer of similar thicknesses rather than due to the deposited layers of presumably variable areal densities.

Varying amounts of ^{210}Po are also present. In general, the ^{210}Po is introduced from ^{210}Po in the original ^{226}Ra solution, but it will also grow in slowly over time.

Remarkably, the ^{214}Po and ^{218}Po peaks of the spectrum show higher energy satellites with increasing energy shift between the main progeny peak and the satellite peaks in the order (^{222}Rn) < ^{218}Po < ^{214}Po . An unresolved satellite peak might be present below the ^{222}Rn peak, since this peak appears much broader than the main ^{226}Ra emission. Due to the varying energy shift increasing along the decay chain, these satellites are thought to be related to the self-implantation of ^{222}Rn and the short-lived progeny (SLP) ^{218}Po and ^{214}Po , as shown schematically in Figure 1. As a result, ^{222}Rn and SLP are either present in the material deposited on the detector or injected into the p-doped region of the IRSD, due to their recoil, which is thought to cause the varying energy shift. In addition, some of the recoil energy might be detected in coincidence with the α -particle under some circumstances, i.e., injection of SLP to within the depletion zone. However, the energy shifts observed are on the order of 10 keV to 30 keV, while the coincidence of the α -particle, with the full recoil energy, would result in peak shifts of up to 200 keV. This indicates that ^{218}Po and ^{214}Po do not get implanted past the dead-layer to within the depletion zone.

Slight right-handed tailing of the ^{226}Ra , ^{222}Rn , and ^{218}Po peaks can also be identified, attributable to random α -e and α -photon coincidences, while the usual pronounced right-handed tailing of the ^{214}Po peak is due to the α - β true coincidence with the ^{214}Bi β -particle, caused by the particularly small half-life of ^{214}Po .

It was found that the ^{214}Po and ^{218}Po peak areas are smaller than the ^{222}Rn peak area under all observed circumstances. The deviation of those two peaks from one another, and especially from the ^{222}Rn peak area, was found to be dependent on the pressure of the environment as shown in Figure 6, depicting a time-series of the initial ingrowth of count-rates of the different nuclei in the deposited layer under reduced pressure and ambient conditions. Under ambient conditions, ^{218}Po and ^{214}Po count rates are observed to be approximately 1% to 2% lower than the ^{222}Rn count rate. This can be explained by ^{218}Po and ^{214}Po recoiling that leads to the additional ejection of ^{218}Po and ^{214}Po , Figure 1. The mean free path of those nuclei in ambient pressure air is on the order of 100 nm, suppressing the recoiling strongly, where ^{218}Po and ^{214}Po that lost enough energy, in proximity to the deposited layer, potentially remain adsorbed. However, some recoiling can still be observed, even in ambient pressure air. Due to this disturbance, with potential pressure sensitivity, the SLP peak areas were not further used to assess the activity of ^{222}Rn remaining in the IRSD.

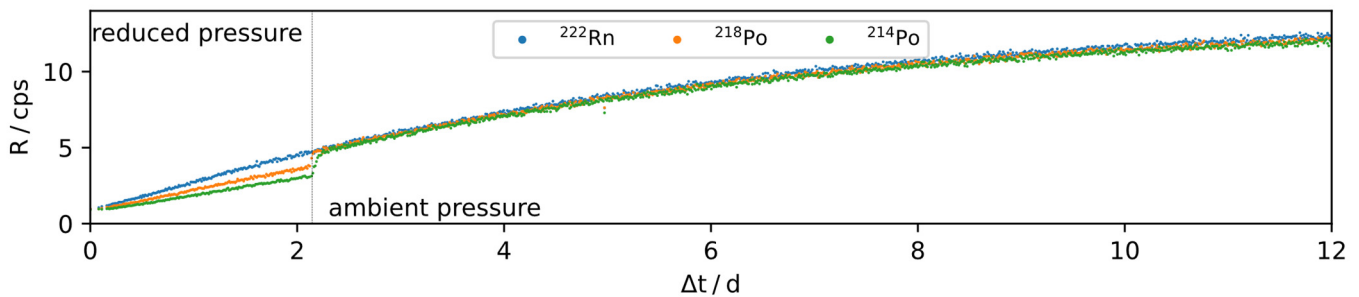


Figure 6. Ingrowth of α -particle count rates of an IRSD after initial ^{226}Ra deposition at reduced and ambient pressure.

3.3. Efficiency Calibration

The counting efficiency of each IRSD was deduced from the data obtained through DSA α -particle spectrometry, Section 2.4, using the peak areas of ^{226}Ra in each detector's spectrum (DSA detector and IRSD), as determined by the regression models in Section 2.4.2. The counting efficiency of the IRSDs is hence given by

$$\epsilon_{\text{Ra}-226} = \frac{N_{\text{Ra}-226, \text{IRSD}} c_{\text{Tail, IRSD}}}{N_{\text{Ra}-226, \text{DSA}} c_{\text{backscatter}} c_{\text{Tail, DSA}}} \frac{t_{\text{DSA}}}{t_{\text{IRSD}}} \frac{1}{4\pi} \frac{\int_A w_{\text{dA}} \Omega_{\text{dA}} dA}{\int_A w_{\text{dA}} dA} \quad (4)$$

where N describes the peak areas of the respective detector, t describes the live times of the respective detector, and c describes correction factors.

An overview of the obtained ^{226}Ra counting efficiencies is given in Table 1, and the deposited ^{226}Ra activity was determined analogously. Considering the uncertainty of this method, the counting efficiencies observed were generally very close to 0.5, with a maximum observed relative deviation of 1.6%. It is presumed that the deviation from the 2π sr geometrical efficiency, 0.5, results from backscattering and self-absorption losses in the deposited layer and the dead-layer of the IRSD. Since the covariance matrix estimate of the peak areas from the inverted Hessian of the regression procedure, outlined in Section 2.4.3, can lead to underestimation of the uncertainty due to non-stochastic residuals and amplification of numerical errors, and based upon the observations in Section 3.2, an additional normally distributed uncertainty, with a standard deviation of 0.3% for each peak area, was introduced to account for possible shortcomings of the modeling procedure. This value is based on the estimated tailing contributions of the short-lived progeny. As pointed out in earlier work, the contribution of scattered particles to the peak areas introduces an uncertainty of approximately 0.2% [16,37]. It is worthy to note that the backscattering causes an anti-correlation of the scattering bias of the DSA peak area and the IRSD peak area. However, this is intentionally not corrected to deduce the counting efficiency of the

IRSD resulting from all effects. Due to layer areal density and random coincidence, the effective counting efficiency is expected to decrease with increasing ²²⁶Ra activity. However, in the investigated activity range this effect could not significantly be observed. Generally, uncertainty on the order of 1% in the counting efficiency or equivalently deposited activity was achieved using this method which is dominated by the uncertainty in the solid-angle resulting from the distance measurement of the recessed Si-surface of the IRSD relative to the standard geometry. An uncertainty budget is given as an example in Table 2 for the determination of the efficiency of the IRSD, with approx. 2 Bq ²²⁶Ra, where the least counting statistics were accumulated.

Table 2. Example uncertainty budget of efficiency determination of an IRSD of 2 Bq ²²⁶Ra.

Description and Type	Value and Uncertainty	Rel. Uncertainty	Rel. Contribution
Solid angle (systematic)	(0.00940 ± 0.00006) 4π sr	0.6%	28.4%
Backscattering _{DSA} (systematic)	1 ± 0.002	0.2%	3%
Tailing _{DSA} (systematic)	1 ± 0.003	0.3%	6.7%
Tailing _{Si} (systematic)	1 ± 0.003	0.3%	6.7%
²²⁶ Ra rate _{DSA} (stochastic)	(0.01796 ± 0.00015) s ⁻¹	0.8%	55.1%
²²⁶ Ra rate _{Si} (stochastic)	(0.9595 ± 0.0004) s ⁻¹	0.04%	0.1%
ϵ_{Ra-226}	0.502 ± 0.006	1.2%	

However, the DSA α-particle spectrometry does not allow for a precise measurement of the counting efficiency for ²²²Rn and SLP that resides within the IRSD, since the recoiling of ²²²Rn and SLP nuclei from the IRSD causes implantation into the geometrical components and the detector of the DSA setup. The emission of α-particles from those recoil implanted nuclides thus contributes to the peak areas of each detector to varying degrees. Due to this, no attempt was made to derive the ²²²Rn and progeny efficiency separately, and for the following, it is assumed that the ²²²Rn and ²²⁶Ra counting efficiencies are close to each other. Since the energy of the emitted α-particles of both nuclides are relatively similar, it is assumed that the backscattering and absorption losses are also similar. However, the recoiling causes slight displacement of the positional distribution of the ²²²Rn nuclei to the ²²⁶Ra positions, thereby possibly introducing a slight difference in the true counting efficiency. To model this effect, we assumed, in the following, that the counting efficiency of ²²⁶Ra and ²²²Rn is given by a multivariate normal distribution with a high correlation coefficient. However, for the following analyses using the counting efficiency, the peak-areas of ²²²Rn and ²²⁶Ra are thought to be anti-correlated, which has the opposite effect, and hence, a relatively balanced correlation coefficient of 0.6 was chosen to approximately model both effects.

$$\begin{bmatrix} \epsilon_{Rn-222} \\ \epsilon_{Ra-226} \end{bmatrix} \sim \mathcal{N}\left(\mu_{\epsilon_{Ra-226}} \begin{bmatrix} 1 \\ 1 \end{bmatrix}, \sigma_{\epsilon_{Ra-226}}^2 \begin{bmatrix} 1 & 0.6 \\ 0.6 & 1 \end{bmatrix}\right) \tag{5}$$

Regression model induced uncertainties can then be neglected, since those systematic factors are already included in the assumed counting efficiency distribution and the statistical uncertainty of the peak areas is estimated by assuming a Poisson distribution.

3.4. Estimation of ²²²Rn Emanation from IRSD Time-Series and its Humidity Dependence

As described in Section 2.5, the emanation of ²²²Rn in non-steady-state situations is estimated using the *SLDS-deconvolution* approach of the observed counts time-series, which is evaluated from the IRSD spectrometric time-series using the methods outlined in Section 2.4.3. The statistical uncertainty of the determined peak areas is estimated, recur-

sively, alongside the prediction step of the filtering algorithm (Section 2.5, [36], Appendix B), accounting approximately for possible tailing contributions, as well as the Poisson statistics, as

$$\Sigma_n \approx \epsilon M \mu_{n-1} M^T \epsilon^T + \sigma_{Area} 2 \epsilon M \mu_{n-1} M^T \epsilon^T \begin{bmatrix} 1 & -0.8 \\ -0.8 & 1 \end{bmatrix} \epsilon M \mu_{n-1} M^T \epsilon^T \quad (6)$$

where μ_{n-1} is the mean of the state variable at the previous step, ϵ is the counting efficiency vector, M is a matrix that maps the state onto the measurement space, Appendix B, and σ_{Area} is an additional uncertainty from uncertain area determinations, which was chosen according to the observations in 3.2 to be 0.005.

Results of the outlined inference procedure for the IRSD, of approximately 160 Bq and 65 Bq, over time-series, consisting of 15,000 and 9000 α -particle spectra, are shown in Figures 7 and 8, respectively. During these times, the relative humidity was varied in the range of 20% rH and 90% rH, while the temperature was kept constant. For the remaining IRSDs, experiments with dynamic conditions were not carried out and, therefore, the steady-state emanation is reported in Table 1, as the detectors showed stable emanation characteristics over 160 days (2 Bq detector) and 15 days (440 Bq detector) respectively, operating in a climate-controlled laboratory. Due to the high counting efficiency of the setup, the statistical uncertainty vanishes quickly alongside repeated observations within the time-series, in which case the combined relative uncertainty reduces to a steady value due to the systematic effects. Based on Equation (3), and using the observations from Section 3.3, the steady-state relative systematic uncertainty of η can thus be expressed by linearization as

$$\frac{\sigma_\eta}{\eta} = \frac{\sigma_\epsilon}{\epsilon} \sqrt{1 + 2 \frac{N_{Ra} N_{Rn}}{(N_{Ra} - N_{Rn})^2} (1 - \rho_\epsilon)} \quad (7)$$

where ρ_ϵ denotes the correlation coefficient of ϵ_{Rn-222} and ϵ_{Ra-226} .

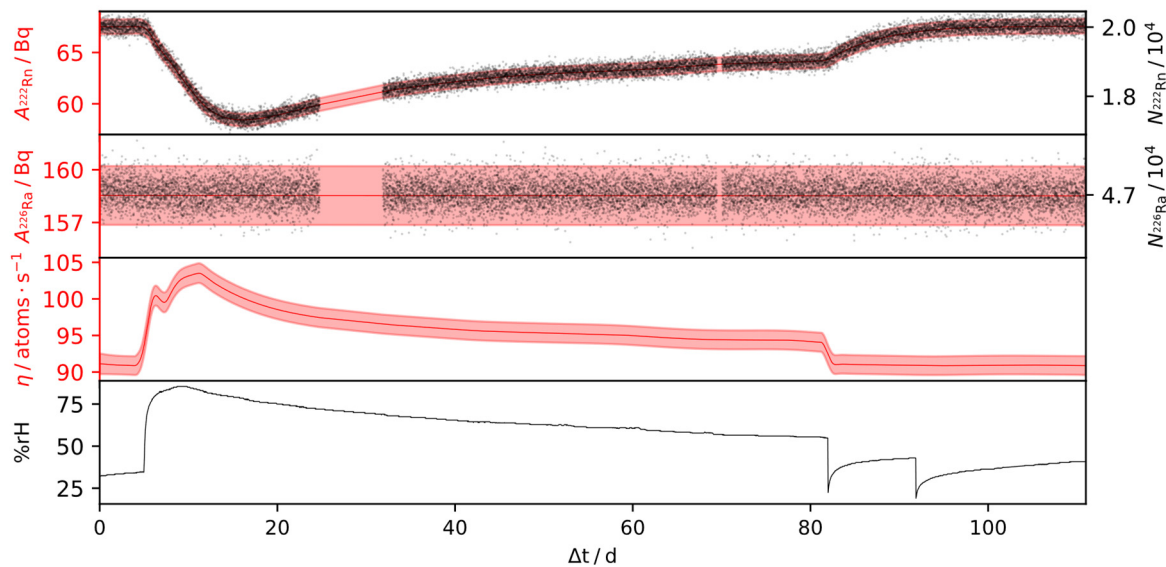


Figure 7. SLDS-deconvolution result for a IRSD of approx. 160 Bq ^{226}Ra . Black dots represent the determined peak areas of a set of approx. 15,000 spectra, taken over 110 days at a sampling interval of 600 s of ^{222}Rn and ^{226}Ra , respectively. Red curves represent the smoothed results for the residual ^{222}Rn - and ^{226}Ra activities and the deconvolved time-series of the emanation η , according to Section 2.5. Shaded areas represent the 1σ credible intervals, almost entirely caused by the systematic uncertainty.

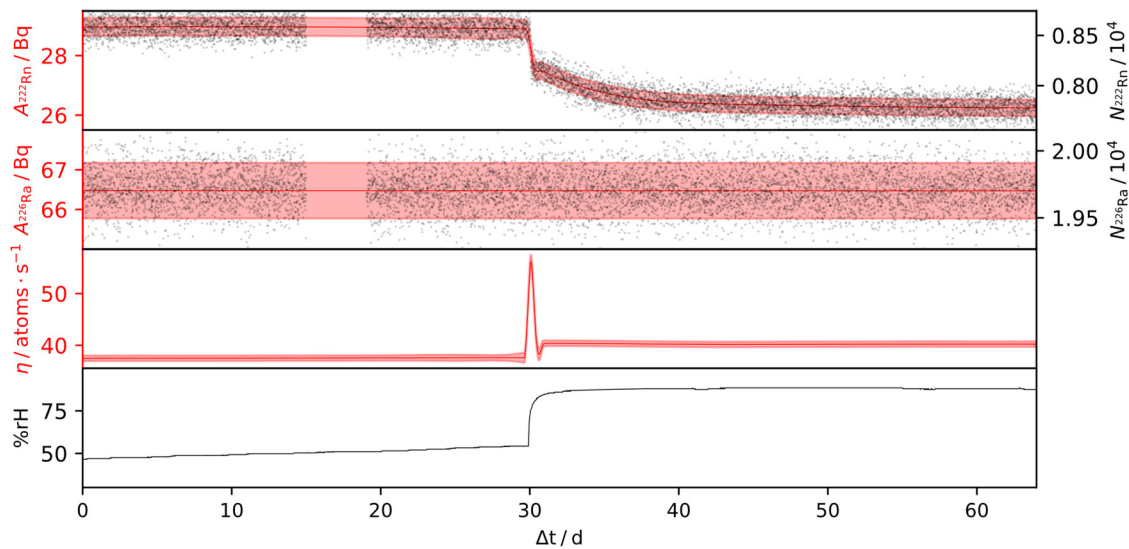


Figure 8. SLDS-deconvolution result for an IRSD of approx. 65 Bq ^{226}Ra . Black dots represent the determined peak areas of a set of approx. 9000 spectra, taken over 65 days at a sampling interval of 600 s of ^{222}Rn and ^{226}Ra , respectively. Red curves represent the smoothed results for the residual ^{222}Rn and ^{226}Ra activities and the deconvolved time-series of the emanation η , according to Section 2.5. Shaded areas represent the 1σ credible intervals, almost entirely caused by the systematic uncertainty.

Note that the relative uncertainty in η decreases with an increasing correlation coefficient of the counting efficiency vector. Based on the proposition of a counting efficiency correlation coefficient of 0.6 and the typically observed 50% emanation, this evaluates to approximately 1.5% to 2% systematic uncertainty in η , depending on its absolute value and the relative uncertainty of the counting efficiency. Based on this observation, the sigma point method outlined in Appendix B proves to be the best option for uncertainty propagation in the SLDS-deconvolution.

From the presented deconvolution results in Figures 7 and 8, it is evident that the relative humidity impacts the emanation positively. Therein, changes of the steady-state values were observed up to 15% on a range between 20% rH and 90% rH. However, the humidity dependence shows non-linear behavior, with an increasing rate of change at higher relative humidity values. Interestingly, peaks in emanation can be observed in response to steep positive gradients in the humidity, while jump changes from high to low humidity do not cause those peaks. Therefore, the behavior of the IRSD depends on the direction of a change in the ambient relative humidity, i.e., whether the deposit is wetting or drying.

The explanation for this effect lies in the state of disequilibrium that results from each of those changes. While most of the ^{222}Rn retained within the IRSD is buried in the silicon wafer, such as in Figure 1, some of it is evidently loosely adsorbed to the surface or within the $^{226}\text{RaCl}_2$ layer. Those ^{222}Rn nuclei can evidently be desorbed in response to a change in relative humidity (Figure 7 10 d and Figure 8 30 d), such that the activity of retained ^{222}Rn quickly drops, resulting in a peak in the emanation. If the release of those ^{222}Rn nuclei, however, is not enough to reach the equilibrium point, a characteristic decay period of the retained ^{222}Rn nuclei, with the kinetics of the radioactive decay, follows. Conversely, during a change from high to low emanation, the only way for the activity of retained ^{222}Rn to reach equilibrium is the ingrowth from the ^{226}Ra decay, since back-diffusion evidently does not occur (Figure 7, >80 d), which follows a characteristic ingrowth curve. Additionally, the change of the effective emanation conditions can follow its own dynamics, as during the initial rise in Figure 7. Given that the rate of re-equilibration of the device depends on the state it was previously in, hysteresis may occur. Nonetheless, it is shown in Figure 7 that the emanation from the IRSD recovers its initial value after exposure to more humid air.

These observations underpin the propositions of Section 2.5 and those given in [35,36].

4. Conclusions

In this work, we have demonstrated the successful development of a novel device, in conjunction with analytical procedures, to standardize the emanation of ^{222}Rn from a solid source of ^{226}Ra . For the first time, a complete approach based on a unique combination of a ^{222}Rn source with a spectrometric detector, the IRSD, was presented. This allows the continuous monitoring of the residual amount of ^{222}Rn in the source by highly efficient, direct α -particle measurements under ambient conditions, which drastically improves the reliability under changing operational characteristics and environmental parameters. Additionally, the direct measurement of the α -particles, emitted by the residual ^{222}Rn , specifically enabled by the design of the IRSD, alleviates some of the sources for systematic uncertainty of previous γ -ray spectrometry based approaches [16,18] while providing a means of achieving unmatched counting efficiency at a negligible background. As was demonstrated, ^{222}Rn is not necessarily in secular equilibrium with the short-lived progeny in a thin-layer, which could result in a bias of approximately 2% if γ -spectrometry of ^{214}Pb and ^{214}Bi was applied as a monitoring tool instead.

The very high counting efficiency of the IRSD technique allows to achieve high statistical accuracy in short integration times and, thereby, leads to improved performance of procedures to infer the emanation. The small sampling interval allowed for identifying even relatively narrow peaks in the emanations that result from increases in the relative humidity of the environment. The continuous reliable measurement of these considerably small ^{222}Rn emanation terms (corresponding to a single ^{222}Rn atom released per second) allows refining calibration procedures in the future, e.g., by down-scaling of reference volumes, injection of collected amounts of ^{222}Rn directly into measurement systems, reductions of flow rates, and other, similar methods. Thereby, the definition of the unit $\text{Bq}\cdot\text{m}^{-3}$ can be realized by integrating the radioactive decay kinetics, driven by the derived emanation source terms ranging from $2\ \mu\text{Bq}\cdot\text{s}^{-1}$ to $440\ \mu\text{Bq}\cdot\text{s}^{-1}$, with a combined uncertainty not exceeding 2% and thus, providing one of the most advanced techniques of low-level ^{222}Rn standardization to this end. The application of the IRSD setup thus allows one to realize and disseminate reference atmospheres of ^{222}Rn in the ambient concentration range, traceable to the SI.

It is presumed that this range can be readily extended in both directions since the statistical uncertainties were low, even in the low ^{226}Ra activity IRSD, while the higher activity ones did not begin to show significant losses from random coincidence and self-absorption.

A possible pathway of improvement of the uncertainty is a refined distance measurement in the defined-solid angle α -particle spectrometry, which was the overall main contributor to the uncertainty of the determined counting efficiency. During the area determinations of the α -particle spectra, a heuristic approach, to estimate the uncertainty arising from the tailing contributions, was applied. This was found necessary due to computational limitations, but it can be improved on once more advanced techniques for deconvolution of α -particle spectra become available. In a similar vein, future improvements in modeling techniques for time-series, similar to those applied in Section 2.5 and Appendix B, as well as increases in available computational resources, will translate to even more realistic uncertainty estimation, potentially allowing us to drop some of the assumptions made.

While it was possible to investigate the behavior of the IRSD setups over approximately 1 year in total, it is expected that certain characteristics of the IRSD will degrade over time, due to the continuous self-implantation of nuclei, leading to potential knock-ons in the p-doped dead-layer of the detector, and thus, to a degradation of its junction properties, especially concerning higher activities of ^{226}Ra than those used in this study. Moreover, the ^{210}Po peak is a disturbance in the spectra that were collected, and hence, the ingrowth of ^{210}Po will additionally degrade the information that can be inferred from the spectra or, at least, increase the uncertainty of the determined emanation. Due to the relatively long half-life of intermediate ^{210}Pb , however, this process takes place on the scale of tens of years. Currently, the technique is only applied at PTB, and this first presentation of it

serves as a proof of principle and to lay down the traceability chain to the SI. However, continuous production of IRSD of different activity, for dissemination and potential future replacements, by the PTB is limited to a low volume of devices. Due to the relative simplicity of the process to create an IRSD, using relatively low-cost and rugged components, supply of such setups can, potentially, be realized in the future by an implementation in industry to disseminate the unit $\text{Bq}\cdot\text{m}^{-3}$, concerning ^{222}Rn in the air, in the presented way.

Author Contributions: Conceptualization, methodology, software, formal analysis, investigation, visualization, writing-original draft preparation F.M.; resources, supervision, project administration, funding acquisition S.R., A.R. All authors have read and agreed to the published version of the manuscript.

Funding: This project 19ENV01 traceRadon has received funding from the EMPIR programme co-financed by the Participating States and from the European Union’s Horizon 2020 research and innovation programme. 19ENV01 traceRadon denotes the EMPIR project reference.

Institutional Review Board Statement: Not applicable.

Informed Consent Statement: Not applicable.

Data Availability Statement: Collected spectrometric data, as well as the custom software for regression analysis and statistical inversion is available on request from the authors.

Acknowledgments: The authors thank Detlef Bergman, PTB, for his help with scanning electron microscopy, and Scott D. Chambers, ANSTO, for his comments on the manuscript.

Conflicts of Interest: The authors declare no conflict of interest.

Appendix A

The models for peak shapes in α -particle spectra described in [29,30] were further refined in this work to provide improved numerical stability, better convergence properties, and more physically reasonable results, as outlined below.

A numerically stable equivalent representation of this peak shape is given by Equation (A1) through a piecewise definition in terms of the scaled complementary error function erfcx ($\text{erfcx}(x) = \exp(x^2)\text{erfc}(x)$), which was computed by Chebyshev approximation [38]. Flipping the sign on x and μ , Equation (A1) is similarly used to represent right tailed Gaussians.

$$f_i(x, \mu_i, \sigma_i, \tau_i) = \begin{cases} \frac{1}{2}\tau_i \exp(a_i)\text{erfc}(b_i) \quad \forall a_i \leq 0 \\ \frac{1}{2}\tau_i \exp(c_i)\text{erfcx}(b_i) \quad \forall a_i > 0 \end{cases} \quad (\text{A1})$$

where $a_i = (x - \mu_i)\tau_i + \frac{1}{2}\sigma_i^2\tau_i^2$, $b_i = \frac{1}{\sqrt{2}}\left(\frac{x-\mu_i}{\sigma_i} + \sigma_i\tau_i\right)$, and $c_i = -\frac{(x-\mu_i)^2}{2\sigma_i^2}$

Each peak in the spectrum is represented as a weighted sum over different realizations of Equation (A2), which represents the probability density function of a mixture of exponentially modified Gaussians (ExGaussian).

$$P_n(x, w_n, \mu_n, \sigma_n, \tau_n) = \sum_{i=0}^k w_{n,i} f_i(x, \mu_{n,i}, \sigma_{n,i}, \tau_{n,i}) \quad (\text{A2})$$

where n represents the peak index and i represents the respective tail index. w_n , μ_n , σ_n , and τ_n represent the corresponding vectors of shape parameters, indexed by i .

The *softplus* transformation was used to constrain the parameters to positive values generally, except for the weights $w_{n,i}$. The k components of the weights vectors w_n are generally restricted as compositional factors on the $k - 1$ dimensional simplex and are thus transformed to a $k - 1$ component vector using an *isometric log-ratio* transformation [39], such that the components of w_n are constrained within (0,1) and sum to 1.

The modeled spectrum \hat{S} can then be written in Matrix notation, where A is a vector containing the peak-areas and R is a matrix made up of the peak-shapes as the column

vectors. The modeled spectrum is thus given by the linear-combination of the column-vectors of \mathbf{R} ,

$$\hat{\mathbf{S}} = \mathbf{R}\mathbf{A} \tag{A3}$$

For a given \mathbf{R} , and a measured spectrum \mathbf{S} of l chosen regression bins and of high statistical accuracy (i.e., where the spectrum can reasonably be assumed to follow a multi-variate Gaussian with covariance matrix $\text{diag}(\mathbf{S})$), \mathbf{A} is given as the solution to the weighted, linear least-squares problem

$$\left(\mathbf{R}^T\mathbf{O}\mathbf{R}\right)\mathbf{A} = \mathbf{R}^T\mathbf{O}\mathbf{S} \tag{A4}$$

where $\mathbf{O} = \text{diag}\left(\mathbf{S}^{-1}\right)$ denotes the diagonal matrix of bin-wise reciprocals of \mathbf{S} .

This linear sub-problem is efficiently solved by Cholesky decomposition.

To determine the shape-parameters stacked in a parameter vector $\boldsymbol{\theta}$ using a spectrum of high statistical accuracy, the following regularized objective is used, splitting the optimization into a linear and a non-linear sub-problem and implicitly defining \mathbf{A} , where $f(\boldsymbol{\theta})$ is a function that regularizes the peak-shape parameters, as explained below.

$$\begin{aligned} \mathcal{L} &= \frac{1}{2l}(\mathbf{S} - \hat{\mathbf{S}})^T\mathbf{O}(\mathbf{S} - \hat{\mathbf{S}}) + f(\boldsymbol{\theta}) = \\ &= \frac{1}{2l}\left(\mathbf{S} - \mathbf{R}(\mathbf{R}^T\mathbf{O}\mathbf{R})^{-1}\mathbf{R}^T\mathbf{O}\mathbf{S}\right)^T\mathbf{O}\left(\mathbf{S} - \mathbf{R}(\mathbf{R}^T\mathbf{O}\mathbf{R})^{-1}\mathbf{R}^T\mathbf{O}\mathbf{S}\right) + f(\boldsymbol{\theta}) \end{aligned} \tag{A5}$$

$\boldsymbol{\theta}$ is optimized by minimizing \mathcal{L} using the quasi-Newton Broyden–Fletcher–Goldfarb–Shanno (BFGS) minimization procedure as implemented in the Python package SciPy [40]. The required gradient $\frac{\partial\mathcal{L}}{\partial\boldsymbol{\theta}}$ is computed exactly by automatic reverse-mode differentiation using the Jax Python framework [41] and custom differentiation rules for Equation (A1).

It is not physically sensible that the peak shapes vary drastically between the different nuclides in the decay chain, apart from the position of the mode. However, due to displacement from recoiling further in the decay chain, and possibly due to α -e and α -photon true coincidence effects, slight differences exist between the peak shapes, which must be addressed in the modeling procedure. For this reason, the shape parameters are not shared across the different peaks resulting in many degrees of freedom. Consequently, those models are strongly dependent on the starting parameters without regularization since the likelihood space is thought to have many local maxima. As a result it is common for flat regions in the spectrum to be erroneously attributed to a single peak while the tailing of the others is strongly underestimated. In this work, a penalty term $f(\boldsymbol{\theta})$ is used to address this observation by capturing the physics of the spectrum to improve the convergence into a physically sensible minimum, i.e., where the peak shapes are similar, but not completely shared. $f(\boldsymbol{\theta})$ regularizes the w - and τ -vectors of each peak, such that they are closely related amongst chosen peaks by a ℓ^2 -penalty,

$$f(\boldsymbol{\theta}) = \frac{1}{2} \sum_{n=1}^j (\hat{w}_0 - \hat{w}_n)^T \left(\kappa \hat{w}_0^2\right)^{-1} (\hat{w}_0 - \hat{w}_n) + (\tau_0 - \tau_n)^T \left(\gamma \tau_0^2\right)^{-1} (\tau_0 - \tau_n) \tag{A6}$$

where \hat{w}_n describes the n -th transformed weight vector, τ_n is the n -th tailing vector, j is the total number of regularized peaks, κ and γ are parameters that control the strength of the regularization. $\kappa = \gamma = 0.04$ was found to provide reasonable regularization, judging from unregularized reduced χ^2 values. Specific values of $\tau_{i,n}$ and $\hat{w}_{i,n}$ (e.g., these corresponding to the ^{214}Po alpha-beta true coincidence region, Figure 5.) are excluded from the regularization function to obtain better results. Due to true coincidence effects already pointed out in earlier work on ^{226}Ra α -particle spectrometry [42], the right-handed tails of the lower energy ^{226}Ra emission were also excluded from the regularization procedure due to the pronounced α -e true coincidence resulting from the high counting efficiency and the highly converted levels in the decay of ^{226}Ra [42]. For each peak, a total of 6 left-handed and 2 right-handed tailing terms were used, which provided good deconvolution results.

It should be noted that the penalization acts on the transformed weights but the untransformed tailing parameters. Due to the *softplus* transformation of each τ and the regularization acting on the untransformed value, this regularizes strongly tailed contributions much more than weakly tailed contributions, which penalizes physically unmeaningful results, i.e., those where low-energy tailings of the peaks are strongly dissimilar. Moreover, when fitting peak-shapes given by Equation (A2), the peak areas are commonly the parameters with the smallest gradient of the objective function. The splitting of the linear sub-problem additionally reduces the sensitivity towards the starting parameters, as, for each **R**, the best fitting **A** is implicitly found during each iteration of the chosen non-linear optimization procedure.

In principle, an asymptotic estimate of the covariance matrix of **A** can be found by truncated Taylor expansion, assuming it follows a multivariate normal distribution and residuals are purely stochastic, as

$$\Sigma_A \approx \frac{1}{I} \left(\frac{\partial A}{\partial \theta} \right) \left(\frac{\partial^2 \mathcal{L}}{\partial \theta^T \partial \theta} \right)^{-1} \left(\frac{\partial A}{\partial \theta} \right)^T \tag{A7}$$

which was generally found to provide unreasonable results due to numerical issues from bad conditioning of the Hessian. The uncertainty is thus instead estimated from heuristic approaches and the underlying Poisson statistics, as outlined in the respective sections of the results.

To determine the peak-areas in spectra of low statistical accuracy (e.g., for the area determinations of spectrometric time-series with small integration times), the shape parameters as deduced from a spectrum of similar shape and high statistical accuracy are held constant to define the Matrix **R** and only the vector **A** is determined for each spectrum at hand. However, obtaining **A** by solving Equation (A4) as the least-squares solution leads to biased results in this case due to the Poisson statistics being much more relevant in cases where a lower number of counts is observed in each bin. In some cases, the bias experienced in this way is as high as 5%, which was found by comparing the least-squares solutions to the asymptotic values. Therefore, the following alternative maximum likelihood formulation was used, where **A** is determined by minimizing the negative log-likelihood under Poisson distributed counts in each channel and for each spectrum for the given **R** matrix,

$$\mathcal{L} \propto \sum_i (\mathbf{RA})_i - S_i \ln(\mathbf{RA})_i \tag{A8}$$

which can not be solved in closed-form, and hence, BFGS is used.

This overall approach allows for a reliable and reasonably fast determination of peak areas in spectra with low statistical accuracy (e.g., in the time-series), since the peak shapes are already determined independently, allowing for better estimation of the tailing contributions. This allows for smaller integration times to be chosen during the collection of time-series and thus a higher temporal resolution.

Appendix B

The filtering and smoothing algorithm denoted by *SLDS-deconvolution* in this work is based on modeling the emanation η as a Gaussian process, such that the state vector **x** follows the following Itô stochastic differential equation, as reported in [36],

$$dx = \mathbf{K}xdt + Ld\beta_t$$

$$\mathbf{x}_s = \begin{bmatrix} A_{Rn-222}^S \\ A_{Ra-226}^S \\ \eta \\ \frac{d\eta}{dt} \end{bmatrix}_s ; \mathbf{K}_s = \begin{bmatrix} -\lambda_{Rn-222} & \lambda_{Rn-222} & -\lambda_{Rn-222} & 0 \\ 0 & \lambda_{Ra-226} & 0 & 0 \\ 0 & 0 & 0 & 1 \\ 0 & 0 & 0 & -\gamma_s \end{bmatrix} ; L_s = \begin{bmatrix} 0 \\ 0 \\ 0 \\ \sigma_s \end{bmatrix} \tag{A9}$$

where γ_s and σ_s denote optimizable parameters and the index *s* corresponds to the active system model.

In the applied switching linear dynamical approach, multiple linear dynamical models indexed by *s* operate by a method analogous to the classical Kalman-Filter [43] and their results are merged into a common PDF according to the likelihood of their prediction. Smoothing is carried out directly using the approach in [44], as reported in [36]. In practice, 2 models with distinct σ_s but shared γ are used to provide better results.

The measurements **y** (which are the vectors of peak areas in the present case) are modeled to be related to the evolution of the state variable by,

$$\mathbf{y}(t, r) = \varepsilon \int_0^r \mathbf{x}(t + \tau) d\tau \tag{A10}$$

such that the joint distribution of measurement and state can be expressed as [36],

$$p(x_n, \mathbf{y}_n | \mathbf{y}_{1:n-1}) \propto \mathcal{N} \left(\begin{bmatrix} \mathbf{F}_r \mathbf{F}_\delta \boldsymbol{\mu}_{n-1} \\ \mathbf{H} \mathbf{M} \mathbf{F}_\delta \boldsymbol{\mu}_{n-1} \end{bmatrix}, \begin{bmatrix} \mathbf{F}_r (\mathbf{F}_\delta \boldsymbol{\Sigma}_{n-1} \mathbf{F}_\delta^T + \mathbf{U}_\delta) \mathbf{F}_r^T + \mathbf{U}_r & \mathbf{H} \mathbf{M} (\mathbf{F}_\delta \boldsymbol{\Sigma}_{n-1} \mathbf{F}_\delta^T + \mathbf{U}_\delta) \mathbf{F}_r^T + \mathbf{H} \mathbf{C}^T \\ \mathbf{F}_r (\mathbf{F}_\delta \boldsymbol{\Sigma}_{n-1} \mathbf{F}_\delta^T + \mathbf{U}_\delta) \mathbf{M}^T \mathbf{H}^T + \mathbf{C} \mathbf{H}^T & \mathbf{H} \mathbf{M} (\mathbf{F}_\delta \boldsymbol{\Sigma}_{n-1} \mathbf{F}_\delta^T + \mathbf{U}_\delta) \mathbf{M}^T \mathbf{H}^T + \mathbf{H} \mathbf{B} \mathbf{H}^T + \boldsymbol{\Sigma} \end{bmatrix} \right) \tag{A11}$$

$$\begin{aligned} \mathbf{F}_a &= e^{\mathbf{K}a} & \mathbf{U}_a &= \int_0^a e^{\mathbf{K}(a-\tau)} \mathbf{L} \mathbf{L}^T e^{\mathbf{K}^T(a-\tau)} d\tau \\ \mathbf{M}_r &= \int_0^r e^{\mathbf{K}\tau} d\tau & \mathbf{C}_r &= \int_0^r \int_\tau^r e^{\mathbf{K}(r-\tau)} \mathbf{L} \mathbf{L}^T e^{\mathbf{K}^T(a-\tau)} da d\tau \\ \mathbf{B}_r &= \int_0^r \int_\tau^r \int_\tau^r e^{\mathbf{K}(a-\tau)} \mathbf{L} \mathbf{L}^T e^{\mathbf{K}^T(b-\tau)} da db d\tau \end{aligned}$$

where *r* denotes the integration time of the spectrometer. This density, recursively evaluated and conditioned on the measurements, is the basis of the filtering procedure and the obtained filtering PDF is recursively corrected into a smoothed posterior PDF conditioned onto the whole time-series.

Due to the Poisson noise of the measurements, and following the propositions in [36,45] as well as approximately including the correlated variance of the peak areas due to tailing, the measurement noise covariance is estimated in each filtering step from the previous state estimate mean as

$$\boldsymbol{\Sigma} \approx \varepsilon \mathbf{M} \boldsymbol{\mu}_{n-1} \mathbf{M}^T \varepsilon^T + \sigma_{\text{Area}} 2\varepsilon \mathbf{M} x_{n-1} \mathbf{M}^T \varepsilon^T \begin{bmatrix} 1 & -0.8 \\ -0.8 & 1 \end{bmatrix} \varepsilon \mathbf{M} \boldsymbol{\mu}_{n-1} \mathbf{M}^T \varepsilon^T \tag{A12}$$

Uncertainty propagation considering the counting efficiency vector ε is given by Equation (A13), which is intractable. The uncertainty of the counting efficiency is approximately propagated across the *SLDS-deconvolution* model by evaluating the model at a select set of *sigma points* in $p(\varepsilon)$ and computation of the enveloping multivariate Gaussian for each of the computed $p(x_n | \mathbf{y}_{1:n}, \varepsilon)$ and $p(x_n | \mathbf{y}_{1:N}, \varepsilon)$.

$$p(x_n | \mathbf{y}_{1:n}) = \int p(x_n | \mathbf{y}_{1:n}, \varepsilon) p(\varepsilon) d\varepsilon \tag{A13}$$

References

1. ICRP. *Lung Cancer Risk from Radon and Progeny & Statement on Radon*; ICRP Publication 115; ICRP: Stockholm, Sweden, 2010; Volume 40, p. 1.
2. ICRP. *Radiological Protection Against Radon Exposure*; ICRP Publication 126; ICRP: Stockholm, Sweden, 2010; Volume 43, p. 3.
3. Darby, S.; Hill, D.; Auvinen, A.; Barros-Dios, J.M.; Baysson, H.; Bochicchio, F.; Deo, H.; Falk, R.; Forastiere, F.; Hakama, M.; et al. Radon in homes and risk of lung cancer: Collaborative analysis of individual data from 13 European case-control studies. *BMJ* **2005**, *330*, 223. [CrossRef]
4. Williams, A.G.; Chambers, S.D.; Conen, F.; Reimann, S.; Hill, M.; Griffiths, A.D.; Crawford, J. Radon as a tracer of atmospheric influences on traffic-related air pollution in a small inland city. *Tellus B Chem. Phys. Meteorol.* **2016**, *68*, 30967. [CrossRef]
5. Chambers, S.D.; Preunkert, S.; Weller, R.; Hong, S.-B.; Humphries, R.S.; Tositti, L.; Angot, H.; Legrand, M.; Williams, A.G.; Griffiths, A.D.; et al. Characterizing Atmospheric Transport Pathways to Antarctica and the Remote Southern Ocean Using Radon-222. *Front. Earth Sci.* **2018**, *6*, 190. [CrossRef]
6. Chambers, S.; Guérette, E.-A.; Monk, K.; Griffiths, A.; Zhang, Y.; Duc, H.; Cope, M.; Emmerson, K.; Chang, L.; Silver, J.; et al. Skill-Testing Chemical Transport Models across Contrasting Atmospheric Mixing States Using Radon-222. *Atmosphere* **2019**, *10*, 25. [CrossRef]

7. Chambers, S.D.; Williams, A.G.; Conen, F.; Griffiths, A.D.; Reimann, S.; Steinbacher, M.; Krummel, P.B.; Steele, L.P.; van der Schoot, M.V.; Galbally, I.E.; et al. Towards a Universal “Baseline” Characterisation of Air Masses for High- and Low-Altitude Observing Stations Using Radon-222. *Aerosol. Air Qual. Res.* **2016**, *16*, 885–899. [[CrossRef](#)]
8. Williams, A.G.; Chambers, S.; Griffiths, A. Bulk Mixing and Decoupling of the Nocturnal Stable Boundary Layer Characterized Using a Ubiquitous Natural Tracer. *Bound. Layer Meteorol.* **2013**, *149*, 381–402. [[CrossRef](#)]
9. Levin, I.; Karstens, U.; Hammer, S.; DellaColetta, J.; Maier, F.; Gachkivskyi, M. Limitations of the Radon Tracer Method (RTM) to estimate regional Greenhouse Gases (GHG) emissions—A case study for methane in Heidelberg. *Atmos. Chem. Phys. Discuss.* **2021**, preprint. [[CrossRef](#)]
10. Levin, I.; Hammer, S.; Eichelmann, E.; Vogel, F.R. Verification of greenhouse gas emission reductions: The prospect of atmospheric monitoring in polluted areas. *Philos. Trans. R. Soc. A Math. Phys. Eng. Sci.* **2011**, *369*, 1906–1924. [[CrossRef](#)]
11. Der Laan, V.; Karstens, U.; Neubert, R.E.; Der Laan-Luijkx, V.; Meijer, H.A.J. Observation-based estimates of fossil fuel-derived CO₂ emissions in the Netherlands using Δ14C, CO and 222 Radon. *Tellus. B Chem. Phys. Meteorol.* **2010**, *62*, 389–402. [[CrossRef](#)]
12. Biraud, S.; Ciais, P.; Ramonet, M.; Simmonds, P.; Kazan, V.; Monfray, P.; O’doherly, S.; Spain, G.; Jennings, S.G. Quantification of carbon dioxide, methane, nitrous oxide and chloroform emissions over Ireland from atmospheric observations at Mace Head. *Tellus B Chem. Phys. Meteorol.* **2002**, *54*, 41–60. [[CrossRef](#)]
13. Perrino, C.; Pietrodangelo, A.; Febo, A. An atmospheric stability index based on radon progeny measurements for the evaluation of primary urban pollution. *Atmos. Environ.* **2001**, *35*, 5235–5244. [[CrossRef](#)]
14. Röttger, A.; Röttger, S.; Grossi, C.; Vargas, A.; Curcoll, R.; Otáhal, P.; Hernández-Ceballos, M.Á.; Cinelli, G.; Chambers, S.; Barbosa, S.A.; et al. New metrology for radon at the environmental level. *Meas. Sci. Technol.* **2021**, *32*, 124008. [[CrossRef](#)]
15. Picolo, J.L. Absolute measurement of radon 222 activity. *Nucl. Instrum. Methods Phys. Res. Sect. A Accel. Spectrom. Detect. Assoc. Equip.* **1996**, *369*, 452–457. [[CrossRef](#)]
16. Mertes, F.; Röttger, S.; Röttger, A. A new primary emanation standard for Radon-222. *Appl. Radiat. Isot.* **2020**, *156*, 108928. [[CrossRef](#)]
17. Röttger, A.; Honig, A.; Linzmaier, D. Calibration of commercial radon and thoron monitors at stable activity concentrations. *Appl. Radiat. Isot.* **2014**, *87*, 44–47. [[CrossRef](#)]
18. Linzmaier, D.; Röttger, A. Development of a low-level radon reference atmosphere. *Appl. Radiat. Isot.* **2013**, *81*, 208–211. [[CrossRef](#)] [[PubMed](#)]
19. Janik, M.; Omori, Y.; Yonehara, H. Influence of humidity on radon and thoron exhalation rates from building materials. *Appl. Radiat. Isot.* **2015**, *95*, 102–107. [[CrossRef](#)]
20. Zhou, Q.; Shubayr, N.; Carmona, M.; Standen, T.M.; Kearfott, K.J. Experimental study of dependence on humidity and flow rate for a modified flowthrough radon source. *J. Radioanal. Nucl. Chem.* **2020**, *324*, 673–680. [[CrossRef](#)]
21. Stranden, E.; Kolstad, A.K.; Lind, B. The Influence of Moisture and Temperature on Radon Exhalation. *Radiat. Prot. Dosim.* **1984**, *7*, 55–58. [[CrossRef](#)]
22. Fialova, E.; Otáhal, P.P.S.; Vosahlik, J.; Mazanova, M. Equipment for Testing Measuring Devices at a Low-Level Radon Activity Concentration. *Int. J. Environ. Res. Public Health* **2020**, *17*, 1904. [[CrossRef](#)] [[PubMed](#)]
23. Mertes, F.; Kneip, N.; Heinke, R.; Kieck, T.; Studer, D.; Weber, F.; Röttger, S.; Röttger, A.; Wendt, K.; Walther, C. Ion implantation of ²²⁶Ra for a primary ²²²Rn emanation standard. *Appl. Radiat. Isot.* **2021**, *181*, 11093. [[CrossRef](#)] [[PubMed](#)]
24. Ziegler, J.F.; Ziegler, M.D.; Biersack, J.P. SRIM—The stopping and range of ions in matter (2010). *Nucl. Instrum. Methods Phys. Res. Sect. B Beam Interact. Mater. At.* **2010**, *268*, 1818–1823. [[CrossRef](#)]
25. Maier, C.G. *Vapor Pressure of the Common Metallic Chlorides and a Static Method and High Temperatures*; Department of the Interior, Bureau of Mines: Washington, DC, USA, 1925.
26. Van Westenburg, J.A. *Activities of Alkaline Earth Metals in Their Molten Chlorides*; Iowa State University: Ames, IA, USA, 1964.
27. Garcia Ruiz, R.F.; Berger, R.; Billowes, J.; Binnersley, C.L.; Bissell, M.L.; Breier, A.A.; Brinson, A.J.; Chrysalidis, K.; Cocolios, T.E.; Cooper, B.S.; et al. Spectroscopy of short-lived radioactive molecules. *Nature* **2020**, *581*, 396–400. [[CrossRef](#)] [[PubMed](#)]
28. Philip Horwitz, E.; Chiarizia, R.; Dietz, M.L. A Novel Strontium-Selective Extraction Chromatographic Resin. *Solvent. Extr. Ion. Exch.* **2007**, *10*, 313–336. [[CrossRef](#)]
29. Marx, S. *Purification of Radium-226 for the Manufacturing of Actinium-225 in a Cyclotron for Alpha-Immunotherapy*; Technical University Munich: Munich, Germany, 2014.
30. Pommé, S. Methods for primary standardization of activity. *Metrologia* **2007**, *44*, S17–S26. [[CrossRef](#)]
31. Stefaan, P.; Goedele, S. Alpha-Particle Counting and Spectrometry in a Primary Standardisation Laboratory. *ACTA Chim. Slov.* **2008**, *55*, 111–119.
32. Arinc, A.; Parfitt, M.J.; Keightley, J.D.; Wilson, A. Defined solid angle alpha counting at NPL. *Appl. Radiat. Isot.* **2016**, *109*, 198–204. [[CrossRef](#)]
33. Bortels, G.; Collaers, P. Analytical function for fitting peaks in alpha-particle spectra from Si detectors. *Int. J. Radiat. Appl. Instrum. Part* **1987**, *38*, 831–837. [[CrossRef](#)]
34. Pommé, S.; Caro Marroyo, B. Improved peak shape fitting in alpha spectra. *Appl. Radiat. Isot.* **2015**, *96*, 148–153. [[CrossRef](#)]
35. Mertes, F.; Röttger, S.; Röttger, A. D3.3 Approximate Sequential Bayesian Filtering to Estimate Rn-222 Emanation from Ra-226 Sources from Spectra. In Proceedings of the SMSI 2021—Measurement Science, Wenstorf, Germany, 3–6 May 2021; pp. 256–257.

36. Mertes, F.; Röttger, S.; Röttger, A. Approximate sequential Bayesian filtering to estimate ^{222}Rn emanation from ^{226}Ra sources using spectral time-series. *J. Sens. Sens. Syst.* 2021, *under review*.
37. Pommé, S. The uncertainty of counting at a defined solid angle. *Metrologia* **2015**, *52*, S73–S85. [[CrossRef](#)]
38. Shepherd, M.M.; Laframboise, J.G. Chebyshev approximation of $(1 + 2x) \exp(x^2) \operatorname{erfc}(x)$ in $0 \leq x < \infty$. *Math. Comput.* **1981**, *36*, 249–253. [[CrossRef](#)]
39. Egozcue, J.J.; Pawlowsky-Glahn, V.; Mateu-Figueras, G.; Barceló-Vidal, C. Isometric Logratio Transformations for Compositional Data Analysis. *Math. Geol.* **2003**, *35*, 279–300. [[CrossRef](#)]
40. Virtanen, P.; Gommers, R.; Oliphant, T.E.; Haberland, M.; Reddy, T.; Cournapeau, D.; Burovski, E.; Peterson, P.; Weckesser, W.; Bright, J.; et al. SciPy 1.0: Fundamental algorithms for scientific computing in Python. *Nat. Methods* **2020**, *17*, 261–272. [[CrossRef](#)]
41. Bradburry, J.; Frostig, R.; Hawkins, P.; Johnson, M.J.; Maclaurin, D.; Necula, G.; Paszke, A.; van der Plas, J.; Wanderman-Milne, S.; Zhang, Q. JAX: Composable Transformations of Python + Numpy Programs. 2018. Available online: <https://github.com/google/jax> (accessed on 1 November 2021).
42. Marouli, M.; Pommé, S.; Van Ammel, R.; García-Toraño, E.; Crespo, T.; Pierre, S. Direct measurement of alpha emission probabilities in the decay of ^{226}Ra . *Appl. Radiat. Isot.* **2017**, *125*, 196–202. [[CrossRef](#)] [[PubMed](#)]
43. Kalman, R.E. A New Approach to Linear Filtering and Prediction Problems. *J. Basic Eng.* **1960**, *82*, 35–45. [[CrossRef](#)]
44. Barber, D. Expectation Correction for Smoothed Inference in Switching Linear Dynamical Systems. *J. Mach. Learn. Res.* **2006**, *7*, 2515–2540.
45. Ebeigbe, D.; Berry, T.; Schiff, S.J.; Sauer, T. Poisson Kalman filter for disease surveillance. *Phys. Rev. Res.* **2020**, *2*, 043028. [[CrossRef](#)]

Chapter 7

Suitability of solid-state scintillators to monitor ^{222}Rn emanation

In principle, newer scintillation materials like $\text{LaBr}_3 : \text{Ce}$, CeBr_3 and SrI_2 may offer a high enough energy resolution for the methods reported in (Linzmaier and Röttger, 2013; Röttger et al., 2014) among others, or its extensions developed throughout this work to be applied to the spectra obtained with them while providing much cheaper costs, a considerably smaller form factor and the ability to operate under ambient temperature conditions. Thereby, it might be possible to implement a portable system to monitor emanation sources that can be disseminated along with them. Essentially, this could allow to apply the methods of Publication III and Publication IV to be applied based on continuous γ -ray spectrometric measurements of the emanation sources. In this section of the work, the usage of such scintillators for this purpose, using the example of a $\text{LaBr}_3 : \text{Ce}$ detector, is discussed.

To investigate this, experimental data were collected by measuring the emanation of both implanted and electrodeposited sources by the (Linzmaier and Röttger, 2013) method with a $\text{LaBr}_3 : \text{Ce}$ detector and a HPGe detector simultaneously. Thereby, any environmental influences can be disregarded as a cause for potentially observed differences between the emanation measured with each detector and it is expected that both detectors yield similar results to within the respective uncertainties. Since ^{226}Ra is not homogeneously distributed in each source, but is rather deposited on the surface of a metal substrate, the sources have been measured in both orientations (facing the HPGe and the $\text{LaBr}_3 : \text{Ce}$ respectively). A schematic drawing of the measurement setup is given in Figure 7.1.

This method of determining the emanation coefficient χ is based on the relationship of count-rate ratios between ^{226}Ra and ^{222}Rn progeny observed in a closed and an open source and is based on the equation

$$\chi = 1 - \frac{A_{222\text{Rn}}^o}{A_{226\text{Ra}}^o} = 1 - \frac{R_{214\text{Pb}}^o}{R_{226\text{Ra}}^o} \frac{R_{226\text{Ra}}^c}{R_{214\text{Pb}}^c} \quad (7.1)$$

where the superscript *o* refers to the open (emanating) source, the superscript *c* refers to the closed (sealed against emanation) source, A_i refers to the activity of nuclide *i* and R_i refers to the net count-rate in a certain peak associated with the nuclide *i*.

However, it was found that the results derived from the scintillator spectra using both the ^{226}Ra and the 352 keV ^{214}Pb emission differ significantly from the results obtained from the HPGe spectra, and that this difference could not be explained by the orientation of the source. Interestingly, the deviation between both results vanished when the count-rates ratio

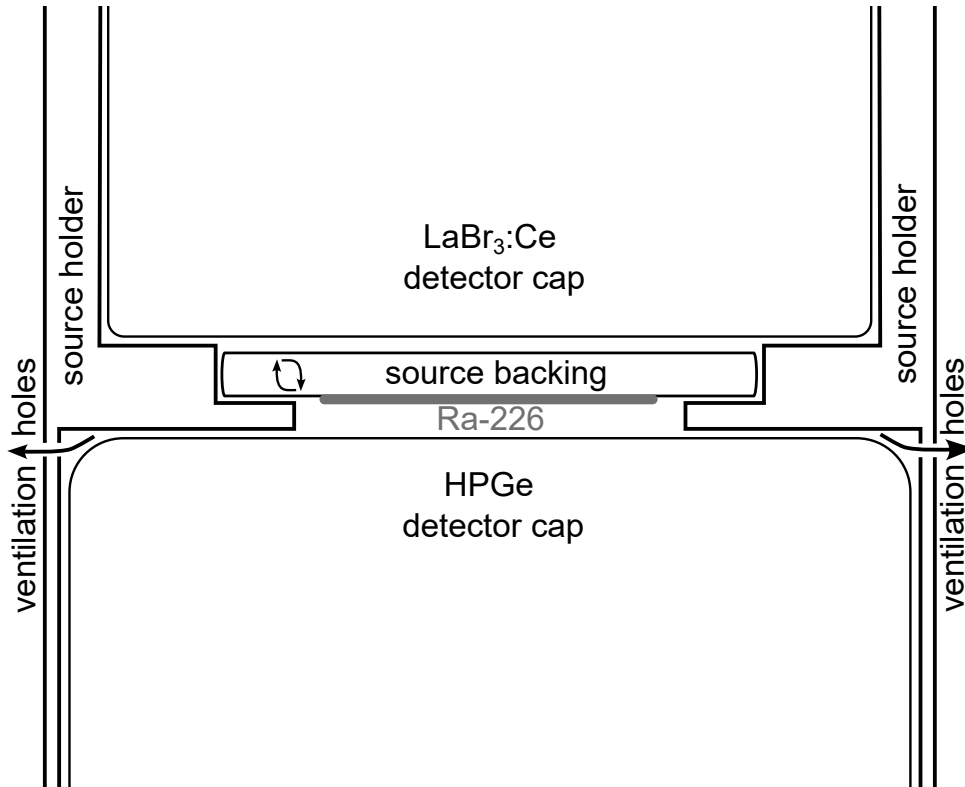


FIGURE 7.1: Schematic drawing of the comparative emanation measurement using a HPGe and a $\text{LaBr}_3:\text{Ce}$ detector simultaneously. Measurements have been carried out with the source backing in both orientations (Ra-^{226} facing up or down respectively).

of the ^{226}Ra peaks of closed reference and open emanation source of the scintillation detector was replaced with the known respective activity ratio, i.e. when changing equation (7.1) to

$$\chi = 1 - \frac{R_{214\text{Pb}}^o A_{226\text{Ra}}^c}{R_{214\text{Pb}}^c A_{226\text{Ra}}^o} \quad (7.2)$$

From this, the conclusion was drawn that the determination of the ^{226}Ra peak area in the scintillator spectra is unreliable.

To explain this effect, the scintillator γ -ray spectrum of the progeny of ^{222}Rn needed to be measured independently of ^{226}Ra . For this purpose, a circular cut from a Makrofol-N sheet (0.05 mm thickness), a polycarbonate material, was glued onto a stainless-steel disc in order to obtain a similar geometry to the electrodeposited sources. The disc was subsequently placed into an evacuated vessel and exposed to the ^{222}Rn created by a 2 MBq ^{226}Ra source. Makofol-N is known to strongly adsorb ^{222}Rn (Pressyanov et al., 2007) and thereby, the short lived progeny (SLP) of ^{222}Rn were accumulated within the glued Makrofol-N sheet. Subsequently, γ -ray spectra of the stainless-steel disc were taken with the scintillation detector in the same geometry as was applied when measuring the emanation sources. While this method does not allow to quantify the efficiency of the detector, since the activity of the absorbed and accumulated SLP is unknown, it allows to gain an overview over the features of such a spectrum.

The low-energy region of the spectrum obtained in this way is shown in Figure 7.2, where a hypothetical ^{226}Ra peak was included for illustration. Clearly, the background created

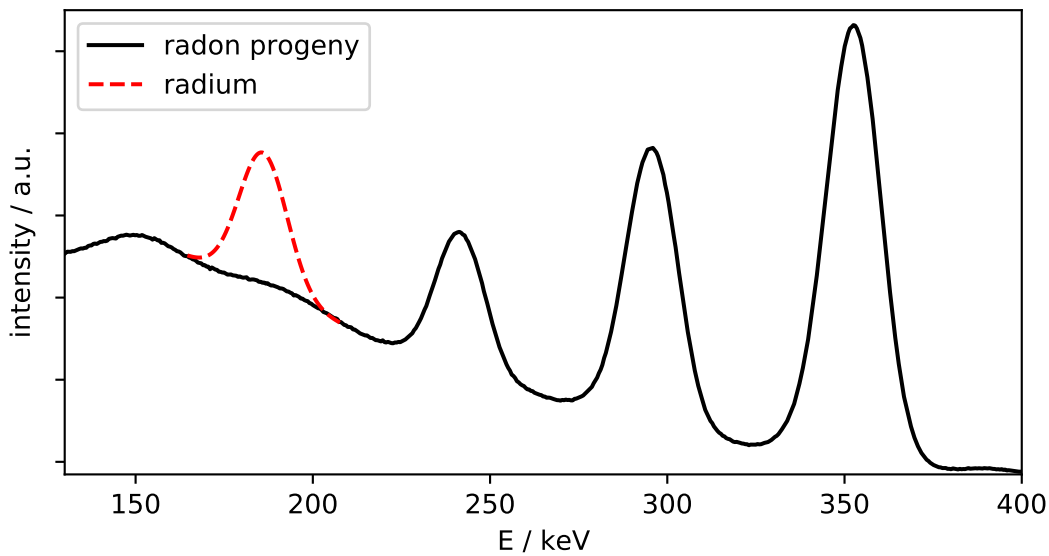


FIGURE 7.2: measured γ -ray spectrum of ^{222}Rn progeny concentrated in a thin sheet of Makrofol-N using a 1.5'' $\text{LaBr}_3 : \text{Ce}$ scintillation detector and illustrated position of a corresponding ^{226}Ra peak.

by the SLP below the region of the 186 keV ^{226}Ra emission is non-linear. The non-linearity is due to both the backscattering peak of the 609 keV ^{214}Bi emission at 180 keV as well as the Compton continuum of the 352 keV ^{214}Pb starting at 204 keV. The relatively low energy resolution of the scintillator smears these into the given non-linear shape in the region from 160 keV to 200 keV, at the position of the ^{226}Ra peak. This non-linearity consequently scales with the amount of the SLP in the source and as such, the bias of the scintillator is dependant on the absolute magnitude of the emanation. Therefore, it may not even be corrected easily by a thorough calibration. Additionally, the bias is supposed to thus also scale with the exact measurement geometry, which impacts the backscattering probability, hence reliable emanation measurements through the scintillator in different locations using the ^{226}Ra peak can not be guaranteed.

However, as already stated, deviating from the method of (Linzmaier and Röttger, 2013), the radium count-rate does not have to be determined from the spectra, as it may be replaced by the respective radium activities, which are already known, in this specific case, by the DSA α -spectrometric measurements. While this enables application of the γ -ray spectrometric method with scintillators, it has an important implication. The method of (Linzmaier and Röttger, 2013) uses specifically the count-rate- rather than the activity ratio, because this leads to an effective cancellation of most uncertainty sources, e.g. slight variation in measurement geometry between reference and emanation source.

Another adaptation to the method of (Linzmaier and Röttger, 2013) may then be made based on the following observation. The count-rate of a γ -ray spectrum of ^{226}Ra and SLP only depends on the ^{226}Ra content in the energy range below approximately 200 keV. Therefore, it is not necessary to evaluate a single peak in the spectrum to assess the progeny activity of the source. Conversely, one may simply observe the integral count-rate above 200 keV, which is directly proportional to the sum of the respective background count-rate and the SLP activity of the source. If the background count-rate is sufficiently stable, one may calculate the emanation of the source on the basis of the ratio of this integral count-rate of an open and an equilibrated reference source with known ^{226}Ra activity. This is the

mathematically most straight-forward way to incorporate all information contained in a γ -ray spectrum into the inference of the emanation, apart from the ^{226}Ra count-rate. Thereby, the statistical fluctuations are decreased, which is specifically desirable for the case of time-resolved estimation of the emanation, e.g., as in Publication III.

Chapter 8

Case Studies

In this section, specific use case scenarios of the developed emanation sources and analysis techniques are illustrated. Therein, the first traceable calibration of a continuous ^{222}Rn -monitor at the ambient levels is described, using the sources developed in Publications II and IV.

The ^{222}Rn -monitors in question are a 200 L active volume dual-loop dual-filter ^{222}Rn -monitor developed by the Australian Nuclear Science and Technology Organisation (ANSTO) (Chambers et al., 2022), which is schematically depicted in Figure 8.1 and a standard commercially available ^{222}Rn detector, the AlphaGuard Model PQ2000. While the ANSTO device operates by sampling air into its delay- and active volume at a constant flow-rate of nominally $10 \text{ L} \cdot \text{min}^{-1}$, the AlphaGuard is operated in diffusion mode. In the active volume of the ANSTO device, a higher flow-rate loop ensures the deposition of short lived ^{222}Rn progeny (SLP) created only within the active volume onto a filter, which is monitored by a ZnS-scintillating layer. Upon entrance of air into the active volume, it is filtered by first another filter to ensure the removal of already present SLP. On the contrary, the measurement principle of the AlphaGuard is an ionization chamber.

Due to these different measurement principles, an argument can be made that the calibration of the ANSTO device requires the assessment of the measurement dynamics, as outlined in section 8.2. The AlphaGuard measurements can, on the other hand, be considered as static measurements.

8.1 ANSTO 200 L static calibration at the ambient level

At PTB, a 20 m^3 ^{222}Rn -tight climate chamber was available, into which the ANSTO 200 L ^{222}Rn monitor was installed. The chamber has external ports, through which a specifically designed stainless-steel housing can be connected to the chamber. Into this housing, the emanation sources from Publication II were installed and the generated ^{222}Rn was fetched by circulating the chamber air through the housing at a nominal flow rate of $1 \text{ L} \cdot \text{min}^{-1}$. Consequently, the steady-state ^{222}Rn activity concentration in the chamber can be calculated from the ^{222}Rn emanation rate of the sources, as given in Publication II and the known volume of the chamber of $(21.2240 \pm 0.0168) \text{ L}$, also accounting for the displaced volume of the ANSTO 200 L device. Naturally, one observes characteristic ingrowth and decay of the ^{222}Rn activity concentration, as discussed in chapter 2.

Specifically, the sources identified by the description 2018-1121, 2018-1133 and 2018-1120 were used as indicated in Figure 8.2 to generate ^{222}Rn atmospheres in the chamber, whose ingrowth and decay regimes can be well described due to the stable conditions under which they take place and whose steady-state values are below approximately $20 \text{ Bq} \cdot \text{m}^{-3}$.

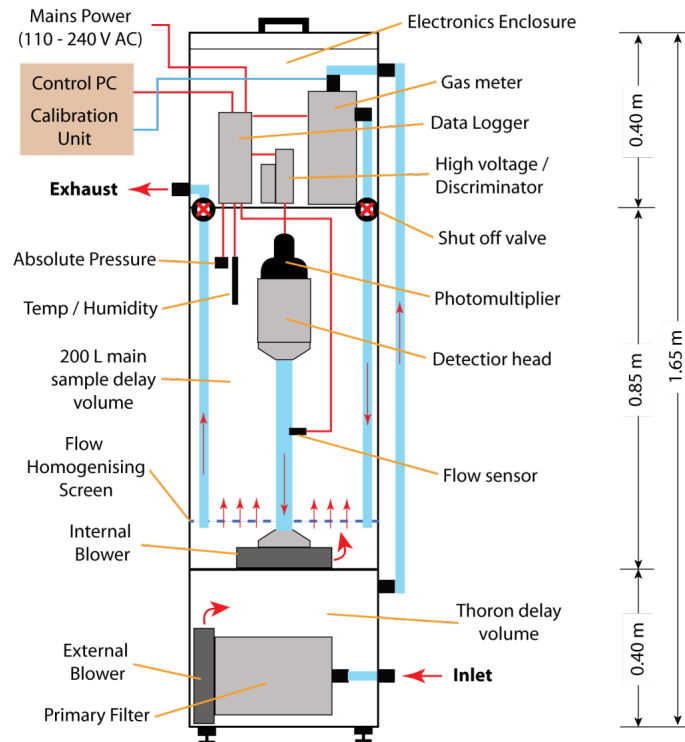


FIGURE 8.1: Schematic drawing of the ANSTO 200 L ^{222}Rn monitor. Courtesy to (Chambers et al., 2022)

The readings provided by the ANSTO 200 L ^{222}Rn monitor were modeled by a piecewise function, consisting of either an ingrowing or a decaying exponential function, depending on the regime, which was regressed by a non-linear least-squares procedure. In this way, for each source (or combination of sources) installed in the experimental setup, the reading of the ANSTO 200 L is determined by extrapolation to the steady-state value.

Additionally, a background value was added to the model which accounts for both the zero-value indication background of the ANSTO 200 L and the fact that some residual ^{222}Rn was experienced to be present in the chamber, which might be caused by the ANSTO 200 L device itself, exhaling minimal amounts of ^{222}Rn . From the experimental data, the ANSTO 200 L showed a background reading of 56 counts per 30 min in the climate chamber. The presence of an additional ^{222}Rn source in the chamber was checked by streaming aged bottled synthetic air through the chamber (with an opened outlet) over a course of 15 hours such that the differential pressure between the chamber and the ambient pressure was stabilized at 200 Pa (setpoint controlled). A total of approximately 15 m^3 of synthetic air were streamed through the chamber in this way.

The evolution of the ANSTO 200 L response during this time is depicted in Figure 8.3, indicating that the exchange of the chamber air with aged synthetic air decreased the ANSTO 200 L readings, leading to the above conclusion. Due to experimental limitations, it was not feasible to entirely flush the climate chamber with synthetic air, since the required amounts of air were deemed to be too high to entirely replace the chamber air several times. It should be noted, however, that this effect does not impact the determination of the sensitivity of the ANSTO 200 L, since it only results in a constant offset on the intercept of a linear relationship between the device indication and the calculated ^{222}Rn activity concentration in the chamber. The parameter of this linear relationship were determined by linear least-squares, also accounting for the uncertainty in the independent variable (the activity concentration

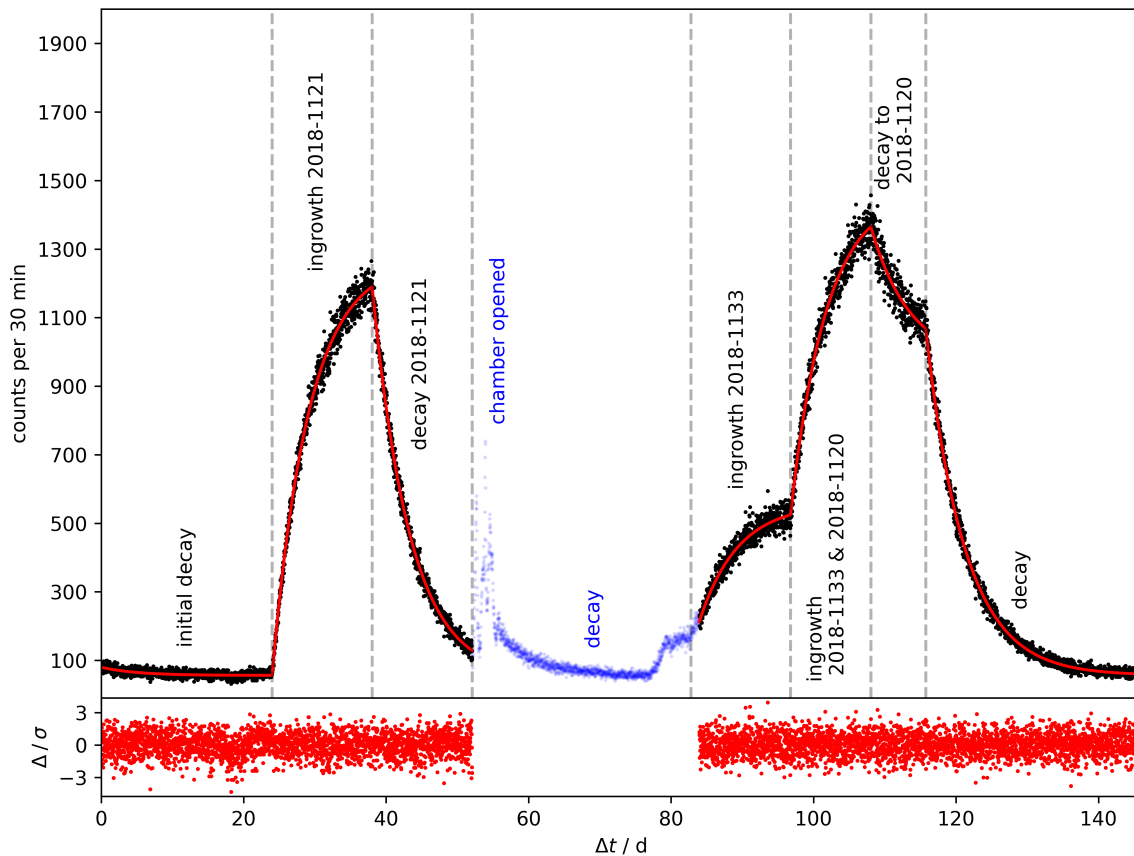


FIGURE 8.2: Response of the ANSTO 200 L ^{222}Rn monitor in a climate chamber to which several emanation sources are connected to provide stable characteristics. Black dots indicate data that was taken into account for non-linear regression of a piecewise model (red curve), whereas blue dots indicate data that was not modeled. Different regimes are indicated by descriptive text and vertical dashed lines. The bottom panel shows the normalized residuals between the model and the ANSTO 200 L readings.

in the chamber) by utilizing orthogonal distance regression as implemented in SciPy. The result of this procedure is given in Figure 8.4, and yields a sensitivity of $(0.0380 \pm 0.0006) \frac{\text{m}^3}{\text{s} \cdot \text{Bq}}$ and an intercept of $(-22 \pm 16) \frac{1}{30 \text{ min}}$. Notably, the intercept is negative in this case, which underpins the finding that the true ^{222}Rn activity concentration in the chamber was actually slightly higher due to exhalation of ^{222}Rn from the ANSTO 200 L device itself.

8.2 ANSTO 200 L pulse calibration method

While the previous method of static calibration seems to offer a straight forward way for calibration, it implies two important factors. First of all, the method only allows for an application in a reference volume that is several times bigger than the detector's active volume and that can fit the detector in question. For measurement devices intended to be used outdoors, like the ANSTO ^{222}Rn monitors, this is a severe limitation in practice, since calibration requires to ship the detector in question to a sufficiently equipped calibration facility. While still possible for the 200 L monitor, this is not practicable for the larger models like the 1500 L ANSTO device, which is in routine operation (Chambers et al., 2018; Griffiths et al., 2016). Furthermore, calibration factors may correlate with environmental parameters, and it is a

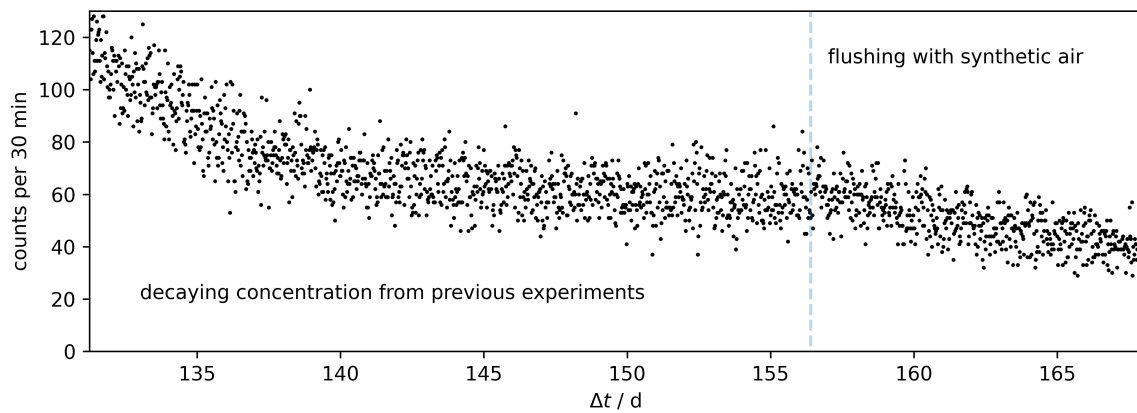


FIGURE 8.3: Response of the ANSTO 200 L ^{222}Rn monitor in a climate chamber under a continuous stream of synthetic air. See text for details.

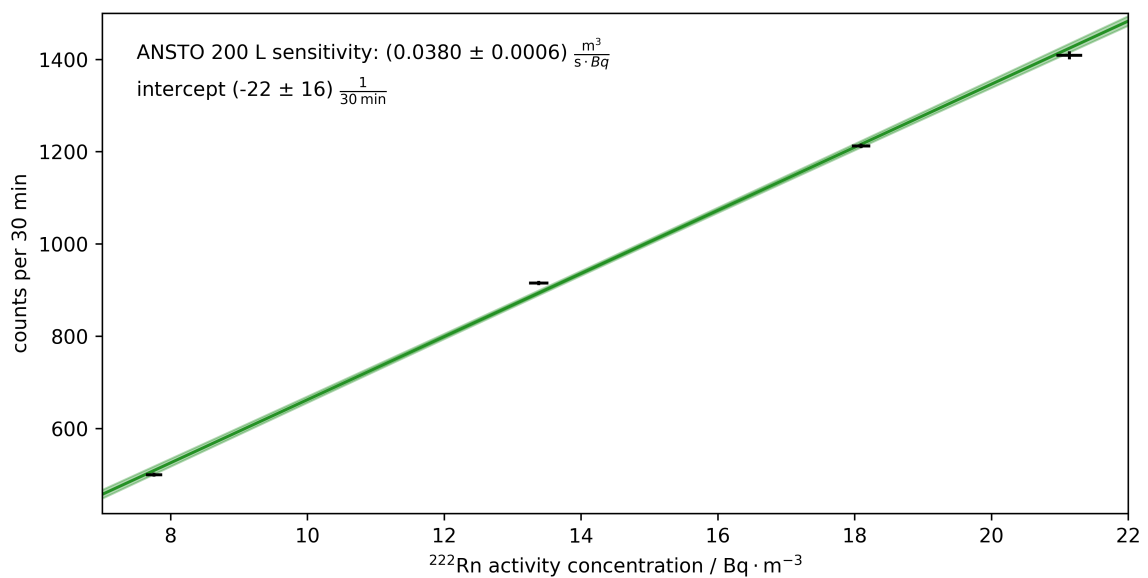


FIGURE 8.4: Depiction of extrapolated ANSTO 200 L ^{222}Rn monitor readings at different ^{222}Rn activity concentrations in the climate chamber (black). 1σ uncertainty is depicted in both x- and y-directions. The green curve represents the calibration curve determined by orthogonal distance regression and the associated 68 % confidence band (faint green).

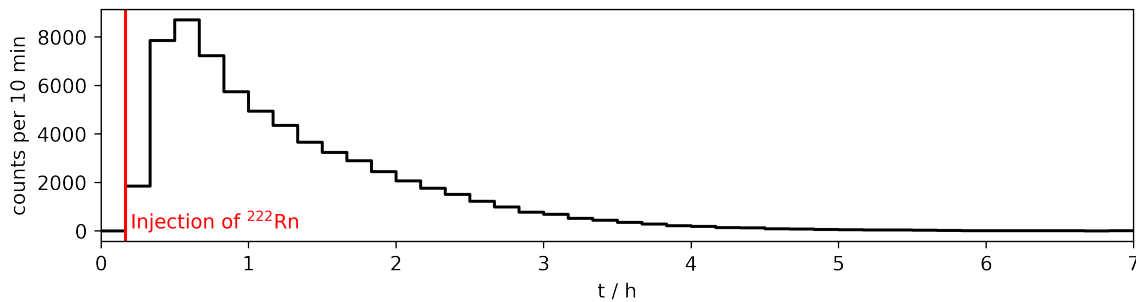


FIGURE 8.5: Observed response of the ANSTO 200 L ^{222}Rn monitor to an approximately Dirac Delta input of (284 ± 3) Bq of ^{222}Rn .

very time consuming endeavour and experimentally difficult to assess every combination of environmental parameters the detector in question may experience during its operation in the field.

On the other hand, the specific design of the ANSTO monitors, as well as any other monitor that relies on sampling air and measuring ^{222}Rn progeny, such as the ARMON developed by the Polytechnic University of Catalunya (Grossi et al., 2012; Vargas et al., 2015) and the Heidelberg Radon Monitor (Levin et al., 2002), has a temporal response characteristic that can not be assessed under static calibration conditions. Specifically, the fact that the ANSTO device measures the ^{222}Rn progeny ^{218}Po and ^{214}Po that is accumulated onto a filter by sampling outdoor air with a certain flow-rate leads to a deviation of the temporal response from the actual outdoor ^{222}Rn concentration in question. This is due to the time required for the decay of intermediate ^{214}Bi and ^{214}Pb and that the concentration of ^{222}Rn inside the active volume does not equal the outdoor concentration at every instantaneous moment in time due to the sampling, especially in response to steep temporal gradients of the outdoor concentration. Applications of ^{222}Rn -based methods in the environmental sciences are, however, often concerned with its temporal evolution. Outdoor ^{222}Rn concentrations show a diurnal cycle correlated with vertical mixing in the atmosphere with a typical strong drop of outdoor ^{222}Rn concentrations following the onset of vertical mixing in the mornings after a time of nocturnal stability and correspondingly high ^{222}Rn concentration, (Griffiths et al., 2016; Desideri et al., 2006) among others. This effect can be used in atmospheric studies, e.g. in (Perrino et al., 2001; Williams et al., 2013; Williams et al., 2016; Chambers et al., 2019b; Chambers et al., 2019a) among others.

The device's signal is therefore given by a convolution of the actual ^{222}Rn concentration, and this has been addressed previously by the manufacturers using numerical deconvolution techniques (Griffiths et al., 2016). Such a method requires, however, that the kernel function of this convolution operation is known. In the following, an outline and specific results of a previously unreported method of calibration by using a pulse of ^{222}Rn of known activity that is directly injected into the inflow air-stream of such a device is given, which may be applied to both in-field calibration and to assessment of the temporal response behaviour. In practice, this is realized by placing an emanation source inside a small, hermetically sealed volume such that it acts as a ^{222}Rn integration volume. After a certain ingrowth time, the ingrown and known activity of ^{222}Rn is injected by passing a stream of aged, technical air through this volume and into the detectors active volume, at a flow rate that ensures quick flushing of the integration volume. The ANSTO 200 L radon monitor readings in response to such an input are shown in Figure 8.5.

Through a numerical model, the resultant response characteristics may be related to the initial ^{222}Rn activity and hence, both a calibration factor and the temporal response properties of such a device may be assessed. For comparison with the results from the static calibration, here, the focus is on deriving an equivalent, effective efficiency ϵ or calibration factor. This technique relies on a theoretical model of the detector, which is laid down in the following, and, which is closely related to the model reported in (Griffiths et al., 2016).

A state vector describing the state of the ANSTO ^{222}Rn monitor is chosen as

$$\mathbf{x} = [A_{214\text{Po}} \quad A_{214\text{Bi}} \quad A_{214\text{Pb}} \quad A_{218\text{Po}} \quad A_{222\text{Rn},V_a} \quad A_{222\text{Rn},V_d}]^T$$

It is assumed, that air is drawn into the delay volume V_d and across the active volume V_a by a certain flow-rate Q . Any SLP that enters V_d is removed by passage through a particulate filter and any SLP that is generated by the decay of ^{222}Rn within V_a is plated out on a particulate filter and measured by the ZnS-scintillator, see Figure 8.1. In practice, this is realized by circulation of air within V_a across the measurement filter with a flow-rate orders of magnitude higher than Q . In the experimental setup, Q is controlled by a calibrated mass-flow-controller (MFC) and set to the value of $10 \text{ L} \cdot \text{min}^{-1}$ with a standard uncertainty of 0.25 %. Assuming instantaneous mixing and hence volumetric homogeneity of activity within the volumes V_d and V_a , the evolution of the state may be approximately described as

$$\frac{d\mathbf{x}}{dt} = \begin{bmatrix} -\lambda_{214\text{Po}} & \lambda_{214\text{Po}} & 0 & 0 & 0 & 0 \\ 0 & -\lambda_{214\text{Bi}} & \lambda_{214\text{Bi}} & 0 & 0 & 0 \\ 0 & 0 & -\lambda_{214\text{Pb}} & \lambda_{214\text{Pb}} & 0 & 0 \\ 0 & 0 & 0 & -\lambda_{218\text{Po}} & \lambda_{218\text{Po}} & 0 \\ 0 & 0 & 0 & 0 & -\lambda_{222\text{Rn}} - \frac{Q}{V_a} & \frac{Q}{V_a} \\ 0 & 0 & 0 & 0 & 0 & -\lambda_{222\text{Rn}} - \frac{Q}{V_d} \end{bmatrix} \mathbf{x} = \mathbf{F}\mathbf{x}$$

As stated before, the solution is given as an initial value problem in terms of the matrix exponential and a convolution integral in case of an inhomogeneous term, such as an input term acting on $A_{222\text{Rn},V_d}$.

It is assumed, that the ZnS-scintillator measures only the activities of captured ^{214}Po and ^{218}Po with distinct counting efficiencies of $\epsilon_{214\text{Po}}$ and $\epsilon_{218\text{Po}}$. This measurement is understood as being related to the time integrated state with an integration time of r , in this example chosen to be 600 s. Hence, the ANSTO device measurements are related to the state vector by

$$\mathbf{y}_t = \mathbf{H} \int_t^{t+r} \mathbf{x}(\tau) d\tau$$

where

$$\mathbf{H} = [\epsilon_{214\text{Po}} \quad 0 \quad 0 \quad \epsilon_{218\text{Po}} \quad 0 \quad 0]$$

When a pulse described by a Dirac-Delta distribution of area A_i , centered on time t_i , is injected into the air stream of the delay volume V_d , the resultant state may thus be modeled as

$$\mathbf{x}(t) = \begin{cases} 0 \cdot \mathbf{L} & t < t_i \\ e^{F(t-t_i)} A_i \mathbf{L} & t \geq t_i \end{cases}$$

where $\mathbf{L} = [0 \ 0 \ 0 \ 0 \ 0 \ 1]^T$.

And thus, \mathbf{y}_t can be evaluated as the piecewise function

$$\mathbf{y}_t = \begin{cases} b & t, t+r < t_i \\ b + \mathbf{H} \int_{t_i}^{t+r} e^{F\tau} A_i \mathbf{L} d\tau & t < t_i, t+r \geq t_i \\ b + \mathbf{H} \int_t^{t+r} e^{F\tau} A_i \mathbf{L} d\tau & t \geq t_i \end{cases}$$

where b signifies a certain background signal observed over the respective integration time r .

The matrix exponential required for these calculations is evaluated using symbolic computation of the Eigenvalue decomposition of F and the following identities

$$\exp(Ft) = P \exp(\Lambda t) P^{-1}$$

where P signifies the stacked Eigenvectors and Λ signifies the diagonal matrix of corresponding Eigenvalues of F and

$$\int_a^b \exp(F(\tau - c)) d\tau = P (\exp(\Lambda(b - c)) - \exp(\Lambda(a - c))) \Lambda^{-1} P^{-1}$$

for the non-singular F .

Once again, \mathbf{y}_t corresponds to a counting process, and hence, the actual observed counts $\hat{\mathbf{y}}_t$ under knowledge of all parameters, signified by a parameter vector $\boldsymbol{\theta}$, are modeled by a Poisson distribution

$$\hat{\mathbf{y}}_t | \boldsymbol{\theta} \sim \text{Poisson}(\mathbf{y}_t) \quad (8.1)$$

In such a model, the interest lies in simultaneously determining the counting efficiencies $\epsilon_{218\text{Po}}$ and $\epsilon_{214\text{Po}}$, such that they may be used to compute the effective steady state efficiency ϵ relatable to the previous section's results as

$$\epsilon = \frac{\epsilon_{214\text{Po}} + \epsilon_{218\text{Po}}}{V_a}$$

keeping also in mind, that V_d and V_a are both not precisely known, but may be estimated from the respective geometrical dimensions of the device. However, it is possible to determine these using this modeling approach together with the detection efficiency. One may observe, that the specific observed shape of the sequence $\hat{\mathbf{y}}_t$ is a function of the relationships between the parameters V_d , V_a and $\epsilon_{214\text{Po}}$, $\epsilon_{218\text{Po}}$ and the not infinitely well determined input point t_i . In practice, observing a specific shape of $\hat{\mathbf{y}}_t$ (Fig. 8.5) thus only offers limited information on V_a and V_d , and therefore, these two parameters are poorly identifiable without

additional prior information. Moreover, uncertainties of the decay constants λ_i and flow-rate Q propagate non-linearly across the model. The estimation of the resultant uncertainty in the derived quantity ϵ is therefore not straight-forward.

The way that was chosen to address both these factors lies in Bayesian analysis to estimate the resultant uncertainty in ϵ and to introduce prior distributions on V_a and V_d that are essential for convergence of this model into a physically reasonable result. As described above, the model suffers from poor identifiability under flat (i.e. improper) priors, due to the strong correlation of V_a , V_d , t_i and the efficiencies. The probability distribution of the full parameter vector θ in light of the observed data \hat{y}_t time-series is of interest in order to quantify the resultant uncertainty and is given by Bayes theorem (omitting normalization) as

$$p(\theta | \hat{y}_t) \propto p(\hat{y}_t | \theta)p(\theta)$$

where $p(\hat{y}_t | \theta)$ is referred to as the likelihood given by Eq. (8.1) and $p(\theta)$ signifies the prior distribution of the parameters.

Markov-Chain Monte-Carlo methods allow to draw samples from the probability distribution $p(\theta | \hat{y}_t)$, the posterior, given that it can be evaluated, such as the Metropolis-Hastings (Hastings, 1970) algorithm and more recently, derivatives of Hamiltonian Monte-Carlo. In the specific implementation used herein, the Hamiltonian Monte-Carlo method given by the efficient No-U-Turn-Sampler (NUTS) (Hoffman and Gelman, 2011), as implemented in the Python framework PyMC3 (Salvatier et al., 2016), was used to draw samples from the full posterior distribution. Thereby, both the uncertainty of the efficiency as well as the correlation between all model parameters are accessible, and, more importantly, the propagated uncertainty of all input quantities on to ϵ may be assessed without additional simplifying assumptions such as the commonly applied truncated Taylor expansion (linearization).

V_d and V_a have been reparametrized to capture the fact that by construction $V_d < V_a$ as

$$\begin{aligned} V_a &\sim \text{LogNormal} \\ z &\sim \text{Beta} \\ V_d &= z \cdot V_a \end{aligned}$$

signifying, that V_a is given a LogNormal prior (with support only on $V_a > 0$) and introducing the auxiliary variable z with a Beta distribution (with support only on $0 < z < 1$) such that $V_a > V_d > 0$ is always fulfilled. These distributions have been parametrized such that they have reasonably high density at the crude approximations of $V_a \approx 200$ L and $V_d \approx 50$ L, but do not introduce a lot of information. Figure 8.7 shows samples from the prior PDF of model parameters used in the modeling of the response of the ANSTO 200 L detector to an input of (284 ± 3) Bq of ^{222}Rn , established from the implanted emanation source 2018-1120 from Publication II at a flow-rate of (10.0000 ± 0.0025) L \cdot min $^{-1}$. The pairwise correlations and marginal histograms of the full posterior from $5 \cdot 10^5$ samples drawn with the NUTS sampler are shown in Figure 8.8 detailing the strong correlation between V_a and V_d and, indicating by comparison with the static calibration result in red, the remarkably good agreement between both methods. The uncertainty in the thus determined efficiency is almost entirely due to the uncertainty of the input ^{222}Rn activity, i.e., the emanation source. The modeling approach also allows to compute the activity in each of the compartments of the ANSTO 200 L (delay and measurement volume) in response to the input activity and

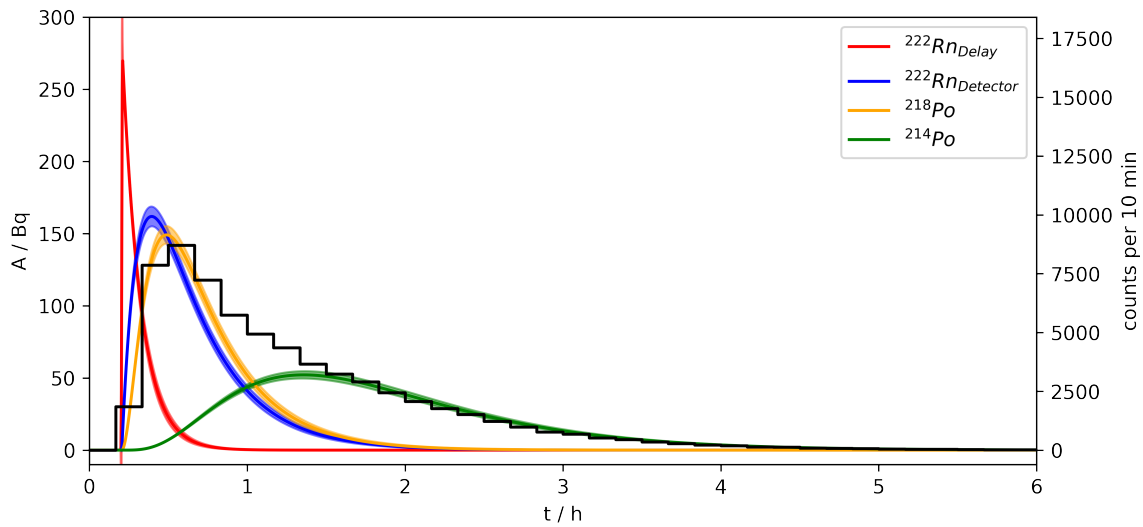


FIGURE 8.6: Observed response of the ANSTO 200 L ^{222}Rn monitor to a approximately Dirac Delta input of (284 ± 3) Bq of ^{222}Rn (black) and modeled activities of each nuclide (colored) with 1σ confidence bands (faint colors).

given its observations, as shown in 8.6. These results may be utilized for deconvolution approaches in order to correct for the temporal response characteristics of this device.

Notably, the time for calibration in the pulse method equates to around 6 hours, plus some additional 2-4 hours for flushing the residual ^{222}Rn from the detector to determine the intrinsic background, b . The integration time of the ^{222}Rn source required for ingrowth of a desired and suitable amount of the nuclide, does not impair the usual operation of the detector. This makes the method very applicable to in-field calibrations, which may be repeatedly carried out by an automatized procedure, as referenced in (Griffiths et al., 2016), e.g., by automatically injecting and analyzing a pulse at certain times. Notably, and as can be seen in Figure 8.8, this modeling approach also allows to assess the volumes of both compartments of the device, and the obtained results compare well to crude approximations of both these volumes.

While in the specific application herein, an implanted ^{222}Rn source with very stable properties from Publication II was used that produced a relatively high amount of ^{222}Rn in the integration time, the IRSD development from Publication IV may be readily employed instead. This in turn also allows for the indirect determination of the ingrown ^{222}Rn activity from the α -particle spectrometric measurements by the IRSD. It should be highlighted, that this method has the crucial benefit of not requiring an environment of negligible background ^{222}Rn concentration (a ^{222}Rn -tight reference chamber), requires only little time (6 hours in comparison to the several weeks of static calibration), and additionally allows assessment of temporal response characteristics. The development of the IRSD setup also enables this method to be applied in-field, as the IRSD allows to accurately calculate the ingrown activity in the integration volume that is subject to be injected in light of actual measurement data, and hence, allows to correct any influence of environmental parameters that may arise in practical applications.

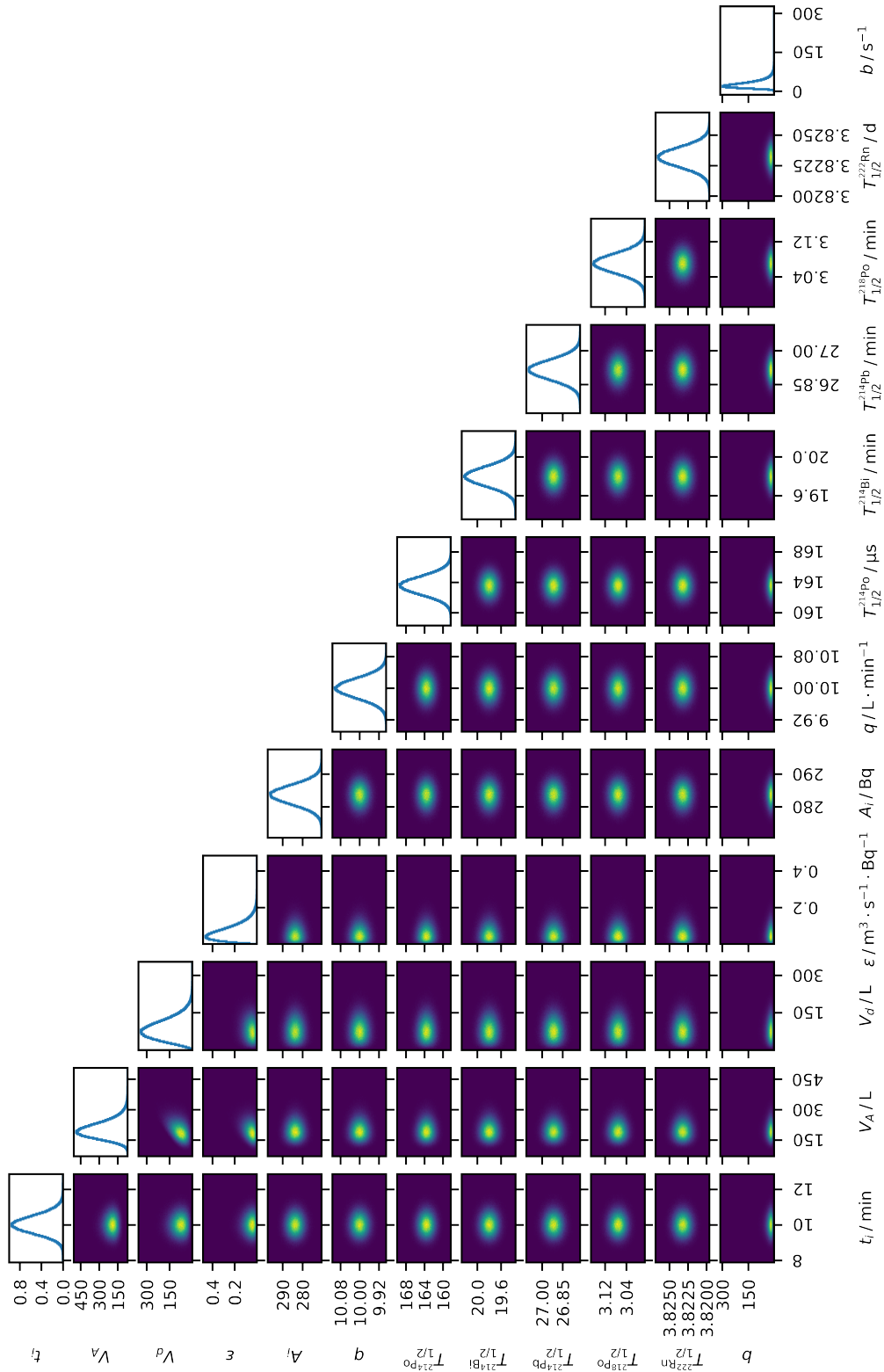


FIGURE 8.7: Prior distribution used for evaluation of the pulsed calibration method for a (284 ± 3) Bq pseudo Diarc-Delta input into the ANSTO 200 L ^{222}Rn monitor at a flow rate of (10.0000 ± 0.0025) $\text{L} \cdot \text{min}^{-1}$.

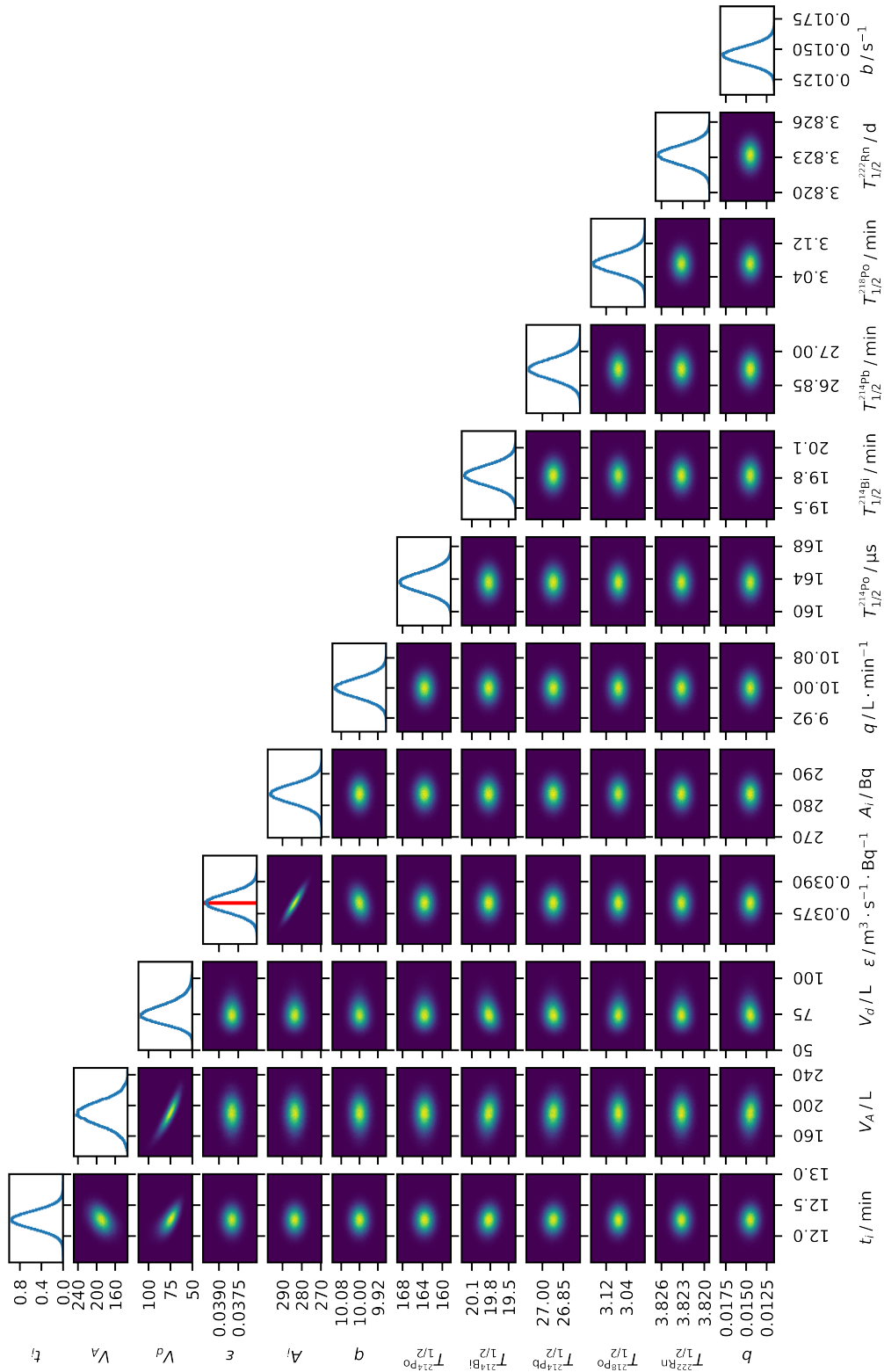


FIGURE 8.8: Posterior distribution obtained from the pulsed calibration method for a (284 ± 3) Bq pseudo Dirac-Delta input into the ANSTO 200 L ^{222}Rn monitor at a flow rate of (10.0000 ± 0.0025) L \cdot min $^{-1}$. The red bar signifies the efficiency obtained from the static calibration method.

8.3 AlphaGuard Calibration using IRSD and State-Space Modeling

In this section, a specific use case of the developments in Publication IV, namely the IRSD to calibrate ^{222}Rn -measurement devices in the static mode is outlined. Static herein refers to an experimental setup, where the IRSD is placed inside of a hermetically sealed container, in which the ^{222}Rn -measurement instrument, in this case the AlphaGuard model PQ2000, measures the ^{222}Rn concentration.

Herein, it is shown how the propositions of section 2.2.3 can be used in order to infer the approximate statistics of the ingrown volumetric ^{222}Rn from the repeated IRSD α -spectra collection at the times of interest, i.e. the times at which the AlphaGuard reported its measurement. In a second step, assuming a linear response of the AlphaGuard, linear regression is used in order to derive its sensitivity, using the previously inferred ^{222}Rn activity concentration values. Specifically, two datasets are available, which were analyzed using the same methodology as outlined below.

8.3.1 Model specification

Following the derivations from section 2.2.3, one can make the observation that the volumetric activity of ^{222}Rn may be included into a state-vector \mathbf{x} . The assumptions of a random-walk to describe the time-variability of η is adopted from section 2.2.3 to arrive at the following SDE, which may be used to described the evolution of the system.

$$d\mathbf{x} = \mathbf{F}\mathbf{x}dt + \mathbf{L}d\beta_t$$

with the matrices and vectors given as

$$\mathbf{x} = \begin{bmatrix} A_{Rn}^V \\ A_{Rn}^S \\ A_{Ra}^S \\ \eta \end{bmatrix}, \mathbf{F} = \begin{bmatrix} -\lambda_{Rn} & 0 & 0 & \lambda_{Rn} \\ 0 & -\lambda_{Rn} & \lambda_{Rn} & -\lambda_{Rn} \\ 0 & 0 & -\lambda_{Ra} & 0 \\ 0 & 0 & 0 & 0 \end{bmatrix}, \mathbf{L} = \begin{bmatrix} 0 \\ 0 \\ 0 \\ \sigma \end{bmatrix}$$

where A_{Rn}^V and A_{Rn}^S refer to the activity of ^{222}Rn in the volume and in the source respectively, A_{Ra}^S refers to the ^{226}Ra activity of the source, $d\beta_t$ refers to the increments of a standard 1-dimensional Wiener-process and σ is a tunable parameter, i.e. the square root of the spectral density of the respective Wiener-process.

Inference, in terms of filtering and smoothing using integrating measurements, such as the α -particle spectrum collection of the IRSD is described in section 2.2.3 and in part in Publication IV. As stated therein, this requires knowledge of the measurement matrix \mathbf{H} , which is used to map the evolved state onto the measurement space. This requires a suitable definition of the measurement vectors, which are the inputs to the model. In this case, non-linear regression of the collected α -particle spectra as outlined in section 2.3.4 and Appendix A1 of Publication IV was used to derive the peak-areas with respect to ^{222}Rn and ^{226}Ra of each α -particle spectrum collected by the IRSD. Together with the time-differences between the endpoint of each spectrum, real- and dead-time of each spectrum, these peak areas were dead-time corrected to form the input to the filtering and smoothing algorithms. The measurement matrix denoted by \mathbf{H} necessary for deriving the measurement prediction from the state-evolution is given by

$$\mathbf{H} = \begin{bmatrix} 0 & 0.494 & 0 & 0 \\ 0 & 0 & 0.494 & 0 \end{bmatrix}$$

as determined using the primary DSA spectrometer in Publication IV and which only applies to the exact IRSD that was used. The values and shape of this matrix was chosen such that its multiplication with the integrated state vector yields the corresponding correct alignment of the input measurement vectors, which are constructed by the stacked peak-areas. Specifically, the values correspond to the counting efficiency of the IRSDs with respect to each of the nuclides in question.

This formalism allows to extract the set of marginal PDFs, $p(A_{Rn}^V(t_k) | \mathbf{y}_{1:T})$, for a finite set of time-instants t_k in the set of AlphaGuard measurement time instants and where $\mathbf{y}_{1:T}$ denotes the set of all collected IRSD spectra in the analyzed time-period.

However, the initial state at a specified instant in time t_0 is not infinitely well known. In the experiments, the sealed volume may have not been flushed entirely from ^{222}Rn that may have been present from previous experiments or from the laboratory air. Additionally, the formalism simply projects the initial state of the volumetric ^{222}Rn activity to the future, and therefore, the specified prior distribution for x_0 impacts the earlier measurements, where the initial ^{222}Rn in the volume has not decayed entirely. It should also be noted, that the AlphaGuard usually has a non-zero blank indication, especially after higher exposures due to built-up contamination with ^{210}Pb and ^{210}Po .

The blank indications were measured afterwards by flushing the volume with aged synthetic air, that is known to not contain significant quantities of ^{222}Rn . These values are then used to fix the intercept of the linear response of the AlphaGuard and the initial ^{222}Rn concentration in the volume is estimated using the fixed intercept as the value that produces the smallest χ^2 -statistic of a linear regression between and AlphaGuard-measured- and IRSD-inferred ^{222}Rn activity concentration, i.e., such that it maximizes the linearity of the calibration.

8.3.2 Experimental results in a 50 L reference volume

This first dataset was recorded in conjunction with the experiments from Publication IV. In a hermetically sealed container of $(0.0490 \pm 0.0005) \text{ m}^3$ in volume, the IRSD with approximately 185 Bq ^{226}Ra was operated using a KF-flange feedthrough. Inside of the 50 L container, an AlphaGuard recorded the temperature, relative humidity and the activity concentration of ^{222}Rn . The AlphaGuards inherent background reading was determined to $(30.6 \pm 1.7) \text{ Bq} \cdot \text{m}^{-3}$. Prior to the measurements, the container was flushed with laboratory air of low, but unknown ^{222}Rn activity concentration. At a specific time, 3 mL of hot water were introduced into the chamber in order to increase the relative humidity to investigate the dependency of the ^{222}Rn emanation of the IRSD on the relative humidity. The total measurement period spans approximately 3 months and both IRSD α -particle spectra and AlphaGuard measurements were sampled on 10 minute intervals. Hence, the entire dataset contains roughly 12000 α -particle spectra and AlphaGuard measurements respectively.

The formalism outlined in section 8.3.1 was applied to the IRSD α -particle spectra and the results are shown in Figure 8.9. Therein, derived peak areas of the IRSD spectra are shown as purple dots, AlphaGuard measurements are shown as green dots and the inferred evolution of the state according to the modeling procedure outlined in section 8.3.1 is shown as black lines together with a shaded 1σ confidence interval that reflects the statistical uncertainty stemming from the employed modeling procedure. It should be noted, that this

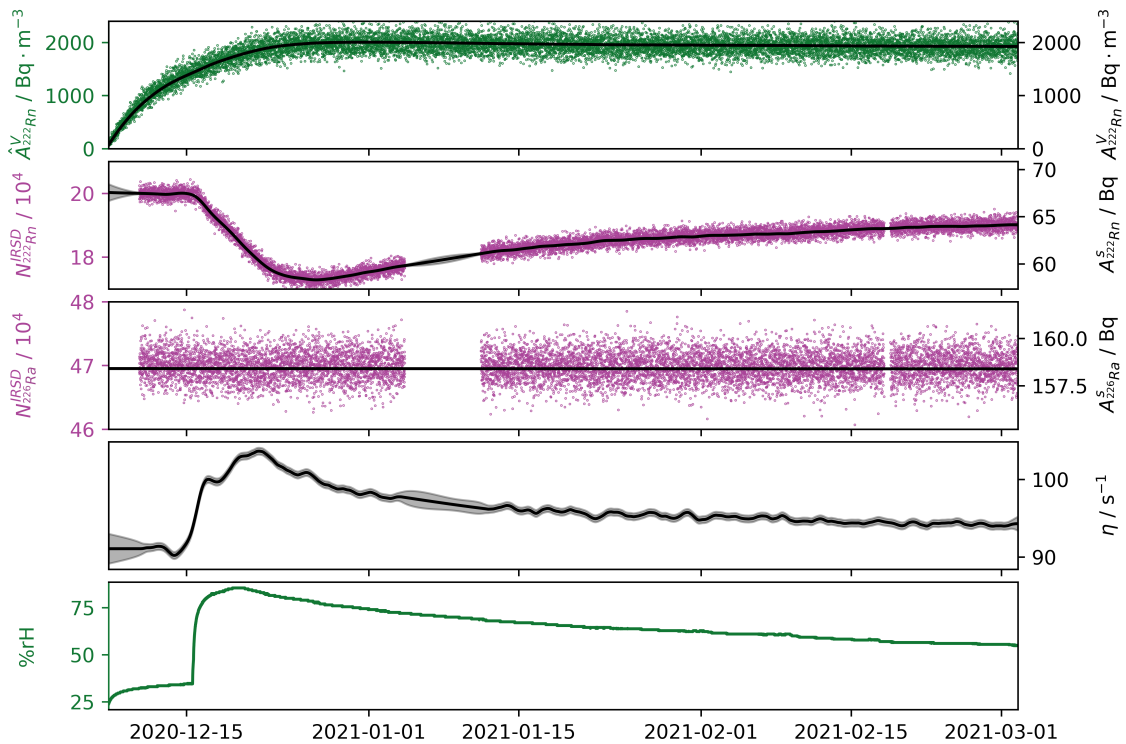


FIGURE 8.9: State (black mean, grey confidence interval) inferred from IRSD measurements using the Filtering and Smoothing approach of IRSD data (purple). Associated measurements of an AlphaGuard are shown in green. See section 8.3.1 for an explanation of the quantities.

uncertainty does not reflect the systematic contributions that are due to the uncertainty of the IRSD efficiency. Note, that due to specification of the model, the uncertainty of the ^{222}Rn emanation and thus the uncertainty of the associated quantities increases in the absence of IRSD measurements, such as in the beginning of the depicted time-series.

Since the dataset contains many AlphaGuard readings at very close inferred ^{222}Rn concentration levels, the linearity of the regression curve is depicted as a box-plot, i.e., over binned values of the inferred ^{222}Rn concentration, in Figure 8.10. The underlying linear regression, however, was computed from linear least-squares using the entire, unbinned data. The box-plot signifies the span of the y-data (AlphaGuard readings) in each bin by the notched lines, its median value by the colored bar and the range into which 75 % of the data falls by the box. The notched lines therefore should not be mistaken with the standard uncertainty and it should be noted, that those statistical quantities are computed from the actual observations, rather than from statistical modeling. It can be seen, that the AlphaGuard shows a very linear response with the inferred ^{222}Rn concentration, which indicates the correctness of the modeling procedure, assuming that the AlphaGuard truly has a linear response over the range of the data. Notably, this is despite the relatively strong increase in the emanation by almost 10 %, which leads to a ^{222}Rn ingrowth-curve that does no longer follow the expected shape (i.e. that of Equation (2.15) for an undistorted ingrowth). Despite this, the presented model allows to correct this dependency, and therefore, to perform calibration outside of the steady-state regime, specifically enabled by the design of the IRSD and its

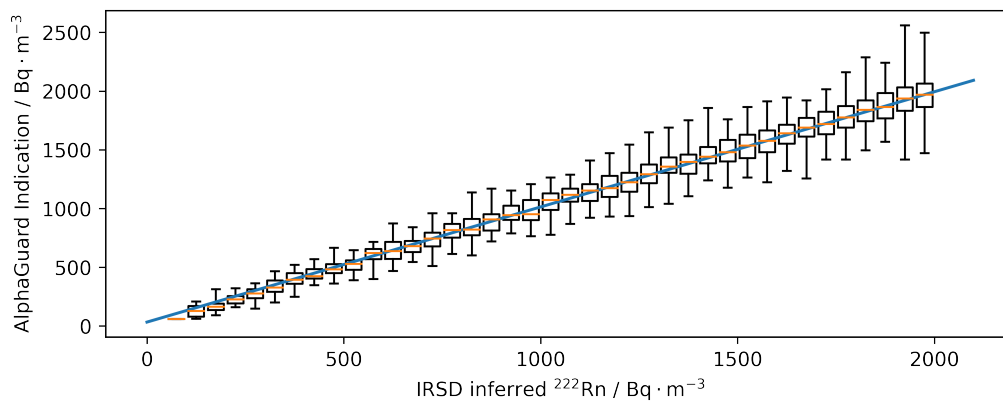


FIGURE 8.10: Linear regression result of AlphaGuard indicated ^{222}Rn concentration and IRSD inferred ^{222}Rn concentration to calibrate the AlphaGuard response. AlphaGuard data is depicted as a box-plot, where the binning was carried out with respect to the IRSD inferred data. Total sample-size: 12210 AlphaGuard readings.

operation together with the approach of statistical inversion outlined in this work.

Due to the very high number of sampled data-points, the statistical uncertainty of the AlphaGuard readings is only a negligible contributor to the overall uncertainty. The combined calibration uncertainty may be thus specified to amount to 1.5 %, which is due to the uncertainty of the IRSD measurements, as determined in Publication IV.

8.3.3 Experimental results in a 600 L reference volume

For this second experiment, the IRSD with approximately 66 Bq ^{226}Ra from Publication IV was used to produce a stable ^{222}Rn atmosphere in a reference volume of $(0.667 \pm 0.007) \text{ m}^3$. A different AlphaGuard (with respect to the previous section) was measuring the ^{222}Rn activity concentration inside of the reference volume. The inherent background of this AlphaGuard was determined to $(7.6 \pm 0.10) \text{ Bq} \cdot \text{m}^{-3}$ by exposing it to an atmosphere of aged synthetic air. Within the volume, the relative humidity was stable with respect to time. The results were determined similarly to the methods reported previously in 8.3.1. This data-set spans around 1 month or approximately 4000 α -particle spectra and AlphaGuard readings respectively. Figures 8.11 and 8.12 show the results similarly to the previous experiment. It should be noted, that in the top-panel of Figure 8.11, the curve does not follow the lines, since the AlphaGuard readings are biased by the inherent background of the AlphaGuard. Due to the specifically low ^{222}Rn activity concentration in this experiment, this is a bigger contribution in comparison to Figure 8.9.

Even in this case of low ^{222}Rn activity concentration, the uncertainty of the determined AlphaGuard sensitivity is almost entirely due to the IRSD systematic uncertainty of its efficiency (1.5 %, Publication IV). The statistical uncertainty of the sensitivity due to the statistics of the AlphaGuard measurements is only on the order of 0.2 %.

8.3.4 Comparison to a source from the Czech Metrology Institute

Within the *traceRadon* project, it was possible to receive a source with a specified activity of $(1144 \pm 17) \text{ Bq}$ ^{226}Ra and an emanation coefficient of (0.9626 ± 0.0026) from the Czech Metrology Institute (ref. Calibration certificate). This source's activity is traceable to the

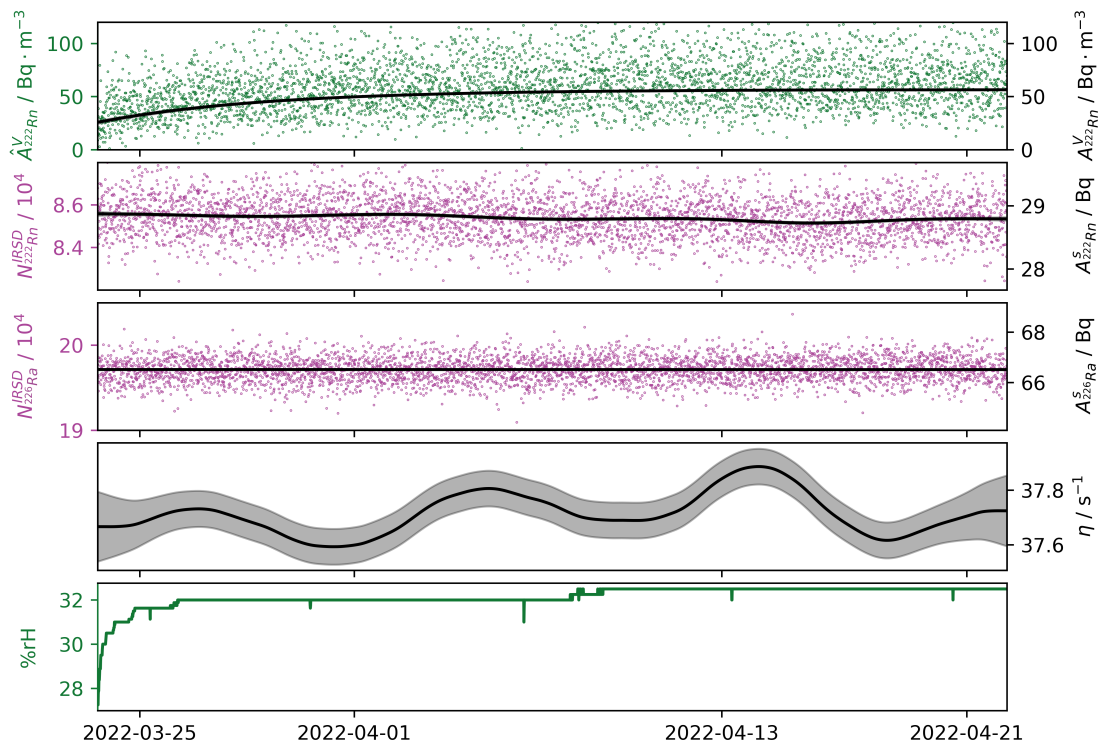


FIGURE 8.11: State (black mean, grey confidence interval) inferred from IRSD measurements using the Filtering and Smoothing approach of IRSD data (purple). Associated measurements of an AlphaGuard are shown in green. See section 8.3.1 for an explanation of the quantities.

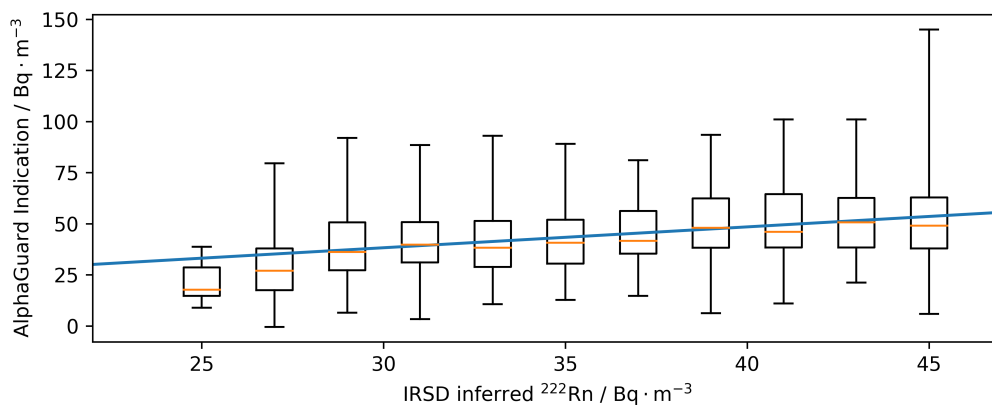


FIGURE 8.12: Linear regression result of AlphaGuard indicated ^{222}Rn concentration and IRSD inferred ^{222}Rn concentration to calibrate the AlphaGuard response. AlphaGuard data is depicted as a box-plot, where the binning was carried out with respect to the IRSD inferred data. Total sample-size: 4275 AlphaGuard readings.

Czech Hönigschmid standard and its emanation coefficient was determined by CMI using supporting γ -ray measurements, where full-energy peak efficiencies are determined from Monte-Carlo simulation, similar to the report given in (Fialova et al., 2020). Therefore, the CMI source's traceability to the SI is entirely independent of the IRSD. This source was used to produce stable ^{222}Rn atmospheres of approximately $21500 \text{ Bq} \cdot \text{m}^{-3}$ and $1600 \text{ Bq} \cdot \text{m}^{-3}$ in the respective reference volumes from section 8.3.2 and 8.3.3 and thus to determine a calibration factor for both AlphaGuards with respect to this source. Table 8.1 shows a comparison of the calibration factors for both of the AlphaGuards using the different sources, as outlined in the previous sections.

TABLE 8.1: Comparison of results from sections 8.3.2 and 8.3.3 with static calibration results obtained with a source from the CMI

	IRSD		CMI source		$k_{\text{CMI}}/k_{\text{IRSD}}$
	k	A / $\text{Bq} \cdot \text{m}^{-3}$	k	A / $\text{Bq} \cdot \text{m}^{-3}$	
AlphaGuard #1	1.019(15)	1925	1.056(19)	21500	1.036
AlphaGuard #2	0.979(15)	56.3	1.022(17)	1600	1.043

Despite the clear difference in ^{222}Rn activity concentration produced by the CMI source in comparison the IRSDs of considerably lower activity, the calibration factors obtained with each method and for each AlphaGuard are compatible with each other with respect to the estimated uncertainty. It should, however, be noted, that the uncertainty for both IRSDs is not independent, since they have both been calibrated against the same primary standard (DSA α -particle spectrometer). Therefore, the comparison is also concerned with the ratio of calibration factors obtained with each IRSD and with the CMI source for both AlphaGuards respectively. As indicated in Table 8.1, this ratio is also compatible between both IRSDs. On the other hand, a 3 % difference between the calibration factors obtained from the CMI source and those obtained from the IRSDs is observable. Due to the compatibility of the aforementioned ratio to within 1 %, this difference is likely due to the systematic uncertainties associated with each source. However, the overlap between credible intervals indicates that all systematic contributions to the IRSD uncertainty have been realistically estimated, under the assumption that the CMI source's uncertainty does reflect the true uncertainty.

Chapter 9

Discussion and Outlook

In this work, different techniques of manufacturing ^{222}Rn emanation sources have been investigated. By employment of the absolute measurement technique of DSA α -particle spectrometry and supporting measurements of the emanation of the produced sources, new primary emanation standards were produced. Specifically, the emanation properties from differently produced thin-layers of ^{226}Ra have been investigated in the process, where it was shown, that the nano-scale structural differences cause significant differences in the emanation behaviours.

While the relative humidity was experienced to impact the emanation of ^{222}Rn from electrodeposited ^{226}Ra strongly, and to a lesser extent also from PVD ^{226}Ra , implanted ^{226}Ra did not show this effect. While this, in principle, makes the ion-implantation a very desirable method for source production, it is complicated by the high experimental requirements and costs. Furthermore, higher emanation coefficients may be measured with higher relative accuracy, and the ion-implanted sources showed only emanation coefficients on the order of 0.25 to 0.35. Initially the ion-implantation technique was chosen such that the emanation from resultant sources is entirely due to the recoil of ^{222}Rn nuclei and not due to diffusion, the temperature dependence of the emanation demonstrated in Publication II may allow to judge, that even for ion-implanted ^{226}Ra , a part of ^{222}Rn is still released by a diffusion process, explaining the temperature dependence. Electrodeposition of ^{226}Ra on the other hand is an easily deployed experimental technique, but sources constructed in this way showed lacking performance both with respect to the stability of their ^{222}Rn emanation (Publication III) and in the DSA α -particle spectrometry required for standardization of the deposited ^{226}Ra activity. Overall, this technique was experienced to be difficult to control, specifically since the unavoidable presence and amount of impurities may strongly impact the properties of resultant sources. In fact, the deposited matter by this technique is estimated to be almost entirely due to other materials and not due to ^{226}Ra itself, evidenced also by the fact that the deposits were generally visible to the naked eye (c.f. Figure 2.10). Certainly, the application of this technique may have been optimized further, for example by down-scaling of the volume of employed solvents, which carry a large part of the total amount of impurities. This was, however, not pursued further, since regardless of possible optimizations, the ^{222}Rn emanating from such sources has to be monitored for an application in metrology anyhow. All in all, it was experienced that the overall design and especially the details of the manufacturing procedure can have a significant impact on both the stability properties as well as the overall emanation behaviour of sources. This complicates the situation significantly unless sources show perfectly stable emanation properties, because it calls for the thorough determination of the correlation of the emanation of each source with all possible environmental parameters. In practice, this can not be realized by previously established techniques, such as the (Linzmaier and Röttger, 2013) method of emanation measurements, due to time constraints. Notably, all three methods created sources which

can be classified as thin-layers of ^{226}Ra , and despite this, the emanation characteristics and stability are entirely different.

This led to the developments of the filtering and smoothing techniques (section 2.2.3, Publication III), which for the first time allows for near real-time estimation of ^{222}Rn emanation values based on continuously collected spectrometric data. This technique was also demonstrated with such generality to be employed regardless of the specifics of the measurements, making it applicable to both α -particle (IRSD) and γ -ray spectrometric measurements (Publication III).

Naturally, the measurement of the α -particles of ^{222}Rn is largely preferred over measurements of the γ -rays of SLP, since for one, ^{222}Rn is directly measured and secondly, α -particle spectrometry generally shows both higher efficiency and lower background contributions. As such, α -particle spectrometry can achieve significantly higher statistical accuracy and correspondingly lower limits of detection. However, α -particle spectrometry is notoriously difficult to be applicable to the measurement of the emanation, due to the requirement of vacuum conditions, which are entirely different from the environmental conditions sources are normally operated in. Consequently, the theoretical benefits and the development of the filtering and smoothing approaches inspired the technological approach of covering an α -particle detector in a thin-layer of ^{226}Ra . This was realized in Publication IV by employing the physical vapor deposition of ^{226}Ra . Specifically, this technique was chosen as a compromise between ion-implantation and electrodeposition, leading to ^{226}Ra deposits that do not penetrate the surface but which still are much cleaner than electrodeposited ^{226}Ra . Both these characteristics are necessary for the application of the IRSD method, since thin-layers of higher areal density would lead to significantly more tailing in the collectible spectra and the implantation of relatively high energy ions leads to damage of the crystal structure of the detector and hence ultimately to its destruction. The benefit of the IRSD technique lies in the fact that it allows to measure extraordinarily small emanation terms of ^{222}Rn , where in Publication IV it was demonstrated to still provide good statistical accuracy even for an average of a single emanating ^{222}Rn atom per second, roughly two orders of magnitude lower than previous PTB standards, while retaining a similar relative uncertainty. This allows applications such as the ones outlined in section 8.3.3, where ambient to sub-ambient ^{222}Rn reference atmospheres can be achieved without excessive up-scaling of reference volumes and it may allow even direct injection of ^{222}Rn into measurement devices in order to capture their temporal response characteristics.

A central topic for the application of the IRSD technique lies in the analysis of its streaming α -particle spectrometric data. Specifically, and as pointed out, it entails the modeling of spectra in order to derive the peak-areas and correct for the overlaps due to the tailing contributions. Hence, significant improvements may be achieved by further exploration of the deconvolution procedures applicable to such spectra, specifically regarding the estimation of uncertainty due to this effect. In this work, a heuristic approach was chosen for this purpose, however, it may be more accurately derived using Monte-Carlo methods as computational resources increase going forward.

In a similar vein, the Bayesian time-series analysis techniques applied for the statistical inversion to derive the emanation from such measurements utilized simplifying assumptions, such as the Gaussian assumption of the measurement data. With higher available computational resources, such assumptions may be dropped in future applications resulting in a smaller modeling bias. This includes both non-linear emanation models as well as non-Gaussian noise, both of which may be dealt with by employing non-linear filtering and smoothing techniques such as the Particle filter or the Unscented Kalman-Filter (Särkkä and Solin, 2019). Despite this, the analysis of dynamic measurements and the application

of the GUM to such measurements is also an active area of research, where (Eichstädt et al., 2016a; Eichstädt et al., 2016b) summarizes the challenges imposed on uncertainty estimation by dynamical measurement assessments. Results from this field similarly apply to the application of the IRSD, and to ^{222}Rn metrology in general, for example the application of the GUM to Fourier-transform based deconvolution techniques in (Eichstädt et al., 2016a) and to infinite impulse response filtering in (Eichstädt et al., 2016b), which are, however, often tied to relatively costly sampling based approaches, such as in (Eichstädt et al., 2012).

In terms of the manufacturing procedure of the IRSD, there is room for optimization regarding both the amount of impurities in the deposited ^{226}Ra layers as well as the general construction procedure of such devices. Ultimately, the path-length through any absorbing layers between the active depletion zone of the detector and the thin-layer geometry of the source needs to be as small as possible. While in Publication IV, PVD onto a commercially available detector was carried out, this is not optimal in the sense of retaining a dead-layer in between the ^{226}Ra and the depletion zone, due to the way the commercially available detectors are manufactured. However, it could be ideal to trap the ^{226}Ra within this layer, which may be achieved by either a bottom-up or a top-down approach, i.e., either by constructing the radium layer before the construction of the dead-layer or by implanting ^{226}Ra ions into a previously manufactured dead-layer. Care must however be taken in order to retain the junction characteristics required for the correct operation of such a device, and as a result, the implantation of high energy ^{226}Ra ions may be too harsh concerning the resultant radiation damage. One way to achieve this may be by using an implantation process with much lower energy while ideally, retaining the mass-to-charge ratio selection as in Publication II. A simpler alternative, however, may be given by the techniques of sputter deposition, or even, by subsequent implantation of a previously deposited thin-layer by using a *knock-on* (sometimes also referred to as *knock-in*) effect with another ion-beam (e.g. Ishiwara and Furukawa, 1977b; Ishiwara and Furukawa, 1977a), i.e. displacement of surface ^{226}Ra atoms into the bulk layer by recoiling from impinging ions.

Regardless of possible technical optimization paths, this work provides for the first time a pathway to both utilize and quantify dynamic ^{222}Rn reference atmospheres on the basis of supporting measurements of the emanation sources, as well as extending the range of currently available ^{222}Rn emanation sources to the Becquerel to sub-Becquerel level. Specifically, and as outlined in section 8.3.2, possible applications of the developments herein are manifold. For example, but not limited to, the down-scaling of reference volumes, the extension of the possible ranges of reference atmospheres down to the ambient and possibly sub-ambient levels and the employment of dynamic calibration procedures. As such, the developments, most notably the IRSD, can be considered a milestone improvement of current state-of-the-art ^{222}Rn metrology, and for the first time, ^{222}Rn reference atmospheres can be provided and reliably disseminated down to the ambient levels. All the while, dependency on the Hönigschmid standard and derived secondary standards was dropped throughout these developments, providing also an additional means of quality assurance in ^{222}Rn metrology, that is, by realization of a traceability chain to the SI that is entirely independent of both the Hönigschmid standards and the method of Picolo (Picolo, 1996) and any other prior ^{222}Rn emanation standards.

Appendix A

Derivation of integrated Gaussian process joint density

As outlined in section 2.2.3, the activity inside of an emanation source (and possibly also derived quantities like the ingrown activity inside of a volume, for example) may be modeled as a first order SDE of the form

$$\mathbf{x} = \mathbf{F}xdt + \mathbf{L}d\beta_t \quad (\text{A.1})$$

where \mathbf{x} describes the state vector, \mathbf{F} and \mathbf{L} describe time-independent matrices and $d\beta_t$ the increments of a Wiener process.

The act of measuring this sources with a spectrometer of any sort may be modeled as

$$\mathbf{y}_b = \mathbf{H} \int_a^b \mathbf{x}(s)ds \quad (\text{A.2})$$

where the time-points are chosen such that they relate to some previous time t_{n-1} as $a = t_{n-1} + \delta$ and $b = t_{n-1} + \delta + r = t_n$ where δ is some arbitrary time-offset between t_{n-1} and the beginning of the integration period and r specifies the respective integration time.

As discussed in 2.2.3, the solution to (A.1) can be expressed in terms of Itô's definition of the stochastic integral as

$$\mathbf{x}_a = \mathbf{\Psi}_{a|b}\mathbf{x}_b + \int_a^b \mathbf{\Psi}_{b|\tau}\mathbf{L}d\beta_\tau \quad (\text{A.3})$$

where $\mathbf{\Psi}_{a|b} = \exp(\mathbf{F}(a-b))$.

Suppose the state at t_{n-1} is described by the probability density $\mathcal{N}(\boldsymbol{\mu}_{n-1}, \boldsymbol{\Sigma}_{n-1})$, it can be used together with the transition density to compute the joint density of \mathbf{x}_{n-1} and \mathbf{x}_δ at time $t_{n-1} + \delta$ as

$$p(\mathbf{x}_{n-1}, \mathbf{x}_\delta) \propto \mathcal{N}\left(\left[\begin{array}{c} \boldsymbol{\mu}_{n-1} \\ \boldsymbol{\Psi}_{\delta|0}\boldsymbol{\mu}_{n-1} \end{array}\right], \left[\begin{array}{cc} \boldsymbol{\Sigma}_{n-1} & \boldsymbol{\Sigma}_{n-1}\boldsymbol{\Psi}_{\delta|0}^T \\ \boldsymbol{\Psi}_{\delta|0}\boldsymbol{\Sigma}_{n-1} & \boldsymbol{\Psi}_{\delta|0}\boldsymbol{\Sigma}_{n-1}\boldsymbol{\Psi}_{\delta|0}^T + \mathbf{U}_{\delta|0} \end{array}\right]\right) \quad (\text{A.4})$$

where $\mathbf{U}_{a|b} = \int_a^b \mathbf{\Psi}_{b|\tau}\mathbf{L}\mathbf{L}^T\boldsymbol{\Psi}_{b|\tau}^T d\tau$, as a direct consequence of the Chapman-Kolmogorov equation (2.19), which is well known, e.g. (Särkkä and Solin, 2019).

Combining equations (A.1) and (A.2) yields

$$\begin{aligned} \mathbf{y}_n &= \mathbf{H} \int_{\delta}^{\delta+r} \mathbf{x}(s) ds = \mathbf{H} \int_0^r \mathbf{x}(\delta + s) ds = \\ &= \mathbf{H} \int_0^r \left[\Psi_{\delta+s|\delta} \mathbf{x}_{\delta} ds + \int_{\delta}^{\delta+s} \Psi_{\delta+s|\tau} \mathbf{L} d\beta_{\tau} \right] \end{aligned}$$

which using *Fubini's theorem* may be rewritten as

$$\mathbf{y}_n = \mathbf{H} \int_0^r \Psi_{s|0} \mathbf{x}_{\delta} ds + \mathbf{H} \int_0^r \int_{\tau}^r \Psi_{s|\tau} \mathbf{L} ds d\beta_{\tau}$$

Since the ordinary integration (i.e. Riemann integral) can be expressed as the limit of a sum, and the multiplication with the matrix \mathbf{H} is a linear operation, \mathbf{y}_n must have a Gaussian distribution if it is assumed that the process $\mathbf{x}(t)$ takes continuous sample paths and is integrable. Furthermore, \mathbf{x}_{n-1} , \mathbf{x}_{δ} , \mathbf{x}_n and \mathbf{y}_n have a joint Gaussian distribution, which is hence completely characterized by its first- and second-order moments.

The first order moments, the mean-vector, of this joint distribution is just given by omitting the terms associated with the Wiener-process and may be simply computed by taking expectations and using the fact that $\langle \int d\beta_t \rangle = 0$ by definition.

The components of the variance-covariance matrix of this joint distribution are computed as follows.

Variance of \mathbf{y}_n

$$\begin{aligned} & \langle (\mathbf{y} - \langle \mathbf{y} \rangle) (\mathbf{y} - \langle \mathbf{y} \rangle)^T \rangle = \\ &= \left\langle \mathbf{H} \left(\int_0^r \Psi_{s|0} \mathbf{x}_{\delta} ds + \int_0^r \int_{\tau}^r \Psi_{s|\tau} \mathbf{L} ds d\beta_{\tau} + \left\langle \int_0^r \Psi_{s|0} \mathbf{x}_{\delta} ds \right\rangle + \left\langle \int_0^r \int_{\tau}^r \Psi_{s|\tau} \mathbf{L} ds d\beta_{\tau} \right\rangle \right) \right. \\ & \left. \left(\int_0^r \Psi_{s|0} \mathbf{x}_{\delta} ds + \int_0^r \int_{\tau}^r \Psi_{s|\tau} \mathbf{L} ds d\beta_{\tau} + \left\langle \int_0^r \Psi_{s|0} \mathbf{x}_{\delta} ds \right\rangle + \left\langle \int_0^r \int_{\tau}^r \Psi_{s|\tau} \mathbf{L} ds d\beta_{\tau} \right\rangle \right)^T \mathbf{H}^T \right\rangle \end{aligned}$$

where $\langle \cdot \rangle$ denotes the *expected value* operator.

The terms resulting from the expansion of this equation can be bunched into three different types, firstly the transformation of the variance of \mathbf{x}_{δ} as

$$\begin{aligned} & \mathbf{H} \left\langle \left(\int_0^r \Psi_{s|0} \mathbf{x}_{\delta} ds + \left\langle \int_0^r \Psi_{s|0} \mathbf{x}_{\delta} ds \right\rangle \right) \left(\int_0^r \Psi_{s|0} \mathbf{x}_{\delta} ds + \left\langle \int_0^r \Psi_{s|0} \mathbf{x}_{\delta} ds \right\rangle \right)^T \right\rangle \mathbf{H}^T = \\ &= \mathbf{H} \left(\int_0^r \Psi_{s|0} ds \right) \Sigma_{\delta} \left(\int_0^r \Psi_{s|0} ds \right)^T \mathbf{H}^T. \end{aligned}$$

where Σ_{δ} signifies the covariance matrix of \mathbf{x}_{δ} contained in Equation A.4.

Secondly, the mixed terms which consist of the product of the Wiener process with the other terms, such as

$$\mathbf{H} \left\langle \left(\int_0^r \int_\tau^r \Psi_{s|\tau} \mathbf{L} ds d\beta_\tau \right) \left(\int_0^r \Psi_{s|0} \mathbf{x}_\delta ds \right)^T \right\rangle \mathbf{H}^T$$

which all evaluate to 0. This is due to the independence of the stochastic integral contained therein from the random variable \mathbf{x}_δ (which allows to evaluate the expected value of the product as the product of the expected values) and that by definition, the expected value $\langle \int d\beta_\tau \rangle = 0$ (and thus also linear operations thereof).

Finally, the remaining term can be evaluated by Itô's isometry as

$$\begin{aligned} \mathbf{H} \left\langle \left(\int_0^r \int_\tau^r \Psi_{s|\tau} \mathbf{L} ds d\beta_\tau \right) \left(\int_0^r \int_\tau^r \Psi_{s|\tau} \mathbf{L} ds d\beta_\tau \right)^T \right\rangle \mathbf{H}^T &= \\ &= \mathbf{H} \int_0^r \int_\tau^r \int_\tau^r \Psi_{a|\tau} \mathbf{L} \mathbf{L}^T \Psi_{a|\tau}^T da db d\tau \mathbf{H}^T \end{aligned}$$

Hence, the variance of \mathbf{y}_n is given as

$$\begin{aligned} &\langle (\mathbf{y} - \langle \mathbf{y} \rangle) (\mathbf{y} - \langle \mathbf{y} \rangle)^T \rangle = \\ &= \mathbf{H} \left(\int_0^r \Psi_{s|0} ds \right) \Sigma_\delta \left(\int_0^r \Psi_{s|0} ds \right)^T \mathbf{H}^T + \mathbf{H} \int_0^r \int_\tau^r \int_\tau^r \Psi_{a|\tau} \mathbf{L} \mathbf{L}^T \Psi_{a|\tau}^T da db d\tau \mathbf{H}^T. \end{aligned}$$

Covariance of \mathbf{x}_δ and \mathbf{y}_n

For the derivation of the covariance, the same observations as for the derivation of the variance of \mathbf{y}_n apply, namely, that the mixed terms evaluate to 0 and that $\langle \int d\beta \rangle = 0$.

$$\begin{aligned} &\langle (\mathbf{x}_\delta - \langle \mathbf{x}_\delta \rangle) (\mathbf{y}_n - \langle \mathbf{y}_n \rangle)^T \rangle = \\ &= \left\langle (\mathbf{x}_\delta - \langle \mathbf{x}_\delta \rangle) \left(\int_0^r \Psi_{s|0} \mathbf{x}_\delta ds + \int_0^r \int_\tau^r \Psi_{s|\tau} \mathbf{L} ds d\beta_\tau + \left\langle \int_0^r \Psi_{s|0} \mathbf{x}_\delta ds \right\rangle \right)^T \right\rangle \mathbf{H}^T, \end{aligned}$$

which can be simplified using the same facts as before, to yield

$$\begin{aligned} &\langle (\mathbf{x}_\delta - \langle \mathbf{x}_\delta \rangle) (\mathbf{y}_n - \langle \mathbf{y}_n \rangle)^T \rangle = \\ &\quad \Sigma_\delta \left(\int_0^r \Psi_{s|0} ds \right)^T \mathbf{H}^T. \end{aligned}$$

Covariance of \mathbf{x}_n and \mathbf{y}_n

For the derivation of this covariance, it is helpful to keep in mind that

$$\mathbf{x}_n = \Psi_{r|0}\mathbf{x}_\delta + \int_0^r \Psi_{r|\tau} \mathbf{L} d\beta_\tau$$

and hence the equation for the covariance of \mathbf{x}_n and \mathbf{y}_n reads

$$\begin{aligned} & \langle (\mathbf{x}_n - \langle \mathbf{x}_n \rangle) (\mathbf{y} - \langle \mathbf{y} \rangle)^T \rangle = \\ & \left\langle \left(\Psi_{r|0}\mathbf{x}_\delta + \int_0^r \Psi_{r|\tau} \mathbf{L} d\beta_\tau + \langle \Psi_{r|0}\mathbf{x}_\delta \rangle + \left\langle \int_0^r \Psi_{r|\tau} \mathbf{L} d\beta_\tau \right\rangle \right) \right. \\ & \left. \left(\int_0^r \Psi_{s|0}\mathbf{x}_\delta ds + \int_0^r \int_\tau^r \Psi_{s|\tau} \mathbf{L} ds d\beta_\tau + \left\langle \int_0^r \Psi_{s|0}\mathbf{x}_\delta ds \right\rangle + \left\langle \int_0^r \int_\tau^r \Psi_{s|\tau} \mathbf{L} ds d\beta_\tau \right\rangle \right)^T \mathbf{H}^T \right\rangle \end{aligned}$$

which should again be split up in several different terms.

Firstly, the terms that contain \mathbf{x}_δ but not $d\beta$ to yield

$$\left\langle \Psi_{r|0} (\mathbf{x}_\delta - \langle \mathbf{x}_\delta \rangle) (\mathbf{x}_\delta - \langle \mathbf{x}_\delta \rangle)^T \left(\int_0^r \Psi_{s|0} ds \right)^T \mathbf{H}^T \right\rangle = \Psi_{r|0} \Sigma_\delta \left(\int_0^r \Psi_{s|0} ds \right)^T \mathbf{H}^T.$$

Secondly, the multiplication of the mixed terms of \mathbf{x}_δ and $d\beta$ once again yield 0, due to the independence of these quantities, and lastly, using Itô's isometry,

$$\begin{aligned} & \left\langle \left(\int_0^r \Psi_{r|\tau} \mathbf{L} d\beta_\tau \right) \left(\int_0^r \int_\tau^r \Psi_{s|\tau} \mathbf{L} d\beta_\tau \right)^T \mathbf{H}^T \right\rangle = \\ & \int_0^r \int_\tau^r \Psi_{r|\tau} \mathbf{L} \mathbf{L}^T \Psi_{s|\tau}^T ds d\tau, \end{aligned}$$

such that this covariance reads

$$\begin{aligned} & \langle (\mathbf{x}_n - \langle \mathbf{x}_n \rangle) (\mathbf{y} - \langle \mathbf{y} \rangle)^T \rangle = \\ & \Psi_{r|0} \Sigma_\delta \left(\int_0^r \Psi_{s|0} ds \right)^T \mathbf{H}^T + \int_0^r \int_\tau^r \Psi_{r|\tau} \mathbf{L} \mathbf{L}^T \Psi_{s|\tau}^T ds d\tau \end{aligned}$$

Appendix B

Monte-Carlo method for solid-angle calculations

As mentioned in section 2.3.2, calculation of the counting efficiency in DSA α -particle spectrometry entails computation of the solid-angle subtended by the detector, constrained by one or several apertures.

By generation of random directional vectors and random origin vectors and checking their passage through all relevant apertures and their intersection with the active volume of the detector, the counting efficiency can thus be computed by Monte-Carlo integration. As a reference, Figure B.1 shows this scheme. The intersection point of a ray specified by an origin vector \vec{o} and a normalized directional vector \vec{d} and a plane specified by a normalized plane normal \vec{n} and a point on the plane \vec{p} can be computed by seeking $t > 0$ for which

$$(\vec{o} + t\vec{d} - \vec{p}) \cdot \vec{n} = 0 \quad (\text{B.1})$$

is fulfilled.

The passage through a circular aperture centered on \vec{p} can then be checked by computing the point of intersection \vec{l}

$$\vec{l} = \vec{o} + t\vec{d} \quad (\text{B.2})$$

If $|\vec{l} - \vec{p}| < r$, where r specifies the radius of the aperture opening, the ray traverses the aperture. For computational reasons, one may have to specify a lower bound on $\vec{n} \cdot \vec{d}$, below which no further computation is carried out. In the case of very high t , or conversely low values of the dot product $\vec{n} \cdot \vec{d}$, one can be sure that the point of intersection \vec{l} does not lie within the opening of the aperture anyhow.

Iterating these sets of equations for a set of randomly generated rays, where directional vectors are sampled isotropically, and counting the detector hits (i.e. intersections) and relating the fraction of hits with the total number of generated rays yields the geometrical counting efficiency. Upon failed passage through any of the specified apertures, the specific ray in question is terminated.

Note, that potential tilting of apertures and the detector with respect to the source support can be specified by the respective plane normals \vec{n} .

Variance reduction is carried out by specifying a maximum polar angle θ , after which re-sampling occurs. The activity distribution on the source can be taken into account by the

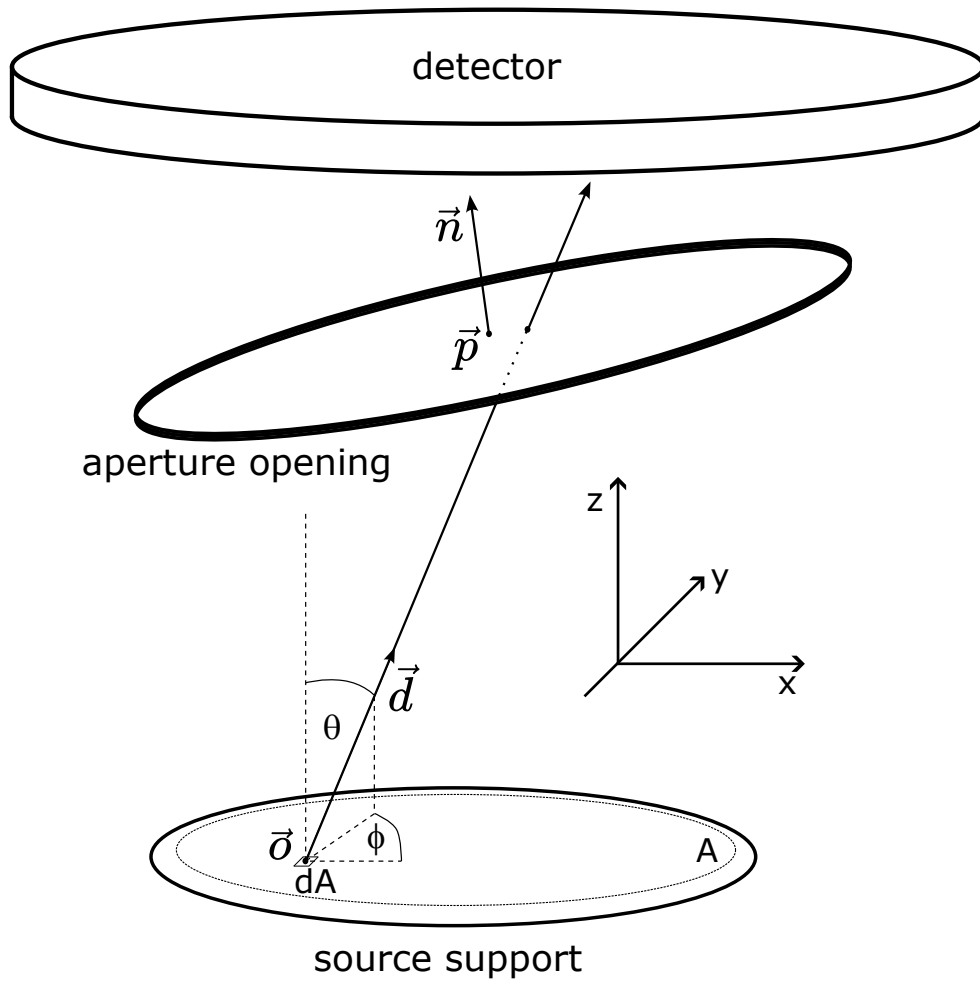


FIGURE B.1: Schematic of parametric ray solution to solid-angle calculations in defined solid-angle spectrometry methods.

sampling scheme by which the origin vectors \vec{o} of the rays are being generated. Therefore, any arbitrary 2D distribution can be considered, however, in this work, usually discretely sampled autoradiography data was used, from which the origin points were being generated. As a computational approach for doing so, the *Alias method* (Walker, 1977) was chosen, which allows to sample with constant time complexity the indexes subject to a probability matrix $\in \mathbb{R}^{a \cdot b}$, given by the radiography data. Since the true activity distribution is, however, continuous in nature, oversampling is carried out by assuming uniform distributions within each pixel of the radiograph.

Geometrical uncertainty, e.g. in r , in the pixel-size of the radiography data, the components of each of the \vec{n} and \vec{p} vectors, among others, is readily included by resampling these respective parameters within their specified uncertainty (distributed, for example, as a normal or a truncated normal distribution) after each N rays (where N is typically chosen on the order of 10^7). As such, the specific counting efficiency of a source can be computed while considering all relevant geometrical uncertainties, also considering possible joint influences between the source activity distribution and the geometrical uncertainties on the effective solid-angle subtended by the detector.

Extensions of this algorithm are readily possible, for example, computing the intersections with apertures specified by rasterized/meshed data, which may be available from measurements, inclusion of parametrized source activity distributions, and inclusion of an arbitrary number of apertures.

Bibliography

- Allison, J. et al. (2006). "Geant4". In: *IEEE Transactions on Nuclear Science* 53 (1). DOI: 10.1109/TNS.2006.869826.
- Amaku, M., P. R. Pascholati, and V. R. Vanin (Jan. 2010). "Decay chain differential equations: Solution through matrix algebra". In: *Computer Physics Communications* 181 (1), pp. 21–23. DOI: 10.1016/j.cpc.2009.08.011.
- Amaral Turkman, M. A., C. D. Paulino, and P. Müller (2019). *Computational Bayesian Statistics: An Introduction*. Institute of Mathematical Statistics Textbooks. Cambridge University Press. DOI: 10.1017/9781108646185.
- Amemiya, Y. and J. Miyahara (Dec. 1988). "Imaging plate illuminates many fields". In: *Nature* 336, pp. 89–90. DOI: 10.1038/336089a0.
- Arinc, A., M. J. Parfitt, J. D. Keightley, and A. Wilson (2016). "Defined solid angle alpha counting at NPL". In: *Applied Radiation and Isotopes* 109, pp. 198–204. DOI: 10.1016/j.apradiso.2015.11.073.
- Barber, D. (2006). "Expectation Correction for Smoothed Inference in Switching Linear Dynamical Systems". In: *Journal of Machine Learning Research* 7, pp. 2515–2540.
- Bateman, H. (1910). "Solution of a system of differential equations occurring in the theory of radioactive transformations". In: *Proc. Cambridge Philos. Soc.* 15, pp. 423–427.
- Bé, M.-M. et al. (2008). *Table of Radionuclides*. Vol. 4. Monographie BIPM-5. Pavillon de Breteuil, F-92310 Sèvres, France: Bureau International des Poids et Mesures. URL: http://www.bipm.org/utils/common/pdf/monographieRI/Monographie_BIPM-5_Tables_Vol4.pdf.
- BIPM (2022). *KCDB: CIPM MRA database of approved CMC*. URL: <https://www.bipm.org/kcdb/>.
- Biraud, S. et al. (Jan. 2002). "Quantification of carbon dioxide, methane, nitrous oxide and chloroform emissions over Ireland from atmospheric observations at Mace Head". In: *Tellus B: Chemical and Physical Meteorology* 54 (1), pp. 41–60. DOI: 10.3402/tellusb.v54i1.16647.
- Bortels, G. and P. Collaers (1987). "Analytical function for fitting peaks in alpha-particle spectra from Si detectors". In: *International Journal of Radiation Applications and Instrumentation. Part 38* (10), pp. 831–837. DOI: 10.1016/0883-2889(87)90180-8.
- Bradbury, J. et al. (2018). *JAX: composable transformations of Python+NumPy programs*. Version 0.3.13. URL: <http://github.com/google/jax>.
- Bratsch, S. G. (1989). "Standard Electrode Potentials and Temperature Coefficients in Water at 298.15 K". In: *Journal of Physical and Chemical Reference Data* 18 (1), pp. 1–21. DOI: 10.1063/1.555839.
- Broyden, C. G. (Mar. 1970). "The Convergence of a Class of Double-rank Minimization Algorithms 1. General Considerations". In: *IMA Journal of Applied Mathematics* 6.1, pp. 76–90. DOI: 10.1093/imamat/6.1.76.
- Caro Marroyo, B., M. Sánchez, and J. Vargas (2013). "ALFITeX: a new code for the deconvolution of complex alpha-particle spectra". In: *Journal of Radioanalytical and Nuclear Chemistry* 296, pp. 1247–1252. DOI: 10.1007/s10967-013-2428-8.

- Chabaux, F., D. B. Othman, and J. L. Birck (1994). "A new RaBa chromatographic separation and its application to Ra mass-spectrometric measurement in volcanic rocks". In: *Chemical Geology* 114 (3-4), pp. 191–197. DOI: 10.1016/0009-2541(94)90052-3.
- Chambers, S. D. et al. (2022). "Portable two-filter dual-flow-loop ^{222}Rn detector: stand-alone monitor and calibration transfer device". In: *Advances in Geosciences* 57, pp. 63–80. DOI: 10.5194/adgeo-57-63-2022.
- Chambers, S. D. et al. (2016). "Towards a Universal Baseline Characterisation of Air Masses for High- and Low-Altitude Observing Stations Using Radon-222". In: *Aerosol and Air Quality Research* 16 (3), pp. 885–899. DOI: 10.4209/aaqr.2015.06.0391.
- Chambers, S. D. et al. (Nov. 2018). "Characterizing Atmospheric Transport Pathways to Antarctica and the Remote Southern Ocean Using Radon-222". In: *Frontiers in Earth Science* 6. DOI: 10.3389/feart.2018.00190.
- Chambers, S. D. et al. (Jan. 2019a). "Characterizing the State of the Urban Surface Layer Using Radon-222". In: *Journal of Geophysical Research: Atmospheres* 124 (2), pp. 770–788. DOI: 10.1029/2018JD029507.
- Chambers, S. D. et al. (Jan. 2019b). "Skill-Testing Chemical Transport Models across Contrasting Atmospheric Mixing States Using Radon-222". In: *Atmosphere* 10 (1), p. 25. DOI: 10.3390/atmos10010025.
- Choppin, G. R., J.-O. Liljenzin, and J. Rydberg (2002). "CHAPTER 8 - Detection and Measurement Techniques". In: *Radiochemistry and Nuclear Chemistry (Third Edition)*. Ed. by G. R. Choppin, J.-O. Liljenzin, and J. Rydberg. Third Edition. Woburn: Butterworth-Heinemann, pp. 192–238. DOI: <https://doi.org/10.1016/B978-075067463-8/50008-X>.
- Colle, R., J. Hutchinson, and M. Unterweger (Mar. 1990). "The NIST primary radon-222 measurement system". In: *Journal of Research of the National Institute of Standards and Technology* 95 (2). DOI: 10.6028/jres.095.018.
- Conway, J. T. (2006). "Generalizations of Ruby's formula for the geometric efficiency of a parallel-disk source and detector system". In: *Nuclear Instruments and Methods in Physics Research Section A: Accelerators, Spectrometers, Detectors and Associated Equipment* 562.1, pp. 146–153. DOI: 10.1016/j.nima.2006.02.197.
- Cox, D. R. (1955). "Some Statistical Methods Connected with Series of Events". In: *Journal of the Royal Statistical Society: Series B (Methodological)* 17.2, pp. 129–157. DOI: 10.1111/j.2517-6161.1955.tb00188.x.
- Cubiccioni, D., A. N. Laboratory, and U. A. E. Commission (1947). *High Temperature Equilibria in Metal: Metal Halide Systems*. United States. Atomic Energy Commission. MDDC. Technical Information Division, Atomic Energy Commission.
- Darby, S. et al. (Jan. 2005). "Radon in homes and risk of lung cancer: collaborative analysis of individual data from 13 European case-control studies". In: *BMJ* 330 (7485), p. 223. DOI: 10.1136/bmj.38308.477650.63.
- Delley, R. (1985). "Series for the exponentially modified Gaussian peak shape". In: *Analytical Chemistry* 57.1, pp. 388–388. DOI: 10.1021/ac00279a094.
- Derkatch, A., C. Lundevall, L.-E. Berg, and P. Royen (2000). "Lifetime measurements of the $A^2\Pi$ state of BaCl using laser spectroscopy". In: *Chemical Physics Letters* 332.3, pp. 278–282. DOI: [https://doi.org/10.1016/S0009-2614\(00\)01264-1](https://doi.org/10.1016/S0009-2614(00)01264-1).
- Desideri, D., C. Roselli, L. Feduzi, and M. Meli (Dec. 2006). "Monitoring the atmospheric stability by using radon concentration measurements: A study in a Central Italy site". In: *Journal of Radioanalytical and Nuclear Chemistry* 270, pp. 523–530. DOI: 10.1007/s10967-006-0458-1.
- Dosne, A.-G., M. Bergstand, K. Harling, and M. O. Karlsson (2016). "Improving the estimation of parameter uncertainty distributions in nonlinear mixed effects models using sampling importance resampling". In: *Journal of Physics G: Nuclear and Particle Physics* 43, pp. 583–596. DOI: 10.1007/s10928-016-9487-8.

- Doví, V., O. Paladino, and A. Reverberi (1991). "Some remarks on the use of the inverse hessian matrix of the likelihood function in the estimation of statistical properties of parameters". In: *Applied Mathematics Letters* 4.1, pp. 87–90. DOI: [https://doi.org/10.1016/0893-9659\(91\)90129-J](https://doi.org/10.1016/0893-9659(91)90129-J).
- Drebert, J. et al. (2013). "Smooth crack-free targets for nuclear applications produced by molecular plating". In: *Nuclear Instruments and Methods in Physics Research Section A: Accelerators, Spectrometers, Detectors and Associated Equipment* 714, pp. 163–175. DOI: [10.1016/j.nima.2013.03.003](https://doi.org/10.1016/j.nima.2013.03.003).
- Dresser, M. J. (Jan. 1968). "The Saha-Langmuir Equation and its Application". In: *Journal of Applied Physics* 39 (1), pp. 338–339. DOI: [10.1063/1.1655755](https://doi.org/10.1063/1.1655755).
- Ebeigbe, D., T. Berry, S. J. Schiff, and T. Sauer (Oct. 2020). "Poisson Kalman filter for disease surveillance". In: *Physical Review Research* 2 (4), p. 043028. DOI: [10.1103/PhysRevResearch.2.043028](https://doi.org/10.1103/PhysRevResearch.2.043028).
- Eberhardt, K. et al. (2014). "Quantitative molecular plating of large-area ^{242}Pu targets with improved layer properties". In: *Applied Radiation and Isotopes* 95, pp. 36–43. DOI: [10.1016/j.apradiso.2014.10.002](https://doi.org/10.1016/j.apradiso.2014.10.002).
- Egozcue, J. J., V. Pawlowsky-Glahn, G. Mateu-Figueras, and C. Barceló-Vidal (2003). "Isometric Logratio Transformations for Compositional Data Analysis". In: *Mathematical Geology* 35 (3), pp. 279–300. DOI: [10.1023/A:1023818214614](https://doi.org/10.1023/A:1023818214614).
- Eichstädt, S., A. Link, P. Harris, and C. Elster (Apr. 2012). "Efficient implementation of a Monte Carlo method for uncertainty evaluation in dynamic measurements". In: *Metrologia* 49.3, pp. 401–410. DOI: [10.1088/0026-1394/49/3/401](https://doi.org/10.1088/0026-1394/49/3/401).
- Eichstädt, S., N. Makarava, and C. Elster (Oct. 2016a). "On the evaluation of uncertainties for state estimation with the Kalman filter". In: *Measurement Science and Technology* 27.12, p. 125009. DOI: [10.1088/0957-0233/27/12/125009](https://doi.org/10.1088/0957-0233/27/12/125009).
- Eichstädt, S. et al. (June 2016b). "On challenges in the uncertainty evaluation for time-dependent measurements". In: *Metrologia* 53.4, S125–S135. DOI: [10.1088/0026-1394/53/4/s125](https://doi.org/10.1088/0026-1394/53/4/s125).
- European Union (2013). "Council Directive 2013/59/Euratom of 5 December 2013 laying down basic safety standards for protection against the dangers arising from exposure to ionising radiation". In:
- Fedosseev, V. et al. (Aug. 2017). "Ion beam production and study of radioactive isotopes with the laser ion source at ISOLDE". In: *Journal of Physics G: Nuclear and Particle Physics* 44 (8), p. 084006. DOI: [10.1088/1361-6471/aa78e0](https://doi.org/10.1088/1361-6471/aa78e0).
- Fialova, E., P. P. S. Otahal, J. Vosahlik, and M. Mazanova (Mar. 2020). "Equipment for Testing Measuring Devices at a Low-Level Radon Activity Concentration". In: *International Journal of Environmental Research and Public Health* 17 (6), p. 1904. DOI: [10.3390/ijerph17061904](https://doi.org/10.3390/ijerph17061904).
- Flores-Mendoza, J., J. L. Iturbe, and M. Jimenez-Reyes (Sept. 1992). "Separation and electrodeposition of ^{226}Ra ". In: *Journal of Radioanalytical and Nuclear Chemistry Articles* 162 (1), pp. 131–138. DOI: [10.1007/BF02039933](https://doi.org/10.1007/BF02039933).
- Getoff, N., H. Bildstein, and E. Proksch (1967). "Molecular plating, V. The influence of some experimental factors on the deposition yield". In: *Nuclear Instruments and Methods* 46 (2), pp. 305–308. DOI: [10.1016/0029-554X\(67\)90088-2](https://doi.org/10.1016/0029-554X(67)90088-2).
- Gill, J. and G. King (2004). "What to Do When Your Hessian is Not Invertible: Alternatives to Model Respecification in Nonlinear Estimation". In: *Sociological Methods & Research* 33.1, pp. 54–87. DOI: [10.1177/0049124103262681](https://doi.org/10.1177/0049124103262681).
- Goodacre, T. D. et al. (Dec. 2018). "Radium ionization scheme development: The first observed autoionizing states and optical pumping effects in the hot cavity environment". In: *Spectrochimica Acta Part B: Atomic Spectroscopy* 150, pp. 99–104. DOI: [10.1016/j.sab.2018.10.002](https://doi.org/10.1016/j.sab.2018.10.002).

- Gotoh, H. and H. Yagi (1971). "Solid angle subtended by a rectangular slit". In: *Nuclear Instruments and Methods* 96.3, pp. 485–486. DOI: 10.1016/0029-554X(71)90624-0.
- Griffiths, A. D., S. D. Chambers, A. G. Williams, and S. Werczynski (2016). "Increasing the accuracy and temporal resolution of two-filter radon-222 measurements by correcting for the instrument response". In: *Atmospheric Measurement Techniques* 9.6, pp. 2689–2707. DOI: 10.5194/amt-9-2689-2016.
- Grossi, C. et al. (2012). "Atmospheric 222Rn concentration and source term at El Arenosillo 100 m meteorological tower in southwest Spain". In: *Radiation Measurements* 47.2, pp. 149–162. DOI: <https://doi.org/10.1016/j.radmeas.2011.11.006>.
- Hancock, G. J. and P. Martin (1991). "Determination of Ra in environmental samples by α -particle spectrometry". In: *International Journal of Radiation Applications and Instrumentation. Part 42* (1), pp. 63–69. DOI: 10.1016/0883-2889(91)90125-K.
- Hartikainen, J. and S. Särkkä (Feb. 2012). "Sequential Inference for Latent Force Models". In: URL: <http://arxiv.org/abs/1202.3730>.
- Hassan, S. S., S. Särkkä, and Á. F. García-Fernández (2021). "Temporal Parallelization of Inference in Hidden Markov Models". In: *IEEE Transactions on Signal Processing* 69, pp. 4875–4887. DOI: 10.1109/TSP.2021.3103338.
- Hastings, W. K. (Apr. 1970). "Monte Carlo sampling methods using Markov chains and their applications". In: *Biometrika* 57.1, pp. 97–109. DOI: 10.1093/biomet/57.1.97.
- Heinke, R. et al. (2020). "Atom beam emission from hot cavity laser ion sources". In: *Nuclear Instruments and Methods in Physics Research Section B: Beam Interactions with Materials and Atoms* 463, pp. 449–454. DOI: <https://doi.org/10.1016/j.nimb.2019.04.026>.
- Hoffman, M. D. and A. Gelman (2011). "The No-U-Turn Sampler: Adaptively Setting Path Lengths in Hamiltonian Monte Carlo". In: DOI: 10.48550/ARXIV.1111.4246. URL: <https://arxiv.org/abs/1111.4246>.
- Hofmann, W. et al. (2015). *ICRU Report 88: Measurement and reporting of Radon exposures*. Ed. by T. I. C. on Radiation Units and Measurements. Oxford University Press.
- Hönigschmid, O. (1912). *Revision des Atomgewichtes des Radiums und Herstellung von Radiumstandardpräparaten*. Mitteilungen aus dem Institute für Radiumforschung.
- Horwitz, E. P., R. Chiarizia, and M. L. Dietz (Apr. 1992). "A NOVEL STRONTIUM-SELECTIVE EXTRACTION CHROMATOGRAPHIC RESIN*". In: *Solvent Extraction and Ion Exchange* 10 (2), pp. 313–336. DOI: 10.1080/07366299208918107.
- Human, H. and P. Zeegers (1975). "Molecular fluorescence of CaOH, SrOH and BaCl in flames". In: *Spectrochimica Acta Part B: Atomic Spectroscopy* 30.6, pp. 203–209. DOI: [https://doi.org/10.1016/0584-8547\(75\)80019-X](https://doi.org/10.1016/0584-8547(75)80019-X).
- Ishiwara, H. and S. Furukawa (1977a). "Formation of Highly-Doped Thin Layers by Using Knock-on Effect". In: *Ion Implantation in Semiconductors 1976*. Ed. by F. Chernow, J. A. Borders, and D. K. Brice. Boston, MA: Springer US, pp. 375–382. DOI: 10.1007/978-1-4613-4196-3_39.
- Ishiwara, H. and S. Furukawa (Jan. 1977b). "Schottky Barrier Height Control by Using Knock-on Effect in Ion Implantation". In: *Japanese Journal of Applied Physics* 16.S1, p. 53. DOI: 10.7567/JJAPS.16S1.53. URL: <https://dx.doi.org/10.7567/JJAPS.16S1.53>.
- Jäckel, B., W. Westmeier, and P. Patzelt (Nov. 1987). "On the photopeak efficiency of germanium gamma-ray detectors". In: *Nuclear Instruments and Methods in Physics Research Section A: Accelerators, Spectrometers, Detectors and Associated Equipment* 261 (3), pp. 543–548. DOI: 10.1016/0168-9002(87)90367-6.
- Jackson, N. (May 1960). "Vacuum sublimation apparatus for preparation of thin sources of α -active materials". In: *Journal of Scientific Instruments* 37 (5), pp. 169–171. DOI: 10.1088/0950-7671/37/5/306.
- Kalman, R. E. (Mar. 1960). "A New Approach to Linear Filtering and Prediction Problems". In: *Journal of Basic Engineering* 82 (1), pp. 35–45. DOI: 10.1115/1.3662552.

- Khateeb-ur-Rehman et al. (2016). "Energy resolution measurements of CeBr₃ and LaCl₃:Ce detectors". In: *Journal of Radioanalytical and Nuclear Chemistry* 310 (2), pp. 849–855. DOI: 10.1007/s10967-016-4904-4.
- Kieck, T., S. Biebricher, C. E. Düllmann, and K. Wendt (May 2019). "Optimization of a laser ion source for ¹⁶³Ho isotope separation". In: *Review of Scientific Instruments* 90 (5), p. 053304. DOI: 10.1063/1.5081094.
- Kirby, H. W. and M. L. Salutsky (1964). *The radiochemistry of radium*. National Academy of Sciences - Subcommittee on Radiochemistry.
- Klumpp, J., G. Miller, and D. Poudel (2018). "A new approach to counting measurements: Addressing the problems with ISO-11929". In: *Nuclear Instruments and Methods in Physics Research Section A: Accelerators, Spectrometers, Detectors and Associated Equipment* 892, pp. 18–29. DOI: 10.1016/j.nima.2017.12.016.
- Knudsen, M. (1909a). "Die Gesetze der Molekularströmung und der inneren Reibungsströmung der Gase durch Röhren". In: *Annalen der Physik* 333.1, pp. 75–130. DOI: <https://doi.org/10.1002/andp.19093330106>.
- Knudsen, M. (1909b). "Die Molekularströmung der Gase durch Öffnungen und die Effusion". In: *Annalen der Physik* 333.5, pp. 999–1016. DOI: <https://doi.org/10.1002/andp.19093330505>.
- Laan, V. D. et al. (Jan. 2010). "Observation-based estimates of fossil fuel-derived CO₂ emissions in the Netherlands using $\Delta^{14}\text{C}$, CO and ²²²Radon". In: *Tellus B: Chemical and Physical Meteorology* 62 (5), pp. 389–402. DOI: 10.1111/j.1600-0889.2010.00493.x.
- Lagacé, F., D. Foucher, C. Surette, and O. Clarisse (May 2017). "Quantification of ²²⁶Ra at environmental relevant levels in natural waters by ICP-MS: Optimization, validation and limitations of an extraction and preconcentration approach". In: *Talanta* 167, pp. 658–665. DOI: 10.1016/j.talanta.2017.02.031.
- Larivière, D. et al. (2005). "Micro-extraction procedures for the determination of Ra-226 in well waters by SF-ICP-MS". In: *Analytica Chimica Acta* 528 (2), pp. 175–182. DOI: 10.1016/j.aca.2004.09.076.
- Levin, I. et al. (2002). "Observations of atmospheric variability and soil exhalation rate of radon-222 at a Russian forest site. Technical approach and deployment for boundary layer studies". In: *Tellus B: Chemical and Physical Meteorology* 54.5, pp. 462–475. DOI: 10.3402/tellusb.v54i5.16681.
- Levin, I. (Feb. 1987). "Atmospheric CO₂ in continental Europe-an alternative approach to clean air CO₂ data". In: *Tellus B* 39B (1-2), pp. 21–28. DOI: 10.1111/j.1600-0889.1987.tb00267.x.
- Levin, I. et al. (2021). "Limitations of the Radon Tracer Method (RTM) to estimate regional Greenhouse Gases (GHG) emissions – a case study for methane in Heidelberg". In: *Atmos. Chem. Phys. Discuss. [preprint]*. DOI: <https://doi.org/10.5194/acp-2021-661>.
- Levy, E. (Jan. 2019). "Decay chain differential equations: Solutions through matrix analysis". In: *Computer Physics Communications* 234, pp. 188–194. DOI: 10.1016/j.cpc.2018.07.011.
- Linzmaier, D. (2013). "Dissertation, Entwicklung einer Low-Level-Radon-Referenzkammer". Gottfried Wilhelm Leibniz Universität Hannover.
- Linzmaier, D. and A. Röttger (2013). "Development of a low-level radon reference atmosphere". In: *Applied Radiation and Isotopes* 81, pp. 208–211. DOI: 10.1016/j.apradiso.2013.03.032.
- Marouli, M. et al. (July 2017). "Direct measurement of alpha emission probabilities in the decay of ²²⁶Ra". In: *Applied Radiation and Isotopes* 125, pp. 196–202. DOI: 10.1016/j.apradiso.2017.04.029.

- Marsh, B. (2013). "Resonance Ionization Laser Ion Sources". In: 61 pages, contribution to the CAS-CERN Accelerator School: Ion Sources, Senec, Slovakia, 29 May - 8 June 2012, edited by R. Bailey, 61 p. DOI: 10.5170/CERN-2013-007.203.
- Marx, S. M. (2014). "Radium-Aufreinigung zur Herstellung von Actinium-225 am Zyklotron für die Alpha-Immuntherapie". In:
- Megumi, K. and T. Mamuro (1974). "Emanation and exhalation of radon and thoron gases from soil particles". In: *Journal of Geophysical Research (1896-1977)* 79.23, pp. 3357–3360. DOI: <https://doi.org/10.1029/JB079i023p03357>.
- Mendenhall, M. H. and R. A. Weller (1991). "Algorithms for the rapid computation of classical cross sections for screened Coulomb collisions". In: *Nuclear Instruments and Methods in Physics Research Section B: Beam Interactions with Materials and Atoms* 58.1, pp. 11–17. DOI: 10.1016/0168-583X(91)95672-Z.
- Miklyaev, P. S. and T. B. Petrova (2012). "Studies of radon emanation from clays". In: *Water Resources* 38 (7), pp. 868–875. DOI: 10.1134/s0097807811070116.
- Moler, C. and C. V. Loan (Jan. 2003). "Nineteen Dubious Ways to Compute the Exponential of a Matrix, Twenty-Five Years Later". In: *SIAM Review* 45 (1), pp. 3–49. DOI: 10.1137/S00361445024180.
- Mor, B., S. Garhwal, and A. Kumar (2021). "A Systematic Review of Hidden Markov Models and Their Applications". In: *Archives of Computational Methods in Engineering* 28.3, pp. 1429–1448. DOI: 10.1007/s11831-020-09422-4.
- Nelles, O. (2020). "Nonlinear Local Optimization". In: *Nonlinear System Identification: From Classical Approaches to Neural Networks, Fuzzy Models, and Gaussian Processes*. Springer International Publishing, pp. 93–128. DOI: 10.1007/978-3-030-47439-3_4.
- Øksendal, B. (2003). *Stochastic Differential Equations: An Introduction with Applications*. Universitext (1979). Springer.
- Parker, W., H. Bildstein, and N. Getoff (1964). "Molecular plating I, a rapid and quantitative method for the electrodeposition of thorium and uranium". In: *Nuclear Instruments and Methods* 26 (C), pp. 55–60. DOI: 10.1016/0029-554X(64)90049-7.
- Parker, W. and Y. Grunditz (Mar. 1963). "An improved apparatus for the vacuum deposition of radioactive materials". In: *Nuclear Instruments and Methods* 22, pp. 73–76. DOI: 10.1016/0029-554X(63)90229-5.
- Peddada, S. D. and J. K. Haseman (2005). "Analysis of Nonlinear Regression Models: A Cautionary Note". In: *Dose-Response* 3.3. PMID: 18648618, dose-response.003.03.005. DOI: 10.2203/dose-response.003.03.005.
- Perrino, C., A. Pietrodangelo, and A. Febo (Nov. 2001). "An atmospheric stability index based on radon progeny measurements for the evaluation of primary urban pollution". In: *Atmospheric Environment* 35 (31), pp. 5235–5244. DOI: 10.1016/S1352-2310(01)00349-1.
- Piccolo, J. L. (1996). "Absolute measurement of radon 222 activity". In: *Nuclear Instruments and Methods in Physics Research, Section A: Accelerators, Spectrometers, Detectors and Associated Equipment* 369 (2-3), pp. 452–457. DOI: 10.1016/S0168-9002(96)80029-5.
- Pommé, S. (2004). "A complete series expansion of Ruby's solid-angle formula". In: *Nuclear Instruments and Methods in Physics Research Section A: Accelerators, Spectrometers, Detectors and Associated Equipment* 531.3, pp. 616–620. DOI: 10.1016/j.nima.2004.05.088.
- Pommé, S. and B. Caro Marroyo (2015). "Improved peak shape fitting in alpha spectra". In: *Applied Radiation and Isotopes* 96, pp. 148–153. DOI: 10.1016/j.apradiso.2014.11.023.
- Pommé, S., L. Johansson, G. Sibbens, and B. Denecke (2003). "An algorithm for the solid angle calculation applied in alpha-particle counting". In: *Nuclear Instruments and Methods in Physics Research Section A: Accelerators, Spectrometers, Detectors and Associated Equipment* 505.1. Proceedings of the tenth Symposium on Radiation Measurements and Applications, pp. 286–289. DOI: 10.1016/S0168-9002(03)01070-2.

- Pommé, S. and G. Sibbens (2008). "Alpha-Particle Counting and Spectrometry in a Primary Standardisation Laboratory". In: *ACTA CHIMICA SLOVENICA* 55, pp. 111–119.
- Pommé, S. (2015). "The uncertainty of counting at a defined solid angle". In: *Metrologia* 52 (3), S73–S85. DOI: 10.1088/0026-1394/52/3/S73.
- Pommé, S. and J. Paepen (2007). "A series expansion of Conway's generalised solid-angle formulas". In: *Nuclear Instruments and Methods in Physics Research Section A: Accelerators, Spectrometers, Detectors and Associated Equipment* 579.1. Proceedings of the 11th Symposium on Radiation Measurements and Applications, pp. 272–274. DOI: 10.1016/j.nima.2007.04.054.
- Porstendörfer, J. (1994). "Properties and behaviour of radon and thoron and their decay products in the air". In: *Journal of Aerosol Science* 25.2, pp. 219–263. DOI: 10.1016/0021-8502(94)90077-9.
- Pressyanov, D. et al. (Apr. 2007). "Measurement of radon-222 in water by absorption in Makrofol". In: *Nuclear Instruments and Methods in Physics Research Section A: Accelerators, Spectrometers, Detectors and Associated Equipment* 574 (1), pp. 202–204. DOI: 10.1016/j.nima.2007.01.098.
- Pressyanov, D. S. (Apr. 2002). "Short solution of the radioactive decay chain equations". In: *American Journal of Physics* 70 (4), pp. 444–445. DOI: 10.1119/1.1427084.
- Raeder, S., J. Lassen, H. Heggen, and A. Teigelhöfer (June 2014). "In-source spectroscopy on astatine and radium for resonant laser ionization". In: *Hyperfine Interactions* 227 (1-3), pp. 77–83. DOI: 10.1007/s10751-014-1040-9.
- Röttger, A. and A. Honig (Apr. 2011). "Recent developments in radon metrology: new aspects in the calibration of radon, thoron and progeny devices". In: *Radiation Protection Dosimetry* 145.2-3, pp. 260–266. DOI: 10.1093/rpd/ncr047.
- Röttger, A., A. Honig, and D. Linzmaier (2014). "Calibration of commercial radon and thoron monitors at stable activity concentrations". In: *Applied Radiation and Isotopes* 87. Proceedings of the 19th International Conference on Radionuclide Metrology and its Applications 17–21 June 2013, Antwerp, Belgium, pp. 44–47. DOI: <https://doi.org/10.1016/j.apradiso.2013.11.111>.
- Ruby, L. and J. Rechen (1968). "A simpler approach to the geometrical efficiency of a parallel-disk source and detector system". In: *Nuclear Instruments and Methods* 58.2, pp. 345–346. DOI: 10.1016/0029-554X(68)90491-6.
- Ruby, L. (1994). "Further comments on the geometrical efficiency of a parallel-disk source and detector system". In: *Nuclear Instruments and Methods in Physics Research Section A: Accelerators, Spectrometers, Detectors and Associated Equipment* 337.2, pp. 531–533. DOI: 10.1016/0168-9002(94)91124-X.
- Ruffle, M. (1967). "The geometrical efficiency of a parallel-disc source and detector system". In: *Nuclear Instruments and Methods* 52.2, pp. 354–356. DOI: 10.1016/0029-554X(67)90248-0.
- Ruiz, R. F. G. et al. (May 2020). "Spectroscopy of short-lived radioactive molecules". In: *Nature* 581 (7809), pp. 396–400. DOI: 10.1038/s41586-020-2299-4.
- Salutsky, M. L. and J. G. Stites (Oct. 1955). "Radium-Barium Separation Process". In: *Industrial & Engineering Chemistry* 47 (10), pp. 2162–2166. DOI: 10.1021/ie50550a039.
- Salvatier, J., T. V. Wiecki, and C. Fonnesbeck (2016). "Probabilistic programming in Python using PyMC3". In: *PeerJ Computer Science* 2, e55.
- Sapundjiev, D. et al. (Sept. 2012). "Preparation and characterisation of thin film nuclear targets for neutron physical measurements". In: *Nuclear Instruments and Methods in Physics Research Section A: Accelerators, Spectrometers, Detectors and Associated Equipment* 686, pp. 75–81. DOI: 10.1016/j.nima.2012.05.037.
- Särkkä, S. (2013). *Bayesian filtering and smoothing*. Cambridge University Press.

- Särkkä, S. and A. Solin (2019). *Applied Stochastic Differential Equations*. Institute of Mathematical Statistics Textbooks. Cambridge University Press. DOI: 10.1017/9781108186735.
- Savitzky, A. and M. J. E. Golay (1964). "Smoothing and Differentiation of Data by Simplified Least Squares Procedures." In: *Analytical Chemistry* 36.8, pp. 1627–1639. DOI: 10.1021/ac60214a047.
- Schotanus, P. et al. (2013). "Scintillation and detection characteristics of high-sensitivity CeBr₃ gamma-ray spectrometers". In: *Nuclear Instruments and Methods in Physics Research Section A: Accelerators, Spectrometers, Detectors and Associated Equipment* 729 (0), pp. 596–604. DOI: 10.1016/j.nima.2013.08.005.
- Searle, S. R. (2006). *Matrix Algebra Useful for Statistics*. Wiley.
- Shelyuto, V. A. (1989). "Exact analytic results for the solid angle in systems with axial symmetry". In: *Zeitschrift für angewandte Mathematik und Physik ZAMP* 40.4, pp. 608–612. DOI: 10.1007/BF00944811.
- Shepherd, M. M. and J. G. Laframboise (Jan. 1981). "Chebyshev approximation of $(1 + 2x) \exp(x^2) \operatorname{erfc}(x)$ in $0 \leq x < \infty$ ". In: *Mathematics of Computation* 36 (153), pp. 249–249. DOI: 10.1090/S0025-5718-1981-0595058-X.
- Sibbens, G. and T. Altzitzoglou (Aug. 2007). "Preparation of radioactive sources for radionuclide metrology". In: *Metrologia* 44 (4), S71–S78. DOI: 10.1088/0026-1394/44/4/S09.
- Sibbens, G., A. Moens, and R. Eykens (Sept. 2015). "Preparation and sublimation of uranium tetrafluoride for the production of thin ²³⁵UF₄ targets". In: *Journal of Radioanalytical and Nuclear Chemistry* 305 (3), pp. 723–726. DOI: 10.1007/s10967-015-4137-y.
- Sibbens, G., S. Pommé, L. Johansson, and B. Denecke (June 2003). "Tailoring solid angle calculations to the actual radioactivity distribution of planar sources". In: *Nuclear Instruments and Methods in Physics Research Section A: Accelerators, Spectrometers, Detectors and Associated Equipment* 505 (1-2), pp. 277–281. DOI: 10.1016/S0168-9002(03)01068-4.
- Sibbens, G. et al. (2018). "Morphological and compositional study of ²³⁸U thin film targets for nuclear experiments". In: p. 030007. DOI: 10.1063/1.5035524.
- Sletten, G. (1971). *PREPARATION OF TARGETS OF ALPHA-RADIOACTIVE ISOTOPES*. Proceedings of third international symposium on research materials for nuclear measurements.
- Stein, M. L. (1999). *Interpolation of Spatial Data - Some theory for Kriging*. Springer Series in Statistics. Springer. DOI: 10.1007/978-1-4612-1494-6.
- Stephens, M. (2000). "Dealing with Label Switching in Mixture Models". In: *Journal of the Royal Statistical Society. Series B (Statistical Methodology)* 62.4, pp. 795–809. DOI: 10.1111/1467-9868.00265.
- Stranden, E., A. Kolstad, and B. Lind (Jan. 1984). "The Influence of Moisture and Temperature on Radon Exhalation". In: *Radiation Protection Dosimetry* 7 (1-4), pp. 55–58. DOI: 10.1093/oxfordjournals.rpd.a082962.
- Strong, K. P. and D. Levins (1982). "Effect of moisture content on radon emanation from uranium ore and tailings." In: *Health physics* 42 1, pp. 27–32.
- Styris, D. L. (1984). "Atomization mechanisms for barium in furnace atomic absorption spectrometry". In: *Analytical Chemistry* 56.7, pp. 1070–1076. DOI: 10.1021/ac00271a006.
- Thomas C. Allison (2013). *NIST-JANAF Thermochemical Tables - SRD 13*. DOI: 10.18434/T42S31. URL: <https://janaf.nist.gov/>.
- Tompkins, E. R. (Oct. 1948). "Separation of Radium from Barium by the Use of an Ion-exchange Column Procedure ^{>1}". In: *Journal of the American Chemical Society* 70 (10), pp. 3520–3522. DOI: 10.1021/ja01190a515.</sup>
- Tryka, S. (1997). "Angular distribution of the solid angle at a point subtended by a circular disk". In: *Optics Communications* 137.4, pp. 317–333. DOI: 10.1016/S0030-4018(96)00789-4.

- Vargas, A. et al. (2015). "Analysis of the vertical radon structure at the Spanish "El Arenosillo" tower station". In: *Journal of Environmental Radioactivity* 139, pp. 1–17. DOI: <https://doi.org/10.1016/j.jenvrad.2014.09.018>.
- Vargas, M. J. and F. F. D. Soto (1995). "Influence of Ba on the electrodeposition of ^{226}Ra ". In: *Journal of Radioanalytical and Nuclear Chemistry Articles* 198 (1), pp. 143–150. DOI: 10.1007/BF02038252.
- Vascon, A. et al. (2013). "The performance of thin layers produced by molecular plating as α -particle sources". In: *Nuclear Instruments and Methods in Physics Research, Section A: Accelerators, Spectrometers, Detectors and Associated Equipment* 721, pp. 35–44. DOI: 10.1016/j.nima.2013.04.050.
- Vascon, A. et al. (2014). "Fundamental aspects of molecular plating and production of smooth crack-free Nd targets". In: *Journal of Radioanalytical and Nuclear Chemistry* 299 (2), pp. 1085–1091. DOI: 10.1007/s10967-013-2631-7.
- Virtanen, P. et al. (2020). "SciPy 1.0: fundamental algorithms for scientific computing in Python". In: *Nature Methods* 17 (3), pp. 261–272. DOI: 10.1038/s41592-019-0686-2.
- Walker, A. J. (Sept. 1977). "An Efficient Method for Generating Discrete Random Variables with General Distributions". In: *ACM Transactions on Mathematical Software* 3 (3), pp. 253–256. DOI: 10.1145/355744.355749.
- Whitehead, N. E., R. G. Ditchburn, W. J. McCabe, and R. V. D. Raaij (1992). "Factors affecting the electrodeposition of ^{226}Ra ". In: *Journal of Radioanalytical and Nuclear Chemistry Articles* 160 (2), pp. 477–485. DOI: 10.1007/BF02037123.
- Williams, A. G., S. Chambers, and A. Griffiths (Dec. 2013). "Bulk Mixing and Decoupling of the Nocturnal Stable Boundary Layer Characterized Using a Ubiquitous Natural Tracer". In: *Boundary-Layer Meteorology* 149 (3), pp. 381–402. DOI: 10.1007/s10546-013-9849-3.
- Williams, A. G. et al. (Dec. 2016). "Radon as a tracer of atmospheric influences on traffic-related air pollution in a small inland city". In: *Tellus B: Chemical and Physical Meteorology* 68 (1), p. 30967. DOI: 10.3402/tellusb.v68.30967.
- World Health Organisation (2009). *WHO handbook on indoor radon: a public health perspective*. World Health Organisation.
- World Health Organisation (2021). *World Health Organisation Fact Sheets: Radon and Health*. World Health Organisation. URL: <https://www.who.int/news-room/fact-sheets/detail/radon-and-health>.
- Zhou, Q. et al. (May 2020). "Experimental study of dependence on humidity and flow rate for a modified flowthrough radon source". In: *Journal of Radioanalytical and Nuclear Chemistry* 324 (2), pp. 673–680. DOI: 10.1007/s10967-020-07081-0.
- Ziegler, J. F., M. Ziegler, and J. Biersack (June 2010). "SRIM – The stopping and range of ions in matter (2010)". In: *Nuclear Instruments and Methods in Physics Research Section B: Beam Interactions with Materials and Atoms* 268 (11-12), pp. 1818–1823. DOI: 10.1016/j.nimb.2010.02.091.

Declaration of Authorship

Hiermit versichere ich, dass die vorliegende Dissertation selbstständig verfasst und keine anderen als die angegebenen Quellen und Hilfsmittel verwendet wurden. Alle Stellen der Dissertation, die wörtlich oder sinngemäß aus anderen Quellen übernommen wurden, sind als solche kenntlich gemacht. Tabellen und Abbildungen, die nicht mit einer Quelle gekennzeichnet sind, wurden selbst erstellt. Ferner versichere ich, dass die vorliegende Dissertation noch nicht als Prüfungsarbeit für andere Prüfungen eingereicht worden ist.

Unterschrift:

Ort, Datum:

Curriculum Vitae

Personal

full name Florian Mertes
date of birth 1990-06-13
place of birth DE-84048 Mainburg

Academia

2018-2023 **Doctoral studies**
 Leibniz University Hannover
 thesis title: *"Primary ²²²Rn emanation standards for low-level applications"*

2013-2017 **Master studies Chemistry**
 University of Regensburg
 thesis title: *"Entwicklung einer Methode zur schnellen Charakterisierung gamma-strahlender Radionuklide in Lebensmitteln"*

2009-2013 **Bachelor studies Chemistry**
 University of Regensburg
 thesis title: *"Graphen aus chemischer Gasphasenabscheidung und chemisch reduziertes Graphenoxid im Vergleich als sensitive Schicht zur Gasedektion"*

Professional

since 03/2022 **Scientific Officer**
 Federal Office for Radiation Protection, BfS

2017-02/2022 **Scientist/Doctoral Student**
 Physikalisch-Technische Bundesanstalt, PTB Braunschweig

Education

until 2009 **Abitur, Gabelsberger Gymnasium Mainburg**

Publications

Peer-reviewed articles

- Ballé, T. J., S. Röttger, F. Mertes, A. Honig, P. Kovar, P. Otáhal, and A. Röttger (2023). "Two new ^{222}Rn emanation sources – a comparison study [preprint]". In: *EGUsphere* 2023, pp. 1–19. DOI: 10.5194/egusphere-2023-1158.
- Mertes, F., S. Röttger, and A. Röttger (Apr. 2023a). "Approximate sequential Bayesian filtering to estimate ^{222}Rn emanation from ^{226}Ra sources using spectral time series". In: *Journal of Sensors and Sensor Systems* 12, pp. 147–161. DOI: 10.5194/jsss-12-147-2023.
- Röttger, S., A. Röttger, F. Mertes, V. Morosch, T. Ballé, and S. Chambers (Feb. 2023). "Evolution of traceable radon emanation sources from MBq to few Bq". In: *Applied Radiation and Isotopes* 196, p. 110726. DOI: 10.1016/j.apradiso.2023.110726.
- Chambers, S. D., A. D. Griffiths, A. G. Williams, O. Sisoutham, V. Morosh, S. Röttger, F. Mertes, and A. Röttger (2022). "Portable two-filter dual-flow-loop ^{222}Rn detector: stand-alone monitor and calibration transfer device". In: *Advances in Geosciences* 57, pp. 63–80. DOI: 10.5194/adgeo-57-63-2022.
- Mertes, F., S. Röttger, and A. Röttger (Jan. 2022a). "Development of ^{222}Rn Emanation Sources with Integrated Quasi 2π Active Monitoring". In: *International Journal of Environmental Research and Public Health* 19, p. 840. DOI: 10.3390/ijerph19020840.
- Röttger, S., A. Röttger, C. Grossi, A. Vargas, U. Karstens, G. Cinelli, E. Chung, D. Kikaj, C. Rennick, F. Mertes, and I. Radulescu (Mar. 2022). "Radon metrology for use in climate change observation and radiation protection at the environmental level". In: *Advances in Geosciences* 57, pp. 37–47. DOI: 10.5194/adgeo-57-37-2022.
- Mertes, F., N. Kneip, R. Heinke, T. Kieck, D. Studer, F. Weber, S. Röttger, A. Röttger, K. Wendt, and C. Walther (Dec. 2021b). "Ion implantation of ^{226}Ra for a primary ^{222}Rn emanation standard". In: *Applied Radiation and Isotopes* 181, p. 110093. DOI: 10.1016/j.apradiso.2021.110093.
- Pierre, S., P. Cassette, B. Sabot, C. Fréchou, A. Antohe, C. Barna, P. Blahușiak, F. Cardellini, R. Dersch, A. Honig, F. Juget, M. Krivošik, A. Luca, F. J. Maringer, F. Mertes, S. Röttger, M. Sahagia, J. Slučiak, M. Stietka, L. Szücs, and C. Teodorescu (Aug. 2021). "International comparison of activity measurements of radon 222 - EURAMET Project n°1475 - EURAMET.RI(II)-S8.Rn-222". In: *Metrologia* 58.1A, p. 06015. DOI: 10.1088/0026-1394/58/1A/06015.
- Röttger, A., S. Röttger, C. Grossi, A. Vargas, R. Curcoll, P. Otahal, M. Á. Hernández Ceballos, G. Cinelli, S. Chambers, S. Barbosa, M.-R. Ioan, I. Radulescu, D. Kikaj, E. Chung, T. Arnold, C. Yver, M. Fuente, F. Mertes, and V. Morosh (Sept. 2021). "New metrology for radon at the environmental level". In: *Measurement Science and Technology* 32. DOI: 10.1088/1361-6501/ac298d.
- Mertes, F., S. Röttger, and A. Röttger (Oct. 2019a). "A new primary emanation standard for Radon-222". In: *Applied Radiation and Isotopes* 156, p. 108928. DOI: 10.1016/j.apradiso.2019.108928.

Oral and poster presentations

- Mertes, F.** (2023). "Assessment of potential radiological consequences of nuclear detonations using dispersion modeling". In: presented at the Global Conference on Radiation Topics - Preparedness, Response, Protection, Research (ConRad), Munich.
- Mertes, F., S. Röttger, and A. Röttger** (2021a). "Approximate Sequential Bayesian Filtering to Estimate Rn-222 Emanation from Ra-226 Sources from Spectra". In: presented at the Sensors and Measurement Science International, Nuremberg. DOI: 10.5162/SMSI2021/D3.3.
- Mertes, F., S. Röttger, and A. Röttger** (2019b). "A new primary emanation standard for Radon-222". In: presented at the 22nd International Conference on Radionuclide Metrology and its Applications (ICRM), Salamanca.
- Mertes, F., S. Röttger, and A. Röttger** (2019c). "New primary emanation standard for Rn-222". In: presented at the EURADOS Annual Meeting, Winter-School, Łódź.
- Mertes, F., S. Röttger, A. Röttger, R. Heinke, T. Kieck, N. Kneip, D. Studer, and K. Wendt** (2019d). "Ion-Implanted Ra-226 as a primary Rn-222 emanation standard". In: presented at the DPG-Frühjahrstagung der Sektion kondensierte Materie, Regensburg.
- Mertes, F.** (2018). "New Radon sources for low-level calibrations [poster]". In: presented at the 5th European IRPA Congress, The Hague.
- Mertes, F., S. Röttger, A. Röttger, and A. Honig** (2018). "Entwicklung von Radonquellen für die Erzeugung von low-level Referenzatmosphären". In: presented at the DPG-Frühjahrstagung der Sektion Materie und Kosmos, Würzburg.

Acknowledgments

Zunächst gilt mein aufrichtiger Dank allen, die mich während der Zeit meiner Promotion unterstützt haben.

Insbesondere aber danke ich sowohl aus fachlicher, als auch persönlicher Sicht Dr. Annette Röttger und Dr. Stefan Röttger, die stets vollstes Vertrauen in mich hatten und mir in der PTB die besten Voraussetzungen für meine Arbeit geschaffen haben. Immer konnte ich neue Ideen, Entwicklungen oder Ansätze vorurteilslos ansprechen und selbst Unkonventionelles mit vollster Unterstützung in die Tat umsetzen. Ohne diesen Beistand wäre das, vorwiegend die Innovation des "IRSD", nicht möglich gewesen. Ich danke auch allen Kolleginnen und Kollegen aus den Arbeitsgruppen 6.11, 6.12 und 6.13 der PTB, die sich, während der vielen Routineaufgaben, stets Zeit für mich genommen haben und selbst meine oft schwierigen Anfragen mit mir besprochen, verbessert und jederzeit sehr gut umgesetzt haben. Besonders danke ich hierfür Frank Stephan, Thomas Reich, Anja Honig, Peggy Jessica Krause, Gerrit Heine und Dr. Daniel Zapata García, welche mir sehr gute Anregungen geliefert haben, den Kontakt zu weiteren, notwendigen Personen in der PTB für mich hergestellt haben, und mir oft auch einfach ein offenes Ohr und viele gute Witze während den Kaffeepausen geschenkt haben.

Darüber hinaus danke ich meiner Lebenspartnerin Kristina Schweiger, die mit mir gemeinsam den Weg nach Braunschweig gegangen ist. Sie hat mir immer geduldig den Rücken gestärkt und ist bedingungslos die ganze Zeit über an meiner Seite gewesen, hat mich wenn es gewünscht war auch mal von der Arbeit abgelenkt und mir viele, viele andere Aufgaben abgenommen.

Des Weiteren danke ich Prof. Dr. Clemens Walther dafür, dass er die universitäre Betreuung dieser Arbeit übernommen hat, mir viele, sehr gute Ideen geliefert hat, mich stets ermutigt hat und immer einen Weg zur Umsetzung meiner Anfragen gefunden hat.

Außerdem bedanke ich mich bei Prof. Dr. Klaus Wendt und seiner Arbeitsgruppe an der Universität Mainz, insbesondere Dr. Nina Kneip, Dr. Tom Kieck und Dr. Dominik Studer, für die gute Zeit und die gute Zusammenarbeit am RISIKO in Mainz.

Nicht zuletzt bedanke ich mich bei meinen Eltern und meiner Schwester, die immer an mich geglaubt haben, mich motiviert haben und es mir ermöglicht haben, diesen Weg zu gehen.